Magnetic and Electronic Structure of Frustrated Antiferro/Ferrimagnetic Pyrochlore Spinels

A Thesis Submitted to
Indian Institute of Technology Guwahati
for the degree of

Doctor of Philosophy

By

Prativa Pramanik

Roll. No: 156121022

Department of Physics
Indian Institute of Technology Guwahati
Guwahati-781039, Assam (India)

To

My Family and Teachers

INDIAN INSTITUTE OF TECHNOLOGY GUWAHATI

Department of Physics

Guwahati – 781039

Declaration

"Magnetic and Electronic Structure of Frustrated Antiferro/Ferrimagnetic Pyrochlore Spinels" is the result of my own doctoral research work. This work was carried out under the supervision of Dr. Subhash Thota at the Department of Physics, Indian Institute of Technology Guwahati. To the best of my knowledge, the work presented in this thesis has not been submitted to any other Institute/University for the award of any degree.

Prativa Pramanik
Research Scholar
Roll No: 156121022
Department of Physics
Indian Institute of Technology Guwahati
Guwahati-781039, India

INDIAN INSTITUTE OF TECHNOLOGY GUWAHATI

Department of Physics

Guwahati – 781039

Certificate

It is certified that the work described in this thesis, entitled "Magnetic and Electronic Structure of Frustrated Antiferro/Ferrimagnetic Pyrochlore Spinels", done by Ms. Prativa Pramanik, a Ph.D. student of Department of Physics, Indian Institute of Technology Guwahati, for the award of degree of Doctor of Philosophy has been carried out under my supervision. This work has not been submitted elsewhere for the award of any degree.

Dr. Subhash Thota
Associate Professor
Department of Physics
Indian Institute of Technology Guwahati
Guwahati-781039, India

Synopsis Report

The concept of geometrical frustration in magneto ceramics provide an intriguing platform for the scientists to understand the magnetic interactions at the fundamental level [19,20,24,76]. Usually, frustration in a spin system can give rise to unique ordered states and as a consequence several novel physical phenomena can be expected, among them the most important being; multiferroics, reentrant spin-glass behavior, quantum spin-liquid state, anomalous Hall effect, sign reversal exchange bias, giant magneto-caloric effect, canted ordering (Yafet-Kittel and spiral), and high-temperature superconductors [13,77,80,81]. Recently, cubic spinels AB_2O_4 with magnetic *B* ions (occupying the octahedral sites) have attracted much interest in the light of the geometrical frustration which is inherent at the *B*-site sublattice of corner-sharing tetrahedral [22]. Among the family of magnetic spinels cobalt orthogermanate $GeCo_2O_4$ shows highly frustrated magnetic properties below its anti-ferromagnetic ordering temperature ($T_N \sim 20.3$ K) due to the competing spin-orbital exchange interactions among the Co^{2+} cations [137,138]. This compound contains pyrochlore-like lattice structure for the magnetic Co^{2+} ions (*B*-site), for which magnetic frustration is inherently present as first pointed out by Anderson [136]. Interesting fact of this system is that it exhibits cubic to tetragonal crystal structure transition and displays three field induced transitions below 16 K (T_D) [146]. Despite a number of reports available on this system, the question of the nature of magnetic ground state with effective spin S = 1/2 versus S = 3/2 was not unambiguously determined when we initiated this work. Hence, in this Thesis work an attempt was made to understand the magnetic ground state of this system by reestablishing the *H-T* phase diagram with a proper interpretation of the temperature dependence of the paramagnetic susceptibility in terms of the High-Temperature series expansion associated with the Curie-Weiss law or more elaborate models and its correlation with the measured values of the magnetization for temperatures below antiferromagnetic Néel temperature (T_N). Besides geometrical frustration, spinel oxides also exhibit features such as negative magnetization including compensation phenomena, magnetoelectric coupling and tunable exchange-bias [13,77,84-90,229-241]. In this direction we have also chosen an inverse spinel, $MnCo_2O_4$, aiming to understand its magnetic ordering and cationic distribution by systematic site-dilution with Jahn-Teller active ions such as Ti and Cu. In total the present Thesis consists of seven Chapters and the layout of the thesis work is given below:

Chapter 1 provides a brief introduction to the spinel compounds, concepts of geometrical frustration, exchange-bias, magnetic exchange interactions in triangular and Kagomé lattice based on molecular field theory. This chapter also reviews an important up-to-date research on the reentrant spin-glass behavior negative magnetization, canted spin configuration in spinels (Yafet-Kittle type) and magnetic compensation phenomena. This chapter also provides the motivation behind the present research work and a general overview of the selected compounds.

Chapter 2 describes an overview of various experimental techniques employed in this research work including the synthesis procedure using standard solid-state reaction method and low-temperature sol-gel processing (for the synthesis of Nanostructures). This chapter also presents the structural characterization of the samples using x-ray and electron diffraction techniques. For the verification of phase purity of the samples we performed the Rietveld refinement of diffraction data using Fullprof and Powder-cell software. Details of elemental analysis performed by the X-ray photoelectron spectroscopy (XPS) and morphology/microstructure characterization of the nanostructures by transmission electron microscopy (TEM) was described thereafter.

In the subsequent sections we discussed the basic of neutron diffraction studies, low-temperature magnetic measurements using superconducting quantum interference device (SQUID) based magnetometer.

Chapter 3 presents a detailed electronic structure, magnetic properties of $GeCo_2O_4$ polycrystalline samples. The high resolution XPS studies reveal the evidence for tetra and divalent electronic states of Ge and Co ions, respectively in $GeCo_2O_4$. Whereas the Rietveld refinements of the XRD patterns confirm that the Ge^{4+} and Co^{2+} ions occupying the tetrahedral and octahedral sites, respectively. Our results demonstrate that $GeCo_2O_4$ orders antiferromagnetically (AFM) at T_N = 20.4 K but with significant short-range ferromagnetic (FM) order up to $T \sim 5T_N$. The paramagnetic susceptibility (χ) fitted with the modified Curie–Weiss law ($\chi = \chi_o + C/(T - \theta)$), with θ = +51 K for 100 K < T < 800 K. Also, the high-temperature-series expansion of $\chi(T)$ yields the exchange constant J_1/k_B = 14.7 K as the dominant FM exchange coupling for the pyrochlore lattice of Co^{2+} spins consist of alternate planes of Kagomé (KGM) and Triangular (TRI) spins lying perpendicular to [111] direction. Three critical magnetic fields (H_d, H_{C1} and H_{C2}) are identified from the differential M-H hysteresis plots recorded at low temperatures (2 K) in which $H_d \sim$ 11 kOe occurs due to AFM domain orientation, $H_{C1} \approx$ 44 kOe is associated to spin-flips and FM ordering of the TRI spins, and $H_{C2} \approx$ 97 kOe is related to FM ordering of the KGM spins. For $H > H_{C2}$, $GeCo_2O_4$ acts as a forced ferromagnet with canted spin configuration. This chapter also discusses the H-T phase diagram constructed from the magnetic field dependence of T_N (i.e. $T_N(H)$) along with the temperature dependence of H_d, H_{C1}, and H_{C2}. Interestingly, $T_N(H)$ follows the relation $T_N(H) = T_N(0) - D_1H^2$ obtained from the mean-field theory which perfectly validating the antiferromagnetic ordering of spins with D_1 = 6.63×10^{-10} K/Oe^2. From the magnitudes of the Curie-constant (C) and the saturation magnetization ($M_S \sim$34,372 emu/mol) at 2 K it is shown that Co^{2+} ions in $GeCo_2O_4$ have the ground state with effective spin S = 1/2. This chapter also deals with the band structure analysis and density of states obtained from the first principle calculation based on DFT+U of $GeCo_2O_4$ system which are in good agreement with the experimental findings.

Chapter 4 presents a systematic study of the magnetic ordering in B-site Mn diluted $TiCo_2O_4$ ($Mn_xTi_{1-x}Co_2O_4$) using neutron diffraction, ac-magnetic susceptibility and dc-magnetization in the temperature interval 2 K ≤ T ≤ 300 K in a great detail. Our observations provide evidence for reentrant spin-glass behaviour in $Ti_{0.6}Mn_{0.4}Co_2O_4$ with freezing temperature ~ 110.1 K below the ferrimagnetic ordering ~ 110.3 K. Significant cooperative distortions of the T_BO_6 octahedra (T being B-site cation) has been noticed in $Mn_xTi_{1-x}Co_2O_4$ system for all the Jahn-Teller active ions T_B = Mn^{3+}, Ti^{3+} and Co^{3+} ions, having the electronic configurations $3d^1$, $3d^4$ and $3d^6$, respectively which are confirmed by the x-ray photoelectron spectroscopy. Two specific compositions (x = 0.2 and 0.4) have been chosen in this study because these two systems show unique features such as; (*i*) Noncollinear Yafet-Kittel type magnetic ordering, and (*ii*) Weak tetragonal distortion with c/a < 1, in which the apical bond length d_c(T_B-O) is longer than the equatorial bond length d_{ab}(T_B-O) due to the splitting of e_g level of Mn^{3+} ions into a $d_{x^2-y^2}$ and d_{z^2}. For the composition x = 0.4, the distortion in the T_BO_6 octahedra is stronger as compared to x = 0.2 because of the higher content of trivalent Mn. Ferrimagnetic ordering in $Ti_{0.6}Mn_{0.4}Co_2O_4$ and $Ti_{0.8}Mn_{0.2}Co_2O_4$ sets in at 110.3 and 78.2 K, respectively due to the unequal magnetic moments of cations occupying at octahedral (Ti^{3+}, Mn^{3+}, Co^{3+}) and tetrahedral (Co^{2+}) sites. For both compounds an additional weak antiferromagnetic component could be observed lying perpendicular to the ferrimagnetic component. The composition $Ti_{0.8}Mn_{0.2}Co_2O_4$ exhibits negative magnetization and magnetic compensation effect at T_{COMP} = 25.4 K along with weak spin-glass like nature. However, the composition $Ti_{0.6}Mn_{0.4}Co_2O_4$ exhibits re-entrant spin-glass behaviour with freezing temperature ~ 110.1 K. The magnetic compensation effect in $Ti_{0.8}Mn_{0.2}Co_2O_4$ is characterized by sign reversal of exchange bias effect below T_{COMP} with its magnitude depending on the

direction of external magnetic field and the cooling protocol. This chapter also presents a systematic correlation between the heat-capacity data and temperature dependence of magnetization.

Chapter 5 focuses on the nature of magnetic ordering and cationic distribution of the polycrystalline bulk inverse spinels $MnCo_2O_4$ and $MnCo_{2-x}Cu_xO_4$. This chapter also deals with a thorough neutron diffraction studies of these samples at different temperatures between 2 K and 300 K for two selected compositions x = 0 and 0.2. These results provide evidence for weak tetragonal (space group $I4_1/amd$) distortion in which the Co_A and Cu_A are located at the Wyckoff position $4b(0,\frac{1}{4},\frac{3}{8})$, while the B site cations Mn^{3+} and Co^{3+} ions are positioned at $8c(0,0,0)$. The nuclear (N) and magnetic (M) reflections reveal that the strongest magnetic contribution arises from the coherent Bragg reflections (101) and (200)/(112) with spin sequences + + – – and + – + – below T_{FN}. Analysis of these results provide the evidence for noncollinear spin arrangement and weak tetragonal distortion with $c/a < 1$. Both the systems exhibit ferrimagnetic (FI) ordering below 184 K and 171.8 K with net moment $2\mu_{FI}(Mn_B/Co_B) - \mu_{FI}(Co_A) = 0.89\ \mu_B$ and $2\mu_{FI}(Mn_B/Co_B) - \mu_{FI}(Co_A/Cu_A) = 1.93\ \mu_B$ for x = 0 and 0.2, respectively at 2 K. Nonetheless, the temperature dependence of net ferrimagnetic moment $\Delta\mu_{FI}(T)$ exhibit a maximum (2.081 μ_B) at 154.1 K for x = 0.2, whereas, the undoped system does not exhibit any cusp in $\Delta\mu_{FI}(T)$. The presence of additional magnetic reflections (110) and (002) in both the compositions suggest the loss of a least one of the d-glide planes signifies the existence of additional antiferromagnetic component lying perpendicular to the ferrimagnetic component.

Chapter 6 is devoted to the nanostructures of Cu and Zn substituted $MnCo_2O_4$ where a detailed investigation of the dilution effects on the electronic structure and magnetic properties has been made. From the XPS and the Rietveld analysis of XRD patterns the cationic distribution of these nanostructures are determined as: $(Co_{1-x}^{2+}\Sigma_x)_A[Mn^{3+}Co^{3+}]_BO^{2-}$ and $(Co^{2+})_A[Mn_{1-x}^{3+}Zn_x^{2+}Co^{3+}]_BO_{1\pm\delta}^{2-}$ (where Σ: Cu and Zn) i.e. Cu^{2+}/Zn^{2+} substitutes on the tetrahedral-A or octahedral-B sites. In $MnCo_{2-x}Cu_xO_4$ samples the ferrimagnetic Néel temperature T_{FN} = 165 K for x = 0 is significantly lowered to T_{FN} = 155 K for the x = 0.2 sample and this decrease is interpreted to be the effect of Cu doping. On the other hand, the dc-magnetic susceptibility of the Zn substituted $MnCo_2O_4$ compounds reveal the presence of ferrimagnetic ordering of $T_{FN} \sim$ 157 K for 10 at% Zn dilution at tetrahedral A-site and 127 K for the 20 at% of Zn doped at the octahedral B sits. However, the analysis of temperature dependence of ac-susceptibility studies reveals that these nanocrystallites exhibit reentrant spin-glass transition just below T_{FN}. Further analysis using the dynamic scaling laws; namely Vogel-Fulcher law and Power law, of χ_{ac}-T we evaluated the spin-glass temperature T_F and other related parameters: T_F = 162.5 and 138.16 K, critical exponent $z\nu$ = 6.01 and 8.91, relaxation time $\tau_0 = 1.6\times10^{-8}$ and 8.9×10^{-11}s and activation energies E_a = 12.6 and 16.5 k_B for the Cu compositions x = 0 and 0.2, respectively. Similarly, for $Mn_{0.8}Zn_{0.2}Co_2O_4$ and $MnCo_{1.9}Zn_{0.1}O_4$ system we obtained $\tau_0 = 4.4\times10^{-15}$ and 5.4×10^{-14}s, T_F = 125.7 and 154.3 K, $z\nu$ = 6.17 and 5.2 and E_a = 29.8 and 10.6 k_B, respectively. The linear behavior of the peak maximum in $\chi_{ac}(T)$ versus $H_{dc}^{2/3}$ (AT-line) further supports the existence of glassy states in these nanocrystallites. At the end of this chapter we provide a detailed analysis of the exchange constants (J_{ij}) evaluated for both the systems using $\chi^{-1}(T)$ data for $T > T_{FN}$ by fitting the Néel's expression for two-sublattice model which follows the general trend shown by the inverse spinels i.e. $J_{AB} > J_{BB} > J_{AA}$ among the A and B cations.

Chapter 7 presents a brief summary of important findings of our experimental results. In this chapter we also identify some open issues which are potentially interesting for the future studies.

List of Publications:

Peer Reviewed Journals:

[1] "*Neutron diffraction evidence for local spin canting, weak Jahn–Teller distortion, and magnetic compensation in $Ti_{1-x}Mn_xCo_2O_4$ spinel*",
P. Pramanik, D. C. Joshi, M. Reehuis, A. Hoser, J.-U. Hoffmann, R. S. Manna, T. Sarkar and S. Thota
Journal of Physics: Condensed Matter **32**, 245801 (2020).

[2] "*Magnetic ground state, field-induced transitions, electronic structure, and optical band gap of the Frustrated antiferromagnet $GeCo_2O_4$*",
P. Pramanik, S. Ghosh, P. Yanda, D. C. Joshi, S. Pittala, A. Sundaresan, P. K. Mishra, S. Thota and M. S. Seehra
Physical Review B. **99**, 134422 (2019).

[3] "*Cubic phase stability, optical and magnetic properties of Cu-stabilized zirconia nanocrystals*",
P. Pramanik, S. Singh, D. C. Joshi, A. Mallick, K. Pisane, A. H Romero, S. Thota and M. S. Seehra
Journal of Physics D: Applied Physics **51**, 225304 (2018).

[4] "*Cationic distribution, exchange interactions, and relaxation dynamics in Zn-diluted $MnCo_2O_4$ nanostructures*",
P. Pramanik, D. C. Joshi, N. Tiwari, T. Sarkar, S. Pittala, O.O. Salman, M.-M. Manga, and S. Thota
Journal of Applied Physics **125**, 124302 (2019).

[5] "*Effects of Cu doping on the electronic structure and magnetic properties of $MnCo_2O_4$ nanostructures*",
P. Pramanik, S. Thota, S. Singh, D. C Joshi, B. Weise, A. Waske and M. S. Seehra
Journal of Physics: Condensed Matter **29** (42), 425803 (2017).

[6] "*Size-dependent structural, magnetic, and optical properties of $MnCo_2O_4$ nanocrystallites*",
S. Singh, P. Pramanik, S. Sangaraju, L. Giebeler, and S. Thota
Journal of Applied Physics **121**, 194304 (2017).

Research work presented in international/national conferences and workshops:

[1] "Phase Stability of $ZnCo_2O_4$ Nanostructures and their Magnetic Properties",
P. Pramanik, S. Singh, S. K. Jena, S. Mehta, S. Ghosh, and S. Thota
2nd International Conference on Nanoscience and Nanotechology, November 29,2019 - December 1, 2019, Center for Nanotechnology Research, Vellore Institute of Technology, Vellore, India.

[2] "*Altered Antiferromagnetic State and Exchange Bias of Bulk Co_3O_4 Granular Matrix Dispersed in Nonmagnetic CeO_2*"
S. Singh, P. Pramanik, D. C. Joshi and S. Thota
Research Conclave-2019, 14-17 March 2019, IIT Guwahati, India.

[3] "*Compositional dependence of Vibrational Excitations in Fe substituted $MnCo_2O_4$ Ferrimagnetic Spinels*"
S. Singh, P. Pramanik, S. K. Jena, B. Yadav, M. Sehrawat and S. Thota
UGC-SAP (DRS II) Sponsored Second National Conference On Hard and Soft Condensed Matter Physics, (NCHSCMP-2019), March 4-6,2019, Tezpur, Assam, India.

[4] "*High Temperature Dielectric Behavior of Spin-1/2 Frustrated Kagome Magnet $Co_3V_2O_8$*"
A. Thakur, P.Pramanik, D. C Joshi, A. Meher and S. Thota
Research Conclave-2018, 8-11 March 2018, IIT Guwahati, India.

[5] "*Optical and Magnetization studies $MnCo_{2-p}Cu_pO_4$ Ferrimagnetic Spinels*"
P.Pramanik, D. C. Joshi, and S. Thota
International Conference on Advanced Functional Materials (ICAFM 2017) 18-20, December, 2017, RGUKT, Basar, Nirmal-504107, Telangana State, India.

[6] "*Vibrational Excitations in Ferrimagnetic Spinel $MnCo_2O_4$*"
P. Pramanik, D. C. Joshi, S. Ghosh, T. A. Dar, R. T. George, and S. Thota
National Workshop on Fluorescence and Raman Spectroscopy December 17-21, 2017, IIT Guwahati-781039, India.

[7] "*Finite-Size effects in the Optical and Magnetic Properties of $MnCo_2O_4$ Nanostructures*"
S. Singh, P. Pramanik, M. S. Seehra and S. Thota
American Physical Society (APS) March 13–17, 2017, New Orleans, Louisiana (USA), Bulletin of the American Physical Society.

[8] "*Quantum-size effects in $MnCo_2O_4$ Nanocrystals*"
P. Pramanik, S. K. Singh, R. Soni, D. C. Joshi, S. Nayak and S. Thota
International Conference on Nanomaterials and Nanotechnology (ICNANO-2017), 1-3 March 2017, VBRI-Allahabad, India.

[9] "*Structural, Magnetic, Micro-Raman and Electron Spin Resonance Studies of $MnCo_2O_4$ Bulk and Nanostructures*"
P. Pramanik, S. Ghosh, D. C. Joshi, S. Nayak, and S. Thota
National Seminar on Advances in Material Sciences 24-25th March 2017 Gauhati University, Assam, India.

[10] "*Ferrimagnetic behavior and Optical properties of $MnCo_{2-p}Cu_pO_4$Nanostructures*"
P. Pramanik, D. C. Joshi, and S. Thota
National Conference on Nanomaterials and its Applications (NCNA-17), 20-21 Sept, 2017, Golaghat, Assam, India.

[11] "*X-ray Photoelectron Spectroscopy and Optical properties of $MnCo_2O_4$ Nanostructures*"
P. Pramanik, D. C. Joshi, S. Nayak, S Sambasivam, B. C. Choi, and S. Thota
2nd International Conference on Materials Science and Technology (ICMST), 5-8 June, 2016 St. Thomas College Pala Arunapuram, Kottayam, Kerala, India.

Acknowledgements

I am delighted to have the opportunity to express my sincere gratitude towards a number of people who supported and supervised me to successfully complete the work presented in this thesis. Firstly, I owe enormous thanks to my research supervisor Dr. Subhash Thota for his dedicated help, advice, inspiration, encouragement and continuous support. I would like to extend my sincere gratitude to my supervisor for introducing me to this new exciting field of science and for providing high-quality work. Over the course of the last five years' research work, I have learnt many extensive knowledge from him, including how to raise new possibilities, and how to approach a problem by systematic analysis. I am extremely thankful to him for his valuable suggestions and guidance to complete the work and for providing a friendly, learning and exciting environment to carry out my thesis work. I would like to express my sincere thanks to my doctoral committee members, Prof. Padma K. Padmanabhan (DC-chairman), Dr. Uday N. Maiti and Dr. Nageswara Rao Peela for their valuable time and patience through all these years. Their critical comments and excellent suggestions guided me to complete the work. I sincerely thank to Prof. S. Ghosh and Prof. P. Poulose, present and former Head of the Department of Physics, for provided me all the facilities to carry out this research work.

My special words of thanks should go to my guide for introducing me with Prof. Mohindar Singh Seehra an Eberly Distinguished Professor Emeritus from the Department of Physics & Astronomy, West Virginia University, USA. I wish to express my sincere thanks and gratitude towards Prof. M. S. Seehra for sharing his time and knowledge with us. He has played a major role in making me understand the concept and been a source of knowledge. Thank you so much sir for your guidance and continuous support. I am grateful to Dr. Manfred Reehuis from Helmholtz-Zentrum Berlin, Germany for his great support in guiding us how to write the research proposal for neutron scattering measurements and for sharing his knowledge with us. I would like to express my sincere thanks to Dr. Manfred. Reehuis, Dr. Andreas Hoser and Dr. Jens-Uwe Hoffmann for helping me to complete my research work by measuring the neutron diffraction data for my reasearch sample. Thanks to Manfred sir for answering my stupid questions and help us in analysing the data and writing the research paper. I am very grateful to Dr. Bruno Weise, Dr. Anja Waske, Dr. Sobhit Singh, Dr. Suresh Pittala, Dr. Rudra Sekhar Manna and Dr. Tapati Sarkar for supporting me by providing the SQUID based magetic measurements reported in this thesis. I also acknowledge the funding agencies DST-FIST and the Central Instruments Facility (CIF) of IIT Guwahati for supporting my research work.

I am very greatful to my senior Dr. Deep chandra joshi who has helped me in numerous way from the begining time till the present day. He teaches me how to synthesized the research sample, experiments and the data analysis procedure. Many thanks for your supports. A special thank to Dr. Sobhit Singh and Mr. Sayandeep Ghosh for sharing their knowledge and helping me in theoritical analysis. I thank Ayush Vardhan Singh and Shashank Ulhare for helping me in proof reading some of the chapters. I acknowledge my present and former lab fellow and intern students; Dr. D. C. Joshi, Sayandeep, Suchit, Shaona, Ravi, Maruthi, Monica, Harish, Sai, Ameer, Anshul, Swati, Ruchika, Sameeksha, Sweta, Subhadra, Sarmistha, Kamal, Praneet, Bikash, Atyant, Soumya, Shouriya, Shalini, Ayush, Shashank, Akshit, Mahesh, Tere, Bhupesh, Mahender for their loving support and pleasent company.

My special regards to my all teachers whose teaching at different stages of education has made it possible for me to continue the research work. I thank to all of my dear friends for thair constant support and cooperation. Their help and friendship shall always be remembered. I am grateful to my institute and department for providing me research funding and experimental facility. I also grateful to my departmental, librarian and administrative staff for their kind cooperation.

I would like to express my sincere thanks to all the family members of my supervisor. I feel very fortunate to have had the opportunity to interact with them and spent a memorable time. I warmly thank to subhash sir, Revathi madam, Veda Samhitha, Sir's parents, Mounica, Harish, Sai and Deep for making my days so much joyful and memorable. My thanks to everyone.

I am deeply thankful to my dear parent Shri Kamaleh Pramanik and Shrimati Anima Pramanik, sister Miss Soma Pramanik and Masi Shrimati Reba Halder for their unconditional love, care and moral support that has always been my strength. I am also very much grateful to my grandparents and all my family members for their constant inspiration and encouragement. This last word of acknowledgment I have saved for Lord Shiva who is the biggest source of my strength, from my deepest I would like to express heartfelt thanks to him for everything.

Prativa Pramanik
Roll No. 156121022
IIT Guwahati, Assam, India
16th March 2020

Contents

List of Figures

List of Tables

List of Abbreviations and Symbols

XRD — X-ray diffraction
XPS — X-ray Photoelectron spectroscopy
B.E. — Binding Energy
T_C — Ferromagnetic Curie temperature
T_N — Anti-ferromagnetic Néel temperature
T_{FN} — Ferrimagnetic Néel temperature
h — hours
ZFC — Zero-Field Cooled
FC — Field Cooled
FM — Ferromagnet
AFM — Anti-ferromagnet
FIM — Ferrimagnet
Å — Angstrom
χ — Magnetic susceptibility
K — Kelvin
M — Magnetization
H — Magnetic field
T — Temperature
U — Coulombic parameter
μ_B — Bohr magnetron
KGM — Kagomé
TRI — Triangular
K-M — Kubelka-Munk
DOS — Density of states
TEM — Transmission-electron micrograph

Chapter 1

Introduction to Correlated Electron Systems: Focus on Oxide Spinels

Background and Motivation

Majority of the research work studied in this thesis is focused on the complex behaviour of strongly correlated systems such as: magnetic ground state using the neutron diffraction, re-entrant spin-glass behaviour, sign-reversal exchange-bias, weak John-Teller distortion and variation in the exchange interactions resulting from disorder. In this chapter we precisely discuss the concepts like complex mixed phase behaviour such as coexistence of magnetic long-range order (LRO) and re-entrant spin glass (RSG) properties in diluted spinels. In the following sections we first briefly describe some of the basic concepts linked to the above mentioned phenomena including the motivation and objectives of the work.

1.1 Magnetic Ordering and Interactions:

It is well known that the atoms comprise many electrons, each spinning about its own axis and moving in its own orbit. Thus, the magnetic moment associated with each kind of motion is a vector quantity, parallel to the axis of spin and normal to the plane of the orbit. Magnetization (*M*) of a material depends on the individual magnetic moments of its constituent elements. The magnitude of magnetization *M* is defined as the magnetic moment (μ) per unit volume. The response of a material in the presence of external magnetic field (*H*) is called magnetic induction or magnetic flux density *B*. In vacuum the general relationship between all the three quantitates *B*, *H* and *M* can be expressed as: $B = \mu_0(H + M)$, where *M* is the characteristic feature of the material. The magnetic properties of materials can be directly measured using various techniques involving the response of the materials in the presence of externally applied magnetic field. Thus, it is important to introduce the quantity called magnetic susceptibility (χ) which is defined as the ratio of differential change in the *M* with respect to *H* ($\chi = dM/dH$). If *M* is parallel to the *H*, $M = \chi H$ with χ being the magnetic susceptibility of the material and is called the linear material. Therefore, in this case a linear relationship between *B* and *H* is applicable $B = \mu_0(1 + \chi)H = \mu_0\mu_r H$ with $\mu_r = 1 + \chi$ being the relative permeability. Typical magnitudes for the relative permeability are; $\mu_r = 1$ for vacuum, inside the magnetic material usually $\mu_r \geq 1$ which can exceed as high as 10^6-10^5 for strong magnets such as Metglas (amorphous metal alloy ribbon) and Permalloy (alloy with 80% nickel and 20% iron content). The following section provides the mathematical basis for the atoms when placed in a magnetic field. The first systematic measurements of the χ was made by Pierre Curie in 1895 in a large number of substances over a wide range of temperatures.

1.1.1 Atoms in a Magnetic Field

The total energy of a single atom (containing Z electrons) is: $\mathrm{E} = \sum_{l=1}^{\mathrm{Z}}(\frac{\mathrm{p}_l{}^2}{2\mathrm{m}} + \mathrm{V}_l)$. Where, $\frac{\mathrm{p}_l{}^2}{2\mathrm{m}}$ represents the kinetic energy and V_l is the potential energy of the electron. However, when the atom is in an external magnetic field *B* then the corresponding Hamiltonian is; $H = \sum_{l=1}^{\mathrm{Z}} \mathrm{H}_l$.

$$\mathrm{H}_l = \frac{\mathrm{p}_l{}^2}{2\mathrm{m}} + \mathrm{V}_l + \frac{\mathrm{e}}{\mathrm{m}}\mathbf{A}.\mathbf{p} + \frac{\mathrm{e}^2}{2\mathrm{m}}\mathbf{A}.\mathbf{A} \qquad 1.1$$

Here H_l represents the Hamiltonian for the l^{th} electron and $\mathbf{A} = \frac{\mathbf{1}}{\mathbf{2}}(\boldsymbol{B} \times \mathbf{r})$ is the magnetic vector potential due to the external magnetic field *B*. The last two terms of equation 1.1 can be expressed as a function of external magnetic field as:

$$\mathbf{A}.\mathbf{p} = \frac{1}{2}(\boldsymbol{B} \times \mathbf{r}).\mathbf{p} = \frac{1}{2}(\mathbf{r} \times \mathbf{p}).\boldsymbol{B} = \frac{1}{2}\hbar\mathbf{L}.\mathbf{B} \text{ and } \mathbf{A}.\mathbf{A} = \frac{\mathbf{1}}{\mathbf{4}}(\mathbf{B} \times \mathbf{r})^{\mathbf{2}}$$

In the above equation, $\hbar\mathbf{L}$ represents the orbital angular momentum. Considering the electron spin angular momentum $\mathbf{S}$, the total Hamiltonian can be written as:

$$\mathrm{H} = \sum_{l=1}^{\mathrm{Z}}\left(\frac{\mathrm{p}_l{}^2}{2\mathrm{m}} + \mathrm{V}_l\right) + \mu_B(\mathbf{L} + g\mathbf{S}).\boldsymbol{B} + \frac{\mathrm{e}^2}{8\mathrm{m}}\sum_{l=1}^{\mathrm{Z}}(\boldsymbol{B} \times \mathbf{r_l})^{\mathbf{2}} \quad 1.2$$

Here, $\mu_B = \frac{e\hbar}{2m}$ is the Bohr magneton and $g = 2$ is the Lande g-factor of an electron. In the equation 1.2, last term $\frac{\mathrm{e}^2}{8\mathrm{m}}\sum_{l=1}^{\mathrm{Z}}(\boldsymbol{B} \times \mathbf{r_l})^{\mathbf{2}}$ represents the 'diamagnetic' contribution present in the material. Due to which the material shows a weak negative magnetization. Meaning the external magnetic field induces magnetic moments which are oriented antiparallel to the external field. However, $\mu_B(\mathbf{L} + g\mathbf{S}).\boldsymbol{B}$ term represents the 'Paramagnetic' contribution which is related to the positive magnetization, that is, the induced magnetic moments orientated parallel to an external magnetic field *B*.

Now we will briefly describe the magnetization of an atom assuming a non-vanishing magnetic moment due to unpaired electrons. Usually, the external magnetic field leads to the preferential orientation of the magnetic moments, such that the total magnetization depends on the magnitude of the external magnetic field and on temperature ($M \propto B/T$). The magnetic moment of an atom can be calculated by considering the total angular momentum $\boldsymbol{J} = \mathbf{L} \pm \mathbf{S}$. According to the Hund's rules J takes the sum value of L and S if the shell is more than half filled and on the contrary if the shell is less than half filled J takes the difference value of L and S. The total number of component of magnetic moment ($g\mu_B \mathrm{m}_J$) parallel to the magnetic field is $2J + 1$. Where m_J is the total magnetic orbital quantum number and take values from $+J$ to $-J$. Consequently, the total magnetization M for a number of atoms with a particular orientation can be determined by the Boltzmann factor $e^{m_J g\mu_B B/kT}$ as given below:

$$M = N\frac{\sum_{+J}^{-J}\mathrm{m}_J g\mu_B e^{m_J g\mu_B B/kT}}{\sum_{-J}^{+J}e^{m_J g\mu_B B/kT}} \quad 1.3$$

Substituting $x = g\mu_B B/kT$ in the above equation *M* can be rewritten as

$$M = Ng\mu_B\frac{d}{dx}ln\sum_{+J}^{-J}e^{m_J x} \quad 1.4$$

Expanding the summation one can obtain as: $\sum_{+J}^{-J}e^{m_J x} = e^{-Jx}(1 + e^x + e^{2x} + \ldots + e^{(2J-1)x} + e^{2Jx})$

Thus, equation 1.4 can be written as,

$$M = Ng\mu_B\frac{d}{dx}\left(lne^{-Jx}\,\frac{1-e^{(2J+1)x}}{1-e^x}\right)$$

$$= Ng\mu_B\frac{d}{dx}\left(ln\,\frac{\sinh\left[\frac{2J+1}{2}\right]x}{\sinh\left(\frac{x}{2}\right)}\right) \quad 1.5$$

By considering $y = g\mu_B JB/kT$, *M* can be can be expressed as,

$$M = Ng\mu_B J\left[\frac{2\mathrm{J}+1}{2J}\coth\left(\frac{2\mathrm{J}+1}{2J}\right)y - \frac{1}{2J}coth\frac{y}{2J}\right] \quad 1.6$$

$$= Ng\mu_B JB_J(y)$$

Here, $B_J(y)$ is popularly known as Brillouin function [1]. Let us define the saturation magnetization $M_\mathrm{S} = Ng\mu_B J$ and following the equation 1.6, the relative magnetization can be expressed in terms of Brillouin function as, $\frac{M}{M_\mathrm{S}} = B_J(y)$. Figure 1.1 shows the variation of the relative magnetization as a function of y for different magnitudes of J. At room temperature (T = 300 K), for $J = 1/2$, under $H \leq 10$ kOe external magnetic field the Brillouin function can be calculated as, $B_J(y) \approx \frac{\mathrm{J}+1}{3J}y$ (as $y = g\mu_B JB/kT \ll 1$).

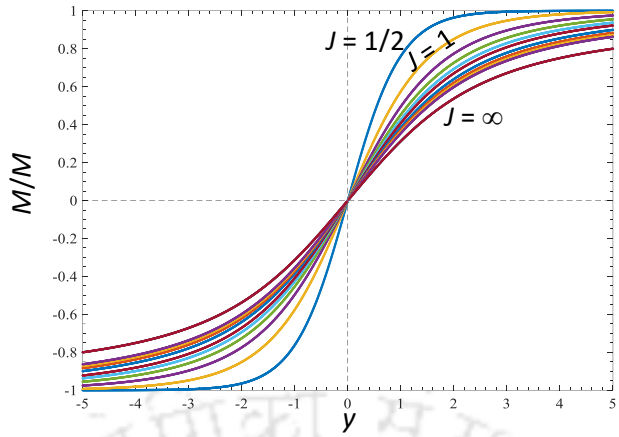

Figure 1.1. Variation of relative magnetization $\frac{M}{M_S} (= B_J(y))$ of a paramagnetic compound for different magnitudes of the total angular momentum quantum number *J*. Here $B_J(y)$ represents the Brillouin function equivalent to $\frac{2J+1}{2J}\coth\left(\frac{2J+1}{2J}\right)y - \frac{1}{2J}coth\frac{y}{2J}$ and $y = \frac{g\mu_B JB}{kT}$.

Thus, one can express the magnetic susceptibility as:

$$\chi = \frac{M}{H} = \frac{\mu_0 N}{3kT} g^2 \mu^2{}_B J(J+1) = \frac{\mathrm{C}}{\mathrm{T}} \qquad 1.7$$

The equation 1.7 is widely known as the 'Curie's Law' [2]. Where, $\mathrm{C} = \frac{\mu_0 N}{3k} g^2 \mu^2{}_B J(J+1)$ is the Curie constant and the effective magnetic moment $\mu_{eff} = g\mu_B\sqrt{J(J+1)}$. Considering this aspect, in figure 1.2 we show the variation of magnetic moment per atom for different compositions of 3d metals and alloys. Such variation of magnetic moments was first presented by John Slater and Linus Pauling and is known as the Slater–Pauling curve [3]. Nevertheless, the experimentally observed magnitudes of χ do not usually obey the Curie law because we assumed magnetic moments are isolated and neglected the magnetic interactions among them. However, Weiss introduced molecular field theory by considering the interactions between the individual magnetic moments leading to the Curie – Weiss law:

$$\chi = \frac{C}{T-\theta} \qquad 1.8$$

where the correction term, θ, has the unit of temperature, and is called the 'Curie – Weiss temperature', which can be calculated from the inverse magnetic susceptibility 1/χ versus T plots discussed in the subsequent sections.

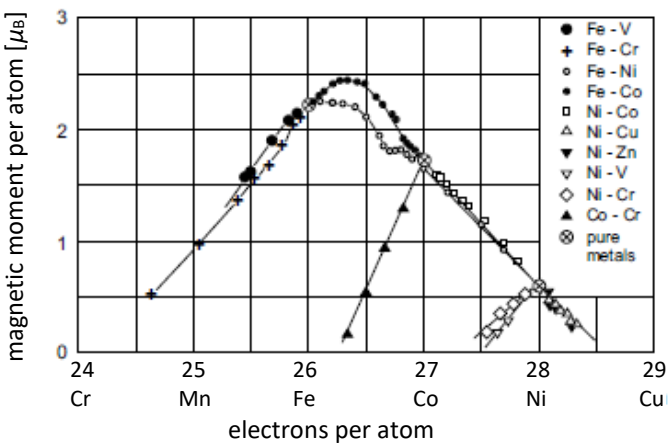

Figure 1.2. The magnetic moment of elements plotted as a function of number of electrons per atom (Adapted from [4,5])

1.1.2 Exchange Interactions:

In this section we briefly discus a qualitative description of interatomic exchange, with reference to the quantum mechanical approach that support the concepts discussed in the subsequent sections. It is well known that the magnetic long-range ordering results from the interactions between the moments of neighbouring magnetic ions. It is energetically favourable for them to arrange in a periodic arrangement either in parallel or anti parallel. There are two types of interactions possible, the first one is the magnetic-dipolar interaction and second kind is magnetic exchange interactions [6]. The magnetic dipolar interaction is generally too weak to account for the ordering of magnetic materials, whereas, the systems studied in the present work are completely determined by the exchange couplings between ions. In order to understand this concept, let us consider the simple case of the exchange interaction between two electrons at positions $\mathbf{r}_1$ and $\mathbf{r}_2$ in which both electrons are in spatial states ϕ_X and ϕ_Y, so that the combined wave function contains the terms $\phi_X(\mathbf{r}_1)\,\phi_Y(\mathbf{r}_2)$ and $\phi_X(\mathbf{r}_2)\,\phi_Y(\mathbf{r}_1)$. Using the Pauli exclusion principle one can write the overall antisymmetric wave function ϕ for both spin and spatial as: an antisymmetric (singlet) spin state χ_S (S = 0) with a symmetric spatial state, or a symmetric (triplet) spin state χ_T (S = 1) with an antisymmetric spatial state. Thus, the total wave function for the singlet (ϕ_S) or triplet (ϕ_T) case can be written as

$$\phi_S = \frac{1}{\sqrt{2}}[\phi_X(\mathbf{r_1})\phi_Y(\mathbf{r_2}) + \phi_X(\mathbf{r_2})\,\phi_Y(\mathbf{r_1})\,].\chi_S$$

$$\phi_T = \tfrac{1}{\sqrt{2}}[\phi_X(\mathbf{r_1})\phi_Y(\mathbf{r_2}) - \phi_X(\mathbf{r_2})\phi_Y(\mathbf{r_1})].\,\chi_T$$

The difference in energies between the singlet and triplet state can be written as

$$\mathrm{E} = (E_T - E_S)\,\mathbf{S}_1.\mathbf{S}_2 = J\,\mathbf{S}_1.\mathbf{S}_2 \qquad 1.9$$

Here J is a measure of the interaction between the two spins. If $J < 0$, E_T should be less than E_S and the triplet state S = 1 is favored; if $J > 0$, E_T is greater than E_S and the singlet state S = 0 is favored. Generalizing these ideas to a many-body system makes it difficult to solve. However, it was recognized early by Heisenberg that equation 1.9 could be generalized to provide a good description of the interactions between magnetic moments on all neighboring ions in a compound. Accordingly, the Heisenberg Hamiltonian can be expresses as

$$\mathrm{H} = -\sum_{k,l} J_{kl}\,\overrightarrow{\mathrm{S}_k}.\overrightarrow{\mathrm{S}_l}$$

where J_{kl} is the exchange-coupling constant between the spins $\overrightarrow{S_k}$ and $\overrightarrow{S_l}$ distributed on a regular lattice and the summation is over all the possible nearest neighbors. The strength and sign of interaction play a key role to determining the magnetic ordering/properties of a compound. Positive value of J_{kl} corresponds the parallel alignment of magnetic moments. Whereas, the negative value favors anti-parallel alignment of nearest moments [7,8]. Nonetheless, $J_{kl} = 0$, signifies no interactions among the spins. Such state is called paramagnetic state which describes the random orientation of spins resulting very low net magnetic moment above the ordering temperatures. The magnetic interactions among the nearest-neighbor cations can take place in two ways: (i) direct interaction and (ii) indirect interaction as shown in figure 1.3. When the electrons on neighbouring ions interact directly without any intermediary, then it is called direct exchange interaction (Figure 1.3(a)) and the strength of this interaction strongly depends on the overlap of the electron shells of the two ions. In transition metals the outermost 3*d* electron wave-functions strongly overlap with the neighbouring ions and causes the direct exchange interaction between the spins. Depending on the magnetic compounds different types of indirect interactions may be possible (figure 1.3). The first category is 'super-exchange interaction' occurring between two non-neighbouring magnetic ions mediated by a non-magnetic O^{-2} ion (figure 1.3(b)) which is located in between them. Such interaction is common in ionic solids and oxide materials.

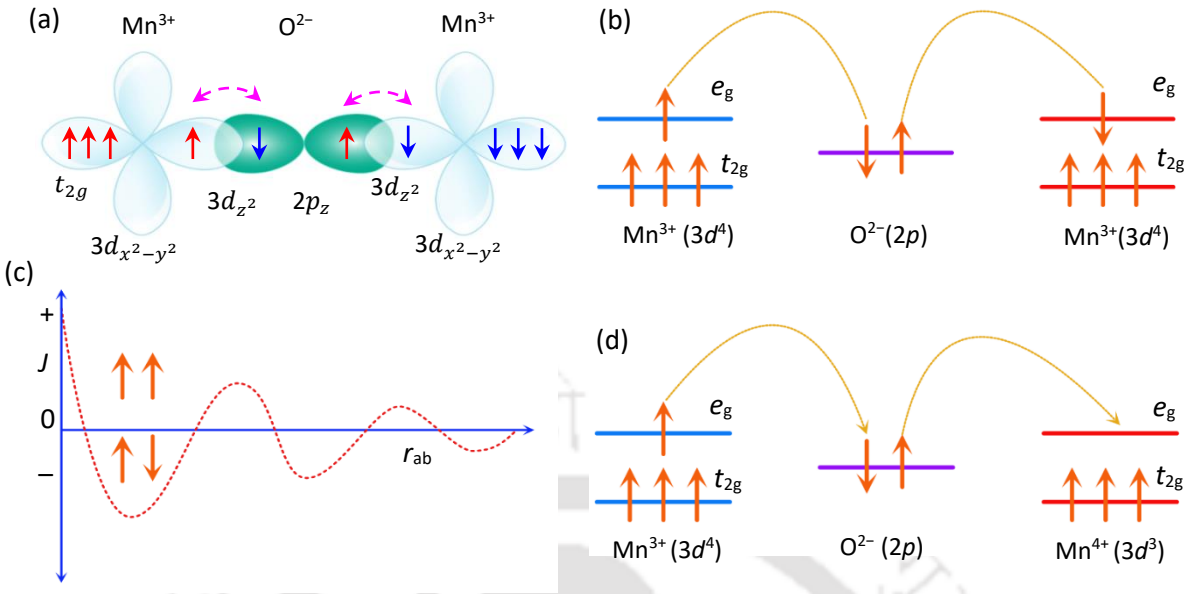

Figure 1.3. Schematic representation of different types of exchange interactions. Figure (a) depicts the direct exchange interaction between two neighbouring ions. (b) the super exchange interaction between two metal cations (Mn^{3+}-Mn^{3+}) through oxygen (O^{2-}) ligand. The possible arrangement of electron spins involved in the interaction are shown as vertical arrows. (c) The RKKY exchange parameter *J* as a function of inter atomic distance r_{ab}. The positive and negative values of this graph signifies the ferromagnetic and an antiferromagnetic oscillatory ordering depending upon the interatomic distance. (d) The Double exchange interactions in Mn_3O_4 system. In the figure arrows indicate the movement of electron from one magnetic ion site to the other.

The super-exchange coupling is ferromagnetic in nature, however, for realization of this kind of coupling the Goodenough-Kanamori proposed the following two rules: First rule is 'an antiferromagnetic exchange occurs when two occupied orbitals at neighbouring places overlap' and second rule is 'the exchange can be ferromagnetic when one empty and one occupied orbital overlap'. The ferromagnetic super-exchange coupling is mostly weaker as compared to the case of antiferromagnetic. Second category is 'RKKY exchange interaction' occurs in metals with localized magnetic moments mediated by the conduction band electrons. The coupling is strongly characterized by the distance dependent exchange integral $J_{\mathrm{RKKY}}(r)$: $J_{\mathrm{RKKY}}(r) \propto \mathrm{F}(2k_F r)$, where, $\mathrm{F}(2k_F r) = \frac{\sin x - x\cos x}{x^4}$. This type of exchange coupling is either ferromagnetic or antiferromagnetic which is oscillatory in nature. Figure 1.3(c) shows the schematic of J_{RKKY} coupling constant plotted as a function of the distance (r_{ab}) between the magnetic moments considering an example of rare-earth metals with their localized 4*f* electrons. In some oxides the magnetic ions exhibit mixed valencies which results in a ferromagnetic ordering through 'Double exchange' mechanism. Typical example is Hausmannite (Mn_3O_4) which contains Mn^{3+} as well as Mn^{4+} ions (Figure 1.3(d)).

1.1.3 Long-range Magnetic Ordering

In this section we will discuss different magnetic ordered states due to the variation in the magnetic exchange interactions between the nearest neighbor magnetic moments as discussed above. A schematic overview of the commonly observable collective magnetic phenomena has been given in Figure 1.4. The most familiar category of magnetic ordering is 'ferromagnetism', which arises when the exchange coupling constant

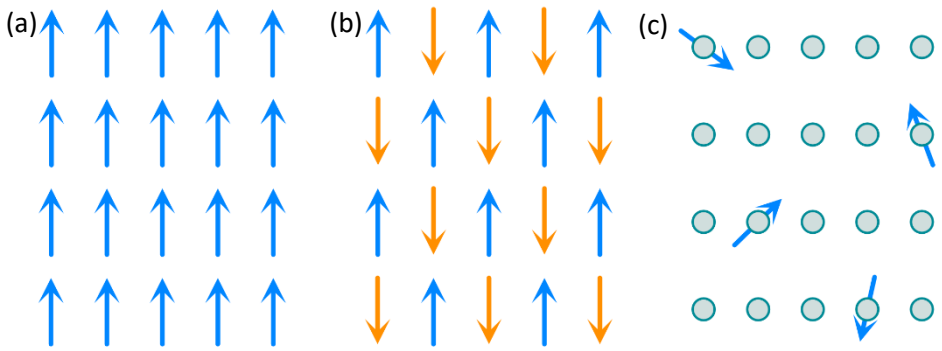

Figure 1.4. Various arrangements of spin in different magnetic systems: (a) spins with parallel arrangement, (b) anti-parallel with each other, and (c) random spin arrangement corresponding to the ferromagnetic ordering, antiferromagnetic ordering, and spin-glass state (short-range ordering), respectively.

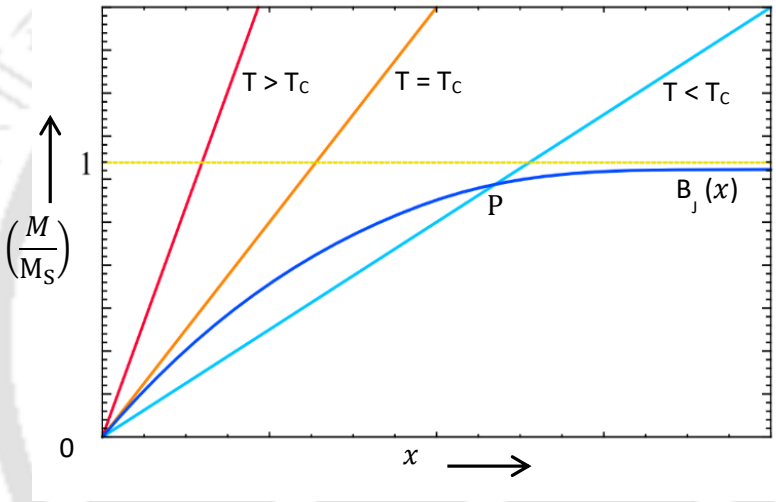

Figure 1.5. The relative magnetization $\left(\frac{M}{M_S}\right)$ as a function of temperature (T) for a ferromagnetic compound having constant J value in the absence of the external magnetic field ($H = 0$ Oe). The exponential variation represents the Brillouin function and straight lines show the spontaneous magnetization calculated for three temperature regions.

is positive ($J > 0$) i.e; all the magnetic moments align in a parallel arrangement. Ferromagnetism is characterized by a spontaneous magnetization even without applying an external magnetic field. At absolute temperature all the magnetic moments align parallelly due to the exchange interaction. Therefore, without an external magnetic field such parallel arrangement of nearest moments may be considered due to some internal magnetic field, B_m present in the material popularly known a Weiss molecular field. On the other hand, the thermal agitation of the atoms opposes such orientation which arises due to field and after a critical temperature the thermal energy is sufficient to destroy such parallel arrangements as a result spontaneous magnetization vanishes. Such critical temperature is defined as the ferromagnetic Curie temperature (T_C). Figure 1.5 illustrates the temperature dependence of the relative magnetization M/M_S for a ferromagnetic compound in absence of the external magnetic field ($B = 0$ Oe). Here $\left(\frac{M}{M_S}\right) = B_J(y) = \left(\frac{kT}{Ng^2\mu^2{}_B J\alpha}\right)y$, where $y = g\mu_B JB/kT$ [7,8]. In this case α represents the molecular field constant due to the internal magnetic field

B_m. In Figure 1.5 three straight lines show the nature of magnetization for different temperature range. The tangent to the Brillouin function ($B_J(y)$) at the origin corresponds to the Curie temperature (T_C). However, at T = 0 K (T<<T_C), the magnitude of Brillouin function $B_J(y) \longrightarrow 1$ as $y = g\mu_B JB/kT \longrightarrow \infty$ and $\frac{M}{M_S} = B_J(y) = 1$. Hence from the graph it can easily noticeable that the straight line crosses the graph at origin and at higher value which represents the spontaneous magnetization in this temperature region. In contrast to the low temperature region, the straight line corresponding to T>>T_C which intersect the Brillouin function at origin and signifying the zero magnetization state. Consequently, θ in Curie – Weiss law (equation 1.8) corresponds the 'Curie temperature' (T_C) for ferromagnetic material. At this temperature the magnetic susceptibility (χ) diverges which corresponds to the phase transition from the spontaneously magnetic ordered phase to disordered state. Another important class of magnetic ordering is 'antiferromagnetic state' in which the magnetic moments of neighboring sub lattice are aligned in the opposite direction (figure 1.4(b)). Such ordering corresponds the negative exchange constant ($J < 0$). In antiferromagnetic ordered state each sublattice (A and B) is arranged antiferromagnetically, such that the net magnetization remains zero ($M = m(A)\uparrow + m(B)\downarrow = 0$). The temperature at which both the sub lattice align antiparallel is called the phase transition temperature, widely known as Néel temperature (T_N). According to Néel two sub lattice model the Curie – Weiss temperature θ takes the negative value (equation (8)) and the magnetic susceptibility $\chi = \frac{C}{T+\theta}$. The temperature variation of χ for a typical antiferromagnetic system is shown in figure 1.6. Arrangement of these sublattices can occur in many different ways because there are many possibilities to arrange the electron spins (the type of crystal lattice also influences this behavior). Different types of antiferromagnetic arrangement of spins in the simple cubic lattice are shown in figure 1.7. It is important to note that the temperature dependence of anisotropic susceptibilities, $\chi_\parallel$ and $\chi_\perp$ shown significant bifurcation below T_N. Here the parallel (||) axis being defined along the magnetization direction, which is called an " easy axis ", whereas, the perpendicular component $\chi_\perp$ represents the 'hard axis'. Therefore, the external magnetic field can be applied either along the easy axis or perpendicular to it and the magnetic susceptibilities, $\chi_\parallel$ and $\chi_\perp$, are illustrated schematically in figure 1.6.

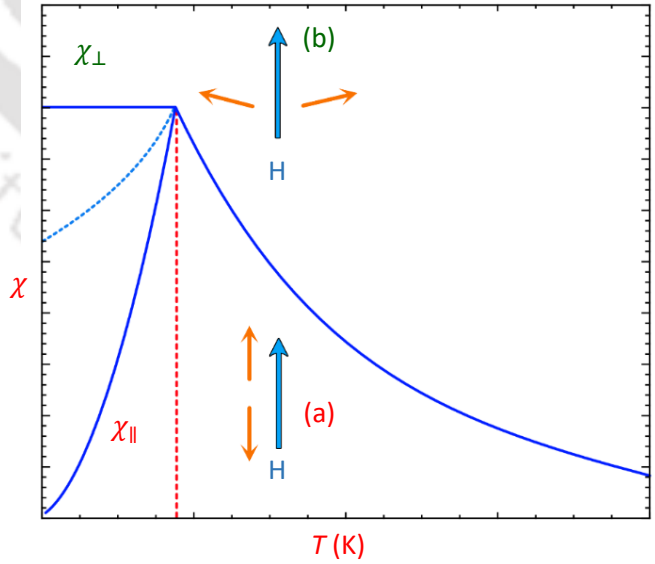

Figure 1.6. Temperature dependence of magnetic susceptibility $\chi(T)$ of an antiferromagnetic compound. For $T < T_N$ region the dashed and solid lines represent $\chi(T)$ for polycrystalline and single crystal system, respectively. Figures (a) and (b) represents the parallel and perpendicular alignment of spins in the presence of external magnetic field (H) in a single crystal.

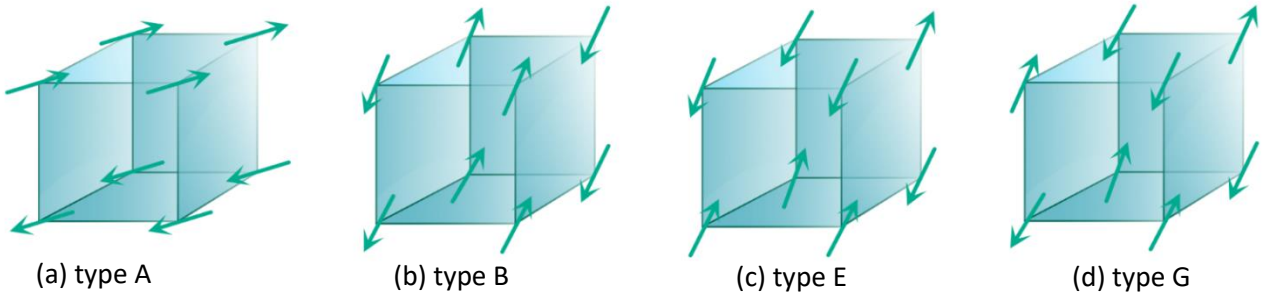

Figure 1.7. Schematic representation of four different types of antiferromagnetic coupling among the nearest neighbor spins in a simple cubic lattice.

In this figure $\chi_{\parallel}$ decreases linearly toward zero on lowering the temperature, whereas, $\chi_{\perp}$ stays constant. In case of polycrystalline compound one can usually take averaged value of $\chi\ (= (\chi_{\parallel} + 2\chi_{\perp})/3)$. The important behavior of $\chi_{\parallel}$(T) and $\chi_{\perp}$(T) in case of antiferromagnetic systems in the presence of strong external magnetic field is that the parallel orientation abruptly changes into the perpendicular one by conserving the antiparallel orientation of spins at a critical field (figure 1.6). This magnetic phase change induced by the magnetic field is called the 'flopping' of the magnetic moments or 'spin-flop' field induced transitions (which will be discussed in detail in Chapter 3). The magnetic phase change can occur when the magnetic energy is in the parallel arrangement (as shown in figure 1.6) exceeds the assumed energy in the perpendicular arrangement (see figure 1.6). Thus, the state is called the spin - flopped state, and the magnetic field which induces the transition is named the 'spin-flop field'. This magnetic phase transition depends on the anisotropic energy of the system under investigation. Ferrimagnetism (figure 1.8) is a special case of antiferromagnetism, where magnetic moments in different sub-lattices has different magnitude and arrange antiparallel resulting a net positive magnetic moment ($M = m(\mathrm{A})\uparrow + m(\mathrm{B})\downarrow \neq 0$). Hence, the total magnetization does not vanish as in the antiferromagnetic case. However, the temperature above which the spontaneous magnetization vanishes is called the ferrimagnetic Néel temperature (T_{FN}). The ferrimagnetic ordering can also be observed in more than two sublattices with variety of spin configurations as shown in figure 1.8. The inverse magnetic susceptibility for ferrimagnets can be expressed as: $1/\chi = T/C + 1/\chi_0 - \sigma_0/(T - \theta)$ [7]. In figure 1.9 we summarize all the above ordered states in terms of the temperature dependence of the inverse magnetic susceptibility χ^{-1}(T). The χ^{-1} for ferro/ferri and antiferromagnetic case shows linear variation in the paramagnetic regime. Whereas, in case of ferrimagnetic system χ^{-1} follow the hyperbolic pattern for $T<T_{FN}$. The linear extrapolation of $\chi^{-1}(T)$ intersect the temperature axis, which defines the critical temperature for the individual magnetic system. It is important to know that the sign of the exchange constant (J) strongly depends on the ratio of the interatomic distances with the radius of the *d* shell (r_{ab}/r_d). A graphical representation of this behavior is shown in figure 1.10 which is commonly known as the Bethe– Slater curve [9-11]. As indicated in the figure this curve allows to distinguish between ferromagnetic (FM) 3*d* elements like Fe, Co, and Ni exhibiting a parallel alignment and thus a positive exchange constant. On the contrary, the antiferromagnetic (AFM) elements like Mn and Cr with an antiparallel orientation of the magnetic moments leads to a negative exchange constant ($J < 0$).

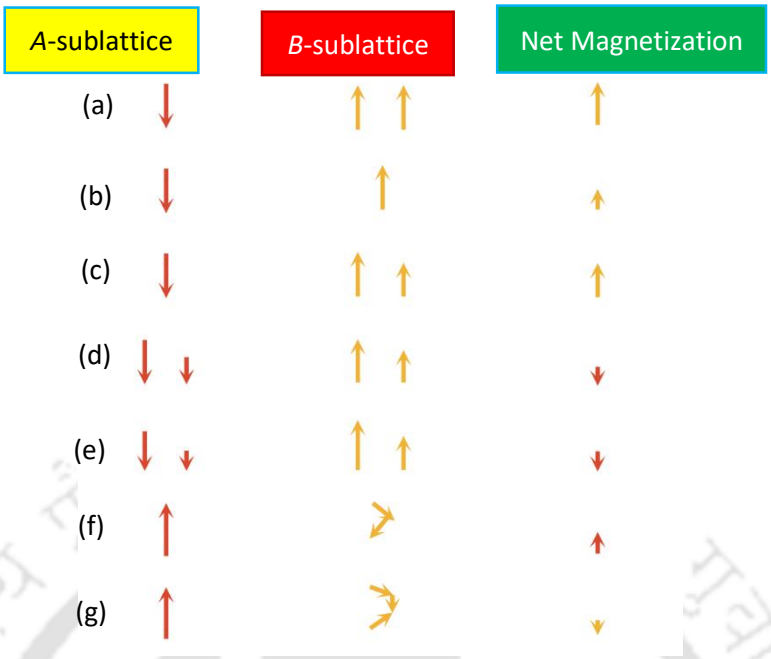

Figure 1.8. Different possible arrangement of spins in the two sub-lattices model. Each vector represents individual magnetic moments or the total magnetic moment per formula unit for each type of ion.

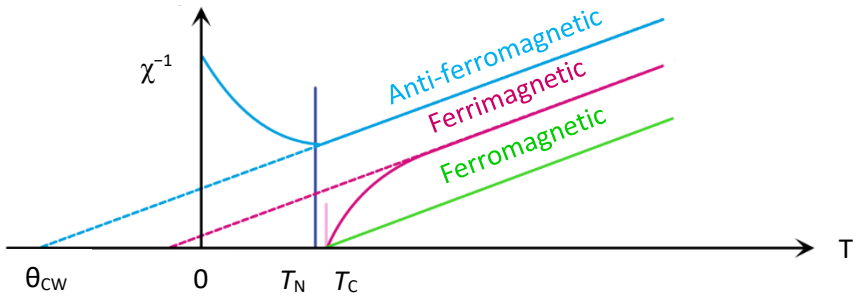

Figure 1.9. Plot of inverse magnetic susceptibility (χ^{-1}) versus temperature (T) for ferromagnetics (FM), antiferromagnetics (AFM), and ferrimagnetics (FiM). The positive (> 0) and negative (< 0) magnitudes of Curie-Weiss temperature (θ_{CW}) indicates FM and AFM/FiM ordering represent in the sample.

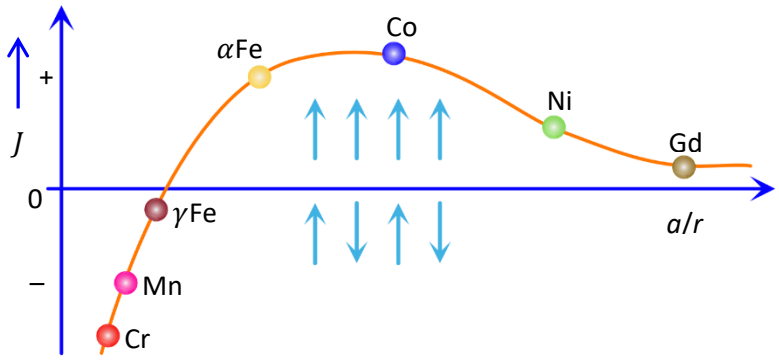

Figure 1.10. The Bethe–Slater curve describes the variation of exchange constant (J) with the ratio of the interatomic distance (r) to the radius of the d shell (a). The elements above the horizontal axis are ferromagnets and below the axis are anti-ferromagnets.

1.1.4 Negative Magnetization and Compensation:

In the present section we discuss about the negative magnetization devoid of any extrinsic or intrinsic diamagnetic contribution of the compound. It is often noticed in several ferri/antiferromagnetic/canted antiferromagnetic sublattice systems, that under both ZFC and FC conditions total magnetic moment (M) at certain temperature collapses to zero and changes its sign on further lowering the temperatures. The temperature at which both M_{ZFC} and M_{FC} approaches to zero is often called as magnetic compensation temperature T_{COMP} which occurs due to the balance of two-sublattice magnetizations (M_1 + (− M_2)) with each other. This phenomenon has been noticed in many crystal systems including spinels, perovskites, rare earth iron garnet, hexacyanide compounds, layered structures, and 3*d*/4*d*/4*f* intermetallic alloys RFe_3 (R = Gd, Tb, Dy, Ho, Eu) [12-14]. For example, as shown in figure 1.11 where the temperature dependence of the magnetization $M(T)$ of inverse spinel, $TiCo_2O_4$ bulk grain sized samples exhibits zero net magnetization across 32 K under both ZFC and FC conditions which is corresponding to the T_{COMP} [13,14]. Also one can notice negative magnetization of $M_{FC}(T)$ branch below T_{COMP}. Such negative magnetization phenomenon occurs in a material having a specific arrangement of two or more spins coupled with a magnetic anisotropy. It is also possible that the magnetic compensation behavior can be observed without any negative magnetization because of an absence of the magnetic anisotropy in such compounds [15,16]. If the magnetic anisotropy is negligible then the principal component of the sublattice magnetization (which was antiparallel initially) becomes parallel to the external applied field which causes the net magnetization of the sample forced to rotates in the direction of the applied field and therefore stops the phenomenon of magnetization reversal to occur below T_{Comp}. Thus, the magnetic anisotropies play a vital role in the negative magnetization phenomenon [17,18]. In the present work we observed the negative magnetization and T_{Comp} in few compositions of Mn doped $TiCo_2O_4$ system along with several other novel magnetic phenomena discussed below.

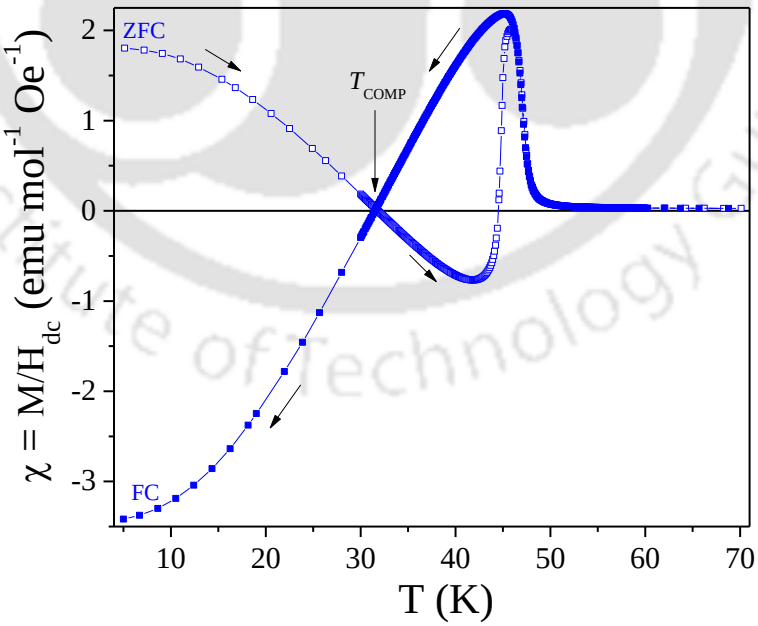

Figure 1.11. Temperature dependence of low-field (H ~ 50 Oe) magnetic susceptibility (χ(T)) of bulk grain sized polycrystalline $TiCo_2O_4$ system measured using SQUID magnetometer under zero-field-cooled (ZFC) and field-cooled (FC).

1.2 Magnetic Frustration:

The word Magnetic-frustration was first coined by Toulouse and Villain in the context of spin glasses to describe the impracticality of satisfying all exchange processes at the same time [19,20]. In any long-range ordered system, the lowest energy configuration can be accomplished by arranging the spins parallelly or antiparallelly. But, in few crystal systems the geometry of lattice structure does not allow to minimize the energy for all the exchange interactions between the neighboring spins. Figure 1.12 represents a typical example of such spin arrangement on the corners of a triangular lattice having the nearest neighbor antiferromagnetic interactions between them. The energy of the system can be minimized when the spins align opposite to its neighboring spins leading to an antiferromagnetic interaction. From the figure 1.12 it is clear that when the first two spins (spin-1 and spin-2) align anti-parallelly with each other, the spin-3 cannot simultaneously satisfy the antiferromagnetic interaction with both spin-1 and -2. Hence, for the spin-3 two orientations are possible (up and down) which corresponds to the same energy and it will become frustrated. Therefore, when such a situation appears in the lattice, the system cannot satisfy a single minimum ground state energy. This phenomenon is known as Magnetic-frustration and leads to a variety of degenerate magnetic ground states. [20,21]. Among various lattices leading to geometrical frustration, the triangular and the Kagomé lattice are the archetypal examples. Figure 1.12 shows the spin configuration for the triangular and square lattice with antiferromagnetic ($J_{ij} < 0$) and ferromagnetic ($J_{ij} > 0$) nearest neighbor exchange interactions, respectively. Among both the systems the triangular configuration is treated as the most common building block of frustrated magnets. The three-dimensional geometrically frustrated lattice includes pyrochlore and spinel lattice, in which the spins reside on a corner-sharing tetrahedral network in the former case while the spins in tetrahedral *A*-site are absent in the later case [22]. Usually, the degree of frustration in any compound can be determined by a parameter called the index of frustration f, which is defined as: $f = |\theta_{CW}|/T_{tran}$. In this expression θ_{CW} is the Curie-Weiss temperature obtained from the linear fitting of the inverse DC susceptibility at high temperatures, where the system is in paramagnetic state and T_{tran} is the phase transition temperature (T_C or T_N) at which the long-range magnetic ordering disappears

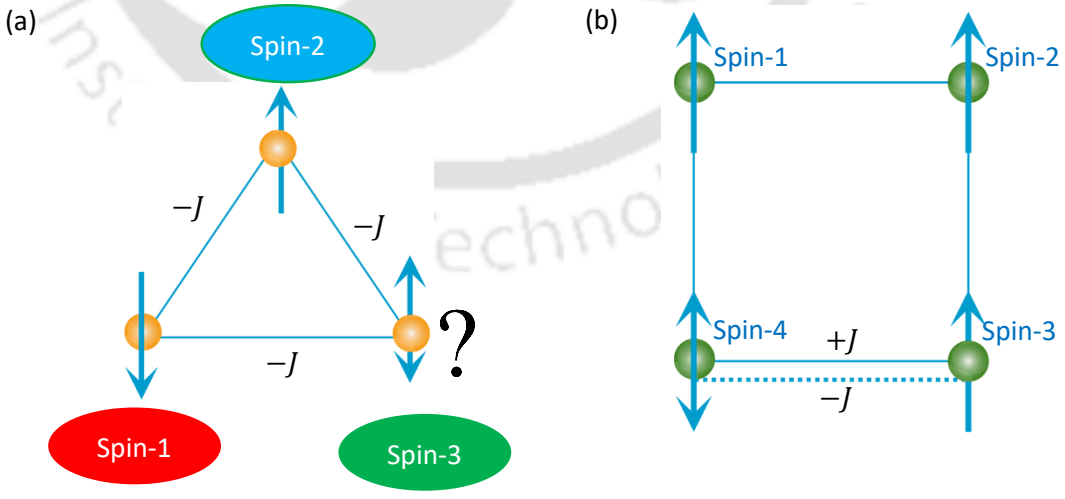

Figure 1.12. Spin configuration for a triangular (a) and square (b) lattice with nearest neighbor anti-ferromagnetic (AFM) and ferromagnetic (FM) Interactions. The Geometrical frustration occurs in the triangular lattice and square lattice at the position of spin-3 and at spin-4, respectively.

Hence the lower value of T_{tran} as compared to θ_{CW} corresponds higher magnetic frustration of a system. However, when $f \rightarrow \infty$, the system fails to order at the absolute zero temperature and new ground state arise known as spin-glass which will be discussed in the subsequent sections. In general, any system is classified as frustrated when f value reaches greater than 10. The quasi-2D spin-glass compounds such as $SrCr_8Ga_4O_{19}$ exhibits a very high degree of magnetic frustration with magnitude of f observed as high as 156 [23].

1.2.1 Spin glass Phenomena:

Spin glass (or Magnetic (spin) disorder (glass)) phenomena has generated substantial physical and mathematical interest over the past thirty years [19,20,24–27]. Physically, they exhibit a magnetically disordered state at low temperatures, which arises from the competing exchange interactions (between ferromagnetic and antiferromagnetic) among randomly distributed localized magnetic moments. Usually, alloys with dilute dispersion of magnetic elements and randomly diluted magnetic insulators displaying spin-glass behavior. One of the central unsolved questions till today in the spin-glass theory is the number of ground states in finite dimension. Spin glass phenomena can also be understood as a random and mixed interacting state of a magnetic system (as shown in figure 1.13), where the competing ferromagnetic/antiferromagnetic interaction increases the frustration and randomness. This leads to disorder and spin freezes randomly at a well-defined temperature T_F often called as freezing temperature or blocking temperature for spin-glass state below which it is highly irreversible, metastable frozen state. The random-site occupancy and random bond are the main possible reasons of the randomness in any compound. Such randomness combined with the competing or mixed interactions causes frustration inside the lattice. Some metallic alloys like $Cu_{1-x}Mn_x$, $Au_{1-x}Fe_x$ are the typical examples of spin glass system in which the site-randomness causes glassy behavior [28,29]. Also, site dilution of the magnetic ions with the non-magnetic ions makes the system chemically disorder such disorderness disturbs the long range interaction and causes the short-range interactions like spin-glass. The magnetic moments of the metal ions in $Cu_{1-x}Mn_x$, $Au_{1-x}Fe_x$ can couple with each other through the RKKY exchange interactions $J_{RKKY}(R)$ and the strength of $J_{RKKY}(R)$ (either ferro- or antiferromagnetic) depends on the distance between two magnetic ions as shown in figure 1.13.

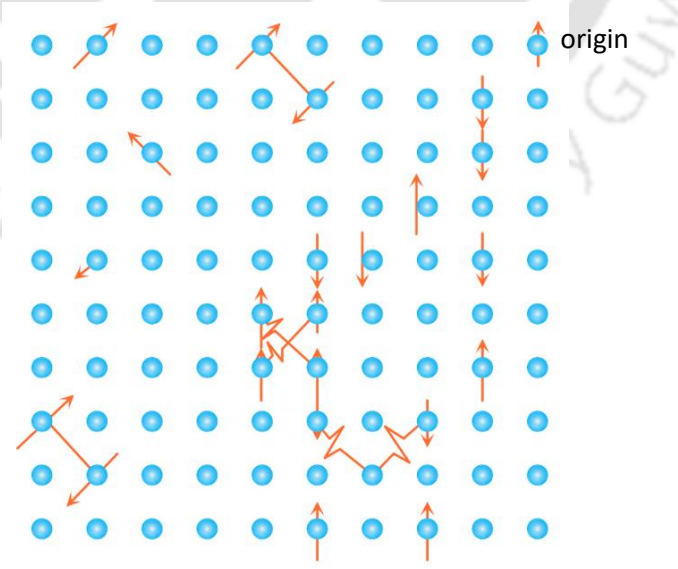

Figure 1.13. Schematic of randomly distributed spins in a square lattice with ferromagnetic coupling between the nearest neighbours (nn) and antiferromagnetic coupling between next-nearest neighbours (nnn). The zig-zag lines represent the unsatisfied coupling and the spin at the bigger circle is frustrated.

Such situation often leads to competing magnetic interactions between the Mn moments which are randomly distributed and therefore, at low temperature these magnetic interactions freezes in random direction (figure 1.14 (a)). On the other hand, the $Rb_2Cu_{1-x}Co_xF_4$ and $Fe_{1-x}Mn_xTiO_3$ compounds are the standard examples of spin glass system which occurs due to the bond-randomness (figure 1.14 (b)). Both the systems have perfect lattice structure, however, due to the competing magnetic exchange interactions (*J*), *J* changes it's sign alternatively between the nearest neighboring spins finally leading to the randomness inside the system [24,30,31]. As the temperature is lowered from T_F, the neighboring spins begin to interact over sufficiently longer in range. For $T<<T_F$, the randomly located and freely rotating spins construct themselves into locally correlated units or clusters (figure 1.14 (c)). Such clusters can even treat as local domains which rotate collectively. Once such clusters coupled ferromagnetically resulting a giant or superparamagnetic moments, or they form from a strongly localized overlapping of RKKY interactions, in which case, because of the (+) parallel, (−) antiparallel oscillations, the net moment will be proportional to the square root of the number of spins taking part. However, it is also possible that few spins act as independent entities which are not belonging to any clusters remains as it is and such spins mediate the interaction between two clusters thereby enhances the cluster sizes and relaxation times. Therefore, the system finds a ground-state (T = 0 K) configuration for the particular distribution of spins and exchange interactions. Such ground-state signifies the lock or freezing of the favorable set of randomly aligned spins generated by the local anisotropy. The temperature at which spin freezes randomly is called the 'freezing temperature' for a spin glass system.

At this point it should be worth to discuss the percolation limit when the magnetic ion substitution take place into the nonmagnetic matrix. Generally, the percolation limit defined as a critical substitution percentage at which each magnetic site has at least one magnetic nearest neighbor i.e. one macroscopic connection that extends from one end of the crystal to the other. There are two types of percolations; (*i*) 'site percolation' and (*ii*) 'bond percolation' (interaction/bond which couples (⊥) two particular sites). Let us consider the 3D f.c.c. lattice of non-magnetic atoms in which few percentage of magnetic atoms are substituted such that the nearest-neighbor magnetic ions interact with each other. Consequently, the substituted magnetic atoms randomly occupy different lattice sites. These magnetic atoms will align parallel if they are nearest neighbours otherwise they remain uncoupled.

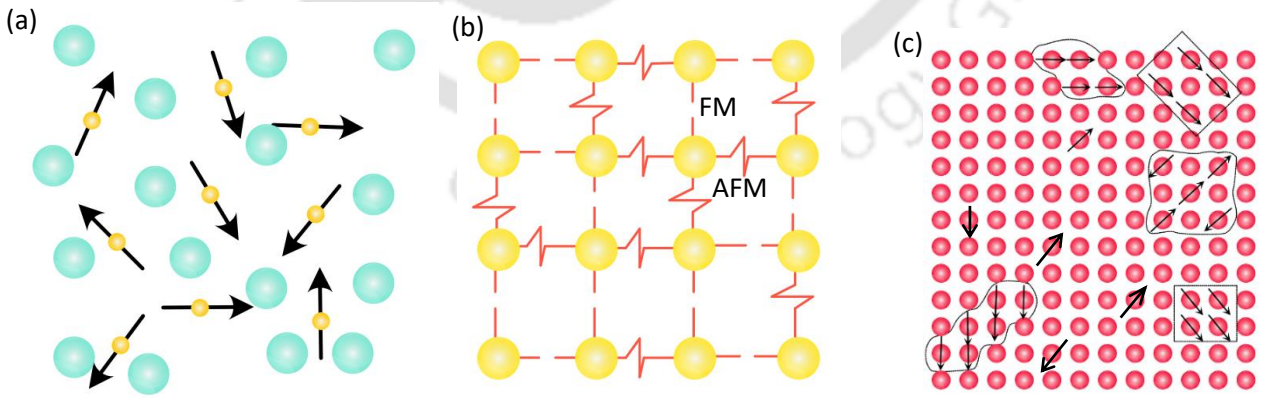

Figure 1.14. Illustration of (a) disordered lattice sites occupied with magnetic ions, (b) the random bond spin-glass and (c) the cluster spin-glass. In figure (b) the dashed lines represent FM coupling and the zig-zag sign signifies the AFM coupling.

Typically, infinite ferromagnetic clusters will form if ~ 17% of the magnetic ions occupy the lattice sites and this leads to the long-range ferromagnetic ordering. Similarly, a minimum of 45% percolation limit is needed to realize long range antiferromagnetic ordering with a characteristic T_N in the same 3D f.c.c. crystal. Figure 1.15 shows the temperature dependence of substitution concentration $x(T)$ phase diagram for a dilute magnetic alloy [24]. In this phase diagram T_K represents the Kondo temperature which decreases as a function of the concentration. For $T_K > T_F$ we have the weak moment concentration regime. As the local environment builds sufficient amount of moments ($x > x_0$) will develop then the spin-glass regime first appears linearly, followed by a less than linear T_F dependence on x. Finally, when the percolation limit is surpassed ($x > x_p$), then there is a rapid rise of Curie or Néel temperatures as the long-ranged ordered state is formed and strengthened. Figure 1.14 clearly shows that the substitution concentration (x) is the most important parameter in determining the magnetic state of any compound. As $T \rightarrow 0$ K, the weak magnetic (cluster glass) phase is created due to the percolated infinite ferromagnetic clusters which is eventually, broken up into large but randomly frozen clusters. Therefore, as the cluster-glass phase develops from a ferromagnetic state, it reenters into the frozen (disordered) phase out of another such states are often called as reentrant spin-glass phase, like for example $Cu_{1-x}Mn_x$, $Au_{1-x}Fe_x$ etc [29,31,32]. There are various theoretical models to explain such reentrant spin-glass behavior at low temperature. In the first model, the temperature dependent random anisotropy describes that at low temperature the anisotropy grows sufficiently large to hold the links between the infinite clusters. Consequently, the anisotropy aligns these divided units along the randomly preferred directions. The second model describes that the ferromagnetic transitions T_C comes due to the ordering of longitudinal spin components and the freezing temperature (T_F) arises due to the freezing of perpendicular spin component. However, the experimental work indicates that the ferromagnetic state appeared due to the infinite-clusters is not truly long-rang in order. Instead, it consists of many extremely large clusters and these clusters dissociate into the collection of smaller clusters at the reentry transition (reentrant spin glass transition).

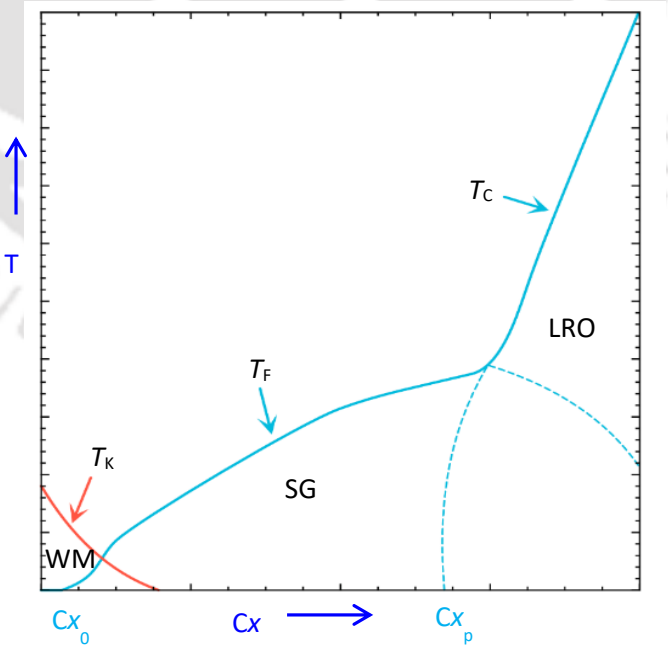

Figure 1.15. Temperature-composition (T - x) phase diagram of a diluted magnetic alloy illustrating various phases like, weak-magnetic (WM), short-range ordering (SRO/spin-glass (SG)), and long-range ordering (LRO).

Further, in contrast to the perfectly ordered ferromagnetic or an antiferromagnetic states the spin glass state shows some non-zero value of the time averaged of spin ($\langle S_i S_j \rangle \neq 0$). Therefore, a spin glass state shows a sharp cusp in the ac-susceptibility measurement. Such properties is shown in figure 1.16 for the $Cu_{1-x}Mn_x$ (0.94 at.%) alloy [28]. This figure shows the real component of ac-susceptibility (χ′) measured at different driving frequencies (2.6, 10.4, 234 and 133 Hz) under zero-field-cooling condition. The peak temperature in χ′ is called the spin-glass freezing temperature T_F. The graph clearly indicates the frequency dependence of χ′ bellow the T_F, where T_F shifts to higher temperatures for increasing frequencies of the applied ac fields which is the most important property of a spin-glass state. Such behavior indicate that the system possesses many metastable ground states which covers a wide range of characteristic excitation and relaxation time scales. The glassy nature of the spin state below T_F results in another feature of the spin glass called remanence which depends on the way the experiment is performed to measure the dc susceptibility (χ_{dc}). Figure 1.17 represents the $\chi_{dc}(T)$ under very small field (~ 6 Oe) for the alloy $Cu_{1-x}Mn_x$ (1 and 2 at.%) with specific measurement protocol as described below. In the first step field was applied above T_F and cooled the sample to T<< T_F and recorded the magnetization data. This process is called field cooling (FC) and (a) and (c) represents the χ_{dc}(FC) data. In the second step the sample was cooled to $T<<T_F$ and at low temperature field was applied and while worming the magnetization data were collected. In the graph (b) and (d) represents such data χ_{dc}(ZFC) and it is called zero-field cooling (ZFC). Whereas, for the ZFC case the graph shows upward drifting, which changes with the rate of increase of temperature dT/dt and becomes irreversible. Therefore, the graph is not only the function of temperature instead it is a function of dT/dt. Therefore, the dc field when applied below T_F creates a metastable, irreversible state, which can be understand by the onset of the irreversibility and the reversible paramagnetic regime exists above T_F. The history dependence of χ_{dc} measurements also unveils various other magnetic phenomena in spin-glass systems such as revolution, aging, and memory effects. In the present thesis we discuss all the above discussed phenomena by means of dynamic ac-susceptibility in insulating spin glasses which exhibits reentrant spin-glass behavior of different time scales.

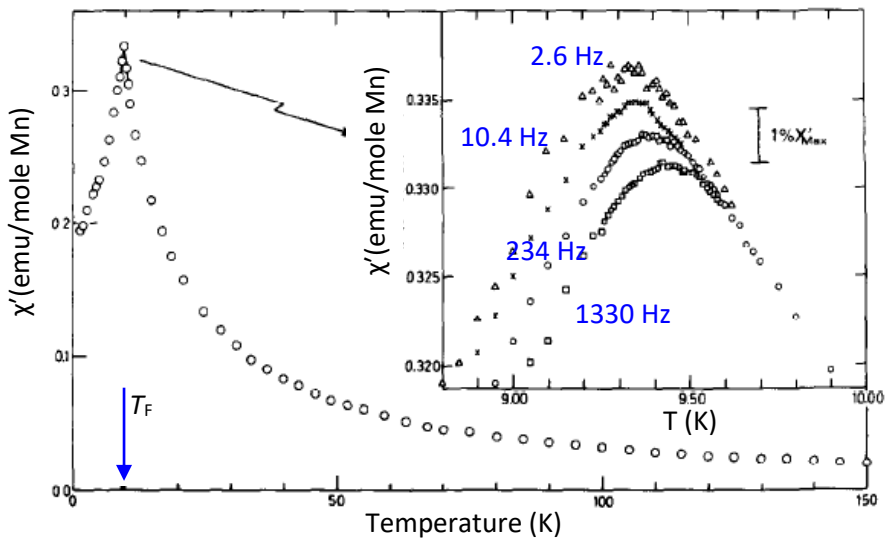

Figure 1.16. Temperature dependence of the zero-field real component of the ac-magnetic susceptibility χ′(T) for $Cu_{1-x}Mn_x$ magnetic alloy measure at different frequencies [28]. The inset shows zoomed view of χ′(T) showing clear cusp at T_{SG} and its shift to higher temperature side with increasing frequency.

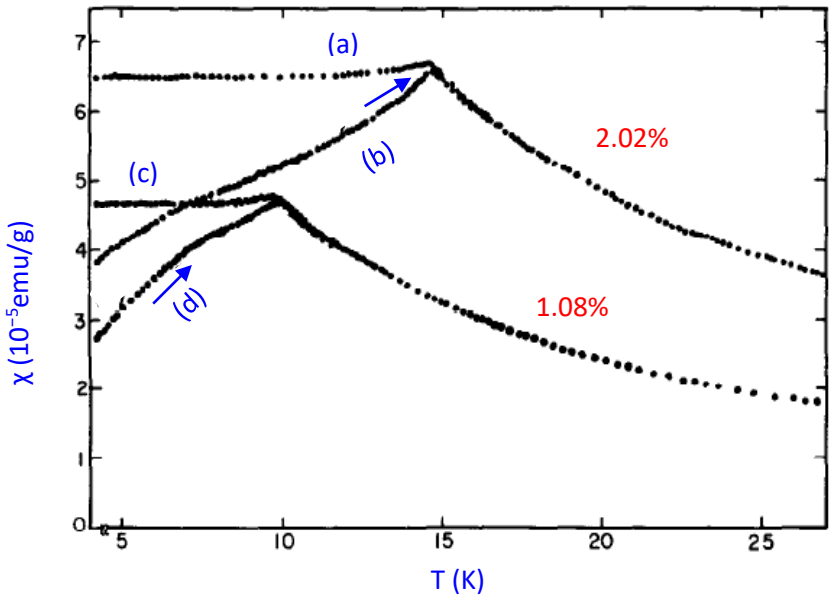

Figure 1.17. The field-cooled (FC) [(a), (c)] and zero-field-cooled (ZFC) [(b), (d)] magnetic susceptibility versus temperature graph for $Cu_{1-x}Mn_x$ (1 and 2 at. %) measured under very low external magnetic field (of 6 Oe) [28].

1.3 Phenomenology of exchange bias:

This section deals with the different phenomenological features of exchange bias effect explained from both theoretical and experimental point of view along with its importance in modern day technology. Our main intention in discussing this phenomenon is that we observed giant exchange bias under both ZFC and FC conditions at low temperatures in the investigated system. Exchange bias phenomena (also called as *M-H* hysteresis loop asymmetry) is defined as the shift of magnetic hysteresis loop along the externally applied magnetic field (H). In 1956, Meiklejohn and Bean first proposed the concept of magnetic exchange anisotropy in Co/CoO core-shell nano-particles [34,35]. The nanoparticles were composed of ferromagnetic (FM) Co core and the antiferromagnetic (AFM) CoO shell. Figure 1.18 demonstrate a clear difference between two magnetic hysteresis loops of Co/CoO nanoparticles, which was measure under different cooling protocol. The field cooled hysteresis loop (solid line) shows a shifted and broadened feature than the zero-field cooled curve (dashed line). This phenomenon arises due to the unidirectional exchange anisotropy which appears at the interface between ferromagnetic and anti-ferromagnetic spin structures. Since the discovery of this phenomena, the FM–AFM exchange interactions has gained immense attention in technological applications due to its microscopic features. In particular, it is extensively used to improve the performance of permanent magnetic materials in information storage technology, magnetic recording media, magnetic random access memories, and magnetic field sensors [36-49]. Although several research works are devoted to develop magnetic nanoparticles which exhibits exchange bias effect, 2D thin film heterostructures become more interesting due to a greater control of the FM–AFM pinned interface, in which the microstructure of both the constituents plays major role. Such controlled spin-structures across interfaces play a major role in deciding the magnitude of exchange bias filed which can be used in spin valves and tunneling devices [36,40,50-55].

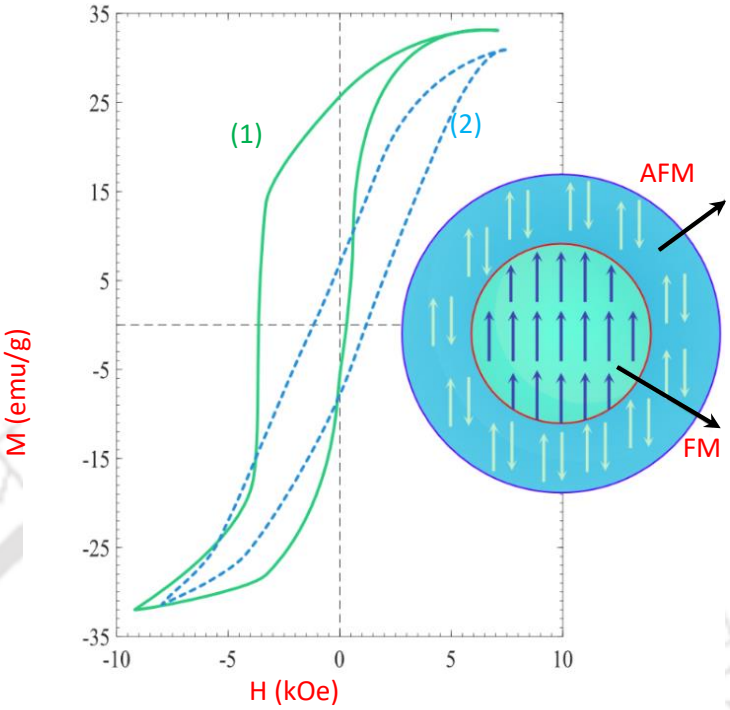

Figure 1.18. Magnetic hysteresis (M-H) loops of partially oxidized Co particles measured at 77 K [34].

For a more detailed understanding of this concept let us consider a layer of FM and AFM material with ordering temperatures T_C and T_N, respectively. At a temperature T ($T_N < T < T_C$), if the applied external field is large enough then all the spins in the FM layer will align parallel to H but spins in the AFM layer will remain random. However, further cooling ($T < T_N$) the system, the anti-ferromagnetic arrangement of spins set up in the AFM layer and at the FM–AFM interface the spins of both layers interact with each other. Therefore, near the interface all the spins in the first monolayer of the AFM layer tends to align parallel to the spins in the FM layers due to the interfacial interactions, while the other residual spins in the AFM layer remain antiparallel to each other which corresponds zero net magnetization in the AFM layer. The most important key results in this procedure is to align the AFM interface spins along the field direction and along the FM spins. The magnetic hysteresis loop (FC mode) shown in Figure 1.19 illustrates the spin configuration in the FM–AFM layers. Figure 1.19 (a) and (c) depicts the high field magnetization with parallel alignment of spins in both FM and FM–AFM interface. However, when the field start reversing all the spins, the FM layer start to align along the magnetic field while the large AFM anisotropy (K_{AFM}) try to keep all the spins pinned in the AFM state. Due to the interface coupling these spins will exert a microscopic torque to the spins in the FM and try to keep them in their original position (figure 1.19 (b)). Therefore, in order to get complete reverse magnetization, high magnetic field is required to overcome the microscopic torque exerted by the spins in the AFM layer. As a result, the coercive field value increases in the negative field direction. On the contrary, when the magnetic field is reversed back to its positive value the rotation of spins in the FM will be easier since the interfacial interaction with the spins in the AFM layer will now favor the magnetization reversal [figure 1.19 (d)]. In this situation the AFM ordering exert a microscopic torque in the direction of applied magnetic field and less magnetic energy required in the positive field direction. Therefore, along the positive and negative field directions an unequal magnetic energy required

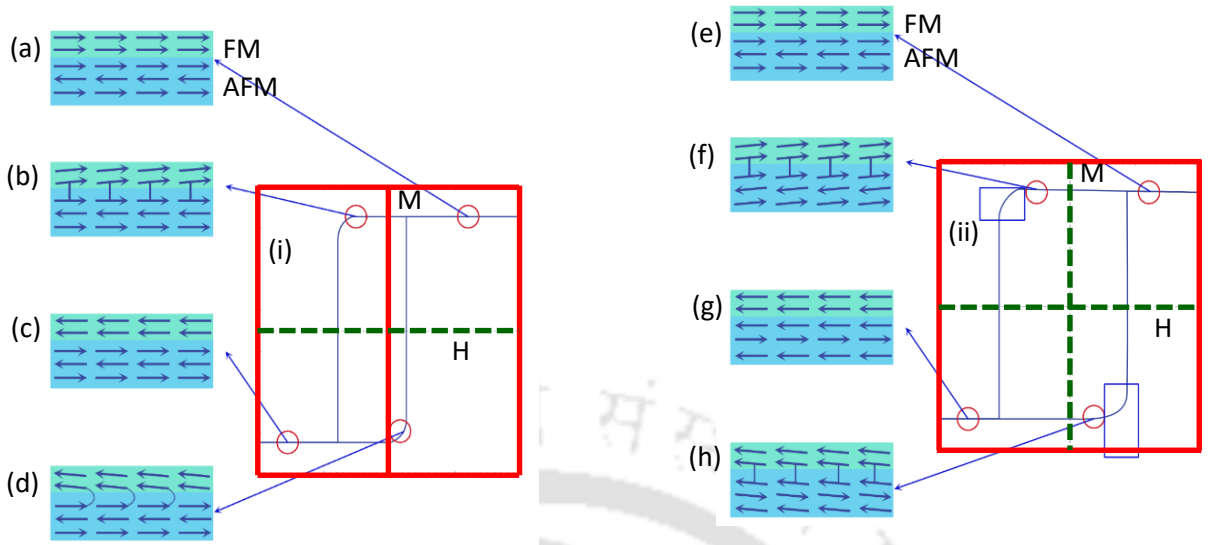

Figure 1.19. The spin configuration schematics corresponding to the FM–AFM coupling at various stages of an asymmetric M-H loop with (*i*) large antiferromagnetic anisotropy and (*ii*) weak anisotropy [34].

to rotate the spins in the FM layers and as a total the whole hysteresis loop shifted towards the negative field direction. The magnitude of exchange bias (H_{EB}) and coercive (H_C) field of a system can be calculated as: $H_{EB} = (H_{C+} + H_{C-})/2$ and $H_C = (H_{C+} - H_{C-})/2$, respectively. Here H_{C+} and H_{C-} signifies the positive and negative coercive field of the hysteresis loop, respectively. On the other hand, for a lower AFM anisotropy (K_{AFM}) case the magnetization reversal can occur more easily than the previous case as shown in figure 1.19 (ii). During the magnetic field reversal, the spins in the FM layer start to rotate and easily dragged the spins in the AFM layers (figure 1.19 (e)). Therefore, due to lower K_{AFM} value it will be energetically more favorable for the spins to rotate together in both the FM and AFM layers. The extra energy needed to make the irreversible twist in the AFM structure convert into an enhanced coercivity. A similar manner can also be observed after saturating in negative fields [figure 1.19 (g) and (h)]. Thus, the unidirectional K_{AFM} of the AFM layers play a crucial role in deciding the *M-H* loop asymmetry and coercivity. The exchange bias phenomena not only obsered in bi-layered systems but also observed in the bulk single-phase alloys and other compounds composed with a variety of coexisting magnetic phases such as ferromagnetic, antiferromagnetic, ferrimagnetic, spin-glass, cluster-glass, charge ordered and disordered magnetic states [56-66]. Another typical example of exchange bias system is the rare-earth inter-metallic compounds where the magnetic moments interact through the indirect RKKY interaction. The oscillating properties of RKKY interaction rises the coexistence of FM and AFM interactions among different magnetic moments and makes the system as a promising candidate of EB effect [67]. Nevertheless, the training effect is the another important property of the exchange biased systems which is defined as the difference between subsequent magnetization reversal loops. The compound is measured through several successive hysteresis loops (designated by 'n' at fixed *T*). This effect reduces the H_{EB} and H_C values in the consecutive hysteresis loops measured at a fixed temperature [68].

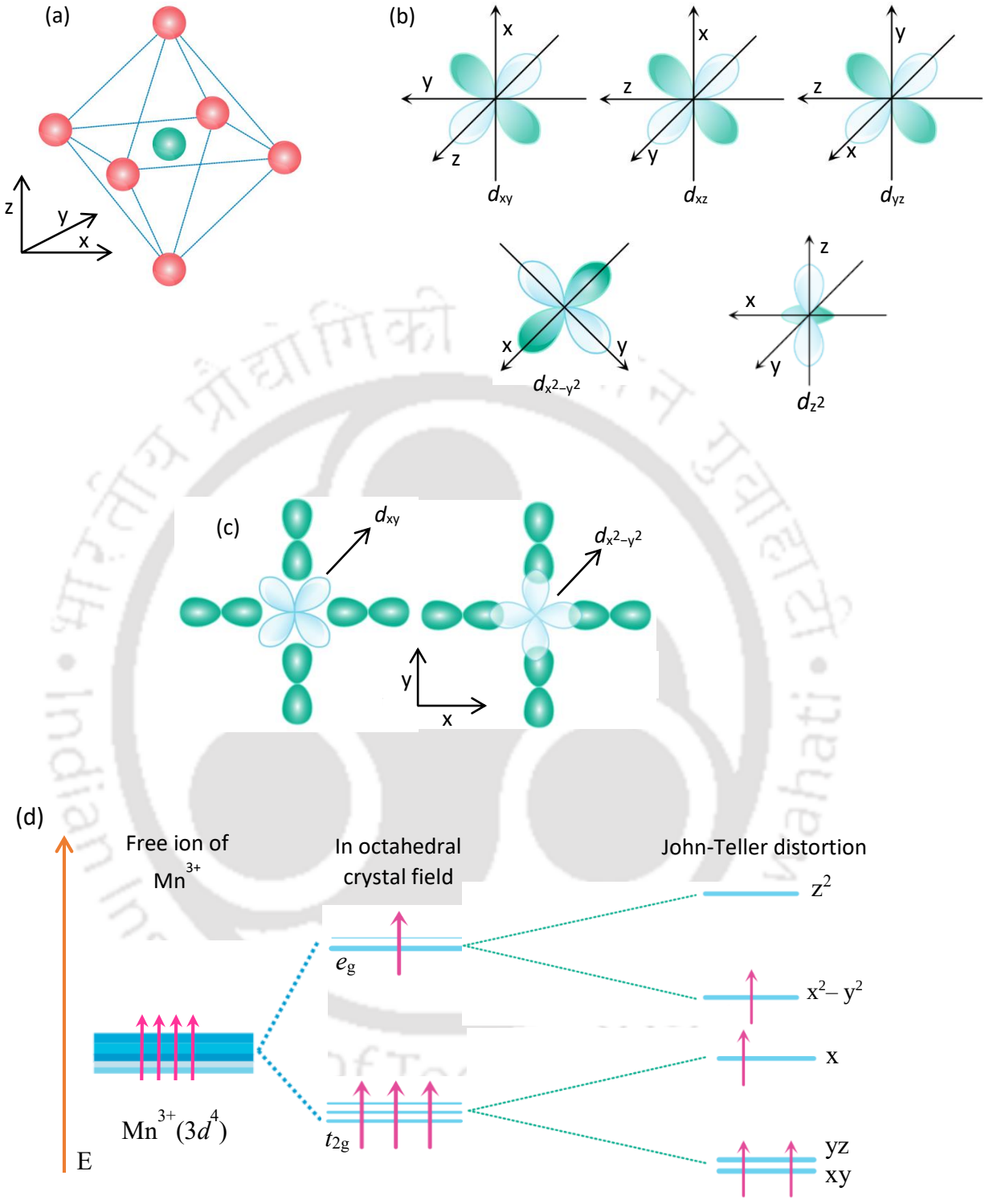

Figure 1.20. (a) Octahedron with center magnetic cation Mn^{3+} surrounded by six oxygen ions. (b) schematic of all the five the *d* orbitals (d_{xy}, d_{xz}, d_{yz}, $d_{x^2-y^2}$ and d_{z^2}) of Mn^{3+}. (c) the e_g (d_{xy}, d_{xz}, d_{yz}) orbital is having lower energy as compared to the t_{2g} ($d_{x^2-y^2}$, d_{z^2}) orbital. (d) The corresponding splitting of the energy levels resulting from the crystal field. (e) Additional splitting of the e_g and t_{2g} levels due to the Jahn-Teller effect.

1.4 Crystal Field effects and Jahn-Teller Distortion:

The electric field experienced by an ion in a solid due to the charge of neighboring ions is known as the crystal field. Crystal field theory was proposed by Hans Bethe in 1929, subsequent modified by J. H. Van Vleck in 1935 which was proposed to allow for some covalence in the interactions [69,70]. Since the introduction of this theory, it has long been used successfully to describe the effect of neighboring ligands on the physical properties of the magnetic ion occupying the tetrahedral or octahedral cage of ligands. In its simplest form crystal field theory calculates the orbital splitting of energy levels of the magnetic ion due to the electrostatic potential exerted by the ligands through Coulomb repulsion. Therefore, the electrons which come close to the ligands experience more repulsion and possesses a higher energy than others. Such effects mostly observed in the transition metal complexes having the unpaired *d*-orbital electrons. As an example let us consider a octahedral complex where the a 3*d* magnetic ion is surrounded by the six oxygen ions (figure 1.20 (a)). It is well known that the five *d*-orbitals can be denoted as d_{xy}, d_{zx}, d_{yz}, d_{x2-y2} and d_{z^2}, shown in figure 1.20 (b). The d_{xy}, d_{zx}, d_{yz} lie in between x-y, x-z, and y-z axes, respectively, and the $d_{x^2-y^2}$ lie along the x and y axes. Whereas, the d_{z^2} shows the two lobes along the z-axis and a ring lies on the xy plane surrounding the vertical lob. Figure 1.20 (b) shows the *d*-orbital–ligaments bonding in the x-y plane of the octahedral complex. It is clear that the d_{xy} orbital has a much lower overlap with the ligands as compared to the $d_{x^2-y^2}$ which is having lower energy. Therefore, due to the ligand field effect the whole *d*-orbitals splits into two levels known as t_{2g} and e_g. The lower energy d_{xy}, d_{zx}, and d_{yz} orbitals belong to t_{2g} level and the higher energy orbitals $d_{x^2-y^2}$ and d_{z^2} forms the e_g level (figure 1.20 (a)). In this line it is worth to discuss an important phenomena related to the crystal field effects known as 'Jahn-Teller distortion' which is defined as the geometrical distortion of a non-linear molecular system which arises due to certain electronic configurations. This phenomenon is mostly observed in transition metal octahedral complexes (figure 1.20 (e)). Jahn-Teller effect implies the splitting of the energy levels to remove the degeneracy and makes the system energetically more favorable. Therefore, in modern physics Jahn–Teller effect is an interesting phenomenon which is linked to the changes occurring in the crystal and magnetic structure. Both the crystal field theory and Jahn-Teller effect will be discussed further in coming chapters in consonance with the results obtained in the current work.

1.5 Motivation and Description of the Problem:

Numerous technological applications and rich fundamental physical properties of the spinel oxides make them very interesting compounds. Spinels (AB_2O_4) gained special attention over other transition metal oxides because of its unique electrochemical performance at nano and micro-dimensions [71-75]. Also, the competing magnetic exchange interactions between the cations in spinel oxides play a major role in deciding their magnetic and crystal structure along with various other physical properties [76-83]. The contribution of orbital degeneracy under very high crystal-field (>2.36 eV), Hund's exchange couplings (~ 0.7 eV) and spin-orbit interactions (5.5 eV) leads to some interesting properties like spin-liquid state, magnetothermal, anisotropic magnetoelastic, magnetodielectric, and magneto-structural distortion driven by cooperative Jahn-Teller effect [77,80,81,84-90]. In particular, giant magnetic anisotropy (650 kOe) and atomic displacements (~ 1/4 Å), negative-magnetization with compensation phenomena, zero-field bipolar exchange-bias effect and reentrant spin-glass behavior in few Mn-, Co- and Cr-based spinels has drawn immense attention [13,14,91-94]. Exploring the tunability of such exotic properties may lead to potential applications in magnetic read/write heads, spin-valves and other switching devices [95-98]. All these aspects motivated us to investigate the spinels oxides from the fundamental point of view. Within this thesis two different strongly correlated electron systems have

been studied, each of which display a different combination of the novel magnetic properties and competing exchange interactions as described in the above sections. Among these two systems we deliberately choose one normal spinel ($(A)_{tetra}[B]_{octa}O_4$; $GeCo_2O_4$) and one inverse spinel ($(B)_{tetra}[AB]_{octa}O_4$; $MnCo_2O_4$) system. On the other hand, coexistence of ferroelectricity and ferrimagnetism was reported previously in such systems because of the non-centrosymmetric arrangement and canted spin structure [41]. Such ferroic properties make them promising candidates for multiferroic applications. Moreover, dilution of octahedral sites with weak/nonmagnetic ions leads to a cross-over from small polaron tunneling to correlated barrier hopping type conduction in the proposed system. Similarly, it was hinted in the literature that dilution with nonmagnetic ions leads to a mixture of long-range ferrimagnetic order and short-range order. Majority of the reports available in the literature on both the systems are primarily focused on the synthesis and characterization of the porous nanostructures with special emphasis on their catalytic and electrochemical properties [57-72]. Little literature is available on the low-temperature neutron diffraction studies of $MnCo_2O_4$ related systems with special emphasis on their magnetic ground state and cationic distribution. In particular, dilution in $MnCo_2O_4$ systems was lacking in the literature when we initiated this work. Motivated by the wide range of applications and unique magnetic properties of these compounds we initiated the present work to investigate primarily a detailed crystal and magnetic structure of the compounds $GeCo_2O_4$, $Mn_xTi_{1-x}Co_2O_4$ and $MnCo_{2-y}Cu_yO_4$. Although the proposed systems are investigated previously in the literature but there are some open issues regarding the nature of magnetic ground state and crystal structure which are not settled when we began this study. Considering all the above open issues, in the present thesis is aimed to fill the gaps in literature by a systematic interpretation of the temperature dependence of the ac- and dc-magnetic susceptibility along with the heat capacity data and neutron diffraction measurements.

भारतीय प्रौद्योगिकी संस्थान गुवाहाटी
Indian Institute of Technology Guwahati

Chapter 2
Fabrication and Characterization Techniques

In this chapter we discuss the fabrication of the investigated system and a detailed description of characterization techniques. A brief summery about the basic theoretical concepts of each characterization method along with its working principle has been outlined in this chapter. These techniques are mainly aimed to understand the crystal structure, electronic and magnetic properties of the chosen compounds.

2.1 Fabrication of Oxide Spinels:

2.1.1 Solid-state reaction method:

All the polycrystalline compounds in the present thesis work were prepared by solvent-less/dry standard solid-state reaction method. This method involves mechanically mixing of the constituent binary metal oxides or carbonates followed by repeated cycles of grinding and sintering at high temperatures. The solid-state reaction method is thermodynamically stable process in which ions diffuses across the solid interface and this diffusion process occurs very slow. Typical reaction time in any solid-state reaction ranges from few days to few weeks and the heat-treatment involves very high temperatures (>1000°C) to overcome the diffusion barrier. In the present case, all the polycrystalline compounds: $GeCo_2O_4$, $MnCo_2O_4$, $Mn_xTi_{1-x}Co_2O_4$, and $MnCo_{2-y}Cu_yO_4$ were synthesized using the solid-state reaction method involving the following methodology. Stoichiometric amounts of commercially available (from Alfa-Aesar GmbH) high purity binary transition metal oxides have been selected as precursors. For the synthesis of $GeCo_2O_4$, $Mn_xTi_{1-x}Co_2O_4$ and $MnCo_{2-y}Cu_yO_4$, we used the precursors GeO_2, Co_3O_4, TiO_2, MnO_2 and CuO. Appropriate precursors are grounded together using an agate mortar with pestle for 6 h duration so that the oxides mix homogeneously. These mixed powders were pressed into cylindrical pellets of size ~ 13 mm in diameter using a KBr die set and hydraulic press (40 kN/m^2). These pellets were placed in an alumina boat and sintered at 1200°C for 12 h in air with heating rate 4°C/minute and then slowly cooled down to room temperature naturally. High temperature sintering leads to the chemical decomposition and resulting in the desired compounds. In order to achieve perfect homogenization, desired density and single phase of the compounds, we crushed the sintered pellets and re-grinded for 2 h and heat treated again at slightly higher temperatures as compared to the initial sintering temperature under same conditions. After the final heat treatment process, all the compounds are tested for the phase purity and for a detailed crystal structure by means of an x-ray diffraction method described below.

2.1.2 Sol-gel Processing:

For the synthesis of nanostructures of $MnCo_2O_4$, $MnCo_{2-y}Cu_yO_4$ and $Mn_{1-x}Zn_xCo_2O_4$, we employed soft-chemistry based sol-gel process because of its inherent advantages. Usually, this technique requires low temperature for processing, allows higher degree of solubility, delivers homogeneous dispersion of substituents and has the advantage of controlling the composition accurately. Sol-gel processing is a simple and versatile method for preparing materials of excellent functionalities with sophisticated nanostructures [99-101]. This technique allows us to select a wide range of precursors as starting materials to synthesize magnetic and non-magnetic colloidal ceramic oxides [99-101]. The most important precursors employed in sol-gel processing are the metal alkoxides ($M(OR)_n$ M^{n+} = metal cation of valence *n* and OR = alkoxy group) and derivatives of ethanol [102-104]. In this process, the metal alkoxides undergo hydrolysis and poly-

condensation resulting in the formation of metalloxane bonds to form a colloid solution (often called as 'sol'). Sol is defined as a suspension of very small size (~ 1 nm – 1 µm) particles in which only short-range forces like Van-der Waals and surface-charge dominate significantly. After the formation of sol, an inorganic continuous network or gel grows with metal-oxo or metal-hydroxo connections in the liquid suspension. Therefore, in the sol-gel process, the suspension undergoes a sol to gel transition irrespective of the precursors. Subsequently, the drying process removes the liquid phase from gel and causes porosity in the material. Finally, thermal treatment is performed for further poly-condensation leading to the stable oxide in the form of fine powder.

Figure 2.1 depicts various steps involved in the sol-gel processing. Initially, the precursors are dissolve in the solvent (distilled water, acid or ethanol) and then mixed homogeneously. For the synthesis of $MnCo_2O_4$, $MnCo_{2-y}Cu_yO_4$ and $Mn_{1-x}Zn_xCo_2O_4$ nanoparticles, we used metal-acetate hydrates ($C_4H_{10}O_6Mn$, $C_4H_{10}O_6Zn$ and $C_4H_{14}O_8Cu$) are chosen as precursors with oxalic acid ($C_2H_2O_4$) and ethanol (C_2H_6O) as solvents to dissolve the acetates [105,106]. Stoichiometric amounts of the above mentioned precursors were first dissolved in ethanolic solution under constant stirring at room temperature for 3 h in air to obtain a light wine color sol. A solution comprising 6 grams of oxalic acid was dissolved in 200 ml of ethanol and added drop-wise to the above prepared warm-transparent sol to obtain a light pink color gel. This gel product was allowed to grow overnight in air and then dried at 80–120°C for two-days to obtain a dehydrated xerogel network. This dried mixed-oxalate product was crushed in an agate mortar and sieved through 240 Mesh to obtain fine particles of uniform distribution. The xerogel network was calcined at temperatures between 300°C and 1000°C to remove the volatile substances such as H_2O, CO and CO_2 to form the final product. Accordingly, all the synthesized samples are calcined at 700°C for 4 h in air for proper decomposition and yield the desired compound which is jet-black in color.

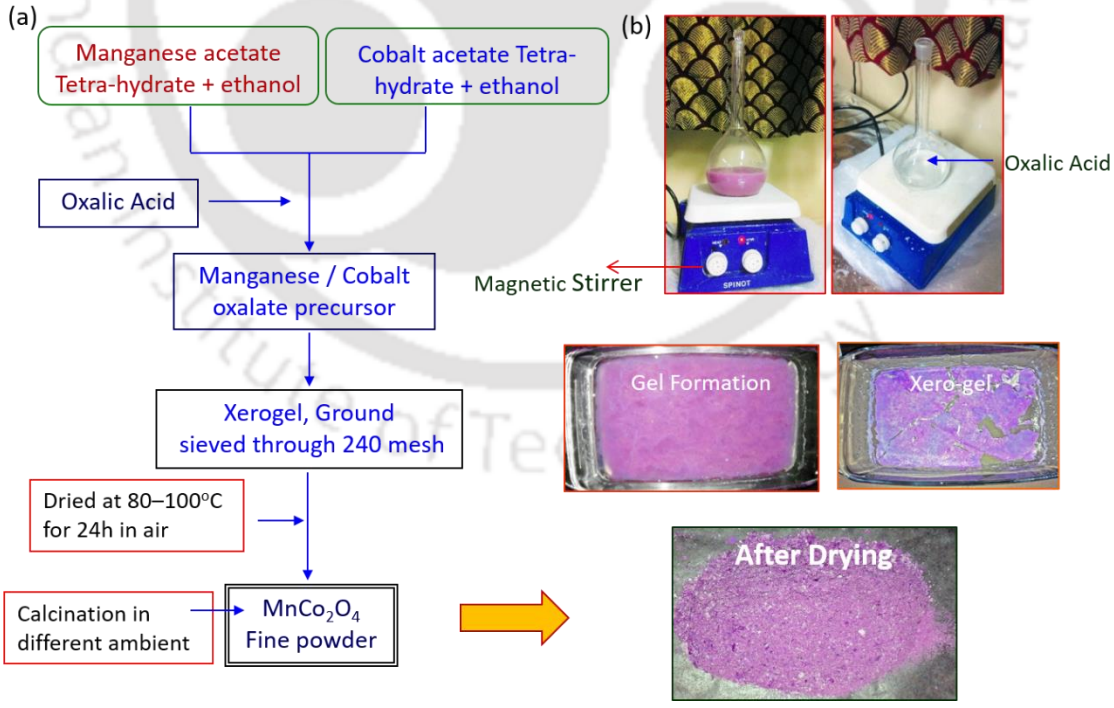

Figure 2.1: (a) The flow chart presenting the important steps involved in the sol-gel synthesis procedure and the corresponding (b) step by step details of the experiment involving the formation of $MnCo_2O_4$ based nanostructures.

2.2 Details of Characterization Techniques:

This section deals with various characterization techniques employed in the present thesis. Firstly, we discuss about the structural characterization of the samples performed using X-ray diffraction measurements including the morphological studies followed by various other experimental techniques.

2.2.1 Crystal Structure and Morphology:

The X-ray diffraction (XRD) is an important non-destructive technique primarily used for the identification of crystal structure and provides detailed information about the unit cell dimensions and interaxial angles of the investigated system. This technique also provides useful information about various structural properties of crystalline compounds such as micro-strain, grain-size, phase composition and defect structure. The XRD analysis is based on constructive interference of monochromatic X-rays after being reflected from the crystalline specimen. When an X-ray beam, generated by a cathode ray tube, it is allowed to incident upon a crystal. Then the beam undergoes diffraction from the set of planes (Miller indices (hkl)) when the geometrical condition satisfies the Bragg's law which is given below (Figure 2.2) [107]:

$$2d_{hkl}\sin\theta = n\lambda \qquad 2.1$$

In the above equation 'd_{hkl}' is the inter-planer spacing between the set of (hkl) planes, θ is the Bragg's angle/or Diffraction angle, 'n' is an integer and λ is the wavelength of X-ray radiation. Figure 2.2 shows the geometry of the Bragg's law for the X-ray diffraction from a set of crystallographic planes. The locus of the diffracted beams taken together from the different sets of planes is collectively known as the diffraction pattern of the crystal. In the present work two different powder X-ray diffractometers were used to study the crystal structure and phase purity; (*i*) high-resolution XPERT-PRO diffractometer of Co-K_α radiation with λ = 1.78901 Å and (*ii*) Rigaku (TTRAX-III) diffractometer (18 kW rotating anode X-ray source) with Cu K_α source radiation with λ = 1.5406 Å. Both these X-ray diffractometers work under the Bragg-Brentano reflection geometry with a specific arrangement where the sample stage is fixed at the center of the circle and both the X-ray source and detector rotates using a goniometer assembly.

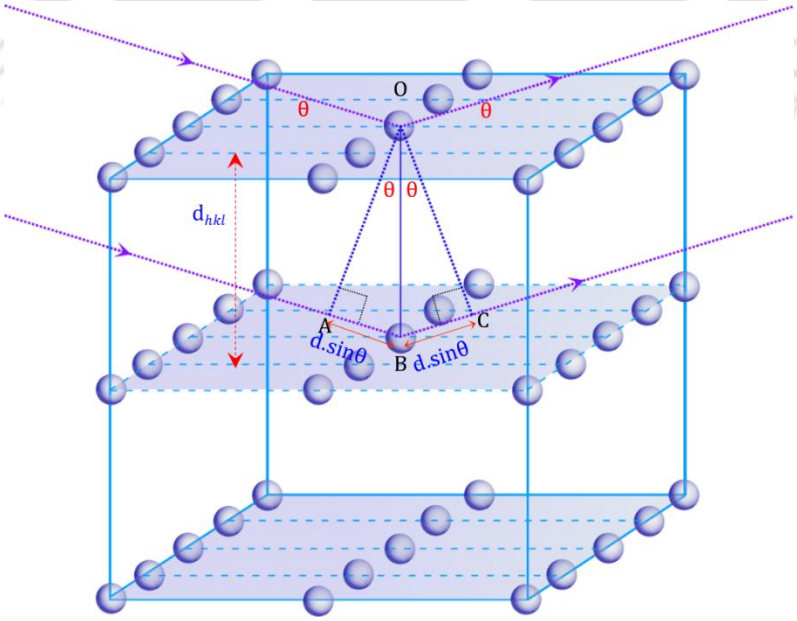

Figure 2.2. Schematic diagram showing the diffraction of X-rays from lattice planes and the Bragg's law.

In order to extract the detailed crystallographic information from the obtained diffraction pattern we also performed the Rietveld refinement using the open source programs FullProf-Suite and Powder-cell [108,109]. On the other hand, to probe the surface morphology and microstructure of the samples investigated in the present work we employed a high-resolution transmission electron microscope (HRTEM, JEOL JEM 2100) operating at 200 kV under SE mode.

2.2.2 Elemental Analysis using the X-ray Photoelectron Spectroscopy:

In the present thesis, X-ray photoelectron spectroscopy (XPS) was employed to probe the chemical states of the investigated samples. This technique is one of the most powerful non-destructive surface sensitive characterization method to study the chemical and physical phenomenon occurring at surfaces of various materials such as metals, oxides, semiconductors, glasses, polymers etc. This technique has gained attention by the scientific community mainly due to the following important reasons: (*i*) It can provide the quantifications of elemental composition from the solid surface up to a thickness of ≤ 10 nm, (*ii*) It can also provide an insight to the chemical and atomic environment of the elements present in the compound, (*iii*) one can obtain the above information with relative ease and minimal sample preparation, (*iv*) ability to explore first few atomic layers and assign chemical states to the detected atoms. Since the mean free path of the electrons in any solid is very small, the detected electrons originated from the top few atomic layers provide important information which makes XPS a unique surface-sensitive technique for chemical analysis. In XPS, a monochromatic beam of soft X-rays (Mg K_α (1253.6 eV) and Al K_α (1486.6 eV)) are exposed to the sample which interact with the core-level electron and transfer its energy to the electron which leads to the emission of core-level electrons (photoelectric effect). The recorded spectrum consists of the core-level photoelectron intensity detected per energy interval (on y-axis) plotted against their kinetic energy or Binding energy (on x-axis). Since each element has a unique XPS characteristic spectrum, different set of elements give a spectrum comprising of the intermixture of individual peaks of the constituent elements.

The basic principle behind the XPS is Photoelectric effect in which electrically charged particles are released from the core of the material when it absorbs electromagnetic radiation as shown in figure 2.3. In the case of XPS, the interaction of soft X-rays with specimen leads to the photoemission process and its energy is analyzed by the spectrometer. Generally, the X-rays are capable in knocking out the electrons not only from outer shells but also from the core levels. The emission of an electron from the 1*s* shell of an atom is schematically represented in figure 2.3. The kinetic energy of an incident photoelectron (E_{KE}) is equivalent to the difference between X-ray photon energy ($h\nu$) and the binding energy of the core-level electron (E_{BE}). Relation between these parameters and the work function of the spectrometer (Φ_s) is given by the below expression [110-112]:

$$E_{KE} = h\nu - E_{BE} - \Phi_{sl} - (\Phi_s - \Phi_{sl})$$

$$E_{KE} = h\nu - E_{BE} - \Phi_s \qquad 2.2$$

In addition, the work function for the sample (Φ_{sl}) is defined as the difference between the energy of the Fermi level (E_F) and the energy of the vacuum level (E_V). E_V is the zero point of the electron energy scale:

$$\Phi_{sl} = E_F - E_V \qquad 2.3$$

Usually, Φ_s is determined from a detailed calibration for the spectrometer used. From equation 2.3 it is clear that only binding energies lower than the excitation radiation (in the present case 1486.6 eV for Al K_α and 1253.6 eV for Mg K_α) can be probed. In addition to the photoelectric process, relaxation of the excited ion may occur by the emission of Auger electrons (figure 2.4). The Auger emission is dominated for elements having low atomic numbers (Z < 30). When an electron is emitted from a core level, another electron from a higher

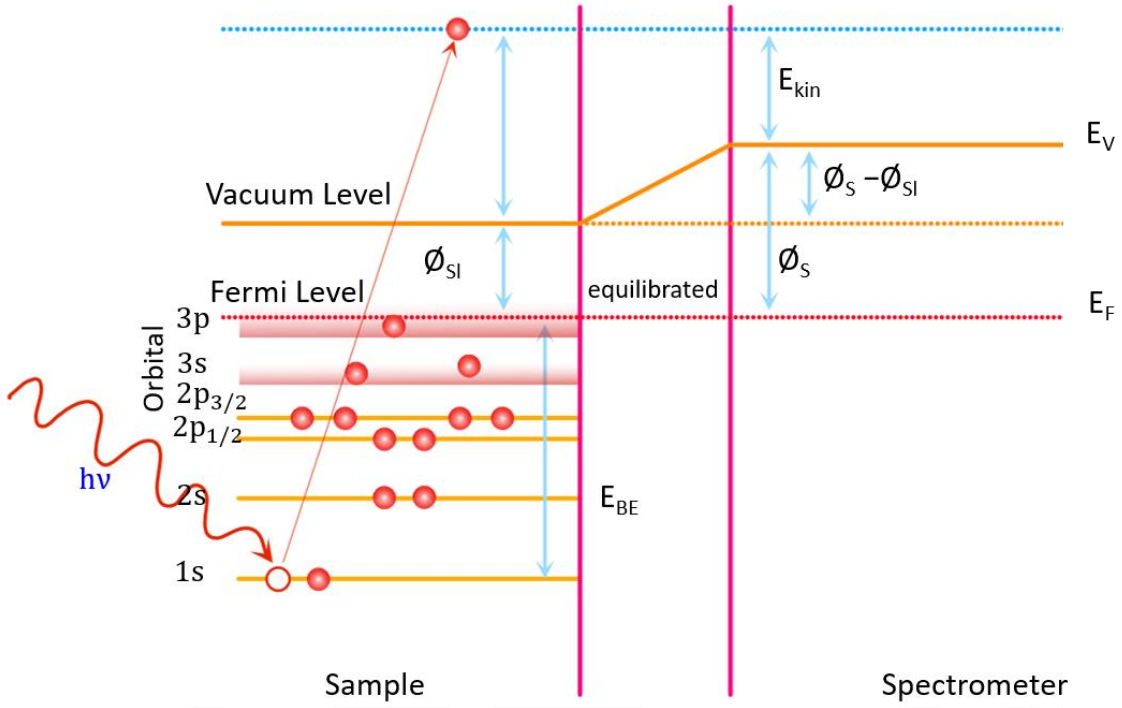

Figure 2.3. Schematic diagram showing the basic principle of the core-level photoelectron emission.

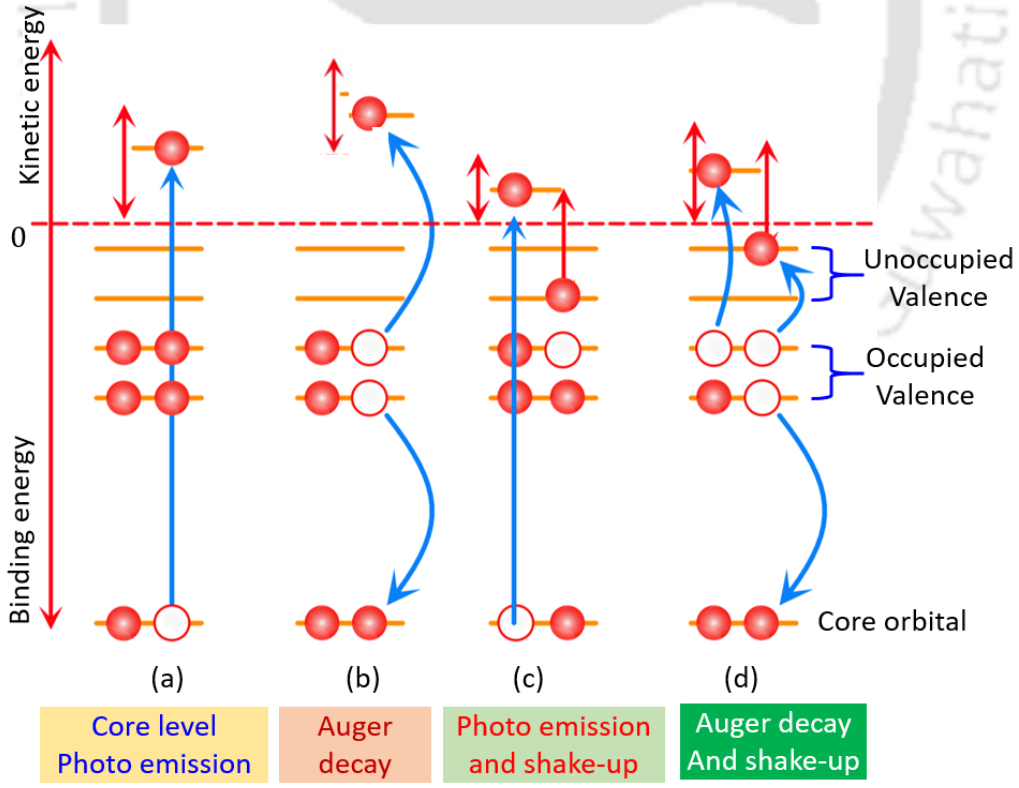

Figure 2.4. schematic representation of the energy level diagram showing various emission procedures of photoelectric effect. In particular, the (a) core level electron emission, (b) emission of Auger electron, and (c, d) emission of electron in shake-up/shake-off process.

level falls to occupy the core level vacancy [110-112]. In order to conserve the total energy of the system, a third electron is emitted during this process which is known as Auger electron (figure 2.4 (b)). Auger emission is independent of the photon energy and therefore the X-ray source. Another important relaxation process, which can significantly contribute to the XPS spectrum, is the "Shake-up"/"Shake-off" process in which electrons from the valence levels are excited to the bound/unbound states (figure 2.4 (c, d)). Moreover, 'Multiplet' splitting of the XPS peaks can also occur when atoms having unpaired electron couple with other unpaired electrons in the atoms giving rise to several possible final state configurations consequently peaks shift to higher binding energy from the principle peak [110-112]. Some less intense Plasmon peaks also appear at higher binding energies from the principle peak at equal spacing due to specific amounts of energy losses when the photoelectron excites free electrons in a material.

2.2.2.1 XPS Instrumentation:

The XPS spectrometer consists a source of primary radiation (Al K_α or Mg K_α), an electron energy analyzer, extraction optics with energy filter and sample holder mounted under an ultra-high vacuum chamber (< 10^{-9} mbar) (Figure 2.5). The following constraints are applicable when operating the XPS instrument under normal conditions: (*a*) The photoelectron and Auger electron emissions are not affected by any external electrostatic or magnetic fields. Thus, the system should be calibrated to compensate the earth's magnetic field. (*b*) The photoelectron and Auger electron emissions are able to travel the region between the sample and the detector (around 1 m in distance). (*c*) Sample from which the emission arises must not be modified in any form during the course of analysis. (*d*) Investigated samples must be stable within the ultra-high vacuum chamber of the spectrometer. Since XPS is associated with the core-level electrons emitting from a solid surface, the sources used in XPS for X-ray generation must be able to produce photons of sufficient energy to interact with suitable number of core electrons [110-112]. X-rays are produced by bombarding an anode material with high-energy electrons. Normally, electrically heated tungsten filament is used as a thermal source for the emission of electrons, however, for some focused X-ray monochromators, a lanthanum hexaboride emitter is used due to its higher current density. The X-ray emission efficiency of an anode is determined by the electron energy relative to the X-ray photon energy. For example, the Al K_α (1486.6 eV) photon flux from an aluminum anode increases by a factor of more than five, if the electron energy is increased from 4 keV to l0 keV [111]. At a given energy, the photon flux from an X-ray anode is proportional to the electron current striking the anode. The maximum anode current is determined by the efficiency with which the heat generated at the anode must be dissipated. For this reason, X-ray anodes are usually connected with water-cooled attachments. Apart from the production of X-rays, it is also important to detect the emitted core level electrons with very high sensitivity. Due to this, energy analyzer with very high detection limit (0.1 to 1 atomic %) and good resolution must be used. In general, two types of electron analyzers are used: (*i*) Cylindrical mirror analyzer (CMA) and (*ii*) Hemispherical sector analyzer (HSA) [110-112]. CMA analyzer is used when the resolution is not the priority (~ 0.4 to 0.6 % of the energy) and sample dimension is smaller than 1mm. For better resolution HAS is used which can achieve better resolution than CMA by a factor of ten. For HAS, the energy of the ejected electron must satisfy the condition given below to reach the detector [110-112]:

$$E = e\Delta V \frac{R_1 R_2}{R_2^2 - R_1^2} \qquad 2.4$$

In the above expression, both R_1 and R_2 are the inner and outer radius of the hemisphere respectively, and ΔV is the applied potential difference between the inner and outer surface of hemisphere. Finally, to count the individual electrons arriving at the detector, dynodes (electron-multipliers) are used.

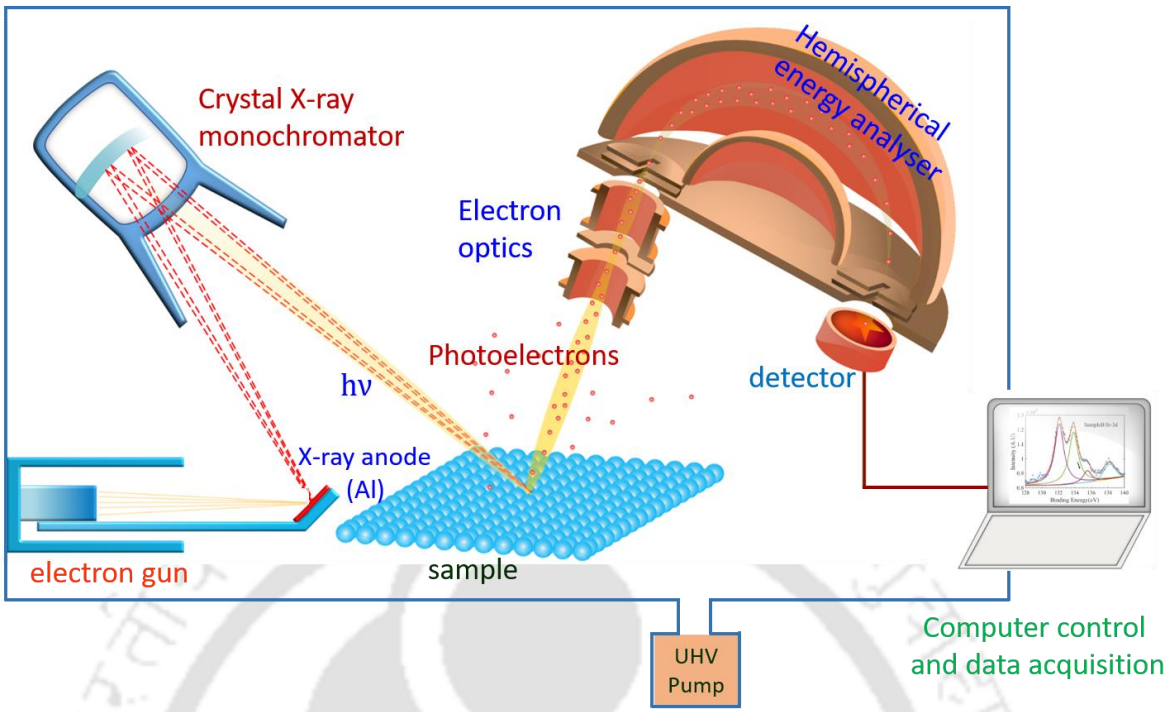

Figure 2.5. Typical components of the XPS instrumentation and schematic demonstration of the measurement method Ref [113].

These dynodes consist of spiral-shaped glass tube with conical collector at one end and a metal anode at other end. In the present thesis, all the spectra were recorded by a high-resolution X-ray photoelectron spectroscope from Kratos Axis Ultra, Model AXIS 165 equipped with an ion-gun (EX-05).

2.2.3 Magnetic Characterization:

This section deals with the detailed description related to the magnetic measurements performed in this work. The magnetic properties of most of the polycrystalline compounds in the present thesis work have been studied by the neutron diffraction measurements as well as by traditional magnetization measurements using superconducting-quantum-interference-device (SQUID) based magnetometer (Magnetic property Measurement system, MPMS-XL5 from Quantum-Design) [114,115]. We also used physical property measurement system (PPMS) with vibrating-sample-magnetometer (VSM) accessory for high field (± 9 T) and low-temperature (1.95 K) measurements. The SQUID magnetometer is the most effective and sensitive tool which can detect low magnetic moments with very high resolution of 10^{-7} emu and very small magnetic field (10^{-18} T) using the Josephson junctions [116,117]. SQUID consists of two superconductors separated by thin insulating layer to form two parallel Josephson junctions as shown in figure 2.6 (a), which act as a magnetic flux-to-voltage transducer. The basic principle governing the operation of SQUID devices are based on the flux-quantization in superconducting loops and the Josephson-effect [118]. In 1962, B. D. Josephson showed that the electrical current density through a weak electric contact between two superconductors depends on the phase difference $\Delta\phi$ of the two superconducting wave functions [114,117]. In the succeeding subsections we discuss about the instrumentation, measurement principles, quantities and units relevant to SQUID magnetometry, sensitivity and detection limits including the typical measurement protocols.

2.2.3.1 DC-Magnetization:

Here we present the details of extraction of DC-magnetization and the working principle of a SQUID. Typically, in a SQUID when the current enters at the terminal 1, it gets divided into two parts, I_1 and I_2which experience a phase shift while passing through the two Josephson junctions X and Y (Figure 2.6 (a)). These two phase shifted currents ($I_1'$and I_2') interfere at the terminal 2 and the resultant current oscillates between a maximum and a minimum value. The magnetic flux inside any superconducting ring is quantized and defined as $\phi = nhc/2e = n\phi_0$, where n is an integer and ϕ_0 is magnetic flux quantum = $hc/2e = 2.07\times10^{-7}$ Gauss-cm^2. The maximum value of the current occurs when the magnetic flux inside the ring is reached to an integral number of flux quantum, whereas, the minimum corresponds to the half integral of the flux quantum. The voltage which also oscillates depending on the change in magnetic flux is measured across the two terminals 1 and 2. Thus SQUID acts as a transducer which converts magnetic flux into voltage. In the magnetometer, this superconducting loop is connected with the pickup coil which is also located inside the magnetic field. The pickup coil is made of superconducting wire with four windings (Figure 2.6 (b)). When a sample moves up and down inside the superconducting wires the magnetic moment of the sample induces an electric current in the coil which couples with magnetic flux through the coil with the SQUID sensor, as shown in Figure 2.6(a). The SQUID sensor changes the magnetic flux to the output voltage which is proportional to the change in magnetic moment of the sample (Figure 2.6 (c)). The voltage is then magnified and read out by the magnetometer electronics. It is well known that SQUID can only detect magnetic flux ϕ (= $\int \boldsymbol{B} \cdot d\mathbf{A}$, magnetic flux density *B* times the area A of the SQUID loop and every SQUID magnetometer has to be calibrated with a sample of known magnetic moment such that one can obtain the fringing/stray field (since the actual area A of each SQUID is not precisely known). However, commercially available SQUID magnetometers generally detect the change of magnetic flux created by mechanically moving the sample through a superconducting pick-up coil which is converted to a voltage V_{SQUID}. In an MPMS, the position is denoted as the *x*-direction which is parallel to the external magnetic field H_{ext} so that one obtains raw data, often called as "lastscan," where V_{SQUID} is plotted against x_{pos} (figure 2.6 (b)).

In order to suppress the influence of all kinds of external magnetic fields, the pick-up coil is made as second order gradiometer. The entire detection system is sketched in figure 2.6 (b) and the inset exemplarily shows a single SQUID scan where the maximum of V_{SQUID} at x_{pos} = 2 cm corresponds to the sample directly positioned in-between the double coil of the pick-up gradiometer. After mounting the sample, this center-position has to be determined using a long scan to accurately adjust the sample position with respect to the pickup coils (this procedure is popularly known as centering). During the centering process one has to record relatively long scans so that not only the maximum but also two minima should be included in the scan. In this process the sample can be imagined like an ideal point dipole which is exactly pinned on the axis of the magnetometer. Usually, the software allows one to perform the fit in two ways: First, it either assumes a fixed sample position and only fits the amplitude of the $V_{SQUID}(x_{pos})$-curve with a single fitting parameter which is the magnetic moment of the assumed point dipole and this known as 'linear-regression-mode' in the MPMS. In the second method the sample position is fitted together with the amplitude by iterative regression mode which is very convenient method when measuring the temperature dependent magnetization. The iterative regression mode easily compensates for the thermal expansion of the sample holder assembly. To minimize errors in the fit due to the point dipole approximation in the either fitting routine, the specimen size should be limited to a maximum of 5 mm along the scan direction. Whereas, the lateral size of sample is naturally limited to 5-6 mm depending upon the design of the sample holder. In the present case we mounted the sample in a gelatin

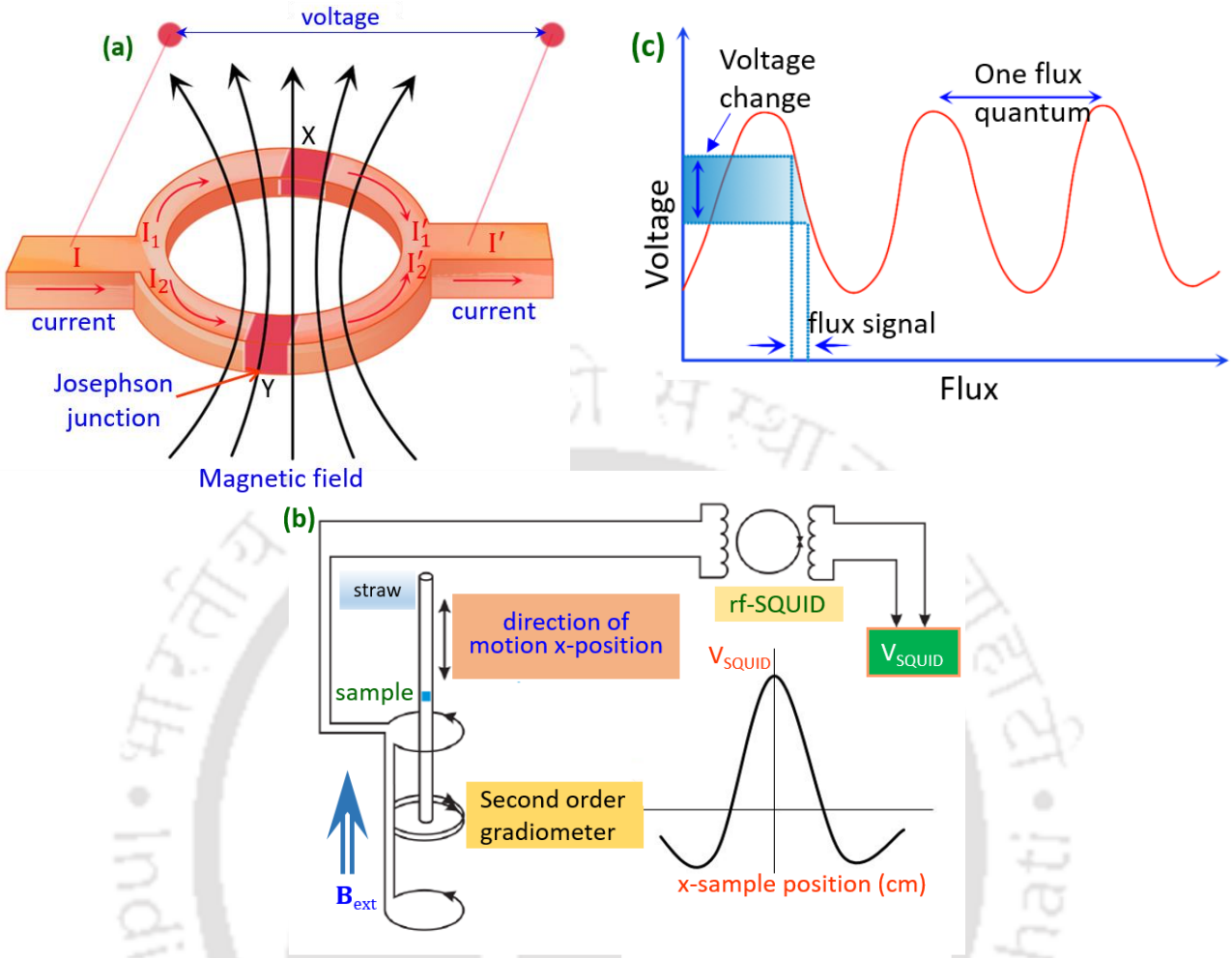

Figure 2.6. (a) Schematic diagram of a superconducting ring consists with two Josephson junctions inside the DC SQUID magnetometer. (b) The superconducting pick-up coil with second order gradiometer (four circular rings). Inset shows the SQUID response V_{SQUID} versus sample position (x-pos.). (c) The output voltage plotted as a function of applied flux, here a small change in flux corresponds to the measurable voltage change across the SQUID.

capsule which is inserted in a clear drinking straw. Nevertheless, for highly sensitive measurements, the following parameters turned out to be a good compromise between accuracy and time: 4 cm of sample movement, average over 5 scans with 10 oscillations each at 1 Hz, and iterative regression mode for the fit routine. Concerning the units, magnetization (*M*) of a homogeneous sample of volume (V) is related to the magnetic moment (m) with *M*=m/V. Typically, magnetometry measurements are different from susceptometry measurements where the magnetic susceptibility tensor χ_{ij} is given by $\chi_{ij} = \partial M_i/\partial H_j$. Here *H* represents the magnetic field intensity, which is not to be mistaken with *B* the magnetic flux density (or magnetic induction). In the cgs units, *B* is measured in Gauss (G) while *H* is measured in Oersted (Oe) and in vacuum, both quantities are same. In the SI units, *B* is measured in Tesla (T), whereas, *H* is measured in A/m and in vacuum, $B = \mu_0 H$; the conversion from cgs to SI is 10000 Oe = 1 T. The MPMS uses the cgs-unit emu for 'm', which can be easily converted into the SI-units.

Usually, in the case of powder samples, the measured magnetic moment from SQUID magnetometry is often given in emu/g which is easier to be measured and does not require an exact knowledge of the density

of the used material and this quantity can be easily representable in μ_B/atom (1 μ_B =9.274×10^{-21} emu). The sensitivity of commercial SQUID magnetometers is usually provided in emu; for the MPMS-XL5, it is < 10^{-8} emu below 250 mT and less than 2×10^{-7} emu up to full field conferring to the manufacturers specifications which is ~ 2×10^{-7} emu corresponding to the magnetic moment of a single atomic layer of nickel.

In the present study, fully automated "standard sequences" were used for the temperature dependence of magnetization and magnetic hysteresis loops performed using a SQUID magnetometer. Throughout this work we used standard MPMS sequences for the *M-H* and *M-T* measurements under both zero-field-cooled (ZFC) and field cooled (FC) conditions. For the *M-H* curve we used the following experimental protocol. First, a full *M-H* is measured at 300 K under five cycle hysteresis mode (0→+5T→0→–5T→0→+5T) using the "no overshoot" mode (field is approaching the desired magnetic field from one side and exactly stabilizes the magnetic field at the requested value; magnet is in persistent mode during the actual measurement). Then the sample is cooled down in the presence of field H_{dc} and no-field (H_{dc} = 0 Oe) to 2 K and then a full $M(H)$ curve is recorded. We performed the $M(H)$ curve at 2 K under field-cooled conditions to see whether the investigated system exhibits exchange-bias effects or not. This procedure also allows us to probe the field imprinted magnetic phenomena like the uncompensated antiferromagnets or ferrimagnets. On the other hand, temperature dependence (2 K to 300 K) of magnetization $M(T)$ was measured using the standard protocols, ZFC and FC by cooling the compound in the presence of field/no-field (≤100 Oe) and under settle mode with small temperature interval. However, few measurements were performed under sweep mode (no stabilization of the temperature). Before the beginning of sequence for low-field measurements, 1 kOe field is set using the "oscillation" mode and set to zero, such that one can minimize the residual/stray fields and ensure perfect virgin state. After this procedure, we performed the low-field $M(T)$ measurements in which field is applied with no-overshoot condition.

The principal components of the SQUID measurement system comprise the following major constituents:

(i) Temperature control system: Precision control of the temperature in the range 2 K to 400 K.

(ii) Magnet control system: Current from a power supply is set to provide magnetic fields from zero to ±7 T.

(iii) Superconducting SQUID amplifier system: The DC−SQUID detector is the heart of the magnetic moment detection system. It provides reset circuitry, auto-ranging capability, a highly balanced second-derivative sample coil array.

(iv) Sample handling system: The ability to step and rotate the sample through the detection coils without transmitting undue mechanical vibration to the SQUID is of primary importance.

(v) *Computer operating system:* All operating features of the MPMS are automated and computer controlled. The user interface at the PC console provides the option of working under standard sequence control or diagnostic control which will invoke individual functions.

2.2.3.2 AC-Magnetic Susceptibility:

This particular sub-section is devoted to the theory and experimental methods related to dynamic magnetic susceptibility under time varying magnetic field together with the measurement technique. In the ac-susceptometer, the sample is mounted in the center within the pick-up coil and a small time varying sinusoidal magnetic field $h_{AC} = h_0 \sin(\omega t)$ is applied on the sample. Here ω (= $2\pi f$) is the angular frequency of the oscillating magnetic field.

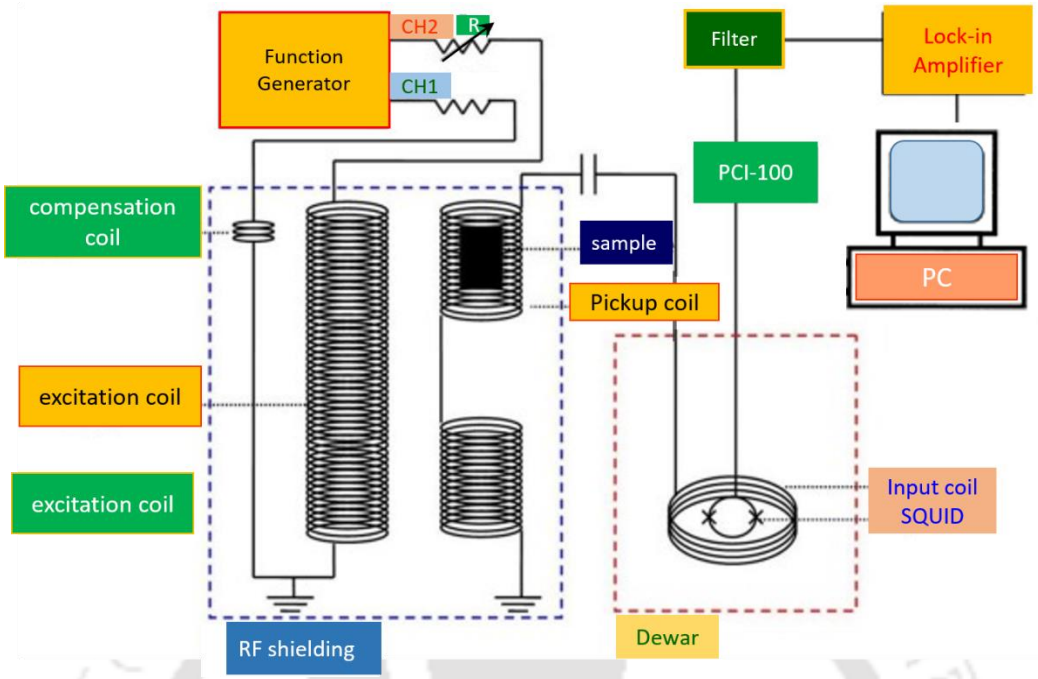

Figure 2.7: Schematic setup of a SQUID-based ac-susceptometer [119].

The frequency (f) is typically in the range 0.1–10 kHz. The response of the magnetization is recorded, $M_{AC} = \frac{dM}{dH} h_0 \sin(\omega t)$; where the AC-susceptibility is defined by the following expression:

$$\chi_{AC} = \frac{dM}{dH} = M_{AC}/h_{AC}$$

Usually, the frequency of the oscillating magnetic field is comparable to the timescale of the magnetic dipole relaxation of the system. It is possible that there may be some phase lag (consequently, dissipation takes place) when the perturbation is slightly faster or slower than the natural frequency of the system. Thus, the response is reported in two parts: in-phase (χ'_{AC}) and out-of-phase (χ''_{AC}) (or real and imaginary components). Here, the imaginary component (χ''_{AC}) relates to dissipation/loss in the system. Thus, the ac-susceptibility may be written as a complex number: $\chi_{AC} = \chi'_{AC} + i\chi''_{AC}$.

Where

$$\chi' = \mathrm{Re}[\chi_{AC}] = \chi_0 \cos\phi = \frac{\chi_0}{1+(\omega\tau_{\mathrm{eff}})^2}$$

$$\chi'' = \mathrm{Im}[\chi_{AC}] = \chi_0 \sin\phi = \frac{\chi_0}{1+(\omega\tau_{\mathrm{eff}})^2}\ \omega\tau_{\mathrm{eff}}$$

and $\chi'/\chi'' = \tan\phi = \omega\tau_{\mathrm{eff}}\ (t)$. In the above expressions, ϕ represents the phase delay of the time-varying magnetization ($M(t)$) relative to the applied ac magnetic field ($h_{ac}(t)$) and τ_{eff} is the effective relaxation rate which characterizes the ability to retain magnetization after an applied dc-field is removed. As compared with the dc-magnetic susceptibility, the temperature dependence of ac-susceptibility $\chi_{AC}(T)$ gives sharp transitions and the ac-data clearly separates out the order - disorder transitions from the local short range magnetic orderings [24].

In the present thesis work we employed the same SQUID magnetometer as discussed above for the temperature and frequency dependence of ac-susceptibility data. However, ac-measurements are performed using a PPMS (Quantum Design) along with the ac-measurement system (ACMS) accessory. In general, any home-made ac-magnetic system contains sensing coils including excitation coil, pick-up coil and compensation coil. First, the excitation coil was excited with a certain frequency of ac signal where the pickup coil is used in

gradient configuration and the compensation coil is used to improve the balance of the pickup coil. By means of a lock-in amplifier the real (Re[χ_{AC}) and imaginary components (Im[χ_{AC}]) of ac-susceptibility can be detected. Figure 2.7 shows a schematic of the detection process of ac-susceptibility.

2.2.3.3 Specific Heat:

In the present work we performed the temperature dependence of specific heat at constant pressure ($C_p(T)$) using PPMS (from Quantum Design) with heat capacity accessory in which heat added and removed from a sample by monitoring the resulting change in temperature [120]. It is well known that heat capacity C is defined as the amount of heat, Q required to effect a corresponding change in temperature T at a constant volume; $C = dQ/dT$. At low temperatures, the heat capacity of material may be written as the sum of electron and phonon contribution: $C = \gamma T + AT^3$, where γ and A are the constants and characteristic of the material under investigation. The contribution from electronic part is linear with T and is dominant at very low temperature. In each measurement cycle, a known amount of heat is supplied to the sample at constant power for a fixed time, then this heating period is followed by a cooling period of the same duration. After each cycle, the software option fits the temperature response of the sample stage to a suitable model. It is possible that weak thermal contact between the sample and sample-platform causes thermal relaxation. Therefore, the model considers the thermal relaxation of the sample stage to the thermal bath and also the relaxation between the sample-platform and the sample itself which offers the accurate value of the C_p of the sample [121]. Figure 2.8 illustrates the schematic of thermal connections to the sample and sample platform in PPMS Heat Capacity accessory. A heater and a thermometer are attached at the bottom of the sample stage. The sample is attached on the stage by thin layer of N-Grease which helps to make thermal contact between sample and the sample-platform. Highly sensitive wiring system is connected with the heater and thermometer to provide electrical and thermal connections. Usually, the addenda measurements are performed before the $C_p(T)$ measurement of the sample, which consists of measuring the C_p of the sample holder. In the addenda run, a thin layer of Apiezon N Grease is placed on the sample stage and the measurement is taken. After the completion of addenda run, the sample is carefully attached with the grease without disturbing it. The measurement is performed once more and the correct value of the C_p of the sample is determined by subtracting the C_p of the sample holder from the total magnitude.

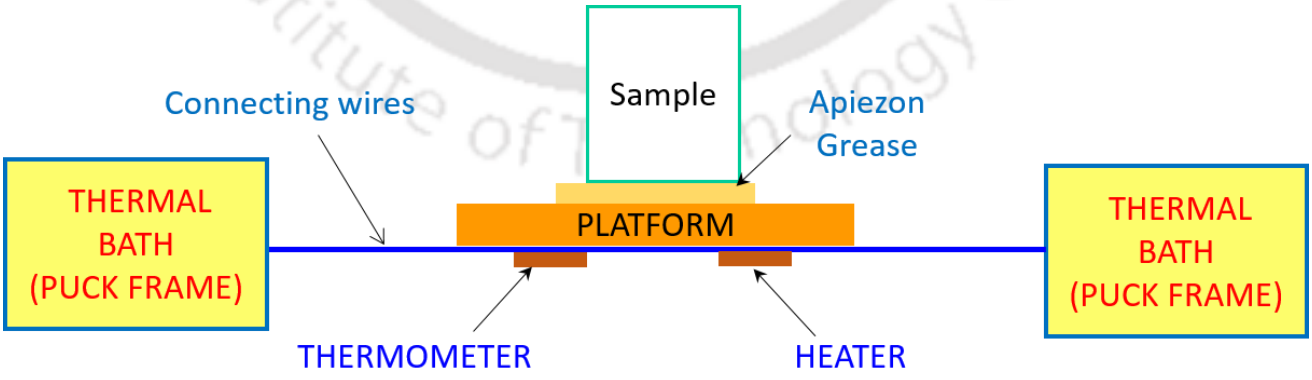

Figure 2.8. Schematic diagram of the specific heat measurement assembly and connections adopted from Quantum Design PPMS.

2.2.4 Neutron Diffraction Measurements:

In the present thesis, we performed Neutron powder diffraction/scattering experiments at Helmholtz Zentrum Berlin (HZB), Germany. These measurements are aimed to probe the magnetic ground state and detailed crystal structure and magnetic ordering of the investigated compounds at various temperatures below the T_C/T_N. In principles the Neutron powder diffraction usages the similar techniques as that of X-ray powder diffraction where x-rays interact with the electron cloud, but neutron scattering occurs at the atom nuclei since the neutrons carry magnetic moment which makes them excellent candidates to probe the magnetic properties of materials. Using this method one can accurately determine the magnitude of magnetic moment of the system.

2.2.4.1 Neutron Properties:

Neutron scattering is a versatile technique, particularly to study the crystal properties of strongly correlated electron systems. Neutrons are uncharged particles, therefore, it experiences very weak or no Coulombic barrier and penetrate deeply into materials and interact directly with the atomic nucleus. On the other hand, Neutron consist quarks and gluons and possesses spin-1/2 with magnetic moment $\mu_n = -1.913\ \mu_N$, where $\mu_N = \frac{e\hbar}{2m_p}$ is the nuclear magnetic moment. Thus, the neutron's magnetic moment interacts with the unpaired electron spins of magnetic atoms with a comparable strength and gives the magnetic structure of the compounds. Furthermore, due to large mass (1.675×10^{-27} kg) neutron leads to a thermal-neutron de-Broglie wavelength [$\lambda = \frac{h}{mv}$] of about 1.8 Å, which is of the order of the interatomic distances, generating possible interference patterns which gives the structural information about the system. Therefore, Neutron Scattering technique is a powerful tool to probe the crystal and magnetic structure of crystalline samples under elastic and inelastic scattering conditions [122-124]. For the scattering measurements the neutron beam is typically produced using two mechanisms: The first one is 'Fission process' in which a steady flux of neutrons is produced inside a nuclear reactor and the second mechanism is 'Spallation source' where neutrons are produced by bombarding heavy metal atoms with energetic protons from accelerators. The neutrons generated from the two sources usually possess very high energies therefore their energy can be categorized in different ranges; cold neutrons and thermal/hot neutrons depending on the temperature/energy range. A brief theory of neutron scattering and working principle of neutron diffractometer is outlined below.

2.2.4.2 Neutron scattering theoretical and Experimental background:

Generally, in the neutron scattering experiment a collimated beam of thermally accelerated neutron source with momentum $\hbar\boldsymbol{k_i}$ and energy E_i scatters from a sample at an angle θ with final wave vector $\boldsymbol{k_f}$ and energy E_f. During the scattering process, the transferred momentum ($\hbar\mathbf{Q}$) and energy (E_T) to the sample is defined as (according to the conservation of total energy and momentum):

$$\hbar\boldsymbol{Q} = \hbar\boldsymbol{k_f} - \hbar\boldsymbol{k_i}, \qquad 2.5$$

where, $Q^2 = k_f^2 + k_i^2 - 2k_i k_f cos\,(2\theta)$

and $E_T = E_f - E_i = \frac{\hbar^2}{2m_n}\,(k_f^2 - k_i^2)$

A pictorial demonstration of the scattering process is shown in figure 2.9. In case of elastic scattering, no energy is transferred from the neutron to the sample, therefore $E_T = 0$, $|k_i| = |k_f|$ and the transferred wave vector is $Q = 2|k|^2 \sin\theta$. Whereas, in an inelastic scattering process both energy and momentum are transferred from

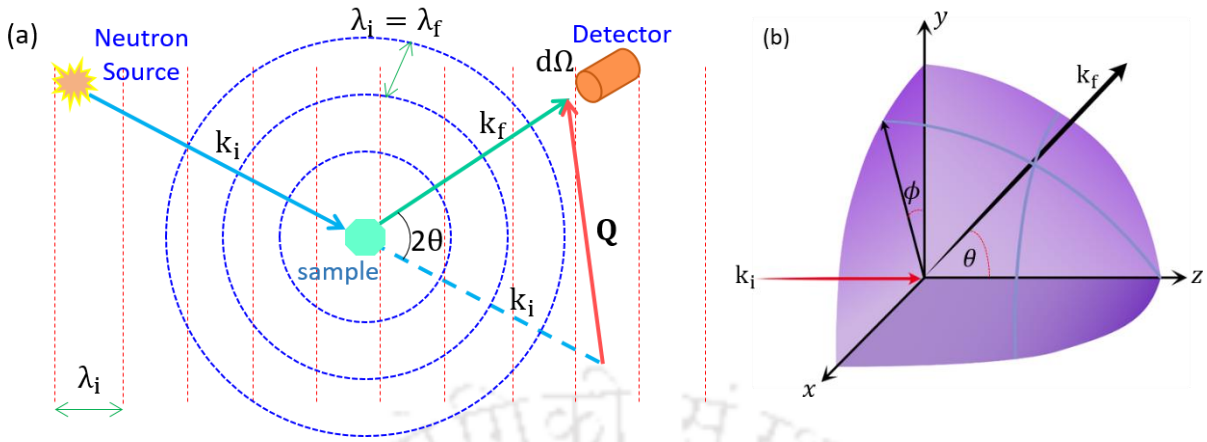

Figure 2.9. Illustration of neutron scattering wave fronts from an atom: (a) k_i (k_f) and λ_i (λ_f) represents the initial (final) wave-vector and wavelength describing a neutron scattering from a single nucleus with positive scattering length. (b) The geometry of a scattering experiment where the incident neutrons with k_i are scattered in the direction θ and ϕ with final wave-vector k_f.

the neutron to the sample, hence $E_T \neq 0$ and $|k_i| \neq |k_f|$. Consequently, the change in energy is measured during the experiment which gives the detailed information about dynamics of the material. Therefore, the number of neutrons scattered into solid angle $d\Omega$ per second around $\Omega(\theta, \phi)$ with the final energy between E_f to $E_f+\Delta E_f$ is called double differential scattering cross section $\left(\frac{d^2\sigma}{d\Omega dE_f}\right)$, where σ represents the flux of scattered neutrons. It is the basic quantity measured during a neutron scattering experiment and depends strongly on the interaction strength between the neutron and the samples. Hence, the partial differential cross section of neutrons scattered by the specimen's internal potential V is given by the below expression [122]:

$$\frac{d^2\sigma}{d\Omega dE}_{k_i \to k_f} = \frac{k_f}{k_i}\left(\frac{m}{2\pi\hbar^2}\right)^2 \left|\langle k_f s_f \lambda_f |V| k_i s_i \lambda_i\rangle\right|^2 \delta(E_{\lambda_i} - E_{\lambda_f} + E_i - E_f) \quad 2.6$$

Here s_i and s_f represents the incident and scattered neutron spin states. After the scattering sample state changes from λ_i to λ_f. Moreover, E_i and E_f represents the corresponding energy of the individual states, respectively. During the neutron scattering experiment an incident neutron interacts with the i^{th} atomic nuclei positioned at r_i through an interaction potential which can be described by a Fermi pseudo potential function as below [122]:

$$V_N(\mathbf{r}) = \frac{2\pi\hbar^2}{m_n}\sum_i b_i \delta(\boldsymbol{r} - \boldsymbol{r_i}) \quad 2.7$$

In the above equation, b_i represents the scattering lengths of each atomic nucleus. The nuclear force is strong within the short range limit and spherically symmetric and the potential is defined by the delta function. Summing over all the nuclei and using the above potential function the total scattering cross section can be calculated [125]. When an un-polarized neutron source falls on the materials the partial differential cross-section can be written as a sum of coherent and incoherent term:

$$\frac{d^2\sigma}{d\Omega dE} = \frac{d^2\sigma_{coh}}{d\Omega dE_f} + \frac{d^2\sigma_{incoh}}{d\Omega dE_f} \quad 2.8$$

On the other hand, the Van Hove method shows that the double differential cross section can be expressed by the dynamic correlation factor S(Q,ω) as:

$$\frac{d^2\sigma}{d\Omega dE} = N\frac{k_f}{k_i}S(\boldsymbol{Q}, \omega) \quad 2.9$$

Where, $S(\boldsymbol{Q},\omega) = \frac{1}{2\pi\hbar \mathrm{N}}\sum_{ll'}\int_{-\infty}^{\infty}\langle e^{-i\boldsymbol{Q}.\boldsymbol{r}_{l'}(0)}\, e^{i\boldsymbol{Q}.\boldsymbol{r}_{l}(t)}\rangle e^{-i\omega t}\, dt$

Here, $\langle e^{-i\boldsymbol{Q}.\boldsymbol{r}_{l'}(0)}\, e^{i\boldsymbol{Q}.\boldsymbol{r}_{l}(t)}\rangle$ term signifies the correlation between the position of one nucleus at time t = 0 with another nucleus at a later time t. Therefore, the above expression can be written as:

$$\frac{d^2\sigma}{d\Omega dE} = \frac{k_f}{k_i}(S_{coh}(\boldsymbol{Q},\omega) + S_{incoh}(\boldsymbol{Q},\omega))$$

Thus, $S(\boldsymbol{Q},\omega)$ provides the microscopic properties of sample by measuring the strength of the correlations collectively. The $S_{coh}(\boldsymbol{Q},\omega)$ arises from the coherent interference between the same nucleus at different times along with the interference from different nuclei at different times. Consequently, the coherent scattering provides information about the crystal structure and lattice excitations. On the other hand, incoherent scattering arises only from interference effects of the same nucleus at different times. It is proportional to the variance in the neutron scattering lengths and causes an isotropic background in the intensity of scattered neutron. For a crystalline sample the major contribution comes from coherent nuclear scattering due to the elastic scattering from the periodic atomic planes which produces peaks in the scattered pattern. These peaks satisfy the Bragg condition and known as Bragg peaks. The scattering cross-section for nuclear elastic scattering is:

$$\left(\frac{d^2\sigma}{d\Omega dE_f}\right)_{\text{nuc. elast.}} = \delta(\hbar\omega)\frac{d\sigma_N}{d\Omega}(\boldsymbol{Q}) = \frac{N(2\pi)^3}{V_0}\,|F_N(\boldsymbol{Q})|^2\delta(\mathrm{Q}-\mathrm{b})\delta(\hbar\omega)$$

Where $F_N(\boldsymbol{Q})$ is call the nuclear scattering factor which gives the results for all nuclei present within one unit cell. On the other hand, magnetic scattering arises from the interaction of the magnetic moment of the neutron with magnetic fields of the spin and orbital momentum of the unpaired electrons. The neutron magnetic moment $\boldsymbol{\mu}_n = -\gamma S\mu_N$, where γ is the gyromagnetic ratio, S is the Pauli spin operator and μ_N is the nuclear magneton. Due to the unpaired electrons of the magnetic ions the local magnetic flux density ($\mathbf{B}$) can be created which is related to the interaction potential (V_M) for magnetic scattering as: $V_M(\mathbf{r}) = -\boldsymbol{\mu}_n.\mathbf{B}(\mathbf{r})$. Using Maxwell's equations, the Fourier transformed interaction potential can be expressed as : $V_M(\mathbf{Q}) = -\boldsymbol{\mu}_n.\,\mu_0\boldsymbol{M}_\perp(\mathbf{Q})$. Where, $\boldsymbol{M}_\perp(\mathbf{Q})$ is the component of the magnetization perpendicular to the scattering vector **Q**. Like the nuclear Bragg peaks, magnetic Bragg peaks originates from the scattering of neutrons from the magnetic lattice when the scattering vector Q coincides with the reciprocal magnetic lattice vector. Consequently, the magnetic scattering differential cross-section for the compound can be obtained by plugging the magnetic interaction potential $V_M(\mathbf{Q})$ into equation 2.6 and the final expression can be written as below [122]:

$$\left(\frac{d^2\sigma}{d\Omega dE_f}\right)_{\text{nuc. elast.}} = \delta(\hbar\omega)\frac{d\sigma_M}{d\Omega}(\boldsymbol{Q})$$

$$= \frac{N_m(2\pi)^3}{V_{0m}}\left(\frac{\gamma r_0}{2}\right)^2\sum_{\alpha\beta}\langle(\delta_{\alpha,\beta}-\hat{Q}_\alpha\hat{Q}_\beta)F^\alpha(Q)F^{\beta*}(Q)\rangle\times\delta(\mathrm{Q}-\mathrm{b}_m)\delta(\hbar\omega)$$

In the above expression the parameter b_m is the reciprocal magnetic lattice vector and the sum over α,β = x; y; z. $\langle\ldots\ldots\rangle$ represents the average value for all the magnetic domains in the lattice, and F^α is called the magnetic structure factor which is expressed as:

$$F^\alpha(\mathrm{Q}=\mathrm{b}_m) = \sum_i \mu_i^\alpha f_i(\boldsymbol{Q})\exp(i\boldsymbol{Q}.\boldsymbol{r}_i)\exp(W_i(Q,T))$$

Here μ_i^α is the α^{th} component of the magnetic moment of the i^{th} ion, $\boldsymbol{r}_i$ is the corresponding position within the magnetic unit-cell. The exponential term $\exp\big(W_i(Q,T)\big)$ represents the Debye-Waller factor and $f_i(\boldsymbol{Q}) = \int s_a(\boldsymbol{r})e^{i\boldsymbol{Q}.\boldsymbol{r}}dr$ is the magnetic form factor. The parameter s_a is the normalized density of the unpaired

electrons of ion a. The form factor originates due to the finite spatial extent of the unpaired electron cloud which cannot be expressed by a δ-function contrary to the case of nuclear scattering. Since the magnitude of $f(\boldsymbol{Q})$ decreases rapidly with *Q*, the range of magnetic scattering is limited and it can be observed in the low-*Q* region only.

2.2.4.3 Neutron Powder Diffractometers

The Neutron scattering measurements were performed at the Helmholtz Zentrum Berlin (HZB), Germany. The neutron source BER II is a research reactor that delivers neutrons. In present thesis work three different diffractometer have been used extensively to obtain detailed crystal and magnetic structures of the spinel-oxides. According to the accuracy/resolution and type of study sought we used three specific diffractometrs, they are (*i*) a fine resolution powder diffractometer (E9), (*ii*) a focusing powder diffractometer (E6) with a 2D detector, and (*iii*) Flat-Cone Diffractometer (E2). A very brief description about all these three diffractometer are given below.

(*i*) Fine Resolution Powder Diffractometer (E9):

The instrument E9 represents the fine resolution powder diffractometer which is dedicated to the determination and refinement of crystal structures. It is an angle-dispersive powder diffractometer optimized for a flat resolution function with a minimum width of the reflections at the 2θ-region which can probe very high density of reflections. The schematic layout of the diffractometer is shown in the figure 2.10. The monochromator is placed at a distance of 11 m from the reactor core, which allows for a large take-off angle at the monochromator. The E9 instrument contains an evacuated beam tube and a sapphire single crystal filter which reduces the air scattering and epithermal neutrons. The different reflecting planes of the Ge-monochromator provides a great flexibility in the choice of wavelength and resolution. The detector consists of eight individual DENEX ^{3}He 2D detectors with 300 x 300 mm active area each and a common radial collimator to reduce background noise. This instruments collects data with fixed detector position which measures parts of the 2θ-range with increased intensity and without loss in quality. Position-sensitive data integration of the Debye cones results in strongly reduced asymmetry of the peaks. The 2D-data in E9 is directly accessible and allows early detection of preferred orientation or spottiness. Depending on sample scattering power, volume and the resolution settings of the instrument, full powder diffraction patterns of a quality suitable for Rietveld refinement can be collected as fast as within 30 minutes. Samples as small as 1 cm^3 and high resolution data between 1 and 6 h can be estimated, depending on the scattering power of the sample.

(*ii*) Focusing Powder Diffractometer (E6)

Using the E6 diffractometer (installed at the T4 beam tube), we probe the magnetic structure of the compounds. It consists of both horizontally and vertically bent monochromator made up of pyrolytic graphite crystals which provides a relatively high neutron flux of ~ 5 x 10^6 n/cm^2 s of wavelength λ = 0.24 nm. Figure 2.11 shows the schematic diagram for E6 diffractometer. It also contains a position sensitive detector and variable in-pile fan collimation which is very useful to study magnetic materials. By varying the horizontal bending of the monochromator and the fan opening of the in-pile collimator one can perform a systematic correlation between the direction of the incoming neutron and its wavelength. Thus the orientation of the resolution ellipsoid can be changed with respect to the scattering vector Q. In the focusing configuration, the resolution ellipsoid orients along the major axis perpendicular to Q, so that the resolution can be maximized under parallel configuration (Q). This mode yields an increase in neutron flux at the sample position by a factor

of two and at the same time one can maintain the resolution high. The diffractometer can also be used in a standard configuration with in-pile collimators.

(*iii*) E2: Flat-Cone Diffractometer:

The flat-cone diffractometer (E2) is very useful to determine the magnetic and crystal structures, phase transitions and diffuse scattering rising from the spin disorderness. The E2 diffractometer (figure 2.12) is equipped with a position sensitive detector based on the flat-cone layer concept. During the measurements the detector was controlled by tilting the axis of detector bank with the help of a computer. E2 is very versatile instrument in the sense that one can choose automatically any collimating angle among the three primary collimations (15', 30', 60') and can select one wavelength among three λ = 0.091 nm [Cu(200)], λ = 0.121nm [Ge (311)], λ = 0.241 nm [PG (002)]. Parasitic scattering from cryostat or furnace walls can be reduced by an oscillating "radial" collimator. The datasets and all the related informations are available in one independent NeXus file format for each measurement and which can be easily archived. The software package TVneXus deals with the raw data sets, data analysis tools (e.g. MatLab) and other relevant data. TVneXus is capable of converting various data sets into powder diffractograms, linear detector projections, rotation crystal pictures or the 2D/3D reciprocal space.

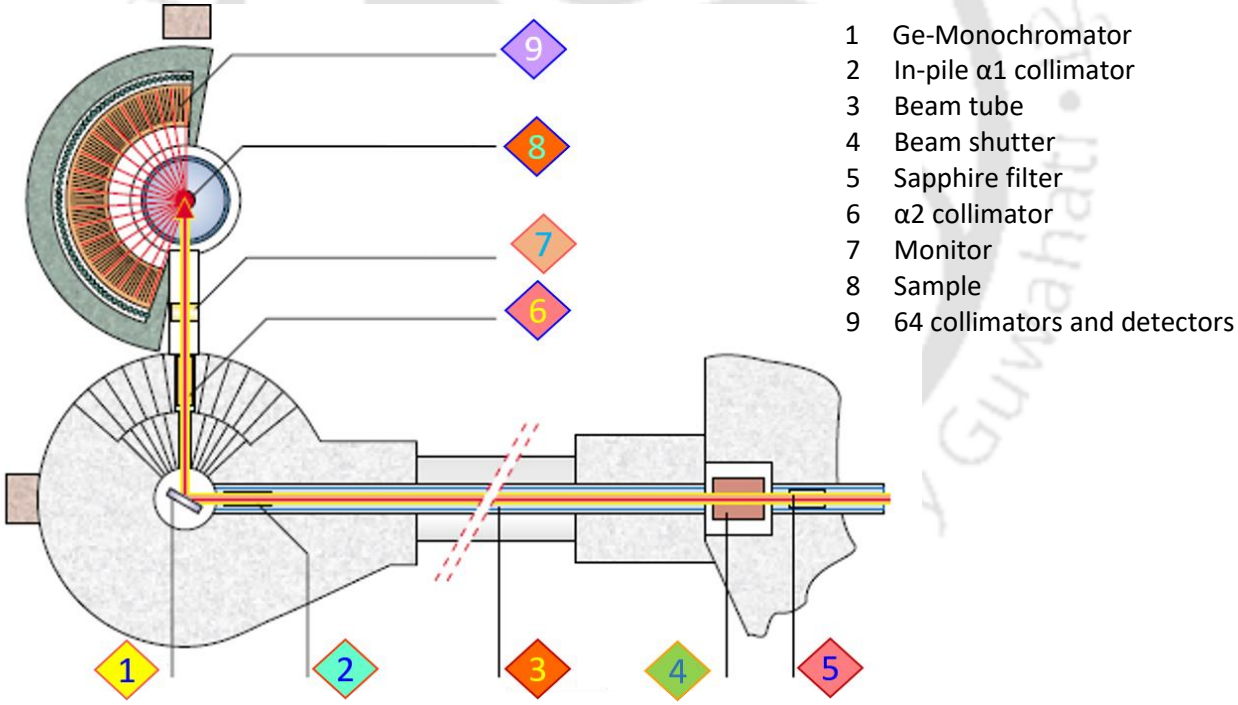

Figure 2.10. The design of instrument E9 neutron powder diffractometer with Ge monochromator in front of 64 ^{3}He single detector tube installed at the beam tube T4 at HZB, Berlin. The angular distance between the two detector is ~ 2.5°.

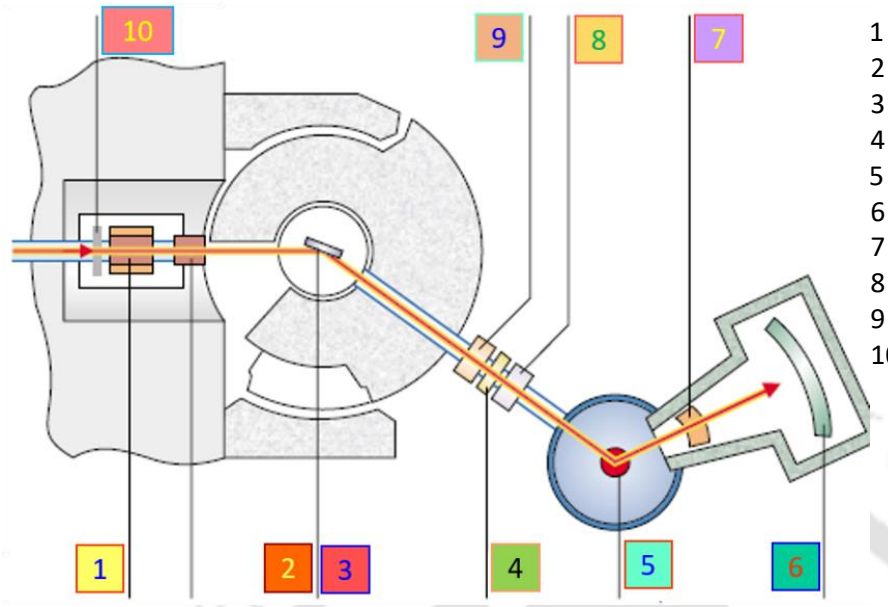

1 Beam shutter and collimators
2 Fan collimator
3 Monochromator
4 monitor
5 sample
6 Detector
7 Radial collimator
8 Graphite filter
9 Secondary shutter
10 Diaphragma

Figure 2.11. The planning of E6 focusing diffractometer installed at the beam tube T4 at HZB, Berlin.

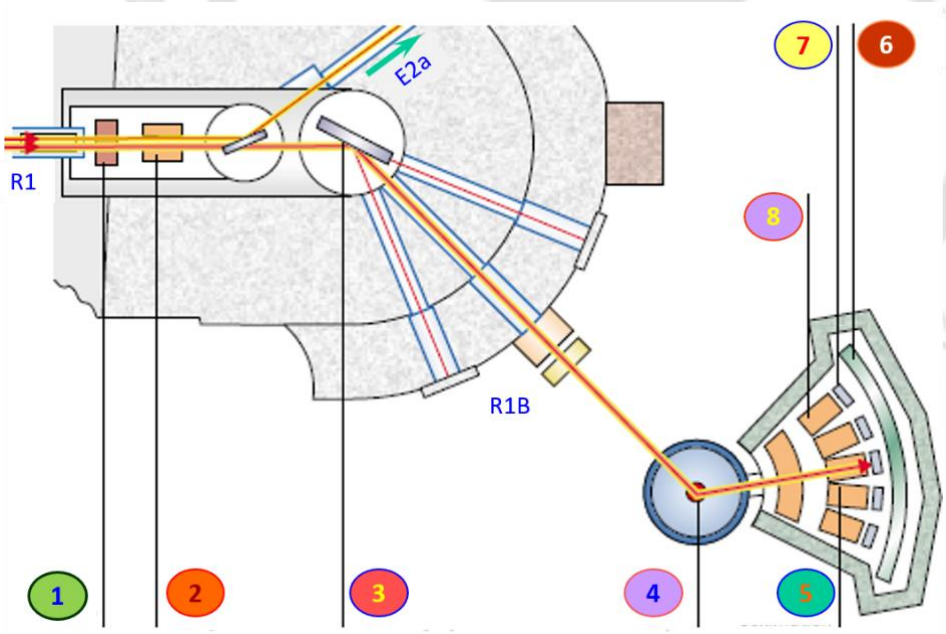

1 Beam shutter
2 collimator changers
3 monochromator
4 Sample
5 Vertical collimation
6 Detector
7 Analyser crystals
8 Radial collimator

Figure 2.12. Architecture of E2 flat cone and powder diffractometers (HZB Berlin).

Chapter 3

Magnetic Ground State and Field-Induced Transitions in Kagomé $GeCo_2O_4$

This chapter deals with the electronic and crystal structure along with a detailed analysis on the magnetic ground state of frustrated antiferromagnet $GeCo_2O_4$. A special emphasis has been given to study the field-induced transitions and magnetic exchange interactions of this compound. In the introductory section of this chapter we elucidate the important properties of $GeCo_2O_4$ and its technological applications in energy sector along with the motivation and objectives of the research work. The gaps in literature related to the magnetic ground state, optical band-gap and band-structure calculations of this compound are also discussed in first few sections. Later sections deal with brief experimental details, results and discussion followed by summary of important findings.

3.1 Introduction:

Transition metal oxysalts of germanate are very important family of inorganic materials due to their excellent thermal stability, electrical, and magnetic properties. In the present work we have chosen cobalt orthogermannate ($GeCo_2O_4$) which belongs to the normal spinel family and exhibits good electrochemical characteristics useful for high performance batteries in addition to their anomalous low-temperature magnetic ordering [126-135]. Recently, the physical properties of $GeCo_2O_4$ have received significant attention because it contains pyrochlore-like lattice structure for the magnetic Co^{2+} ions, a situation for which magnetic frustration is inherently present as first pointed out by Anderson and elaborated in more recent studies on $GeCo_2O_4$ [82,132,136-140]. Unlike the inverse spinels such as Co_2MO_4 (M = Sn, Ru, Ti), $GeCo_2O_4$ crystallizes in the normal spinel structure with non-magnetic Ge^{4+} occupying the tetrahedral *A*-sites and the octahedral *B*-sites occupied by magnetic Co^{2+} ions leading to the structure: $(Ge^{4+})_A[2Co^{2+}]_BO_4$. Other *B*-site magnetic spinels in which considerable amount of magnetic frustration has been reported are $MgMnO_3$, $ZnFe_2O_4$ and AlV_2O_4 [141-144]. Magnetic properties of $GeCo_2O_4$ have been reported using the temperature and magnetic-field dependence of the magnetization as well as neutron diffraction techniques [82,132,137-140,145-148]. These studies reveal that $GeCo_2O_4$ orders antiferromagnetically with a T_N varying between 20 K and 23 K although the temperature dependence of paramagnetic susceptibility for T > 100 K when fit to the Curie-Weiss (CW) law; $\chi = C/(T-\theta)$, yielded positive θ (= 40 K to 80 K) signifying the dominant ferromagnetic exchange coupling between Co^{2+} ions. The different magnitudes of θ resulted from different temperature range used for fitting the χ vs. T data. From the magnetization versus field hysteresis loops measured for $T < T_N$, peaks in (dM/dH) have been reported at $H_{C1} \simeq 44$ kOe and $H_{C2} \simeq 97$ kOe at 4 K [82,138,139]. However, the magnetization at 2 K is not saturated even in applied H up to 550 kOe [138]. Numerous studies in $GeCo_2O_4$ have also reported tetragonal distortion of the cubic lattice accompanying T_N yielding $c/a \simeq 1.001$ although a recent high-resolution x-ray diffraction study by Barton *et al*. showed that the lattice distortion occurs at $T_d \simeq 16$ K below T_N, signifying decoupling of the structural distortion and magnetic ordering [82,140,145-148].

Here it is worth to summarize the previous results of neutron diffraction studies in $GeCo_2O_4$ which provides the following picture of spin ordering in $GeCo_2O_4$ [132,138,139,147,148]. The pyrochlore lattice of Co^{2+} ions (figure 3.1) consist of alternate planes of Kagomé (KGM) spins and spins on triangular (TRI) lattice, all lying in the (111) planes, with the propagation vector $\vec{k}$ = (1/2, 1/2,1/2) and with the likely easy direction of $[11\bar{2}]$. In applied magnetic field $H \neq 0$, the KGM and TRI spins though parallel within each plane are antiparallel

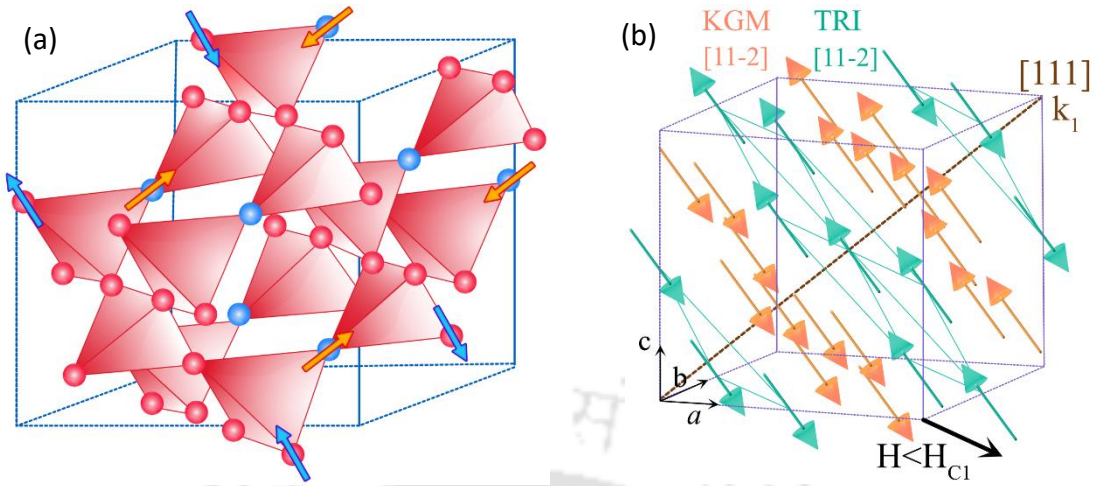

Figure 3.1. Schematic representation of $GeCo_2O_4$ unit-cell with (a) octahedral *B*-site Co^{2+} ions and their spins at the corner sharing tetrahedra. (b) Co^{2+} spins arranged in the triangular and Kagomé plane along the body diagonal direction [111].

to those in neighboring planes thus yielding an overall antiferromagnetic ordering. At $H = H_{C1} \simeq 44$ kOe, any coupling between the KGM and TRI spins breaks down, such that TRI spins become ordered ferromagnetically whereas the KGM spins in neighboring KGM planes remain AFM ordered. At $H = H_{C2} \simeq 97$ kOe, the spins in the neighbouring KGM planes also become ordered ferromagnetically with some canting. This canting produces a weak *H*-dependence of magnetization for $H > H_{C2}$. The magnetic frustration in $GeCo_2O_4$ results from factors such as the geometrical frustration of the pyrochlore lattice of the Co^{2+} spins noted earlier and the presence of several interlayer antiferromagnetic exchange couplings among the KGM and TRI spins, in addition to the dominant in-plane ferromagnetic exchange coupling [139,147-149].

These important findings reported in the literature reveal that there are still some vital issues concerning the nature of magnetism in $GeCo_2O_4$ are not established completely. For instance, an accurate explanation of the temperature dependence of the paramagnetic susceptibility in terms of the CW law or more elaborate models and its correlation with the measured values of the magnetization for $T < T_N$ are not studied when we initiated this problem. Moreover, the results obtained from the magnetization studies need to be reconciled with those from the latest electron magnetic resonance (EMR/ESR) studies in the single crystals of $GeCo_2O_4$ by Okubo *et al.* who reported the observation of a broad EMR line at 86 K with the *g*-value ~ 5.26 for the field applied along [111] with similar *g*-values along the [100] and [110] directions [150]. The ESR line broadens out at higher temperatures because of rapid spin-lattice relaxation and for $T < T_N$, the observed antiferromagnetic resonance lines are not interpreted quantitatively. The above issues are important regarding the nature of the ground state of Co^{2+} in $GeCo_2O_4$. Usually, the Co^{2+} ions in octahedral crystalline field with small trigonal distortion combined with the effects of spin-orbit coupling $\lambda \vec{L}.\vec{S}$ ($\lambda = -180$ cm^{-1}) lead to Kramer doublet as the ground state with effective spin $S = 1/2$ (for example, in $CoCl_2$, β $-Co(OH)_2$ and in $GeCo_2O_4$ [148-152]). This doublet is separated from the nearby levels with effective $S = 3/2$ situated at ~ 450 K and effective $S = 5/2$ at ~ 1000 K. Neutron diffraction measurements in $GeCo_2O_4$ by Diaz *et al.* reported 3.02 μ_B as the magnetic moment on Co^{2+} ion at 1.5 K and about 6.3 μ_B/f.u. as the saturation magnetization [137,138]. These gaps in the literature in the magnetization data of $GeCo_2O_4$ for $T > T_N$ were needed to be reconciled with the magnetization data for $T < T_N$ for a proper understanding of the nature of magnetism in this system. Also, the field-temperature (*H-T)*

phase diagram for $GeCo_2O_4$ needs to be reestablished and magnitudes of the dominant exchange couplings need to be determined. Therefore, in this work we aim to reinvestigate the magnetic ground state and field-induced transitions in $GeCo_2O_4$ with a specific objective of filling the gaps in the literature discussed above. In the following sections we discuss the experimental details including the synthesis procedure and brief characterization details employed to unveil the electronic and magnetic structure of the polycrystalline $GeCo_2O_4$ system.

3.2 Experimental Details:

The polycrystalline sample of $GeCo_2O_4$ with bulk-size grains was synthesized by the standard solid-state reaction technique using the procedure described below. Appropriate amounts of binary transition metal oxides, Co_3O_4 and GeO_2 were mixed in an agate mortar with pestle and the mixed powder is heat treated in air at 1000°C with heating rate 5°C per minute. After the intermediate regrinding and pelletizing process, the sample was finally sintered at 1200°C for 12 hours in air using a high temperature tube furnace from Nabertherm (Germany), followed by natural cooling to room temperature. The structural characterization of the sample was performed using a high-resolution XPERT-PRO diffractometer (Co-K_α radiation with $\lambda = 1.78901$ Å). The Rietveld refinement of the diffraction data was performed using the FullProf program. As discussed in the previous chapter, the magnetization measurements were performed by means of a SQUID based magnetometer MPMS from Quantum Design. For optical characterization we used spectrophotometer from Perkin Elmer Lambda-950 with diffusive reflectance accessory (DRA) between the wavelengths 200 nm and 800 nm. In order to determine the electronic state of the ions and elemental analysis, we used a high-resolution x-ray photoelectron spectroscope from Kratos Axis Ultra, Model AXIS 165 equipped with an ion-gun (EX-05) for cleaning the surface. The binding-energy resolution is 0.01 eV, while background correction was done by using a Tougard algorithm and data was fitted using the x-ray photoelectron spectroscopy software XPSFIT 4.1. Additionally, the core-level binding energies were aligned with the carbon binding energy of 284.8 eV.

3.3 Results and Discussion:

3.3.1 Electronic Structure:

In this section we will focus our investigation on the x-ray photoelectron spectroscopy (XPS) to analyze the electronic structure of $GeCo_2O_4$. Figure 3.2 shows the photoelectron intensity (I) versus binding-energy (eV) spectra of $GeCo_2O_4$ for the individual elements: (*i*) O-1*s*, (*ii*) Co-2*p*, (*iii*) Ge-2*p* and (*iv*) Ge-3*d* core level photoelectrons. All these spectra were calibrated by selecting the binding energy of carbon C-1*s* orbital (located at E_C = 284.8 eV) as an internal reference. The O-1*s* spectrum is resolved into three Gaussian-Lorentzian peaks centred at 530.1 eV, 534.1 eV and 535.9 eV (as shown by arrow marks in figure 3.2(a)) [153-155]. The origin of the most intense peak at 530.1 eV is associated with the bonding between metal and lattice oxygen, in the present case it is Ge-O and Co-O [154,155]. While the second highest intense peak appears at 534.1 eV which is associated with the surface-absorbed oxygen [155]. The additional broad peak at 535.9 eV is mainly associated with the excess oxygen present in the system [155]. The asymmetric behaviour observed in O-1*s* core level spectrum is mainly due to the presence of oxygen vacancies and different atomic environment faced by the O^{2-} anions at the Wyckoff positions 32*e* (0.2378, 0.2378, 0.2378) [153,155]. The Co-2*p* core-level XPS spectrum (figure 3.2(b)) is de-convoluted into two major peaks and two broad satellite peaks centred at 780.33 eV (Co-$2p_{3/2}$), 796.37 eV (Co-$2p_{1/2}$) and 785.03 eV, 802.01 eV, respectively (the Full width of half maximum, FWHM ~ 10 eV for the satellite peak). The binding energy separation between the doublet

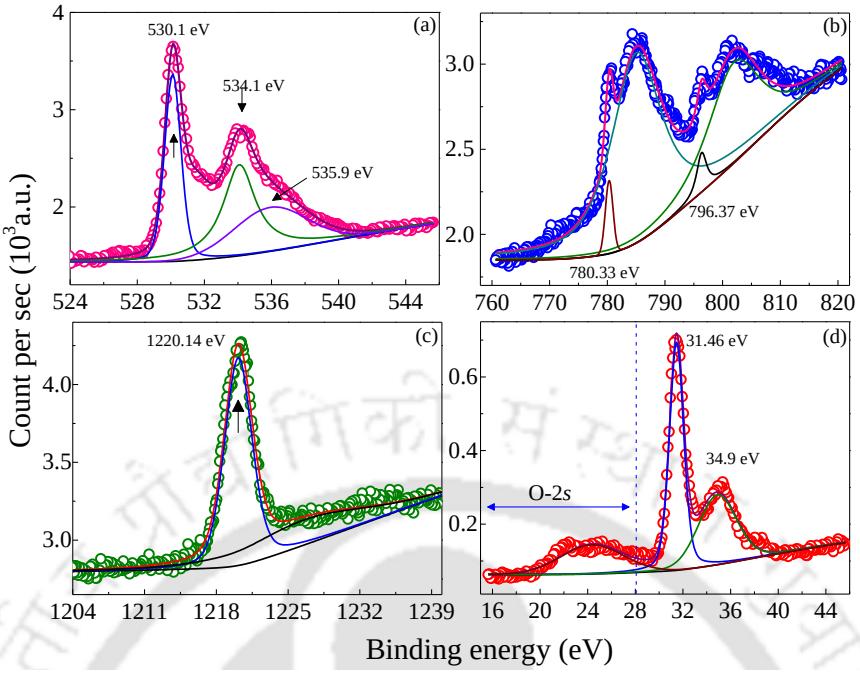

Figure 3.2. The core level X-ray-photoemission spectra of the elements (a) O-1*s* (b) Co-2*p,* and (c, d) Ge-2*p* and Ge-3*d,* within the $GeCo_2O_4$ polycrystal.

$\Delta E_{Co}(2p_{1/2} - 2p_{3/2})$ is 16.04 eV signifying the divalent oxidation state of octahedrally- coordinated 'Co' inside the $GeCo_2O_4$ [156,157]. It is notable that the higher intensities of satellite peaks as compared to the doublets characterize the loss in the system. The electronic state of Ge was analysed by considering only the Ge-2$p_{3/2}$ core level region, since Ge-2*p* exhibits significantly high spin-orbit splitting $\Delta E_{Ge}(2p_{1/2} - 2\ p_{3/2}) \sim 31.1$ eV [158-161]. Figure 3.2(c) shows the Ge-2*p* core level photoelectron spectrum. This spectrum comprises of a main peak and a satellite peak centred at 1220.14 eV and 1226.56 eV, respectively, suggesting the presence of tetravalent oxidation state of Ge [159-161]. To further confirm this, we have analysed the high energy Ge-3*d* x-ray photoelectron spectrum shown in figure 3.2(d). Here, the peak profile of Ge-3*d* is resolved into two peaks located at 31.46 eV and 34.89 eV associated with the binding energies of Ge^{0+} (Ge-3*d*) and Ge^{4+}, respectively and the binding energy separation $\Delta \sim 3.43$ eV confirming the tetravalent oxidation state of germanium ion. An additional photoelectron peak was observed at 24.35 eV which is originating due to the emission of O-2*s* core level photoelectrons [162]. For determining the exact location (either Tetrahedral-*A* or Octahedral-*B* sites) of the cations and site occupancies we performed a detailed crystal structure study presented below [160,161].

3.3.2 Crystal Structure and Phase Evaluation:

This subsection deals with the crystal structure analysis of the investigated system using the powder X-ray diffraction (XRD) technique. Figure 3.3 shows the XRD patterns recorded at room temperature for the $GeCo_2O_4$ sample along with the corresponding Rietveld refinement data. These spectra confirm the cubic spinel structure of $GeCo_2O_4$ (space group *Fd3m*) without evidence of any impurity phase. The Rietveld refinement was done by considering two cases: Ge^{4+} occupying the (a) tetrahedral *A*-sites and (b)octahedral *B*-sites. The red color hollow symbols shown in figure 3.3 represent the experimental data, and the black color solid lines are the simulated XRD patterns. The blue color line is the difference between the experimental and simulated patterns with the vertical straight lines representing the position of the Bragg peaks. The goodness of the fit

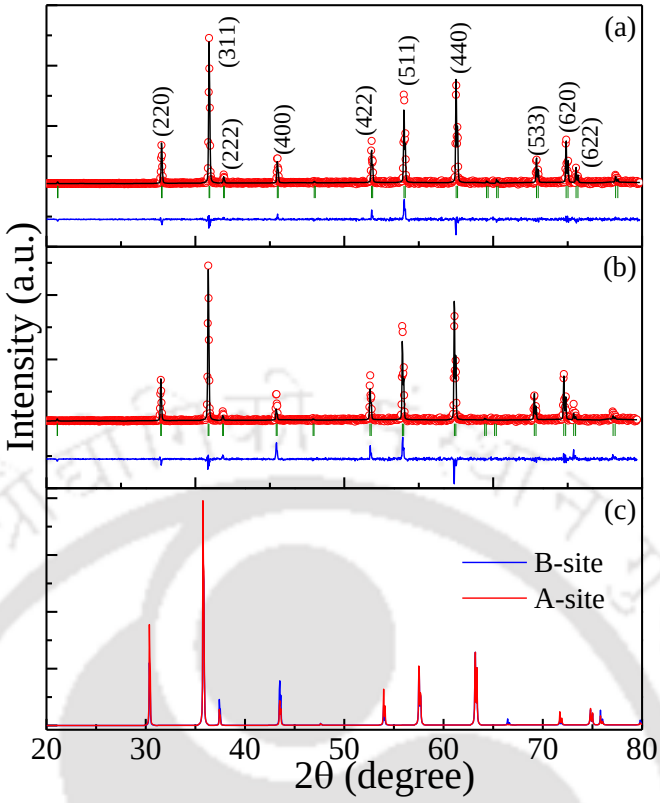

Figure 3.3. The X-ray diffraction (XRD) pattern of $GeCo_2O_4$ along with their Rietveld refinement data for different arrangement of germanium (Ge) atoms: (a) Ge atoms positioned at tetrahedral-*A* site and (b) Ge atoms located at the octahedral *B*-site. Figure (c) shows the simulated XRD patterns for Ge located at tetrahedral-*A* site (shown in red color), whereas, the blue color pattern corresponds to Ge-situated at octahedral *B*-site.

(σ) of the Rietveld refinement is 2.8 when Ge^{4+} occupies the tetrahedral *A*-site and σ ~ 6.8 when it resides in the octahedral *B*-site, indicating that Ge^{4+} occupies the tetrahedral *A*-site (normal spinel) instead of *B*-site (inverse spinel) in $GeCo_2O_4$. This is different from $SnCo_2O_4$ and $TiCo_2O_4$ which exhibits inverse spinel structure in that the non-magnetic elements Sn and Ti occupy the *B* sites. The Wyckoff positions for O^{2-}, Co^{2+} and Ge^{4+} are 32*e* (0.2378, 0.2378, 0.2378), 16*c* (0, 0, 0) and 8*b* (3/8, 3/8, 3/8), respectively if $GeCo_2O_4$ crystallizes in normal spinel structure. However, if $GeCo_2O_4$ crystallizes in inverse spinel structure two Co^{2+} Wyckoff positions locate at (*i*) 16*c* (0, 0, 0) and (*ii*) 8*b* (3/8, 3/8, 3/8); and Ge^{4+} occupies the Wyckoff position 16*c* (0, 0, 0). Considering these two different site occupancies we have simulated the XRD patterns for $GeCo_2O_4$, figure 3.3(c), where the pattern generated for the normal (inverse) spinel configuration is shown in red (blue) color solid line. From these simulated patterns it is noted that if Ge^{4+} occupies the octahedral *B*-sites, then peak intensities of the (222) and (400) lines should be higher as compared to the Ge^{4+} located at *A*-sites. It is noted that our experimental data of intensities matches well with the simulated pattern generated for 8*b* Wyckoff position (*A*-site) occupied by Ge^{4+} ions. Hence these comparisons rule out the possibility of Ge^{4+} occupying the octahedral *B*-sites in $GeCo_2O_4$ which is usually seen in its sister compounds of $SnCo_2O_4$, $TiCo_2O_4$ and $RuCo_2O_4$ [163]. Furthermore, from the Rietveld refinement we have evaluated the bond-angle Co-O-Co (81.1°) and bond-length Co-O (2.96 Å) which are consistent with our density functional theory calculations (89.7° and 2.12 Å) presented at the end of this chapter.

3.3.3 Magnetization Studies:

3.3.3.1 Temperature dependence of DC-Magnetization:

In this section we discuss the temperature dependence of the magnetization (*M*) measured between the temperatures from 2 K to 400 K in the presence of different external magnetic fields (H_{DC} = 100 Oe, 500 Oe, 10 kOe and 50 kOe). These *M*(*T*) measurements were performed under both the zero-field-cooled (ZFC) and field-cooled (FC) protocols in which the data was recorded while warming the sample. The experimentally obtained data is shown in figure 3.4 where no substantial difference between the magnitudes of $M_{ZFC}(T)$ and $M_{FC}(T)$ was observed which signifies the antiferromagnetic ordering. The cusps in magnetization plots near 20 K are associated with the Néel temperature T_N; more accurate determination of T_N and its *H* dependence is presented later. To analyze the temperature dependence of $\chi = M/H_{DC}$ we have incorporated the data of Diaz *et al.* for *T* up to 800 K and these combined data of χ versus *T* is shown in figure 3.5(a) [144]. We first analyzed these data of χ versus *T* in terms of Curie-law given by $\chi = C/T$ with $C = N_A\mu^2/3k_B$ (N_A = Avogadro's number, μ = magnetic moment, k_B = Boltzmann constant). Note that the measured *M* and χ in units of emu/g is multiplied by the molecular weight of $GeCo_2O_4$ (M.W. = 254.50 mol/g) to obtain M and χ in molar units. From the Curie-law, effective $(\mu/\mu_B)^2 = 3k_B\chi T/N_A\mu_B^2$ can be determined. Figure 3.5(b) displays the temperature variation of (μ/μ_B) per formula unit (f.u.) of $GeCo_2O_4$, which shows a maximum near 100 K and the magnitude of (μ/μ_B) decrease monotonically on either sides of this maximum. If there were no exchange coupling among Co^{2+} ions, (μ/μ_B) should be temperature independent. The increase in (μ/μ_B) from 800 K to 100 K shows ferromagnetic (FM) coupling whereas decrease of (μ/μ_B) for *T* < 100 K is indicative of onset of antiferromagnetic (AFM) coupling.

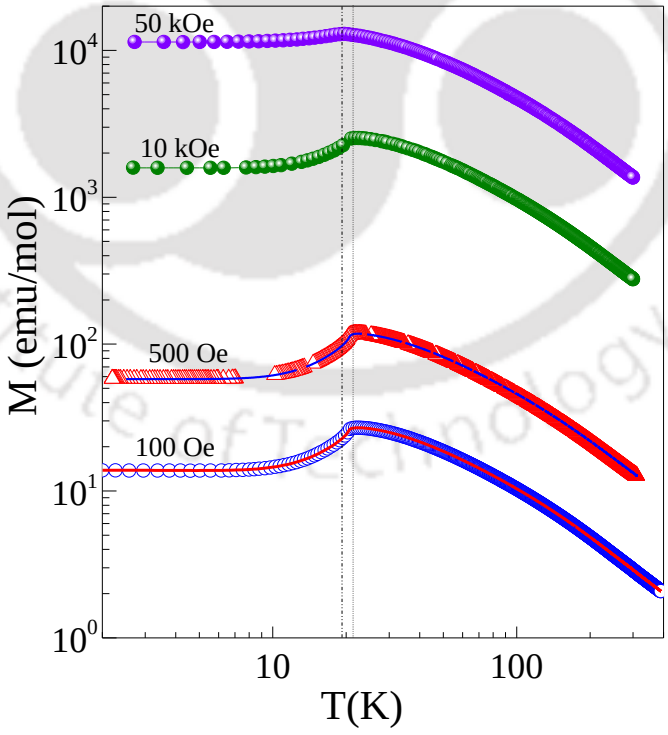

Figure 3.4. Temperature dependence of magnetization, *M*(*T*) of $GeCo_2O_4$ measured with different applied DC-magnetic fields under zero-field-cooled, ZFC (symbols) and field-cooled, FC (solid lines) conditions. Logarithmic scale is used for temperatures to highlight the data at the lower temperatures.

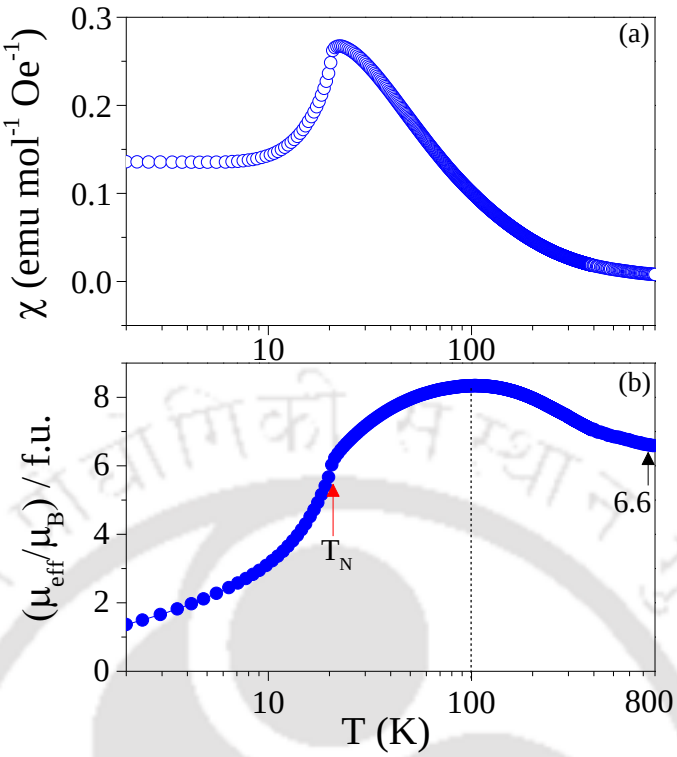

Figure 3.5. (a) Temperature variation of DC-magnetic susceptibility, $\chi(T)$, measured for H_{DC} = 100 Oe. Logarithmic scale is used to focus the low-temperature variations. (b) Temperature variation of the ratio of effective magnetic moment μ_{eff} to the Bohr Magneton μ_B (determined using the Curie law).

The inflexion in the (μ/μ_B) versus T curve near 20 K is due to T_N. It is noted that the peak in (μ/μ_B) near 100 K in figure 3.5(b) is like the broad peak near 100 K in C_P/T versus T data of Lashley *et al.* and it represents considerable amount of short-range FM ordering up to $5T_N$ [145]. The data of χ versus T for $T > T_N$ is often done using the modified Curie-Weiss (CW) law given by:

$$\chi = \chi_0 + C/(T-\theta) \qquad 3.1$$

Here χ_0 represents the contributions from diamagnetic susceptibility which is present in all materials and Van Vleck susceptibility if applicable [164]. Though the magnitude of χ_0 may be comparatively negligible for low temperatures, its inclusion in the high temperature data can be quite important for accurate determination of the parameters C and θ. In order to determine χ_0, the data of χ versus $(1/T)$ is plotted in the inset of figure 3.6(a) and $\chi_0 = \chi$ in the limit of $1/T \longrightarrow 0$ where the contribution of $C/(T-\theta)$ should approaches to zero. This analysis yields $\chi_0 = -1.95 \times 10^{-3}$ emu.mol^{-1}Oe^{-1}. Using this, the plot of $1/\chi_P = 1/(\chi - \chi_0)$ versus T is made to determine C and θ. In figure 3.6(a), we show the plots of χ_P^{-1} versus T and χ^{-1} versus T. The plot of χ_P^{-1} versus T yields a straight line for $T > 100$ K yielding θ = 51 K whereas χ^{-1} versus T plot yields a straight line for $T > 170$ K with θ = 79 K. The magnitudes of θ, C and calculated (μ/μ_B) from C and other derived quantities are listed in Table 3.1. This study shows that the magnitudes of θ and C are affected by χ_0. Since χ_0 was ignored in all previous publications on $GeCo_2O_4$, the magnitudes of C and (μ/μ_B) determined in this study are rather different and in our view more accurate. Since C per f.u. (= $N_A\mu^2/3k_B$) is proportional to μ^2 and $GeCo_2O_4$ contains two Co^{2+} ions/f.u., then μ^2/f.u. = $\mu_1^2 + \mu_2^2$ - - - - where $\mu_1 = \mu_2 = \mu$ (Co^{2+}) in this case. So $\mu/Co^{2+} = (\mu/f.u.)/\sqrt{2}$. This distinction has also not been stressed in other publications. In Table 3.1, we have listed the

magnitudes of C, θ and other derived parameters based on both the χ_P^{-1} versus T and χ^{-1} versus T fits. Using $\mu^2 = g^2 S(S+1)$, the magnitudes of derived g for both S = 3/2 and effective S = 1/2 are also listed along with the magnetic moment $\mu_z = gS$. In the coming sections these magnitudes are compared with other parameters determined experimentally.

3.3.3.2 High Temperature Series and Exchange Interaction:

In this section deals with the temperature dependence of paramagnetic susceptibility and the mathematical fitting to the high temperature series (HTS) expansion of spin S = 1/2. Since the $GeCo_2O_4$ system is a spin S = 1/2 Heisenberg system for a pyrochlore lattice one can write the HTS as [165,166]:

$$\chi_P = \frac{C}{T}\sum_{n=0}^{\infty} C_n \left(\frac{-2J_1}{K_B T}\right)^n \qquad 3.2$$

Using the information given in [165], we determined the coefficients C_0 = 1, C_1 = 3/2, C_2 = 3/2, C_3 = −1.0625, C_4 = 0.664062, C_5 = −0.60624, C_6 = 0.65778, C_7 = −0.49058, and C_8 = 0.187472. Here J_1 is the exchange interaction in the Heisenberg exchange Hamiltonian $-2J_1\overrightarrow{S_1}.\overrightarrow{S_2}$ so that a positive J_1 represents ferromagnetic coupling.

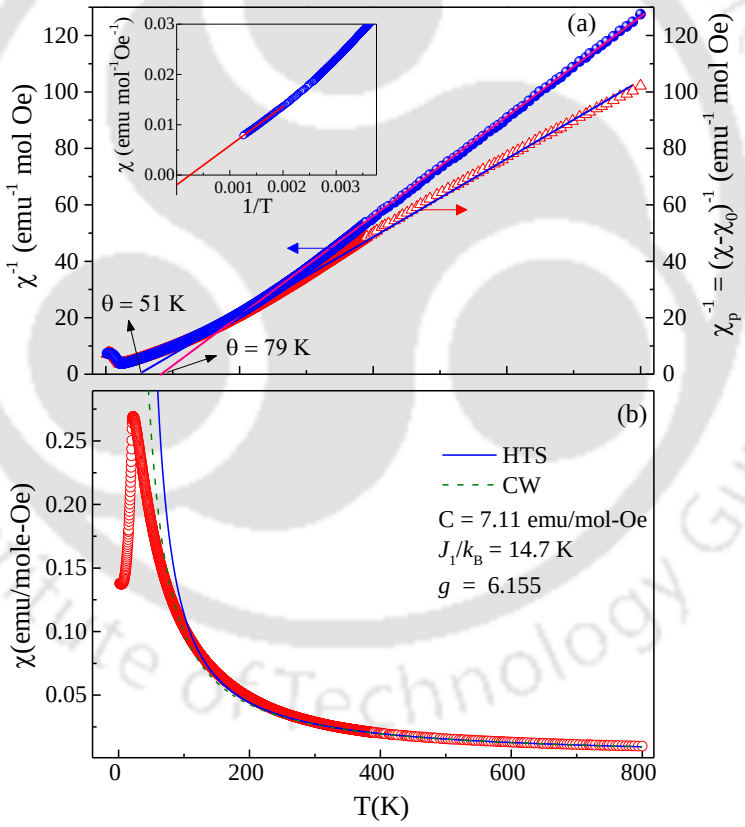

Figure 3.6. (a) Temperature variations of the inverse paramagnetic susceptibility $\chi^{-1}(T)$ without the correction of χ_o (L.H.S scale) and R.H.S. scale represents the corrected data χ_p^{-1} (= $\chi - \chi_o$)$^{-1}$. The inset shows plot of χ versus $1/T$ measured at H = 100 Oe focusing the high temperature region to determine temperature independent term χ_0= −1.95 × 10^{-3} emu.mol^{-1}Oe^{-1} from the y-intercept. Here the solid lines are fits to the Curie-Weiss law. (b) $\chi(T)$ recorded under ZFC condition in which the high temperature data is fitted with the high-temperature-series (HTS) exposition given in the equation 3.2 (shown by the solid line), whereas, the dashed line represents best fit to the Curie-Weiss law (equation 3.1).

The first two terms of series of equation 3.2 can be written in the CW form with $\theta = 3J_1/k_B$. Using θ = 51 K yields J_1/k_B = 17 K as the dominant ferromagnetic interaction. Using all eight terms in the series and C = 7.11 emu.K/mol.Oe and g = 6.155 listed in Table 3.1 yields a pretty decent fit to the χ_P versus T data in the 100 K to 800 K range (see figure 3.6(b)). The fit to the CW law is also shown in figure 3.6(b). The fit to HTS is only a slight improvement over the fit to the CW law with J_1/k_B = 14.7 K determined from HTS compared to J_1/k_B = 17 K evaluated from the CW fit. The fit of the data to HTS for T < 100 K is poor because of the on-set of the weaker antiferromagnetic exchange coupling in this range as noted earlier. Since HTS for more than one exchange constant is not available, no information on the antiferromagnetic exchange constants can be determined from this analysis.

3.3.3.3 Saturation Magnetization and Magnetic Ground State:

As stated in the Introduction, the ground state of Co^{2+} ions in $GeCo_2O_4$ is expected to have an effective spin S =1/2. So, the low-temperature experimental results of saturation magnetization and magnetic moment per Co^{2+} ion should be interpreted on the basis of S = 1/2. Neutron diffraction measurements in $GeCo_2O_4$ by Diaz *et al.* reported 3.02 μ_B as the magnetic moment on Co^{2+} at 1.5 K and about 6.3 μ_B/f.u. as the saturation magnetization [137,138]. The magnitude of 6.3 μ_B/f.u. as the saturation magnetization M_S leads to M_S = 35,184 emu/mol which is in excellent agreement with the calculated M_S = 34,372 emu/mol using S = 1/2 as the ground state. Considering S = 3/2 as the ground state would yield the calculated M_S = 46,208 emu/mol which is over 30% larger than the measured value M_S = 35,184 emu/mol. Using g = 6.1546 determined for S = 1/2 from the Curie constant C (see Table 3.1), $\mu_z = gS$ = 3.077 μ_B per Co^{2+} ion is determined in good agreement the experimental results of Diaz *et al.* [138]. One may question the magnitude of g = 6.1546 derived for the S = 1/2 state using the fit to the CW law. However, g-values up to 6.6 have been reported for Co^{2+} ions [152,167]. Also, EMR measurements reported by Okubo *et al.* in $GeCo_2O_4$ reported a broad line for $T > T_N$ with g = 5.26 for H along [111] as noted in the Introduction [150]. Lashley *et al.* in their fitting of χ^{-1} versus T data above T_N without including the exchange interaction determined g = 6.6 for the ground state [145]. These considerations of the measured magnetic moment and magnetization for $T << T_N$ and their agreement with the calculated values assuming S = 1/2 as the ground state show that the magnetization data above T_N and below T_N in $GeCo_2O_4$ can be reconciled with a single set of parameters. We consider this to be an important contribution of this work.

3.3.3.4 Field dependence of Néel Temperature:

In this subsection we discuss the field dependence of Néel temperature $T_N(H^2)$. Figure 3.4 shows the temperature dependence of the $M(T)$ measured in H = 100 Oe, 500 Oe, 10 kOe and 50 kOe showed a peak near $T_P \simeq$ 22 K with slight decrease in T_P with increase in H. Although T_P is often associated with onset of antiferromagnetic ordering, the position of the Néel temperature T_N in antiferromagnets is more accurately determined by the peak in $\partial(\chi T)/\partial T$ since χT represents the magnetic energy and so specific heat $C_p \propto \partial(\chi T)/\partial T$ [168]. In figure 3.7, the plot of $\partial(\chi T)/\partial T$ versus T is shown giving T_N = 20.4 K, 20.3 K, 20.0 K and 18.0 K for H = 100 Oe, 500 Oe, 10 kOe and 50 kOe, respectively. Our observed T_N = 20.4 K for H = 100 Oe is in good agreement with T_N = 20.6 K reported by Lashley *et al.*, the peak position in the specific heat in zero applied field [145]. Lashley *et al.* also reported the shift in the peak position of the temperature dependence of heat-capacity (C_P versus) data in applied fields up to H = 140 kOe [145]. Thus, the variation of T_N versus H is fitted to the molecular-field based theoretical equation [169,170]:

$$T_N(H) = T_N(0) - D_1H^2, \quad D_1 = g^2\mu_B^2(2S^2 + 2S + 1)/40k_B^2T_N(0) \qquad 3.3$$

The plot of T_N vs. H^2 is shown in figure 3.8 in which we have also included the data reported by Lashley *et al.* [145]. The expected linear variation is observed with D_1= 6.6 × 10^{-10}K/Oe^2. Using g = 6.1546 and S = 1/2 determined earlier for $GeCo_2O_4$ (Table 3.1) yields D_1= 5.24 × 10^{-10}K/Oe^2, in fair agreement with the experimental D_1= 6.6 × 10^{-10}K/Oe^2. A similar discrepancy between the experimental and measured D_1 has been reported in antiferromagnets MnF_2, and Er_2O_3 and it has been attributed to the molecular field approximation used in driving equation 3.3 [169,170]. Using D_1= 6.6 × 10^{-10}K/Oe^2 yields H_C = 176 kOe as the magnetic field for which $T_N(H) \rightarrow 0$ K. This information on H_C is used in the following section.

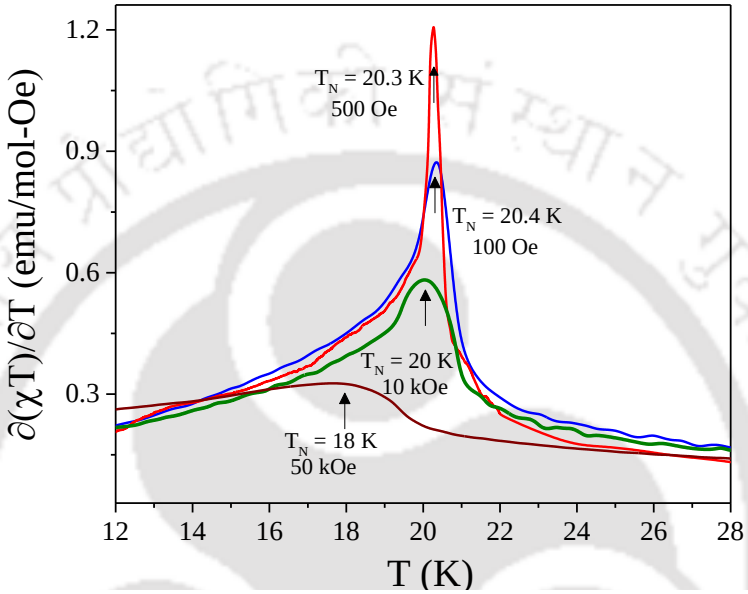

Figure 3.7. Temperature dependence of the susceptibility derivatives ($\partial(\chi T)/\partial T$) plots of the $GeCo_2O_4$ system for different levels of external fields (100-50 kOe). The peaks marked by arrows define T_N.

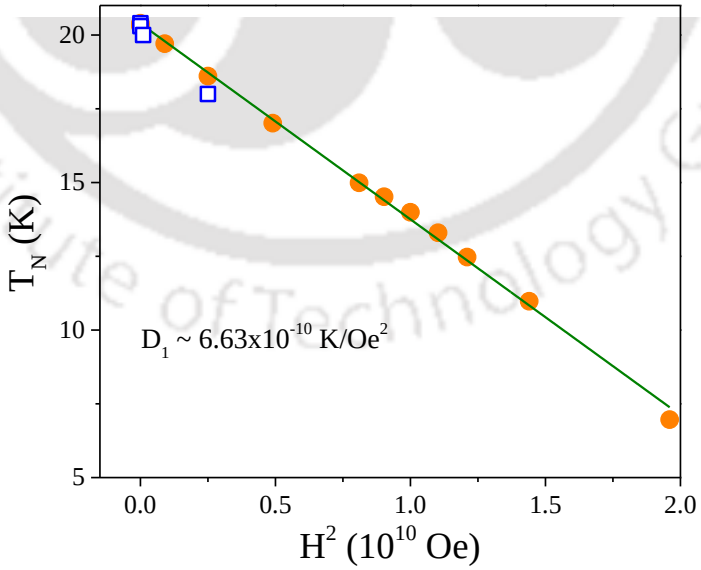

Figure 3.8. Variation of T_N versus H^2 of $GeCo_2O_4$ system. The experimental data points are fitted with the equation 3.3. The solid line is the linear fit to the experimental data points obtained from C_P (T) data of Lashley *et al.* [145] (solid circles) and from the present work (open squares).

3.3.3.5 Magnetic-field-induced transitions and *H-T* phase diagram:

We now focus our attention on the field induced transitions and *H-T* phase diagram. The variation of magnetization versus field with *H* up to 70 kOe recorded at 2 K is shown in the inset of figure 3.9. From such isotherms of *M* versus *H* data at different temperatures, we calculated the *dM/dH* and plotted it as a function of *H* which are shown in figure 3.9. From the peak positions in *dM/dH*, two transitions are evident, one at $H_d \simeq 11$ kOe and the other at $H_{C1} \simeq 44$ kOe. Temperature dependence of H_d and H_{C1} is displaced in figure 3.10 from which it is evident that the intensity of the peak showing H_d weakens rapidly with increasing temperature whereas the peak corresponding to H_{C1} eventually shifts to lower *H* on approach to $T_N \simeq 20.4$ K. Several other groups [137,138,147] have also reported *M* vs. *H* data in $GeCo_2O_4$ for $T \ll T_N$ for H up to 550 kOe and have reported the transition at $H_{C1} \simeq 44$ kOe and $H_{C2} \simeq 97$ kOe. Since our measurements are limited to *H* up to 70 kOe, we did not observe $H_{C2} \simeq 97$ kOe. The recent measurements of Fabréges *et al.* who employed neutron and x-ray diffraction in single crystals of $GeCo_2O_4$ are particularly noteworthy in understanding the nature of the *H*-induced phase transitions in *H* up to 100 kOe [147]. Fabréges *et al.* also reported a broad transition near $H_d \simeq 15$ kOe which they associated with domain reorientation in addition to transitions at H_{C1} and H_{C2} [147]. Below we summarize the nature of three transitions at H_d, H_{C1}, and H_{C2} and present *H-T* phase diagram for $GeCo_2O_4$, not reported before. In the pyrochlore structure of Co^{2+} spins in $GeCo_2O_4$, the spins lying in the (111) planes, consist of Kagomé spins separated by spins in the triangular planes (figure 3.1(b)) as first noted by Anderson [136]. In $H = 0$, and $T \ll T_N$, spins in the neighboring KGM and TRI planes are anti-parallel to each other but parallel within each plane.

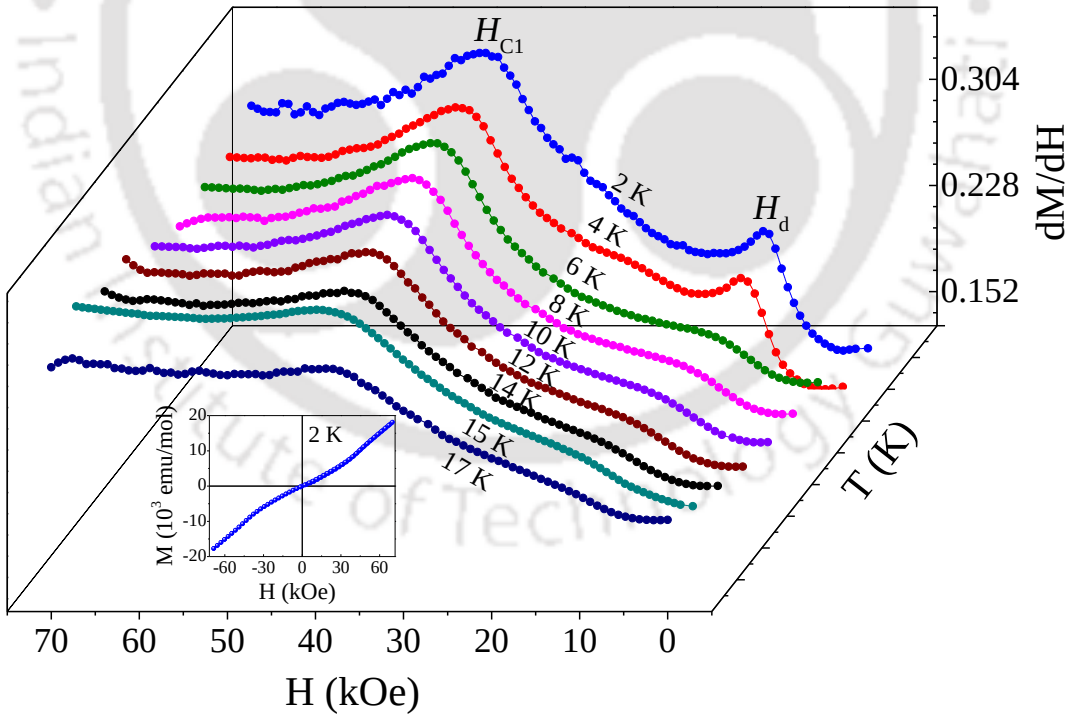

Figure 3.9. Three dimensional representation of the differential magnetization (d*M*/d*H*) with respect to *H* and *T*. The magnitudes of d*M*/d*H* are determined from the isothermal magnetization measurements plotted at different temperatures. One such *M-H* isotherm measured at $T = 2$ K is shown in the inset. The locations of the humps in d*M*/d*H* determine the critical fields H_{C1} and H_d used in the *H-T* phase diagram of figure 3.10.

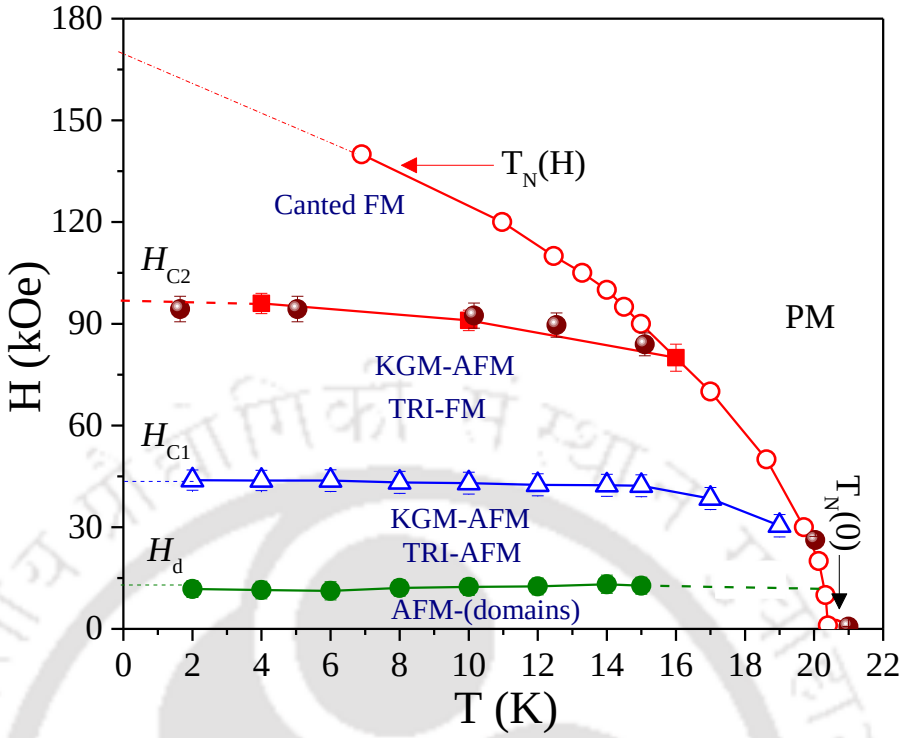

Figure 3.10. The temperature variation of the critical fields H_d, H_{C1}, and H_{C2} determined from the *M-H* data. Here the data for H_{C1} and H_d is from the present work, whereas, the data for H_{C2} is taken from the references [82,137]. The open circles represent magnetic field variation of T_N shown in earlier figure 3.8 with the solid line marked $T_N(H)$ representing the equation $T_N(H) = T_N(0) - D_1H^2$. Other lines connecting the data points are drawn to visualize the variation clarity. Note: refer the text pertaining to the discussion of the nature of magnetic ordering in the different regimes of fields: $H < H_d$, $H_d < H < H_{C1}$, $H_{C1} < H < H_{C2}$ and $H > H_{C2}$.

Table 3.1: The list of parameters obtained from the Curie-Weiss fitting of χ^{-1} versus *T* data.

Parameters	**χ_p^{-1} versus *T* fit**	**χ^{-1} versus *T* fit**
C (emu/mol K)	7.11±0.04	5.78±0.03
θ (K)	51	79
μ/ f.u.	7.538 μ_B±0.023 μ_B	6.796 μ_B±0.014 μ_B
μ/Co^{+2}	5.330 μ_B ±0.016 μ_B	4.80 μ_B±0.01 μ_B
g/Co^{2+} for S = 3/2	2.758±0.002	2.483±0.004
g/Co^{2+} for S = 1/2	6.1546±0.019	5.548±0.012
μ_Z = gS/Co^{+2}, for S = 3/2	4.13 μ_B	3.72 μ_B
μ_Z = gS/Co^{+2}, for S = 1/2	3.077 μ_B	2.776 μ_B
$M_S = 2N_AgS$ for S = 3/2	46,208 emu/mol	41,550 emu/mol
$M_S = 2N_AgS$ for S = 1/2	34,372 emu/mol	31,002 emu/mol

This provides overall AFM ordering although spins within each KGM and TRI planes are parallel to each other and lying in the (111) planes. Although direction of ordering within (111) planes is not uniquely defined, it is likely along either the $[11\bar{2}]$ or $[1\bar{1}0]$ directions, like that reported in cubic antiferromagnet MnO [171]. Since there are three equivalent such directions, this leads to formation of *S*-domains. The weak transitions observed near $H_d \sim 11$ kOe is due to elimination of these domains. Following Fabréges *et al.*, the transition at $H_{C1} \simeq 44$ kOe represents the alignment of the TRI magnetic moments along the applied *H* but the spins in the neighbouring KGM planes are still antiparallel [147]. Finally, at $H = H_{C2} \simeq 97$ kOe, the spins in the KGM planes also flip to become nearly parallel to the applied *H*, applied along $[11\bar{2}]$ directions, although some spins canting remains. This spin canting results in non-zero susceptibility and non-saturation even at *H* = 550 kOe. In summary, the transition at H_{C1} and H_{C2} are spin-flip transitions likely because the magnetic anisotropy in $GeCo_2O_4$ is very large. Based on the above discussion, the *H-T* phase diagram for $GeCo_2O_4$ is represented in figure 3.10. The boundary separating the paramagnetic (PM) phase is based on equation 3.3 describing the variation of T_N with applied *H*.

3.3.3.6 Band Structure and Optical Behavior*:*

In this section we devote our studies on the energy band structure and the optical behavior of $GeCo_2O_4$ and compare the results obtained from the theoretical calculations. The experimental study concerning the optical properties was performed using the diffusive reflectance spectroscopy in the UV-visible and near IR range. In addition, we interpret our experimental results with our theoretically calculated density of states and the band-structure using density functional theory DFT+*U* (*U* being the Columbic potential). We have employed the density functional theory (DFT) based calculations using the projector augmented-wave (PAW) method as implemented in Vienna ab initio Simulation Package (VASP) [172-178]. Perdew-Burke-Ernzerhof (PBE) parameterized generalized gradient approximation (GGA) for exchange correlation functional was employed [179]. The simulations were performed using 650 eV as the kinetic energy cut off of plane wave basis and Monkhorst-Pack of 8×8×8 k-grid mesh. The calculations are carried out using 14 atoms (2 formula units of the spinel primitive cell). The effects of electron localization were addressed by the approach of Dudarev *et al*. [180]. The Hunds coupling parameter, *J* is considered to be 0 eV and the Coulomb Parameter *U* is considered to be 2 eV for Co and 0 eV for Ge. The electronic self-consistency is continued until the energy convergence is of the order of 10^{-7} eV. Structural relaxations are performed until residual forces on each atom converge to less than 10^{-4} eV/Å. To determine the optical band-gap E_g from the Kubelka-Munk (KM) analysis of the experimental data, we employed KM equation $[F(R_\infty)\hbar\omega]^2 = \alpha(\hbar\omega - E_g)$, where R_∞ is the ratio of the reflectance of the sample and $F(R_\infty)$ is the KM function [181,182]. In the above equation, $\hbar\omega$ is the energy of the single photon and α is absorption coefficient. The left-hand scale of figure 3.11(a) shows the intensity of optical absorbance of $GeCo_2O_4$ versus the photon energy ($\hbar\omega$) (eV), and the variation of $F(R_\infty)$ as a function of photon energy is shown in the right-hand scale of figure 3.11(b). To determine the band-gap, the function $[F(R_\infty)\hbar\omega]^2$ versus $\hbar\omega$ is plotted and the extrapolation of the band tail (as shown by the dotted lines) intercepts the photon energy axis at $\hbar\omega$ = 3.156 eV which corresponds to the direct band-gap of the system and is in good agreement with the theoretical calculations $E_g \sim 3.28$ eV. Two additional sub-band are observed at 2.29 eV and 2.66 eV (figure 3.11) below the main absorption band (3.63 eV) which may be associated to the charge transition between $Co^{2+}(e_g^{\uparrow}) \rightarrow Co^{2+}(t_{2g}^{\uparrow})$ and $Co^{2+}(t_{2g}^{\downarrow}) \rightarrow Co^{2+}(e_g^{\downarrow})$, respectively. The main absorption peak arises due to charge transfer between O (2*p*) $\rightarrow Co^{2+}(e_g^{\uparrow\downarrow})$ [183].

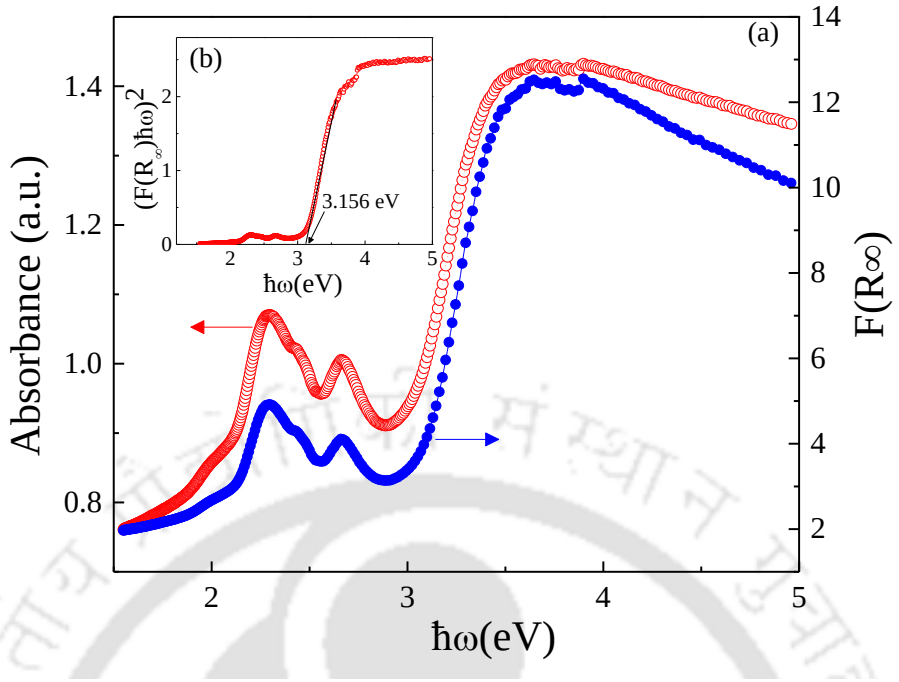

Figure 3.11. (a) Energy (ħω) variation of optical absorbance (Abs.) (shown on L.H.S scale) and its corresponding Kubelka-Munk (K-M) function (shown on R.H.S. scale) for $GeCo_2O_4$ polycrystals. (b) The graph shown in the inset represents the ħω variation of the function $[F(R_\infty)\hbar\omega]^2$. The dotted line represents extrapolation of the linear region of the curve providing the optical energy band-gap, E_g.

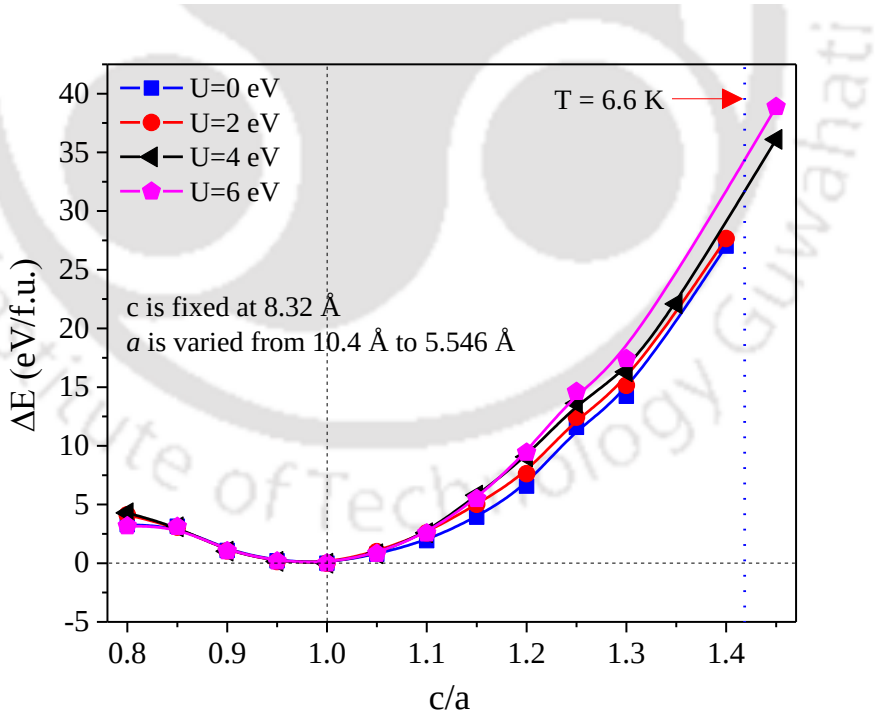

Figure 3.12. The variation of total free energy as a function of tetragonal distortion parameter (c/a) for $GeCo_2O_4$ for different values of Coulombic parameter *U*.

As noted earlier, several publications have reported cubic to tetragonal distortion in $GeCo_2O_4$ at low temperature (T < 16 K) [82,140,145-148]. In order to take account of this we have performed the DFT calculations to compute the total energies per formula unit after distorting the cubic structure, i.e. c is fixed at 8.32 Å and a is varied between 10.4 Å and 5.546 Å. In figure 3.12, the total energy is plotted as a function of c/a ratio for different values of U (= 0, 2, 4 and 6 eV). The experimental observation at T = 6.6 K is shown by blue dotted line in the figure 3.12. The DFT results show the cubic structure is more stable than the tetragonal structure for all the values of U. Hence, we carried out all the electronic structure calculations considering the cubic structure of $GeCo_2O_4$. Generally, in the DFT calculations the coulomb interaction parameter U is used to take account of the valence electron interactions [184]. The free parameter U has been chosen in such a way to match the experimental observations. In order to investigate the effect of U on the electronic structure we performed a detailed computation of the density of states of $GeCo_2O_4$ system by varying U between 0 and 4 eV. Figures 3.13(a)-(c) show the density of states plots for U = 0, 2, 4 eV, respectively. For the all the cases we find that the spin-up and spin-down density of states (DOS) are nearly equal and exhibiting an antiferromagnetic configuration which is consistent with our experimental observations. For U = 0 eV (figure 3.13 (a)), the Fermi level falls below the maximum of the valence band indicating metallic nature of $GeCo_2O_4$ in contradiction to the experimental observations. However, for the finite U values the system displays semiconductor/insulating behavior and the energy band-gap gradually increases while increasing the U values. Figure 3.13 (b) shows the density of states of $GeCo_2O_4$ calculated using U = 2.0 eV for Co-ions. Close examination of these plots reveals the electronic states at $E \sim -1.39$ eV and -2.62 eV pertaining to $e_g^{\uparrow}$ and $t_{2g}^{\downarrow}$, respectively. However, $t_{2g}^{\uparrow}$ states are localized at the top of the valence band maximum (~ -0.88 eV) and the conduction minimum ($\sim$ 1.02 eV). Interestingly, both the octahedral Co ions compensate each other's contribution and yielding a stable antiferromagnetic structure of $GeCo_2O_4$. The contribution from tetrahedral Ge^{4+} is negligible to the total magnitude of density of states. All the optical transitions observed in $GeCo_2O_4$ are listed in Table 3.2 together with those determined from the DFT+U calculations and interpreted using the band-structure and DOS (Figures 3.13 (a)-(c), 3.14). In what follows we discuss the changes occurring in the density of states as U is increased from U = 0 – 4 eV as shown in the Figures 3.13(a)-(c). For U = 2, the $t_{2g}^{\uparrow}$ states of octahedral Co^{2+} are localized both at the top of the valence band and bottom of the conduction band. However, for higher U values (≥ 4 eV) the $t_{2g}^{\uparrow}$ states in the conduction band dominates over the valence band. Similar features are noticeable in case of $t_{2g}^{\downarrow}$ states. For the lower U values, the splitting in the $t_{2g}^{\downarrow}$ states are visible in the valence band, which gradually diminishes and gets delocalized near the Fermi level for higher U values ($\geq$ 4 eV). Upon increasing U all the states ($t_{2g}^{\uparrow\downarrow}$, $e_g^{\uparrow\downarrow}$) move towards higher energies, where, the shift in the $e_g^{\downarrow}$ states are more significant as compared to the others.

To interpret the optical measurements, we use the DOS data to predict the possible optical transitions for different values of U (U = 1 – 4 eV) which are listed in the Table 3.2 along with those values obtained from the experiments. We note that the theoretical values of the optical transitions for U = 2 eV match quite well with the experimentally observed transitions, whereas the optical transitions corresponding to $U \geq 3$ eV appeared to be higher than the experimental results. Moreover, the energy band gap of $GeCo_2O_4$ calculated using the Columbic interaction, U = 2 eV for Co-ions yields at Γ-Γ and X-X points are 1.39 and 2.60 eV respectively, whereas the indirect band gap at Γ-X occurs at 2.28 eV. It is noted that our calculations for U = 4 eV (for the Co ions) gives the direct X-X band gap of 3.28 eV (figure 3.14) which is in good agreement with our experimentally obtained optical band gap of 3.156 eV (figure 3.11).

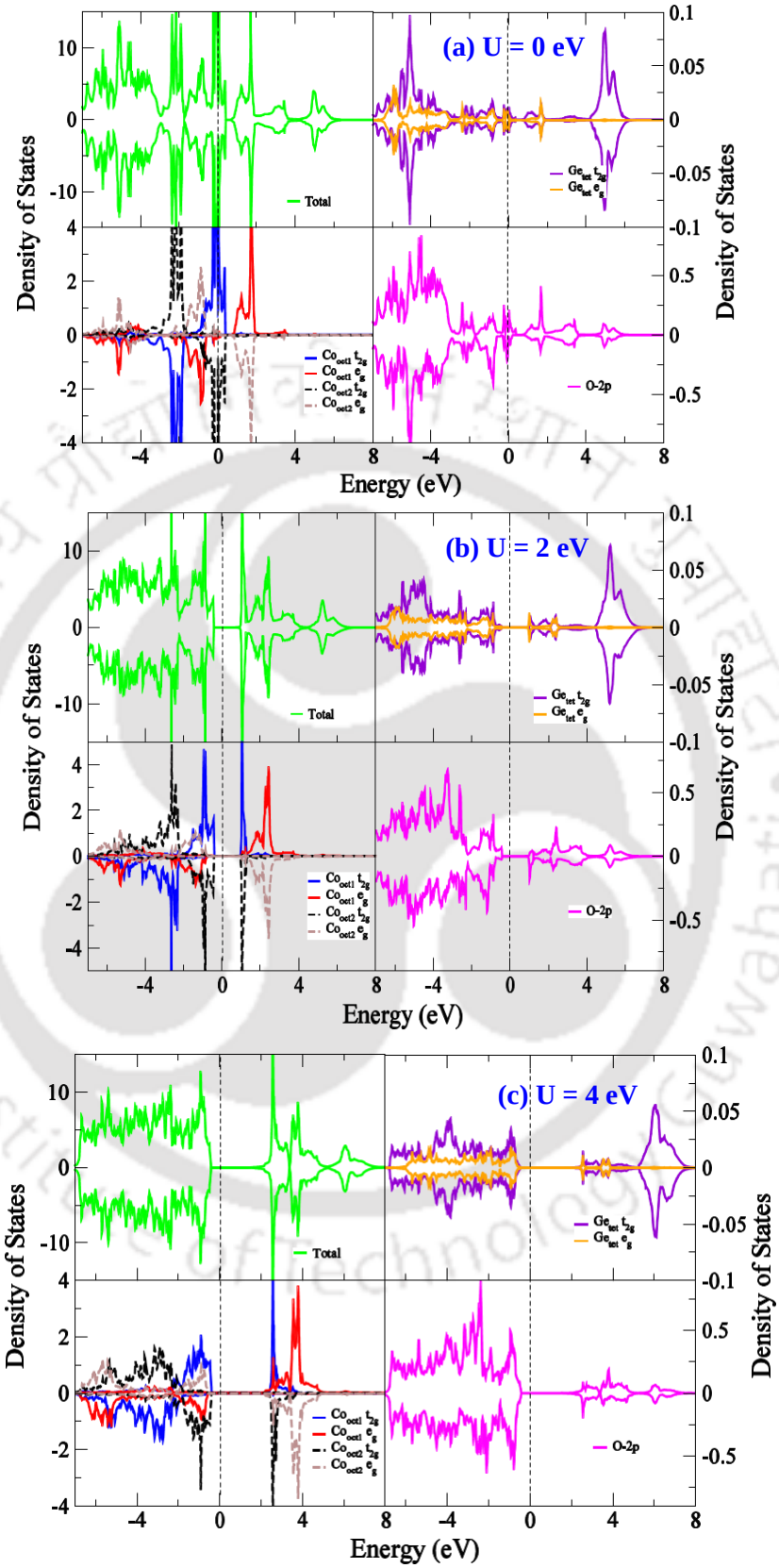

Figure 3.13. Total and atom-projected electronic density of states of $GeCo_2O_4$ are plotted as function of energy for (a) U = 0, (b) U = 2, and (c) U = 4 eV for octahedral Co^{2+} atoms.

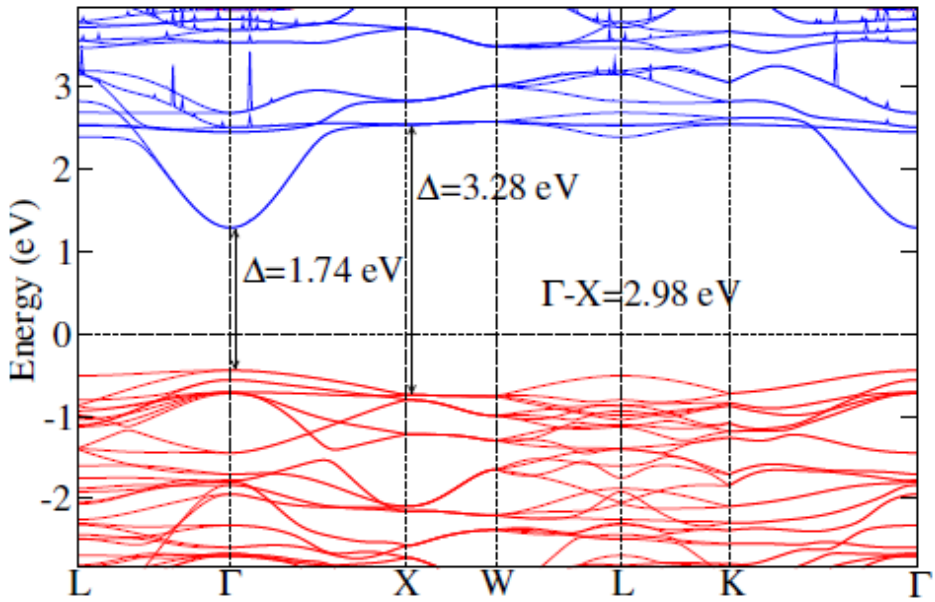

Figure 3.14. The band structure of $GeCo_2O_4$ is plotted with the symmetry points in the reciprocal lattice for U = 4 eV for Co^{2+} ions.

Table-3.2: The list of optical transitions and their positions obtained from the experimental results and DFT+U based theoretical calculations.

Transitions	U (eV)	Type	Theoretical energy (eV)	Experimental energy (eV)
$Co^{2+}(t_{2g}^{\uparrow\downarrow}) \rightarrow Co^{2+}(t_{2g}^{\uparrow\downarrow})$	1.0	*d-d*	1.14	1.95
	2.0		1.96	
	3.0		2.72	
	4.0		3.49	
$Co^{2+}(e_g^{\uparrow}) \rightarrow Co^{2+}(t_{2g}^{\uparrow})$	1.0	*d-d*	1.76	2.29
	2.0		2.25	
	3.0		2.72	
	4.0		3.49	
$Co^{2+}(e_g^{\downarrow}) \rightarrow Co^{2+}(t_{2g}^{\downarrow})$	1.0	*d-d*	1.95	2.67
	2.0		2.38	
	3.0		2.79	
	4.0		3.89	
O (2*p*)$\rightarrow Co^{2+}(e_g^{\uparrow\downarrow})$	1.0	*p-d*	2.45	3.16
	2.0		3.26	
	3.0		3.89	
	4.0		4.48	

3.4 Conclusions:

In this chapter the nature of magnetic ordering of pyrochlore $GeCo_2O_4$ has been extensively studied by means of temperature and field dependence of magnetization. These results demonstrate the following key features:

(i) The paramagnetic susceptibility data above T_N and saturation magnetization below T_N in $GeCo_2O_4$ have been interpreted using the same set of parameters for divalent Co ions with effective spin $S = 1/2$ and $g = 6.155$.

(ii) These parameters successfully explain the measured magnetic moment of ~ 3.02 per Co^{2+} reported by Diaz *et al*. using neutron diffraction.

(iii) Our analysis shows that neglecting the temperature independent term in magnetic susceptibility makes a significant difference on the determined parameters.

(iv) The magnitude of the dominant ferromagnetic exchange constant J_1/k_B (= 14.7 K) has been determined by the mathematical fitting of the magnetic susceptibility data to high-temperature-series expansion method.

(v) Temperature variation of μ_{eff}/μ_B shows the presence of short-range 2D ferromagnetic order near 100 K which is consistent with the broad peak in C_p/T versus T data of Lashley *et al.* reported in Phys. Rev. B **78**, 104406 (2008).

(vi) Electronic states of Ge^{4+} and Co^{2+} in $GeCo_2O_4$ are determined from the XPS studies and Rietveld refinement of the XRD patterns establishes Ge^{4+} and Co^{2+} occupying the tetrahedral and octahedral sites respectively.

(vii) A direct energy band-gap $E_g = 3.156$ eV in $GeCo_2O_4$ is determined from the diffuse reflectance spectroscopy which is in good agreement with those obtained from DFT+U calculations (E_g = 3.28 eV). The remaining issues for complete understanding of the magnetic properties of $GeCo_2O_4$ includes the determination of the important interlayer AFM exchange constants, interpretation of the AFMR modes reported by Okubo *et al.*, and theoretical interpretation of the critical fields of figure 3.10 in terms of the anisotropy and exchange constants in a manner e.g. reported for the quasi-2D, spin 1/2 antiferromagnet copper formate tetrahydrate [150,185]. However, as noted earlier, $GeCo_2O_4$ has two types of spins (KGM and TRI) and several different exchange couplings among them making this task quite challenging.

Chapter 4

Local Spin Canting, Jahn-Teller Distortion, Negative Magnetization and Magnetic Compensation in $Mn_xTi_{1-x}Co_2O_4$ Inverse Spinel

This chapter represents a detailed analysis of the crystal structure and magnetic properties of $Mn_xTi_{1-x}Co_2O_4$ inverse spinel. In this piece of work, we have specifically chosen neutron scattering technique along with the other supporting experimental methods such as x-ray photoelectron spectroscopy, specific heat capacity, dc- and ac-magnetic susceptibility to probe the cationic distribution, magnetic and crystal structure of the proposed system. We have chosen this inverse spinel system to understand the consequences of Jahn-Teller active ion Mn substitution at nonmagnetic sites of the spinel lattice. The parent compound is a spin frustrated reentrant glassy system which differs from the orbitally frustrated pyrochlore antiferromagnetic system worked-out in the previous chapter. The introductory section of this chapter elucidates the importance of the two end-compositions ($MnCo_2O_4$ and $TiCo_2O_4$) from the view point of industrial applications and fundamental physical properties. Several important magnetic properties of these compounds and the gaps in the literature together with the motivation and objectives of the current research work are also discussed. The remaining sections present the details of experimental techniques, results and discussion followed by the summary of important findings.

4.1 Overview, Motivation and Objectives:

It is well known that competing magnetic exchange interactions between the cations in spinel oxides AB_2O_4 at low-temperatures play a major role on the magnetic ordering, electron transport and crystal structure [76-83]. Especially, the influence of orbital degeneracy under high crystal-fields, Hund's exchange couplings and spin-orbit interactions lead to some interesting phenomena like spin-liquid state, magnetothermal, anisotropic magnetoelastic, magnetodielectric, and magneto-structural distortion driven by cooperative Jahn-Teller effect [77,80,81,84-90]. In particular, giant magnetic anisotropy (650 kOe) and atomic displacements (~1/4 Å), negative-magnetization with compensation phenomena, zero-field cooled bipolar exchange-bias effect and reentrant spin-glass behavior in few Mn-, Co- and Cr-based spinels has drawn immense attention [91-94]. Exploring the tunability of such exotic properties may open a constructive approach for the development of magnetic read/write heads, spin-valves and other switching devices [95-98,186].

Precise understanding of the cationic distribution using the neutron diffraction studies in diluted magnetic spinels is a puzzling issue to solve. Dilution with tetravalent nonmagnetic elements like Sn^{4+}, Ge^{4+} or Ti^{4+} play a major role in the disruption of antiferromagnetic ordering of the base system Co_3O_4 and results in short-range ordering with reentrant spin-glass behavior [13,14,187,188]. Coexistence of ferrimagnetic behavior with low temperature-spin-glass state, negative magnetization below the compensation point and giant asymmetry in the hysteresis loops are some of the important features noticed in such diluted inverse spinel oxides [13,14,187-189]. However, diluting the octahedrally coordinated Co^{3+} ions with magnetic element Mn^{3+} leads to the formation of inverse spinel $MnCo_2O_4$ which has tremendous applications in the renewable energy sector, such as, solid-oxide fuel cells, lithium-ion batteries, catalysis and magnetoelectronics [190-192]. Here it is important to note that the Co^{3+} ions at the *B* site carries no magnetic moment (S = 0) in Co_3O_4 due to a large crystal-field splitting of the *d* orbitals [84]. On the other hand, it is interesting to note that the Co^{3+} ions in $TiCo_2O_4$ carry finite magnetic moment [14]. Therefore, the aim of our current research work is two-fold: Firstly,

to understand the magnitude of moment and valence of the individual magnetic metal ions for different compositions of $Mn_xTi_{1-x}Co_2O_4$; Secondly, majority of the reports available in the literature on both end members $TiCo_2O_4$ and $MnCo_2O_4$ are primarily focused on the synthesis and characterization of the porous nanostructures with special emphasis on their catalytic and electrochemical properties, but little literature is available on the low-temperature neutron diffraction studies with special emphasis on their magnetic ground states and cationic distribution [84,129,194-197]. In particular, a detailed study of different compositions of bulk grain sized $Mn_xTi_{1-x}Co_2O_4$ systems was lacking in the literature when we initiated the research work on this system. Moreover, these solid solutions are interesting mainly because of the unique magnetic characteristics of both the end compounds $TiCo_2O_4$ and $MnCo_2O_4$ reported earlier. Some of the intriguing properties of these compounds being: (*i*) co-existence of longitudinal ferrimagnetic order and transverse spin-glass state below freezing point resulting from the dilutants on the *B* sites, (*ii*) negative magnetization below the compensation point and bipolar exchange bias under ZFC condition [13,14,198]. Moreover, the inverse spinel $MnCo_2O_4$ exhibits only ferrimagnetic behavior, without the above mentioned characteristics. Since both the end compounds exhibit very different magnetic ground state, it is worth to investigate the magnetic and crystal structures of the intermediate compositions of these two end compounds which is the primary aim of this work. An additional key motivating factor in investigating this system is to probe the magnitude of permanent magnetic moment on the trivalent *B* site Co ions which usually do not exhibit any magnetic moment due to the large crystal-field splitting (≥ 19000 cm^{-1}) of the 3*d* orbitals by the octahedral cubic field [84]. Hence, motivated by the unique magnetic characteristics of the proposed systems, an effort has been made in the present work to investigate a detailed crystal structure and magnetic ordering of $Mn_xTi_{1-x}Co_2O_4$ polycrystalline samples using the neutron powder diffraction and dc- and ac-magnetization measurements. In the following sections we discuss the particulars of the experiments we performed and their results.

4.2 Experimental details:

In this section we focus our attention on the synthesis of the proposed system $Mn_xTi_{1-x}Co_2O_4$ and various characterization details. Among various compositions ($0 \le x \le 1$) that we prepared, two specific compositions $Ti_{0.8}Mn_{0.2}Co_2O_4$ and $Ti_{0.6}Mn_{0.4}Co_2O_4$ are chosen for a detailed study because they show the evidence for magnetic compensation effect, reentrant spin-glass behavior and exchange-bias effect. Both the compositions $Ti_{0.8}Mn_{0.2}Co_2O_4$ and $Ti_{0.6}Mn_{0.4}Co_2O_4$ were synthesized by the standard solid-state reaction method using the stoichiometric amounts of precursor oxides TiO_2, Mn_2O_3, and Co_3O_4. These mixed oxides were grounded in an agate mortar for 6 hours and pelletized using a hydraulic press with 50 kN pressure followed by sintering at 1100 °C for 8 h duration with 5 °C per minute heating and cooling rates. The structural characterization and phase purity of the sintered pellets were investigated by the X-ray diffraction (XRD) measurements at room temperature, performed using a Rigaku X-ray diffractometer (model: TRAX III) with Cu-Kα radiation (λ = 1.54056 Å). The observed XRD patterns for both the samples belong to the cubic spinel with space group *Fd-3m* (227) (Figure 4.1). Lattice parameter decreases with increasing the Mn concentration (a = 8.384 Å, for $x \sim$ 0.4) due to smaller ionic size of the Mn ($r \sim$ 0.645 Å) as compared to Ti ($r \sim$ 0.67 Å). The electronic structure and elemental analysis of $Ti_{0.8}Mn_{0.2}Co_2O_4$ and $Ti_{0.6}Mn_{0.4}Co_2O_4$ were performed by the XPS measurements using Al-K_α lab source. All the data was recorded using an Omicron hemispherical analyzer. After subtracting the Tougard background, the XPS core-level data were fitted with mixed Lorentzian–Gaussian profile. We have studied the crystal and magnetic structure of both the compounds in detail by performing the neutron scattering measurements (under zero magnetic field) on the power samples using the instruments E2, E6 and

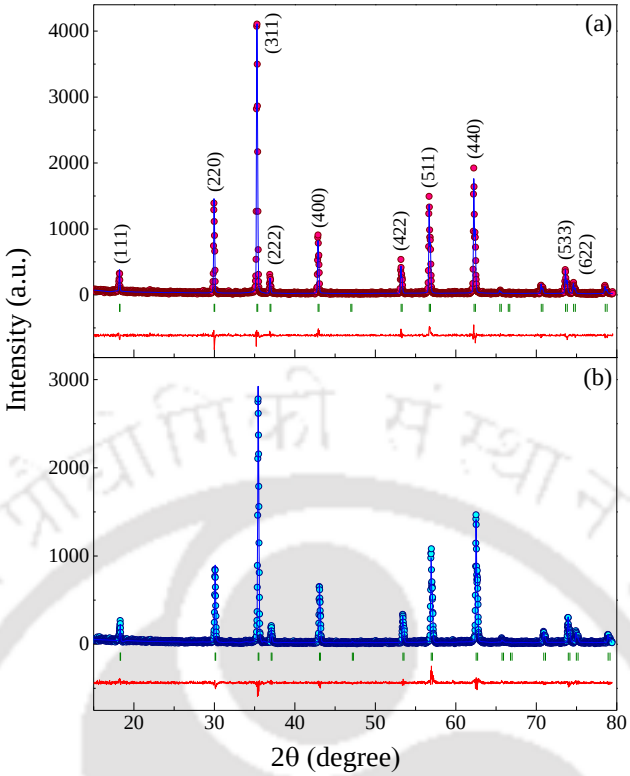

Figure 4.1. X-ray diffraction pattern and the Rietveld refinement data of (a) $Ti_{0.8}Mn_{0.2}Co_2O_4$ and (b) $Ti_{0.6}Mn_{0.4}Co_2O_4$ polcrystals. The circular symbols represent the experimental data and blue color solid continuous lines represent the theoretically simulated pattern. The red lines at the bottom represent the difference between the observed and simulate patterns. The position of Braggs reflections is represented by tiny olive color vertical lines. The lattice parameter a = 8.43 Å and 8.38 Å for x = 0.2 and 0.4, respectively.

E9 of BER II reactor at the Helmholtz-Zentrum Berlin. A Ge monochromator having the neutron wavelength λ = 1.3083 Å has been used in the E9 instrument, while the E2 and E6 instruments use a pyrolytic graphite (PG) monochromator selecting the neutron wavelengths λ = 2.379 and 2.423 Å, respectively. The magnetic properties of the bulk sized polycrystalline samples were studied by the SQUID magnetometer (from Quantum design MPMS XL) in the temperature range 4-300 K and magnetic field (H) up to ± 50 kOe. However, the temperature dependence of specific heat $C_P(T)$ was recorded by means of a physical-property-measurement-systems (PPMS) from Quantum design. Detailed working principle of the above mentioned instruments and their technical details are already discussed in Chapter−2.

4.3 Results and Discussion:

4.3.1 Elemental Analysis using XPS:

In this section we provide the elemental analysis of the investigated system. Figure 4.2 shows the core level x-ray photoelectron spectra of $Ti_{0.6}Mn_{0.4}Co_2O_4$ sample where the photoelectron intensity plotted as a function of binding energy (eV). The XPS spectra obtained from the (a) Mn-2p, (b) Co-2p, (c) Ti-2p and (d) O-1s core levels were calibrated by selecting the binding energy of carbon C-1s orbital (E_C = 284.8 eV) as an internal reference. All these spectra were fitted using the XPSPEAK 4.1 software. During the fitting procedure a constraint was maintained to have the same peak profile within the binding energy range of 0.2 eV.

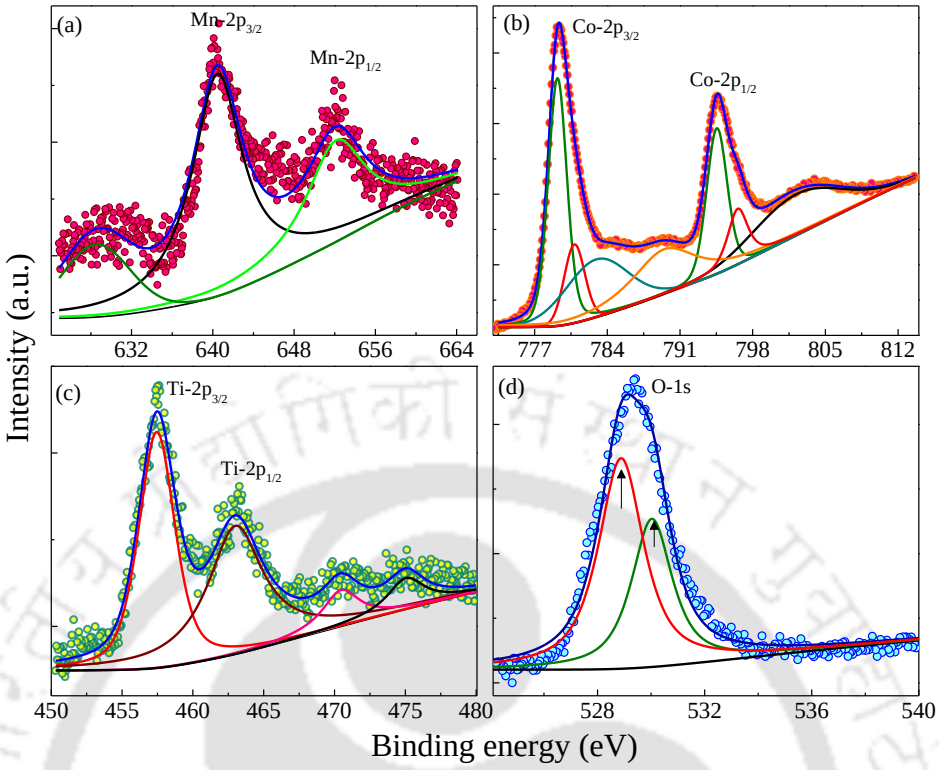

Figure 4.2. The X-ray photoelectron spectra (XPS) of $Ti_{0.6}Mn_{0.4}Co_2O_4$. Figures (a), (b), (c) and (d) show the core level XPS spectra of Mn-2*p*, Co-2*p*, Ti-2*p* and O-1*s*, respectively.

This constrain is relaxed at the final step of the peak fitting. The Mn-2*p* spectrum fitted with the two main peaks at 640.45 eV and 652.12 eV, and one broad satellite peak at 628.52 eV which are shown in figure 4.2(a). The binding-energy separation between the Mn doublet $\Delta E_{Mn}(E_{p1/2} - E_{p3/2})$ ~ 11.67 eV signifies the trivalent oxidation state of Mn inside the core of $Ti_{0.6}Mn_{0.4}Co_2O_4$ [157,199,200]. However, figure 4.2(b) shows the core level XPS spectrum of Co-2*p* consist of two doublets of Co(II) (at 794.6 eV) and Co(III) (at 779.3 eV) together with three broad satellite peaks positioned at 783.4, 789.9 and 804.1 eV. From the fitting analysis, we have calculated the spin-orbit splitting energy (ΔE) between the doublets $\Delta E_{Co3+}(2p_{1/2}-2p_{3/2})$ and $\Delta E_{Co2+}(2p_{1/2}- 2\ p_{3/2})$, which comes out to be 15.3 and 15.78 eV, respectively, signify the trivalent and divalent oxidation states Co ions [14,201,202]. On the other hand, Ti-2*p* core level spectrum (figure 4.2(c)) is deconvoluted into two major peaks (doublet) located at 457.44 and 463.01 eV, together with two high-energy shake up satellite peaks centered at 470.46 and 475.04 eV. The Ti-$2p_{1/2}$ peak profile is slightly broader (~ 0.28 eV) than the Ti-$2p_{3/2}$ peak due to the Coster-Kronig effect [203]. The magnitude of spin-orbit splitting (ΔE_{Ti}) between the Ti-$2p_{1/2}$ and Ti-$2p_{3/2}$ (~ 5.58 eV) signifies the presence of trivalent electronic state of Ti [203]. Further to confirm the Ti^{3+} oxidation state, we have carried out a systematic correlation between the Ti-O bond length (obtained from the Rietveld refinement data) and a robust parameter $\Delta_{O\text{-}Ti}$ i.e. the binding energy difference between the O-1*s* and Ti-$2p_{3/2}$ [204]. The experimentally observed value of $\Delta_{O\text{-}Ti}$ ~ 72.6 eV and the Ti-O bond length ~ 2.058 Å confirm the presence of Ti^{3+} oxidation state. For Ti in tetravalent oxidation sate, the values of $\Delta_{O\text{-}Ti}$ and Ti-O bond length would lie in the range 71 eV ≤ $\Delta_{O\text{-}Ti}$ ≤ 72 eV and 1.94 Å ≤ Ti-O ≤ 1.97 Å, respectively [204]. For divalent oxidation state of Ti the aforementioned parameters would be $\Delta_{O\text{-}Ti}$ ~ 75 eV with Ti-O bond length ~2.08 Å. Finally, the O-1*s* spectrum is deconvoluted into two partially resolved Gaussian-Lorentzian peaks

centered at 530.03 and 528.88 eV as shown by arrow marks in figure 4.2(d). The main origin of highest intensity peak at 528.88 eV is associated with the bonding between metal and lattice oxygen (Mn-O, Ti-O and Co-O), while the low intensity peak at 530.03 eV is associated with the surface-adsorbed oxygen [201]. The slight asymmetric behavior observed in O-1*s* core level spectrum is mainly associated with the presence of oxygen vacancies and different atomic environment faced by the O^{2-} anions [205].

4.3.2 Crystal Structure from Neutron Powder Diffraction:

This section deals with the crystal structure using the temperature dependence of neutron diffraction using E9 instrument discussed in Chapter-2. The crystal structure parameters of $Ti_{0.8}Mn_{0.2}Co_2O_4$ and $Ti_{0.6}Mn_{0.4}Co_2O_4$ has been investigated at 3 K by collecting the data sets between the diffraction angles 5° and 141.8°. Figure 4.3 represent the neutron powder diffraction patterns recorded at 3 K together with their Rietveld refinement of both compounds x = 0.2 and 0.4. An additional neutron diffraction pattern for the sample x = 0.4 was collected at 295 K for comparison. In order to determine the correct composition, we have refined the crystal structure and site occupancies of individual ions for both the compounds. In the first step the occupancies of the Co^{2+} ions at the *A* site and the oxygen atoms were refined, while the occupancies of the *B*-site atoms were fixed.

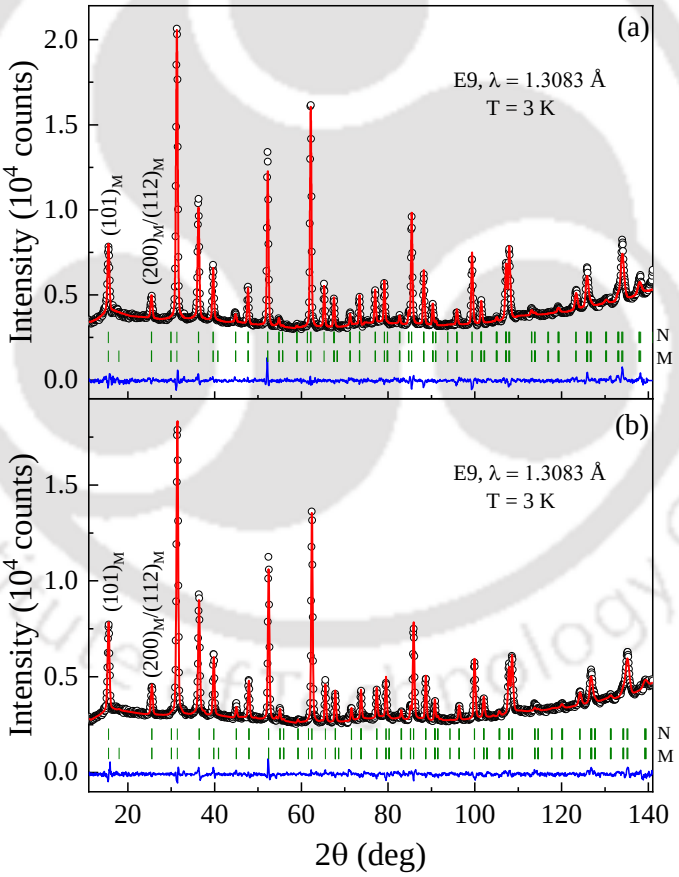

Figure 4.3. The Rietveld refinements of the neutron powder diffraction data of (a) $Ti_{0.8}Mn_{0.2}Co_2O_4$, and (b) $Ti_{0.6}Mn_{0.4}Co_2O_4$ collected on E9 (wavelength, λ = 1.3083 Å) at 3 K. The crystal structure was refined in the tetragonal space group $I4_1/amd$. The calculated patterns (red) are compared with the observed data (black circles). In the lower part of each plot shows the difference pattern (blue) as well as the positions of the nuclear (N) and magnetic (M) Bragg reflections. The strongest magnetic contribution was observed for the reflections (101) and (200)/(112) (see also figure 4.5).

After the refinement the ratio of *occ*(O)/*occ*(Co^{2+}) reached a magnitude 4.11(3) which is slightly larger than the ideal value '4' which indicates that the sample does not show any oxygen deficiency. In the next step of refinement, the occupancies of Co^{2+} and O were fixed. Here one can finds a reduced scattering power at the *B* site which indicate that the manganese and titanium content at the *B* site is higher than that of cobalt. The loss of cobalt at the B site can be explained by the fact that both samples contain minor impurities of Co_3O_4. On the basis of accurate weighting of the components we finally used the constraint for *B* site as (1+*x*) [*occ*(Ti) + *occ*(Mn)] + (1−*x*) *occ*(Co) = 1, where *occ* is the nominal content at the *B* site. Therefore, from the final refinements of data set collected at 3 K we found the chemical compositions are $(Co^{2+})_A[Ti_{0.629(5)}{}^{3+}Mn_{0.420(5)}{}^{3+}Co_{0.951(5)}{}^{3+}]_BO_4$ and $(Co^{2+})_A[Ti_{0.841(5)}{}^{3+}Mn_{0.210(5)}{}^{3+}Co_{0.949(5)}{}^{3+}]_BO_4$ for x = 0.4 and 0.2, respectively. Despite the fact that we could not observe a peak broadening of particular reflections, we also tried to refine the crystal structure in the next lower symmetric space group $I4_1/amd$ (No. 141, cell choice 2) with the cell dimensions $a_t \times b_t \times c_t = a_c/\sqrt{2} \times b_c/\sqrt{2} \times c_c$. In this setting the Co^{2+} ions at the *A* site (labelled as Co_A) are located at the Wyckoff position 4*b*(0,¼,⅜), while at the *B* site the Ti^{3+}, Mn^{3+} and Co^{3+} ions (labelled as Co_B) are located at 8*c*(0,0,0). The oxygen atoms positioned at 16*h*(0, 0.5, 0.25). However, we found from the Rietveld refinements of $Ti_{0.6}Mn_{0.4}Co_2O_4$ system the $c/a\sqrt{2}$ ratios to be 0.9988(3) and 0.9995(3) at 3 and 295 K, respectively. Similarly, $c/a\sqrt{2}$ ratio for $Ti_{0.8}Mn_{0.2}Co_2O_4$ at 3 K was found to be 0.9988(3). These values indicate the presence of a weak tetragonal distortion at low temperature in the magnetically ordered region. Table 4.1 lists the parameters obtained from the Rietveld refinements of neutron powder diffraction data of $Ti_{0.8}Mn_{0.2}Co_2O_4$ and $Ti_{0.6}Mn_{0.4}Co_2O_4$.

Table 4.1. Results of the Rietveld refinements of the neutron powder diffraction data of $Ti_{0.2}Mn_{0.8}Co_2O_4$ and $Ti_{0.4}Mn_{0.6}Co_2O_4$ collected on the instrument E9 at 3 K. The refinements were carried out in the tetragonal space group $I4_1/amd$. The given residuals are defined as $R_F = \sum||F_{obs}|-|F_{calc}||/\sum|F_{obs}|$. Listed are the positional parameters *y* and *z* of the O atom located at the site 16*h*(0,y,z) and the occupancies of the Ti_B, Mn_B and Co_B atoms at the site 8*c*(0,0,0). For all atoms an overall thermal parameter B_{iso} was refined. Further the bond distances in the T_BO_6 octahedra (T_B = Ti_B, Mn_B, and Co_B), and the Co_AO_4 tetrahedra as well as the lattice parameters are also given.

	$Ti_{0.8}Mn_{0.2}Co_2O_4$	$Ti_{0.6}Mn_{0.4}Co_2O_4$	
T [K]	3	3	295
occ(Ti_B)	0.835(4)	0.618(3)	0.628(6)
occ(Mn_B)	0.209(4)	0.412(3)	0.419(6)
occ(Co_B)	0.956(4)	0.970(3)	0.953(6)
y(O)	0.5218(5)	0.5241(4)	0.5246(4)
z(O)	0.2398(5)	0.2414(5)	0.2418(5)
a_t [Å]	5.9499(4)	5.9231(4)	5.9331(5)
c_t [Å]	8.4044(10)	8.3677(11)	8.3867(13)
$c_t/a_t\sqrt{2}$	0.9988(3)	0.9988(3)	0.9995(3)
V [Å^3]	297.53(5)	293.57(6)	295.22(7)
B_{iso} [Å^2]	0.37(5)	0.53(6)	0.71(5)
$d_{ab}(T_B\text{-O}) \times 4$	2.016(2)	1.998(2)	1.997(2)
$d_c(T_B\text{-O}) \times 2$	2.020(5)	2.025(4)	2.033(4)
$d(Co_A\text{-O}) \times 4$	1.976(4)	1.972(3)	1.976(3)
R_F	0.042	0.042	0.041

For the Co^{2+} ions at the *A* site have the $3d^7$ configuration, cooperative distortions of the CoO_4 tetrahedra through the Jahn-Teller effect are absent. However, this is not the case for the TO_6 octahedra, which contain the Jahn-Teller active ions Ti^{3+}, Mn^{3+} and Co^{3+}, having the $3d^1$, $3d^4$ and $3d^6$ electronic configurations, respectively. For the Mn^{3+}, Ti^{3+} and Co^{3+} ions electronic energy can be gained if the t_{2g} levels split into a lower d_{xy} level and a higher twofold generate d_{xz}/d_{yz} level (figure 4.4). This would result in a tetragonal distortion with a c/a ratio smaller than 1, and also a shrinking of the apical bond $d_c(T\text{-O})$ (figure 4.4). But the crystal structure refinements of $Ti_{0.8}Mn_{0.2}Co_2O_4$ showed that the apical bond length $d_c(T_B\text{-O})$ = 2.020(5) Å is slightly longer than the equatorial length $d_{ab}(T_B\text{-O})$ = 2.016(2) Å. This effect is stronger in $Ti_{0.6}Mn_{0.4}Co_2O_4$, because the Mn content is twice than that in $Ti_{0.8}Mn_{0.2}Co_2O_4$ in which the bond lengths are $d_c(T_B\text{-O})$ = 2.025(4) Å and $d_{ab}(T_B\text{-O})$ = 1.998(2) Å. Here it is interesting to note that a tetragonal distortion is not able to be detected in $TiCo_2O_4$, suggesting that the Jahn-Teller activity of the Ti^{3+} and Co^{3+} ions are rather weak in this system [14]. Therefore, we can assume that the elongation of the apical bond $d_c(T\text{-O})$ can be ascribed to the Jahn-Teller activity of the Mn^{3+} ions having the $3d^4$ configuration. In this case electronic energy can be gained if the e_g level splits into $d_{x^2-y^2}$ and d_{z^2} levels, where the fourth electron occupies the lower lying d_{z^2} level. This electronic configuration finally leads to an elongation of the TO_6 octahedra along the *c* axis. Possibly the Jahn-Teller effect on the two ions act along different directions as found earlier in $Ni_{1-x}Cu_xCr_2O_4$ system [80] and lead to compensation of particular distortions.

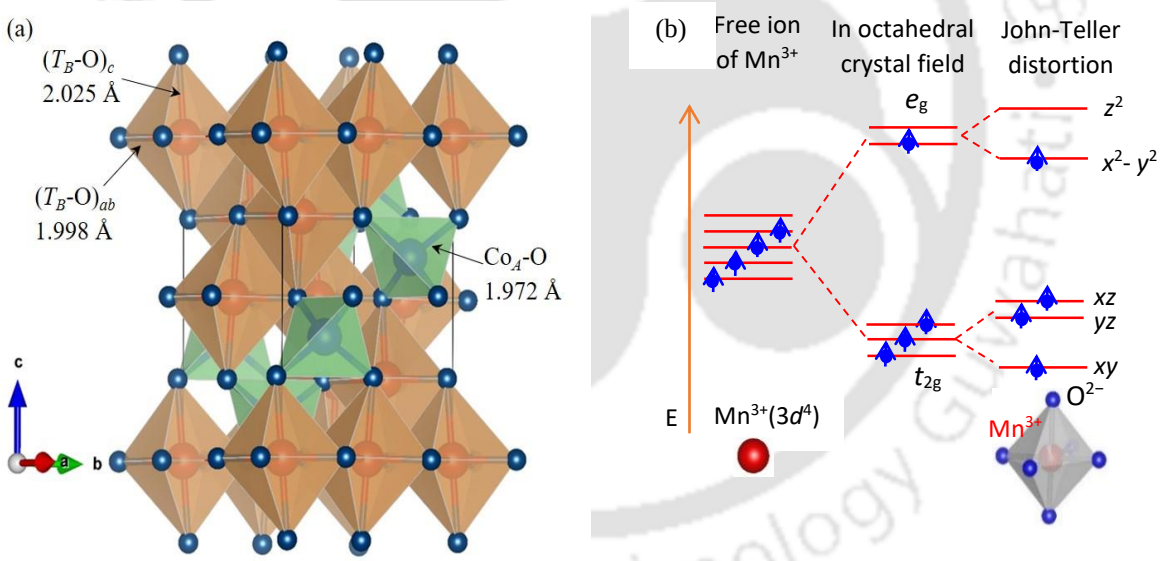

Figure 4.4. (a) The schematic of tetragonally distorted crystal structure of $Mn_xTi_{1-x}Co_2O_4$ unit cell visualized by using software VESTA. The tetrahedral positions (green) are occupied by divalent Co ions, whereas the octahedral sites (orange color) are occupied by trivalent Mn, Ti and Co ions. (b) Graphical illustration of degenerate orbital energy levels of $Mn^{3+}(3d^4)$. In the larger crystal field of octahedral symmetry, the degeneracy of these energy levels are lifted into triply t_{2g} and doubly e_g orbitals. The $Mn^{3+}O_6$ octahedra became distorted due to Jahn–Teller effect.

4.3.3 Magnetic Scattering using E6 and E2 Instruments:

In this section we focus our attention on the magnetic structure of the two compositions x = 0.2 and 0.4 by measuring the neutron powder diffraction data at different temperatures from the E2 and E6 instruments which are completely dedicated for the magnetic properties. The diffraction patterns collected at T = 2 K from the instrument E2 have high counting statistics (24 h/pattern) recorded using a 15-min collimation to improve the instrumental resolution to probe the detailed magnetic structure. Using E2, we collected a second set of diffraction pattern for both the sample in the paramagnetic region (at 90 and 142 K). However, a detailed temperature dependent (from 2 K to 300 K) measurements are performed only on the E6 instrument. The refinements of crystal and magnetic structures were carried out with the *FullProf* program [206]. For the refinement we considered the nuclear scattering lengths b(O) = 5.805 fm, b(Ti) = –3.30 fm, b(Mn) = –3.73 fm, and b(Co) = 2.50 fm [207]. The magnetic form factors of the Ti^{3+}, Mn^{3+}, Co^{2+} and Co^{3+} ions were taken from the Ref. [208]. Figure 4.5 shows the diffraction patterns of $Ti_{0.8}Mn_{0.2}Co_2O_4$ and $Ti_{0.6}Mn_{0.4}Co_2O_4$ collected from E2 at two different temperatures (2 K and 90K/142K). The powder patterns collected at 2 K show additional magnetic intensities due to the magnetic ordering of the Ti, Mn, and Co atoms. Due to the weak tetragonal splitting, we used the cubic setting for data analysis.

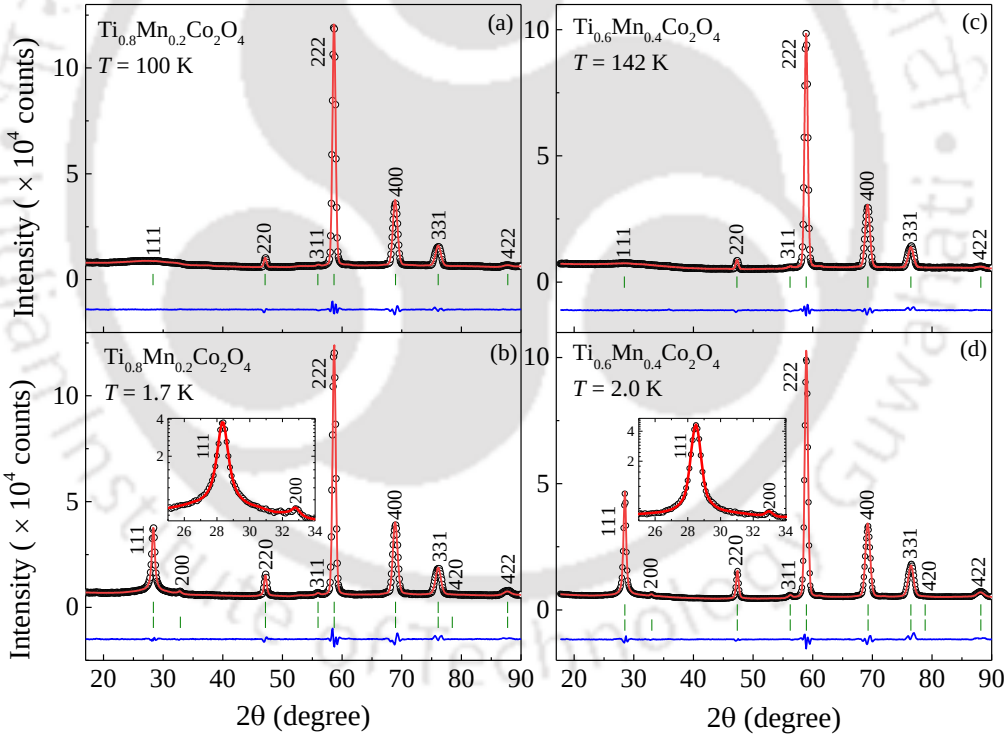

Figure 4.5. Neutron powder patterns of polycrystalline samples $Ti_{0.8}Mn_{0.2}Co_2O_4$ and $Ti_{0.6}Mn_{0.4}Co_2O_4$ collected on the instrument E2 at temperatures well below and above the long-range magnetic ordering. The crystal structure was refined in the cubic space group *Fd-3m*. The powder patterns in the bottom part of the diagram show additional magnetic intensities due to the magnetic ordering of the trivalent Ti, Mn, and Co atoms. The insets present the prominent magnetic reflections of $(111)_M$ and $(200)_M$ in enlarged form. Due to the weak intensity of the reflection $(200)_M$ we used a logarithmic scale representation. The calculated patterns (red) are compared with the observed ones (black circles). The difference patterns (blue) as well as the positions of the nuclear and magnetic Bragg reflections are also shown in the graphs.

For both compounds, the strongest magnetic intensity could be observed at the position of the reflection 111 indicating a ferrimagnetic (FIM) coupling between the atoms located at *A* and *B* sites. A much weaker magnetic intensity could be observed at the position of the reflection (200). An enlarged view of the two magnetic reflections are shown in the inset of figure 4.5 using a logarithmic scale. The (200) reflection is forbidden not only for the cubic space group $Fd\bar{3}m$, but also for the next-lower symmetric tetragonal space group $I4_1/amd$, where the reflections are indexed as (110) and (002). Thus the presence of magnetic intensity suggests loss of at least one of the *d*-glide planes indicating the existence of an additional antiferromagnetic (AFM) component. However, in the tetragonal setting the splitting of the individual reflections (110) and (002) is too weak to distinguish their magnetic contributions and it is not possible to determine the directions of the AFM and FIM components. However, it is possible to determine the spin sequence for the *B*-site atoms (Co_B, Ti_B, and Mn_B) which are located at the positions (1) 0,0,0; (2) ¾,¼,½; (3) ¼,½,¾; (4) ½,¾,¼. In general, the possible spin sequences for the *B*-site atoms can be + + + +, + – + –, + + – –, and + – – +. For the magnetic structure refinement, we fixed the magnetic moment of ferromagnetic (FM) component parallel to the a axis. Several trials have shown that the best fit was achieved using the spin sequences + + – – and + – + – for the AFM components aligned parallel to the *b* and *c* axes, respectively. These modes are compatible with those of the irreducible representation (*irrep*) Γ_8 obtained from the representation analysis using the program *BasIrep* of the *Fullprof* suite [14]. This *irrep* is of dimension 3 and it appears 2 times in Γ_8 which means that the ferromagnetic component can be alternatively aligned parallel to b and c. It can be seen in figure 4.6 that antiferromagnetically coupled moments show a non collinear magnetic ordering, where the moments point along [011] and [01–1] direction. Previously the coexistence of AFM and FIM ordering was also observed in compounds such as $Ni_{1-x}Cu_xCr_2O_4$, where the FIM ordering occurs in the *ab* plane and the AFM component is aligned parallel to the *c* axis [80].

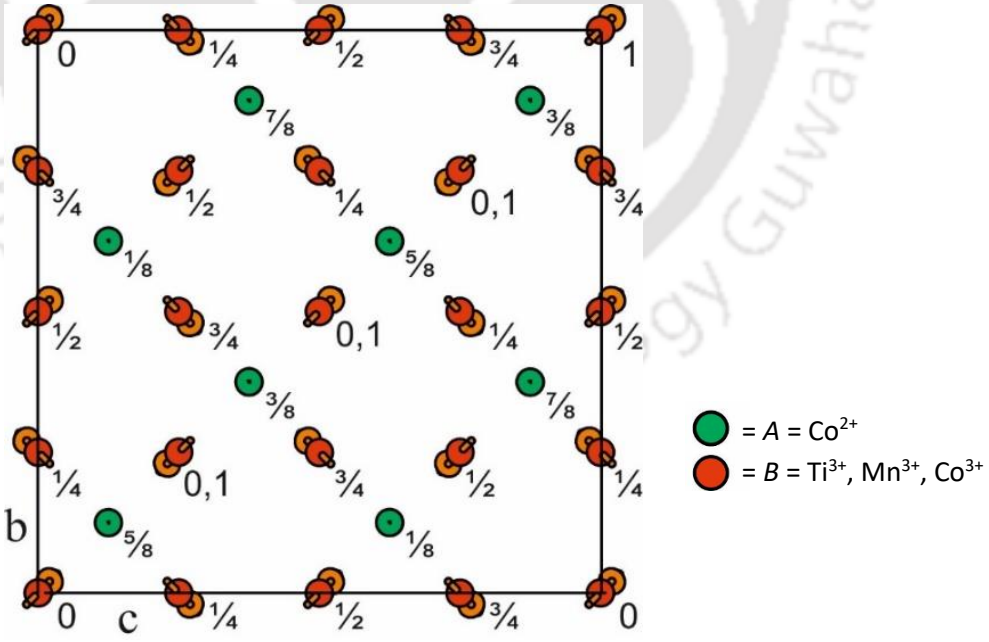

Figure 4.6. Schematic of magnetic structure of $Ti_{0.8}Mn_{0.2}Co_2O_4$ and $Ti_{0.6}Mn_{0.4}Co_2O_4$. Here the ferrimagnetically coupled moments at *A*- and *B*-sites are aligned parallel to the a axis. The noncollinear antiferromagnetic spin alignments occur in the bc plane.

Therefore, it is important to study the variation of magnetic moments as a function of temperature to have a precise understanding of the variation of magnetic moments and thereby determine the ordering temperatures so that one can correlate such temperature dependence with the dc-magnetization data (which will be discussed in later sections). Figure 4.7 shows the temperature variation of averaged moments for the cations situated at *B* site (labelled as T_B) which are coupled ferrimagnetically with the moments of the *A*-site cations (labelled as Co_A).

In the present case, the *B*-site magnetic ions Mn^{3+} and Co^{3+} have the $3d^4$ and $3d^6$ configurations with four unpaired electrons in the high-spin state, while Ti^{3+} ions in the $3d^1$ has only one electron. Therefore, the expected theoretical magnetic moment values for the high-spin state are $\mu_{eff} = g\,S\,\mu_B = 4.0\,\mu_B$ for Mn^{3+} and Co^{3+}, and $\mu_{eff} = g\,S\,\mu_B = 1.0\,\mu_B$ for Ti^{3+}. The Co^{2+} ions at the *A* site have three unpaired electrons in the $3d^7$ configuration. Nevertheless, we have tried to estimate the individual moment values at the *B* site using the constraint $\mu(Mn^{3+}) = \mu(Co^{3+}) = 4 \times \mu(Ti^{3+})$. The results of the refinements are given in Table 4.2. The obtained total moments of the Ti^{3+} ions vary in both compounds between 0.52 and 0.60 μ_B, and those of the Mn^{3+}/Co^{3+} ions between 2.09 and 2.39 μ_B, which are considerably smaller than the theoretical values given above. It has been mentioned that the magnetic moments of the *B* site Co^{3+} ions were found to be zero in Co_3O_4 and $MnCo_2O_4$ due to large crystal field splitting, in contrast to the Co^{3+} ions which exhibits non-zero magnetic moment in $TiCo_2O_4$ [14,84,193]. In order to estimate the magnetic moments of Co^{3+} we used the fixed moment value 3.84 μ_B of Mn^{3+} as determined earlier for $MnCo_2O_4$ [193]. Hence, for the refinements we now used the constraint $\mu(Mn^{3+}) = 4 \times \mu(Ti^{3+})$ and determined the magnitude of magnetic moments of Co^{3+} which vary between 0.75 and 0.80 μ_B for $Ti_{0.8}Mn_{0.2}Co_2O_4$. Whereas, the magnetic moments of Co^{3+} are found to be small in case of $Ti_{0.6}Mn_{0.4}Co_2O_4$ composition which varies between 0.60 and 0.65 μ_B. This may give the trend that the moment of Co^{3+} ion decreases with increasing Mn content. The Co^{2+} ions at the *A* site have three unpaired electrons in the $3d^7$ configuration. On the other hand, the magnetic moment of *A* site Co^{2+} ion lies between 2.60 and 3.10 μ_B, which are close to the theoretically predicted value of the high-spin state $\mu_{eff} = g\,S\,\mu_B = 3.0\,\mu_B$ (Table 4.2). In contrast, the moment of Co^{2+} ion at the *A* site in $TiCo_2O_4$ was found to be reduced which can be ascribed to stronger frustration effects [14].

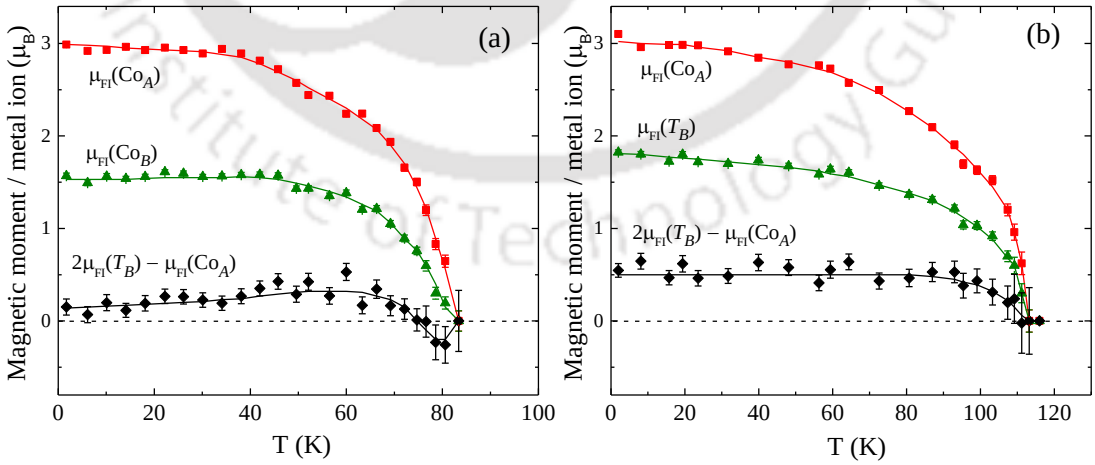

Figure 4.7. Temperature dependence of the magnetic moments of (a) $Ti_{0.8}Mn_{0.2}Co_2O_4$, and (b) $Ti_{0.6}Mn_{0.4}Co_2O_4$ polycrystals in which the cations are located at the *A* and *B* sites. The *A* site ions are occupied with Co^{2+} ions (labelled as Co_A), while the *B* site contains are trivalent Ti, Mn and Co (labelled as T_B). The averaged moments are given for the *B* site cations. Bold lines are for the visual guide.

In Table 4.2 we also compare the resulting ferromagnetic components of $Ti_{0.8}Mn_{0.2}Co_2O_4$ and $Ti_{0.6}Mn_{0.4}Co_2O_4$ determined from magnetization measurement with those obtained from our neutron diffraction study given as $2\mu_{FI}(T_B) - \mu_{FI}(Co_A)$. Due to the fact that the resulting ferromagnetic components are relatively small we were not able to determine them with good accuracy from our neutron diffraction data. Taking this into account the moment values obtained from both methods show more or less a good agreement (Table 4.2). Due to the fact that the AFM component could not be precisely determined from the E6 data in the temperature range close to the ferrimagnetic ordering temperature, we used the ratio $\mu_{FI}(T_B)/\mu_{AF}(T_B)$ as constraint. As given above, we were not able to determine precisely the individual moment values of Ti^{3+}, Mn^{3+}, and Co^{3+} at the *B* site. Therefore, only the averaged moment values at the *B* site (labelled as T_B) are plotted in figure 4.7.

Table 4.2. Magnetic moments of the transition metal atoms in $Ti_{0.2}Mn_{0.8}Co_2O_4$ and $Ti_{0.4}Mn_{0.6}Co_2O_4$ obtained from Rietveld refinements using neutron diffraction data collected on the instruments E2 and E6 at 2 K, respectively. The magnetic Co^{3+}, Ti^{3+} and Mn^{3+} ions (*B* site) in the space group *Fd-3m* are located at the positions: (1) 0,0,0; (2) ¾,¼,½; (3) ¼,½,¾; (4) ½,¾,¼. The Co^{2+} ions (*A* site) are located at (1) ⅜,⅜,⅜; (2) ⅛,⅝,⅛. During the refinements we have used the constraint $\mu(Co^{3+}) = \mu(Mn^{3+}) = 4 \times \mu(Ti^{3+})$, and in the lower part $\mu(Mn^{3+}) = 4 \times \mu(Ti^{3+})$ to estimate the moment of Co^{3+}. Here the moment of Mn^{3+} was determined earlier for $MnCo_2O_4$ [33]. The averaged moments of T_B are also listed. The resultant ferromagnetic moments are compared with spontaneous magnetizations *M* measured at 5 K.

Magnetic moment	$Ti_{0.8}Mn_{0.2}Co_2O_4$ E2	$Ti_{0.8}Mn_{0.2}Co_2O_4$ E6	$Ti_{0.6}Mn_{0.4}Co_2O_4$ E2	$Ti_{0.6}Mn_{0.4}Co_2O_4$ E6
$\mu_{FI}(Co_A)$ [μ_B]	2.60(3)	2.99(2)	2.94(4)	3.10(3)
$\mu_{FI}(Mn_B/Co_B)$ [μ_B]	2.09(5)	2.29(4)	2.13(4)	2.39(4)
$\mu_{FI}(Ti_B)$ [μ_B]	0.52(1)	0.57(1)	0.53(1)	0.60(1)
$\mu_{FI}(T_B)$ [μ_B]	1.43(3)	1.57(3)	1.63(3)	1.82(3)
$\mu_{AF}(Mn_B/Co_B)$ [μ_B]	0.90(4)	0.68(4)	0.72(3)	0.68(3)
$\mu_{AF}(Ti_B)$ [μ_B]	0.22(1)	0.17(1)	0.18(1)	0.17(1)
$\mu_{AF}(T_B)$ [μ_B]	0.61(2)	0.46(2)	0.56(2)	0.52(2)
$\mu_{tot}(Mn_B/Co_B)$ [μ_B]	2.27(4)	2.39(3)	2.25(3)	2.48(3)
$\mu_{tot}(Ti_B)$ [μ_B]	0.57(1)	0.60(1)	0.56(1)	0.62(1)
$\mu_{tot}(T_B)$ [μ_B]	1.55(2)	1.64(2)	1.72(2)	1.90(2)
R_F / R_M	0.019 / 0.041	0.007 / 0.042	0.023 / 0.041	0.012 / 0.052
$2\mu_{FI}(T_B) - \mu_{FI}(Co_A)$ [μ_B]	0.25(10)	0.15(8)	0.31(8)	0.55(7)
M [μ_B]	0.32	0.32	0.35	0.35
$\mu_{tot}(Ti_B)$ [μ_B]	0.96	0.96	0.96	0.96
$\mu_{tot}(Mn_B)$ [μ_B]	3.84	3.84	3.84	3.84
$\mu_{tot}(Co_B)$ [μ_B]	0.75(5)	0.80(4)	0.60(4)	0.65(3)

We also studied the temperature variation of the peak shape. For the Rietveld refinements we used the pseudo-Voigt function which is defined as $pV(x) = \eta L(x) + (1 - \eta)G(x)$, where η gives the contribution of the Lorentzian part. In figure 4.8 it can be seen that the Lorentzian part for $Ti_{0.6}Mn_{0.4}Co_2O_4$ is strongly increasing with the temperature reaching finally a pure Lorentzian peak shape at about 90 K somewhat below the magnetic ordering temperature T_{FN} = 110.3 K. In contrast, for $Ti_{0.8}Mn_{0.2}Co_2O_4$ the pure Lorentzian peak shape is already reached at 10 K below the compensation point. As reported earlier a pure Lorentzian peak shape has been observed for $TiCo_2O_4$ in the full temperature range which was found to be broadened [14]. The change of peak shape can be ascribed to the presence of a superimposed contribution of diffuse scattering. But it has to be mentioned that a Lorentzian peak shape may also describe the distribution of the magnetic mosaic blocks or the presence of short-range order frozen in a spin-glass state. Further studies are needed to give a detailed quantitative description of this behaviour. According to the chemical percolation approach reported by Cowley *et al.* one should expect Bragg scattering occurs from the largely linked clusters, together with a diffuse scattering arising from the limited ferrimagnetic clusters below a critical composition [209]. In such case the correlation length should consist of two components, (i) transverse component which diverges across T_{FN} and decreases and it is associated with critical fluctuations within the infinite cluster. The second one is the (ii) longitudinal component which dominates at low temperature and it is linked to the finite clusters. It is well known that diffuse scattering is an important tool for analyzing such longitudinal and transverse spin components, in particular, the short-range-order of reentrant spin-glass systems in which the disordered reenters at low-temperature below T_{FN}. In the present case a slight decrease of the *A*-site magnetic moment indicates the coexistence of longitudinal and transverse spin components associated with a long-range ordered magnetic network and a glassy state, respectively [210]. Such disordered spins do not give any contribution to magnetic Bragg intensities.

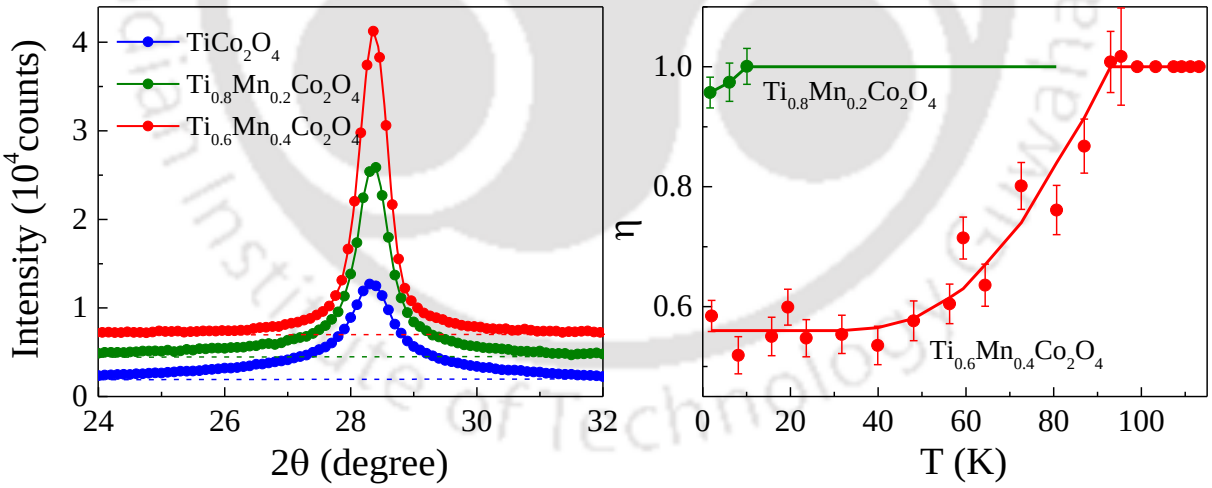

Figure 4.8. (a) Variation of the neutron diffraction peak shape for the magnetic reflection $(101)_M$ with increasing Mn content. A pure Lorentzian peak shape has been observed for $TiCo_2O_4$, whereas, a broad diffuse signal is evident from the background intensity. The data of $TiCo_2O_4$ were taken from [14]. With increasing Mn content significant reduction of the diffuse scattering was observed. Strong increase of the magnetic intensity of $(101)_M$ reflection can be ascribed to the fact that the magnetic moment of Mn is much stronger than Ti. An increase of the Mn content also leads to change of the peak shape, where the Lorentzian part η of the pseudo-Voigt function is decreasing with *T*. (b) Interestingly, the Lorentzian part η is also increasing as a function of temperature which is shown as a function of *T*. Note: Gaussian shape of the reflection $(101)_M$ with FWHM ~ 0.52° and the bold line represents the visual guide.

Neutron diffraction studies of systems like $FeMnTiO_3$ and $Fe_{0.5}Mg_{0.45}Cl_2$ reported the existence of magnetic diffuse scattering due to the coexistence of antiferromagnetic long-range ordering and a transverse spin-glass state [31,211]. The appearance of superimposed magnetic diffuse scattering at the antiferromagnetic Bragg peak indicates the changes taking place in local magnetic ordering. It is also reported that the intensity of such diffuse scattering changes drastically with decreasing temperature, while the intensity of the antiferromagnetic Bragg peak slightly decreases [31,211]. Wong *et al.* reported the coexistence of spin-glass and antiferromagnetic orders in the Ising system $Fe_{0.55}Mg_{0.45}Cl_2$ [211]. In order to probe precisely the transverse spin-glass nature of this system these authors recorded diffuse scattering scans at 1.5 K along the three different crystallographic directions below the freezing temperature (~ 3 K). Consequently, they observed a superimposed Lorentzian diffuse magnetic peak at the position of the nuclear Bragg peak with the correlation length $\xi \sim 10$ Å. Such frozen short-range correlation is probably the source of the spin-glass behavior observed in single crystals of $Fe_{0.55}Mg_{0.45}Cl_2$ [211]. Considering these results, in the present case we performed a detailed ac-magnetic susceptibility and diffuse neutron scattering studies to probe the reentrant glassy behavior. Figure 4.9 shows an enlarged view around the base of (111) neutron-diffraction peak of $Ti_{0.8}Mn_{0.2}Co_2O_4$ and $Ti_{0.6}Mn_{0.4}Co_2O_4$, well below (at 1.7 K/2 K) and above (at 90 K/142 K) the long-range ordering temperature revealing the presence of diffuse scattering superimposed on the (200) reflection. Such well-resolved Bragg reflections, originating from the spatial ordering of the transverse-spin components, indicate the presence of canted local spin configuration on the *B* sublattice (similar to the Yafet-Kittel's (Y-K) three sublattice model) [13,210,212]. Usually, in a non-collinear system, the individual site moments deduced from the neutron diffraction study are due to the longitudinal spin components of the canted site moments, whereas the transverse components do not contribute to the normal Bragg reflections. In a triangular spin-lattice Bragg reflections arise due to the spatial ordering of the transverse spin components. Thus, the origin of the Bragg reflection (200) indicates the presence of a canted local spin configuration on the *B* sublattice. These results are consistent with the previous reports [210,212].

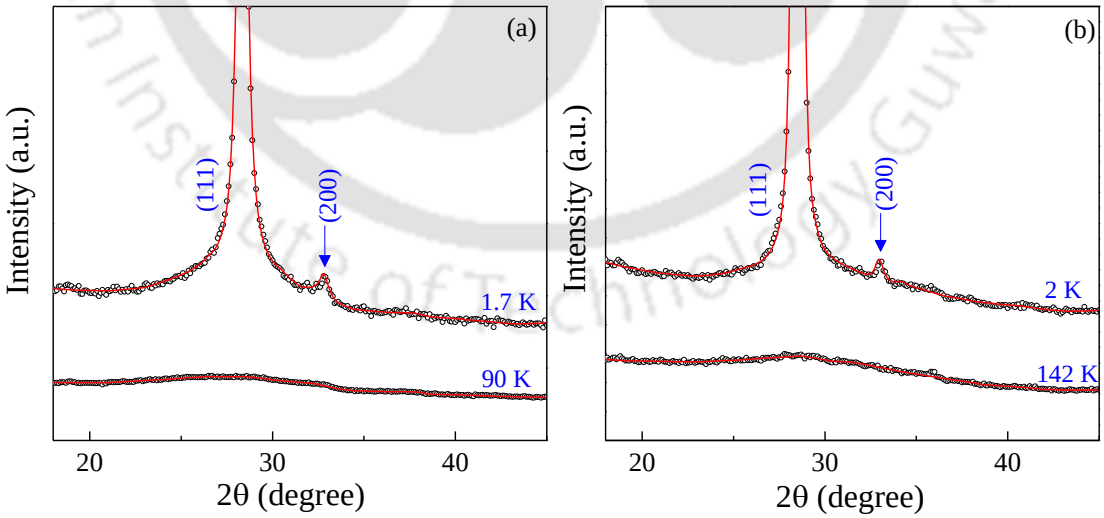

Figure 4.9. Temperature dependence of neutron diffraction pattern around the (200) peak for (a) $x = 0.2$ and (b) $x = 0.4$.

We have evaluated the canting angle ($\alpha_{Y\text{-}K}$) using the individual *B*-site moments (AFM and FIM) derived from the neutron diffraction study of $Mn_xTi_{1-x}Co_2O_4$ with $x = 0.2$ and $x = 0.4$. Accordingly, the canting angle $\alpha_{Y\text{-}K}$ lies between 66.9 and 73.7° for $x = 0.2$, and 71° and 74.1° for $x = 0.4$. Such non-collinear behavior of spins causes substantial decrease of the magnitude of *B*-sublattice moments than the expected value and frequency dispersion of the dynamic susceptibility (which will be discussed in later sections). Usually, the transverse spin-glass component (often called 'semi-spin-glass') coexists with the longitudinal-spin component (LSC) when the magnetic ions are diluted with nonmagnetic ions like Ti^{4+}, Sn^{4+} or Zn^{2+}. Because of such dilution and magnetic frustration, the spins in the *B* sublattice may cant locally [213]. Theoretical studies reported by Villain show that two distinct transitions may occurs in such semi-spin glass systems. The first one is the Néel temperature T_{FN} corresponding to the breakdown of LSC and the second transition is the spin-glass freezing temperature T_F at which the TSC freezes-in [213].

4.3.4 dc-Magnetic Susceptibility:

In this section we provide a clear and vivid picture of magnetic ordering using the dc-magnetization measurements performed by SQUID magnetometer. Here we discuss both the temperature and magnetic field dependence magnetization and make a systematic comparison with the neutron diffraction data both quantitatively and qualitatively. Figures 4.10 and 4.11 depict the temperature variation of dc-magnetic susceptibilities $\chi(T)$ ($M(T)/H$) of both $Ti_{0.6}Mn_{0.4}Co_2O_4$ and $Ti_{0.8}Mn_{0.2}Co_2O_4$ measured under zero-field-cooled (ZFC) and field-cooled (FC) conditions. We have performed these measurements in the presence of different external dc-magnetic fields H_{dc} between 500 Oe and 50 kOe. Figures 4.10(a) and 4.11(a) show the variation of $\chi(T)$ at H_{dc} = 500 Oe, however figures 4.10(b) and 4.11(b) represent the $\chi(T)$ measured at 50 kOe for $Ti_{0.6}Mn_{0.4}Co_2O_4$ and $Ti_{0.8}Mn_{0.2}Co_2O_4$, respectively.

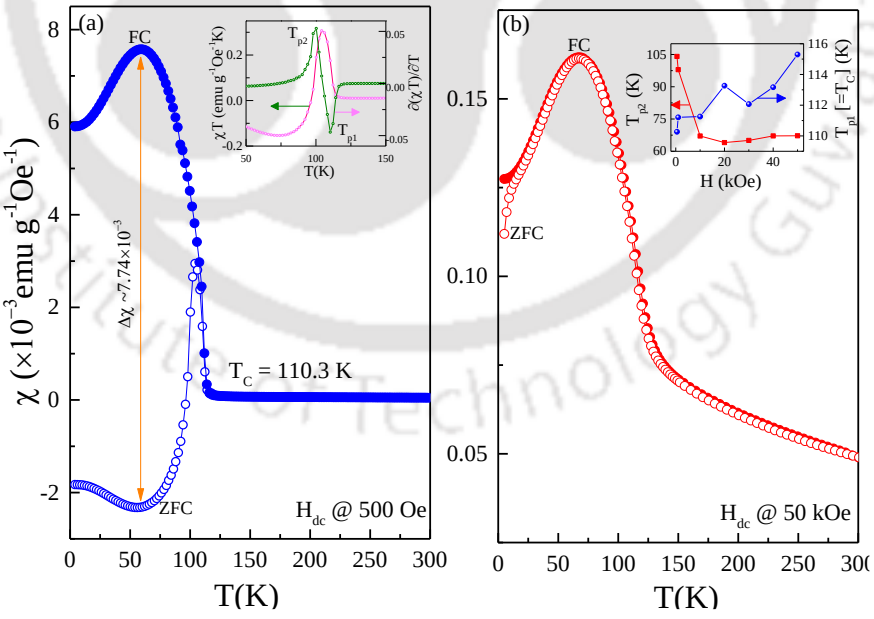

Figure 4.10. Temperature dependence of the dc-magnetic susceptibility $\chi(T)$ of polycrystalline $Ti_{0.6}Mn_{0.4}Co_2O_4$ system measured under zero-field-cooled (ZFC) and field-cooled (FC) conditions in the presence of external dc-magnetic field H_{dc} is equivalent to (a) 500 Oe and (b) 50 kOe. Inset of figure (a) depicts the product χT (left hand side scale) and its derivative (right hand side scale) was plotted as a function of temperature. The filed dependence of T_{p1} and T_{p2} was plotted in the inset of figure (b)

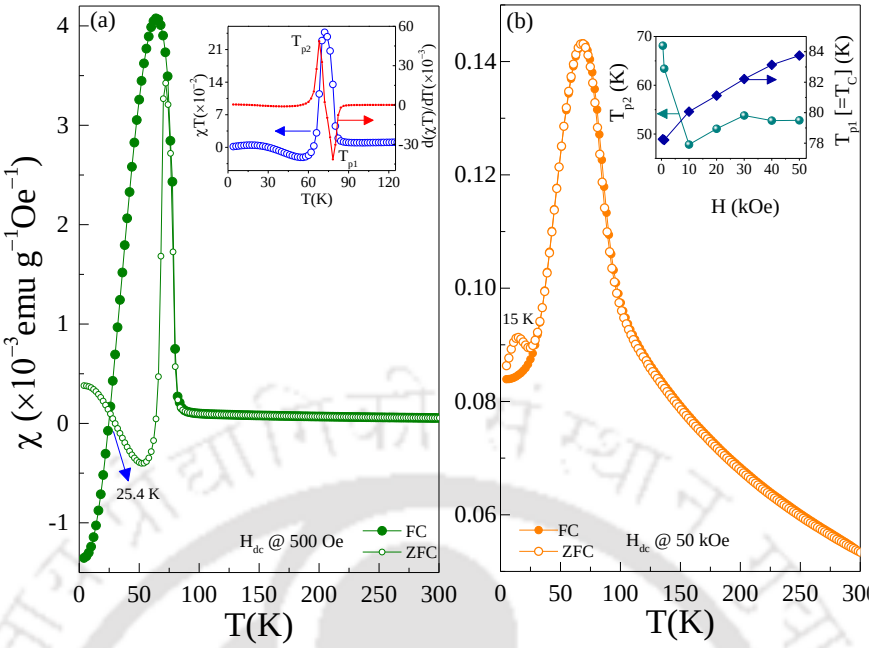

Figure 4.11. The χ versus *T* plots of $Ti_{0.8}Mn_{0.2}Co_2O_4$ measured under ZFC and FC conditions for (a) H_{dc} = 500 Oe and (b) H_{dc} = 50 kOe. Figure (a) clearly shows the magnetic compensation phenomena at T_{COMP} = 25.4 K, represented by blue arrow mark in the main panel. However, such T_{COMP} disappear at very high applied fields as shown in figure (b). Inset of figure (a) depicts the product χ*T* (left hand side scale) and its derivative (right hand side scale) was plotted as a function of temperature. The inset of figure (b) show the T_{p1} and T_{p2} versus H plots.

For $Ti_{0.6}Mn_{0.4}Co_2O_4$ the χ(*T*) curves show ferrimagnetic behavior with a giant bifurcation (Δχ ~ 7.74×10^{-3} emu/g Oe) between the $\chi_{ZFC}(T)$ and $\chi_{FC}(T)$ due to very high magnetocrystalline anisotropy. The ferrimagnetic ordering is resulting due to the unequal/opposite magnetic moments of cations occupied at the tetrahedral *A* site [$\mu_{\downarrow}(Co^{2+})$] and the octahedral *B* site [$\mu_{\uparrow}(Mn^{3+}$, Ti^{3+} and $Co^{3+})$]. For this sample, both $\chi_{ZFC}(T)$ and $\chi_{FC}(T)$ exhibit peaks at 104.1 K ($T_{p\text{-}ZFC}$) and 60 K ($T_{p\text{-}FC}$), and drops to zero across 110.3 K. The critical temperature at which the magnetic moment of ferrimagnetic compound vanishes is called the ferrimagnetic ordering/Néel temperature (T_{FN}). However, we have determined the accurate value of the ordering temperature from the susceptibility derivatives based on the Fisher's relation which links the heat capacity and susceptibility derivative [168]. The insets of figures 4.10(a) and 4.11(a) show the temperature dependence of χ*T* (left hand side scale) and its derivative d(χ*T*)/d*T* (right hand side scale). Interestingly we noticed two peaks T_{P1} and T_{P2} in the d(χ*T*)/d*T* versus temperature plot. The negative minimum denoted by T_{P1} signifying the exact value of T_{FN} and the peak maximum T_{p2} corresponds to the peak temperature of ZFC curve. The inset of figures 4.10(b) and 4.11(b) depicts the variation of T_{p1} (T_{FN}) and T_{p2} as a function of applied field H_{dc} estimated from the d(χ*T*)/d*T*. These plots clearly show the increasing trend of T_{FN} (from 110.27 K to 115.3 K for H_{dc} = 500 Oe to 50 kOe, respectively) with an anomaly across 113 K (for H_{dc} = 20 kOe) for *x* = 0.4. Whereas, T_{p2} decreases drastically from 104 K to 64 K for H_{dc} = 0.5 and 20 kOe, respectively and increases thereafter to 67.21 K (for 50 kOe) indicating the loosely bound spins across T_{p2}.

It is interesting to note that $\chi_{ZFC}(T)$ exhibits negative values for all the temperatures below 96 K with a negative maximum (-2.32×10^{-3} emu/gOe) at 56.1 K, while the magnitude of χ_{FC} decreases significantly below $T_{p\text{-}FC}$ without any negative values. Such markedly different characteristics of $\chi_{FC}(T)$ and $\chi_{ZFC}(T)$ below their peak

values (at $T_{p\text{-}ZFC}$ and $T_{p\text{-}FC}$) are mainly due to the different temperature dependence of the magnetic moments associated with the cations occupying *A* and *B* sites. On the other hand, a remarkable change in the $\chi(T)$ behavior was observed for $Ti_{0.8}Mn_{0.2}Co_2O_4$. Magnetic compensation effect at 25.4 K (T_{COMP}), negative magnetization in χ_{FC} below T_{COMP} and drastic decrease in T_{FN} (82 K) from ($\chi-T$) plot are the noteworthy features observed in this compound (figure 4.11). It is well known that the magnetic compensation occurs in a system when the two sub-lattice magnetization balances each other [14]. Below the compensation point (T_{COMP}) an opposite trend was noticed between χ_{FC} (–ve values) and χ_{ZFC} (+ve values). However, a new field induced transition can be observed at 15 K in χ_{ZFC}. In the ($\chi-T$) plot both $\chi_{FC}(T)$ and $\chi_{ZFC}(T)$ exhibits a cusp like behavior with the peak positions at 72.1 ($T_{p\text{-}ZFC}$) and 64 K ($T_{p\text{-}FC}$) corresponding to the maximum susceptibility values $\chi_{Max}(T_{p\text{-}ZFC}) = 3.42\times10^{-3}$ emu/g Oe and $\chi_{Max}(T_{p\text{-}FC}) = 4.07\times10^{-3}$ emu/g Oe, respectively.

Nevertheless, at high fields both the compounds show the disappearance of the giant bifurcation between χ_{ZFC} and χ_{FC} with unusual broadening of peak temperature. On the other hand, the moments $\mu_{FI}(Co_A)$ and $\mu(T_B)$ obtained from the neutron experiments gradually decreases to zero in consonance with the $\chi_{dc}(T)$, however, we could not able to see any negative moment or any anomaly in temperature dependence of magnetic moments (figure 4.7(a)) across the compensation point. Such discrepancy is arising due to the fact that the neutron diffraction measurements were performed in zero-field, whereas the dc magnetization experiments were performed in the presence of externally applied magnetic field. Moreover, the present neutron diffraction results demonstrate the unequal change of the magnetic moments of the *A*- and *B*-site cations. Their different temperature dependence only plays a key role in realizing the magnetization reversal in the x = 0.2 composition.

4.3.5 Thermal variation of Specific-Heat:

In this section we discuss the temperature variation of the heat capacity under zero-field condition. Figure 4.12 shows the temperature dependence of the total specific heat $C_{P\text{-}Total}(T)$ for the $Ti_{0.6}Mn_{0.4}Co_2O_4$ polycrystalline sample. No sharp peak observed in C_P across T_{FN} and a clear drop in the magnitude of C_P/T at 109.1 K suggesting the entropy loss due to disordering of spins (probable a spin-glass-like state) just below the T_{FN}. In generally, the $C_{P\text{-}Total}(T)$ of a crystalline system is comprised of lattice [$C_{P\text{-}Lattice}(T)$] and magnetic [$C_{P\text{-}Magnetic}(T)$] contributions. More specifically, the contribution of $C_{P\text{-}Lattice}$ is a sum of both electronic $C_{P\text{-}electron}$ and phonon $C_{P\text{-}Phonon}$ parts. Since the electronic contribution is significant only at very low temperatures, the phonon contribution can be extracted from the following expression [214]:

$$C_{P\text{-}Phonon} = N f_D(\Theta_D/T) = 9 N R (T/\Theta_D)^3 \int_0^{\frac{\theta_D}{T}} \frac{x^4 e^x}{(e^x-1)^2} dx \qquad 4.1$$

In the above equation, the quantity $f_D(\Theta_D/T)$ represents Debye function, where N is the number of atoms per formula unit, R is the universal gas constant (8.314 J/mol K), and Θ_D is the Debye temperature. To evaluate the $C_{P\text{-}Phonon}$ contribution and Θ_D, we have fitted the experimentally obtained data of $C_{P\text{-}Total}$ to the equation (4.1) for $T >> T_{FN}$ where the effect of magnetic contribution is negligible [215]. The individual contributions from lattice [$C_{P\text{-}Lattice}(T)$] and magnetic [$C_{P\text{-}Magnetic}(T)$] specific heats after the fitting analysis are shown in Figure 4.12. Such fitting analysis yields Θ_D = 488.7 K for $Ti_{0.6}Mn_{0.4}Co_2O_4$ which is 72 K lower than the Θ_D value of $TiCo_2O_4$ [216]. For T < 47.8 K the contribution from $C_{P\text{-}Magnetic}$ starts dominating over $C_{P\text{-}Lattice}$ due to the freezing down of phonons and the reorientation of spins in preferred directions. It is interesting to note that $C_{P\text{-}Magnetic}$ remains constant (13 J/mol K) between 62 and 108 K. The absence of sharp peak in the $C_P(T)$ motivated us to perform the dynamic response of the magnetic susceptibility and its temperature and frequency dependent characteristics with the aim to probe the existence of spin-glass nature in the system.

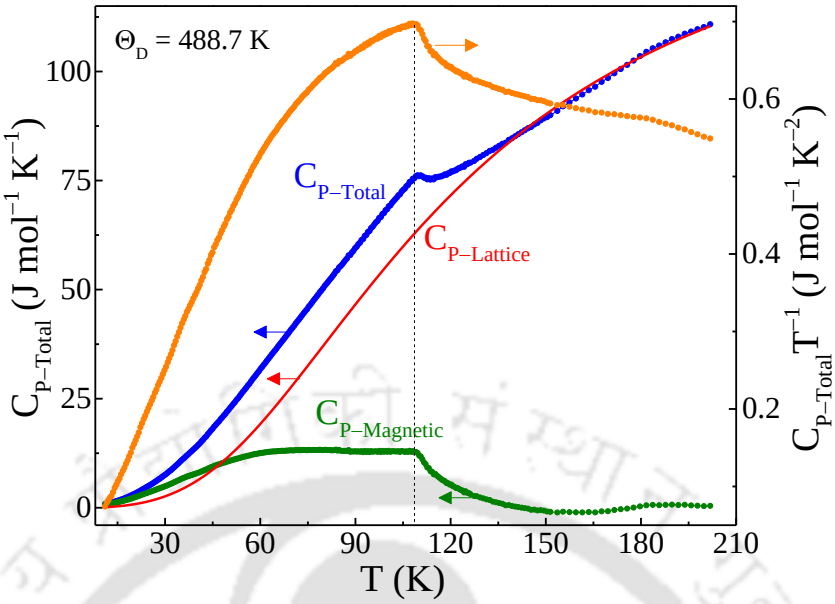

Figure 4.12. Temperature dependent total specific-heat $C_{P\text{-Total}}(T)$ (blue color circular symbols shown on L.H.S scale) of $Ti_{0.6}Mn_{0.4}Co_2O_4$ polycrystalline sample measured at $H_{dc} = 0$. The red color solid line represents the lattice contribution to total specific heat calculated from numerical fits using equation 4.1. Here the green solid circular symbols represent the magnetic contribution to the specific heat. The R.H.S scale shows the temperature dependence of $C_{P\text{-Total}}/T$ clearly showing the transition at 109.1 K.

4.3.6 ac-Magnetic Susceptibility:

This sub-section deals with the magnetization dynamics of $Ti_{0.8}Mn_{0.2}Co_2O_4$ and $Ti_{0.6}Mn_{0.4}Co_2O_4$. Figure 4.13 show the temperature dependence of real and imaginary components of the ac-magnetic susceptibility $\chi_{ac}(f,T) = \chi'(f,T) + i\,\chi''(f,T)$ recorded at constant driving frequency 51 Hz and peak-to-peak amplitude of the ac-magnetic field $h_{ac} \sim 4$ Oe for different dc-bias-fields ($0 \le H_{dc} \le 300$ Oe) superimposed with h_{ac}. Both the in-phase and out-of-phase susceptibility curves exhibit cusp like behavior with significant decrease in the peak position (T_P) and intensity as H_{dc} increases. For $x = 0.4$ (0.2), T_P shifts from 110.7 K (78.22 K) to 102.4 K (71 K) as H_{dc} increases from 0 to 300 Oe. The inset of figure 4.13(b) shows the variation of T_P as a function of $H_{dc}^{2/3}$ which shows a straight–line behavior consistent with the de Almeida-Thouless line (AT-line) [$H_{AT}(T_P) = A_{AT}\left(1 - \frac{T_P(H)}{T_P(0)}\right)^{\alpha}$] [217-219]. The AT-line criteria are often used in the literature to study the characteristic features of spin-glass ordering in amorphous magnets and magnetic ultrafine particles [219-221]. Here AT line defines the onset of a transition from the frozen spin-glass like state to reversible magnetic behavior at the peak temperature in $\chi_{ac}(f,T)$ under zero dc-field. The linear behavior of T_P versus $H_{dc}^{2/3}$ plot for low applied fields confirms the AT-like phase boundary where the linear extrapolation of AT-line on the temperature axis, in the limit H_{dc} approaches to zero yields the freezing temperature T_F. Hence, the above analysis gives the $T_F = T_P(0)$ value ~ 78.15 and 110.5 K for $x = 0.2$ and 0.4 sample, respectively. Such AT-line crossover in the *H-T* plane has been reported for a variety of spin-glass compounds such as CuMn, AgMn, AuFe, $Fe_xMn_{1-x}TiO_3$ etc [222,223,224,225]. However, determination of the freezing temperature using the AT-line criteria as a standard proof is not enough to probe the spin-glass behavior, instead empirical scaling laws are needed [24,226-228].

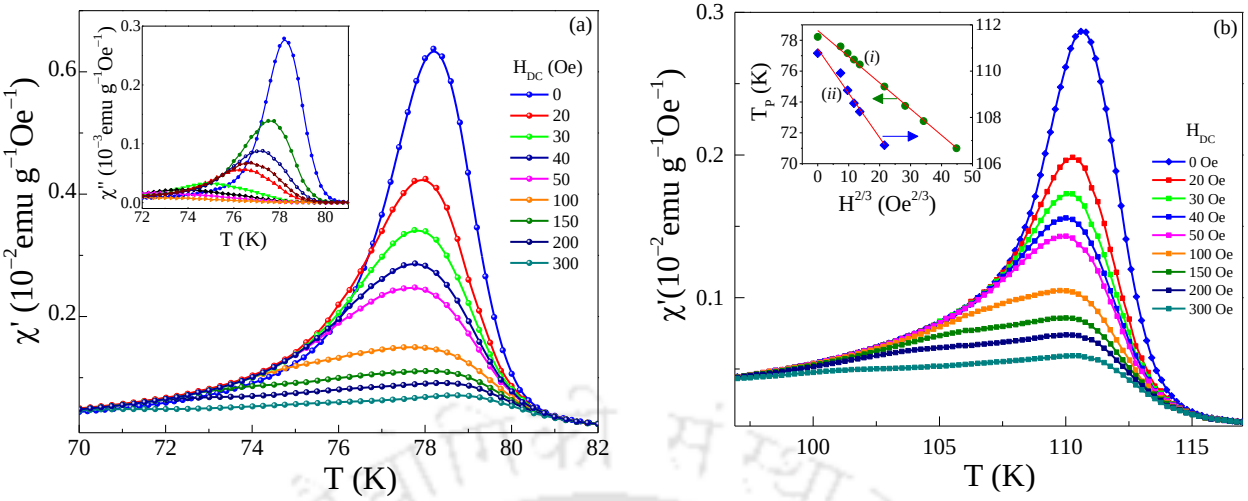

Figure 4.13. The temperature dependence of real χ′(*T*) and imaginary χ′′(*T*) components of ac-magnetic susceptibility $\chi_{ac}(T)$ of (a) $Ti_{0.8}Mn_{0.2}Co_2O_4$, and (b) $Ti_{0.6}Mn_{0.4}Co_2O_4$ recorded at various dc-magnetic fields ($0<H_{dc}<300$ Oe) with a constant ac-field of peak-to-peak amplitude h_{ac} ~ 4 Oe and frequency f ~ 51 Hz. The inset of figure (b) shows the variation of peak maximum temperature obtained from χ′′(*T*) plotted as a function of $H_{dc}^{2/3}$ for both the compositions (*i*) $Ti_{0.8}Mn_{0.2}Co_2O_4$, and (*ii*) $Ti_{0.6}Mn_{0.4}Co_2O_4$.

Therefore, in order to probe the existence of spin-glass nature in the current system we performed a detailed frequency (*f*) dependent study between f = 0.17 Hz and 1.2 kHz. Figure 4.14(a, c) and (b, d) shows the temperature variation of real (χ′) and imaginary (χ′′) component of ac-susceptibility χ_{ac} of $Ti_{0.8}Mn_{0.2}Co_2O_4$ and $Ti_{0.6}Mn_{0.4}Co_2O_4$. All the data were measured using the dynamic field of peak-to-peak amplitude h_{ac} = 4 Oe with zero-dc-bias field under the heating condition. One can clearly notice a shift in the maximum point of the cusp towards high temperature side with increasing the frequency for both the systems. Usually, such dispersion in the peak position signifies the spin-disorderness in the system. In order to confirm the existence of such spin-randomness (spin-glass nature) we used two empirical scaling laws: (*i*) the Vogel–Fulcher-law (VFL) $\tau = \tau_0 \exp(E_a/k_B(T_f - T_0))$ for interacting particle systems, and (*ii*) the Power-law (PL) $\tau = \tau_0[(T/T_F) - 1)^{-zv}]$ describing the critical slowing down [24,228]. In the above expressions, the parameter τ_0 represents the relaxation time constant, T_0 is a measure of the inter-particle interaction strength on magnetic relaxation, k_B is the Boltzmann constant, E_a is an activation energy parameter, zv is a critical exponent and T_F is the spin-glass freezing temperature. Figure 4.14(e) shows the logarithmic variation of the relaxation time (τ) as a function of $\ln (T - T_F)/T_F$. The scattered points represent the variation of the peak temperature (T_P) determined from χ′(*T*) for both the compositions. The solid continuous lines connecting the experimental data points represent the best fit to the PL. On the other hand, figure 4.14(f) shows the variation of $1/\ln(\tau/\tau_0)$ versus T_f related to the VFL described above. During the fitting procedure the τ_0 values obtained from the PL have been used to fit the experimental data points for VFL. In both the cases (VFL and PL) we obtained the straight line behavior with different fitting parameters which are listed in Table 4.3. Furthermore, we have reevaluated the magnitudes of zv from $\ln\left(\frac{40k_BT_0}{E_a}\right) \sim \frac{25}{zv}$ (relation between the VFL and PL,) which are in excellent agreement with the values determined from PL fitting parameters listed in Table 4.3 [218]. In general, typical spin-glass system exhibit 'τ_o' values between 10^{-9} and 10^{-16} s and the zv values between 4 and 12 [24,218]. Thus the τ_o and zv values signify that these compounds exhibit a spin-glass state just below the ferrimagnetic ordering which is often called as reentrant spin-glass state.

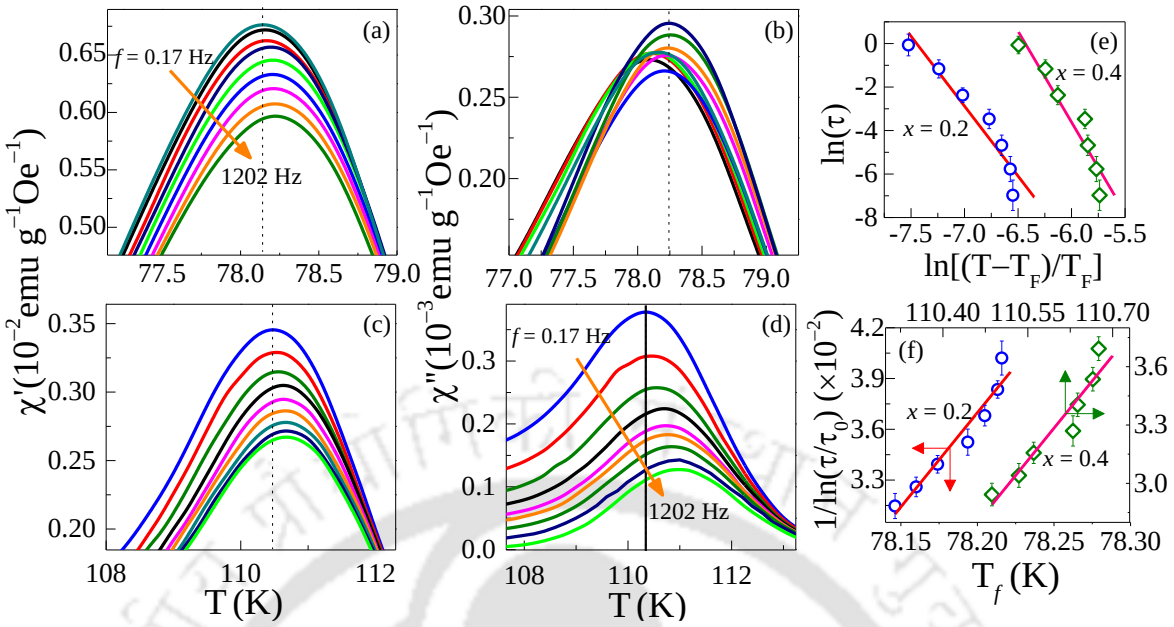

Figure 4.14. Magnified view of $\chi'(T)$ and $\chi''(T)$ measured at different frequencies (f) in the range 0.17 < f < 1202 Hz with h_{ac} = 4 Oe and H_{dc} = 0 Oe under warming condition for x = 0.2 (a and b) and x = 0.4 (c and d). The ln(τ) versus ln[$(T–T_F)/T_F$] (e), and 1/ln(τ/τ_0) versus T_f (f) corresponding to the Power-law (PL) and Vogel-Fulcher law (VFL), respectively for both the compounds. The solid-lines represent the best fits of VFL and PL to the experimental data obtained from χ′ for both the systems.

Table 4.3. The list of various fitting parameters obtained from straight line fitting of ac-susceptibility data using the Vogel-Fulcher law (VFL) and Power law (PL).

Sample	Parameters from PL	Parameters from VFL	zυ values from $\ln\left(\frac{40k_BT_0}{E_a}\right) \sim \frac{25}{z\upsilon}$	
$Ti_{0.8}Mn_{0.2}Co_2O_4$	$\tau_0 = 1.48\times10^{-14}$ s T_F = 78.1±0.02 K zυ = 4.22±0.01	$\tau_0 = 1.48\times10^{-14}$ s E_a = 10.3 k_B T_0 = 77.82±0.02 K	4.37	Using $\chi'(f,T)$
	$\tau_0 = 3.67\times10^{-15}$ s T_F = 78.03±0.02 K zυ = 4.6±0.02	$\tau_0 = 3.67\times10^{-15}$ s E_a = 20.82 k_B T_0 = 77.46±0.01 K	4.9	Using $\chi''(f,T)$
$Ti_{0.6}Mn_{0.4}Co_2O_4$	$\tau_0 = 1.6\times10^{-15}$ s T_F = 110.1±0.02 K zυ = 5.23±0.01	$\tau_0 = 1.6\times10^{-15}$ s E_a = 32.02 k_B T_0 = 109.56±0.02 K	5.18	Using $\chi'(f,T)$
	$\tau_0 = 3.48\times10^{-14}$ s T_F = 109.99±0.02 K zυ = 5.38±0.03	$\tau_0 = 3.48\times10^{-14}$ s E_a = 48.87 k_B T_0 = 108.82±0.02 K	5.94	Using $\chi''(f,T)$

4.3.7 Magnetic Hysteresis and Remanence Magnetization:

We now focus on the field dependence of magnetization at various temperatures measured under field cooled protocol. Figure 4.15 shows the magnetization versus field (*M-H*) hysteresis loops of $Ti_{0.6}Mn_{0.4}Co_2O_4$ and $Ti_{0.8}Mn_{0.2}Co_2O_4$ measured between −50 and +50 kOe at selected temperatures below T_{FN} after 50 kOe field cooling. The temperature of each sample was raised up to 300 K (>>T_{FN}) before each *M-H* measurement to ensure perfect paramagnetic state to avoid any remanence field in the samples. All the hysteresis loops are unsaturated even up to 50 kOe and the magnetization increases linearly with field. Also, the spontaneous magnetization per formula unit is slightly larger than the magnitude of magnetic moments determined from the neutron diffraction and the linear contribution represents the non-collinear arrangement of spins. The angle of the spins usually changes due to the torque exerted by the magnetic field, thus leading to a linear increase in the magnetization value with increasing the field within the magnetically ordered state. The magnitude of coercive (H_C) and exchange bias (H_{EB}) fields are estimated using the relations $H_C = (H^+ - H^-)/2$, and $H_{EB} = (H^+ + H^-)/2$, where the quantities H^+ and H^- are the magnetic field values at which magnetization becomes zero. The temperature variation of both H_C and H_{EB} are shown in figure 4.16 (*i*) and (*iii*) for the compositions x = 0.4 and 0.2, respectively. Both H_C and H_{EB} value decreases gradually as the temperature approaches T_{FN}. We also observed that a weak ferrimagnetic component M_{WFi} is essentially superimposed on a linear AFM component in the ordered state. No significant coercivity or remanence was noticed in the *M-H* loops for $Ti_{0.8}Mn_{0.2}Co_2O_4$ which were recorded below 5 K, but as the temperature increases loops open-up and exhibits significant H_C and M_R values for T > 5 K. The magnitude of H_C gradually increases with increasing the temperature (H_C ~ 0.98 kOe at 5 K) and reaches its maximum value of 9.4 kOe at 40 K and drops to 0.44 kOe at 70 K. While a crossover from H_{EB} = +3.7 kOe to −1.3 kOe was noticed in the H_{EB} values when the temperature increases from 5 to 25 K, respectively. behavior. For T > 25 K, the H_{EB} decreases and gradually approaches to zero as $T \rightarrow T_{FN}$. On the other hand, the hysteresis loops of $Ti_{0.6}Mn_{0.4}Co_2O_4$ exhibit giant coercive field H_C ~ 26.3 kOe which decreases gradually to 4.6 kOe at 60 K.

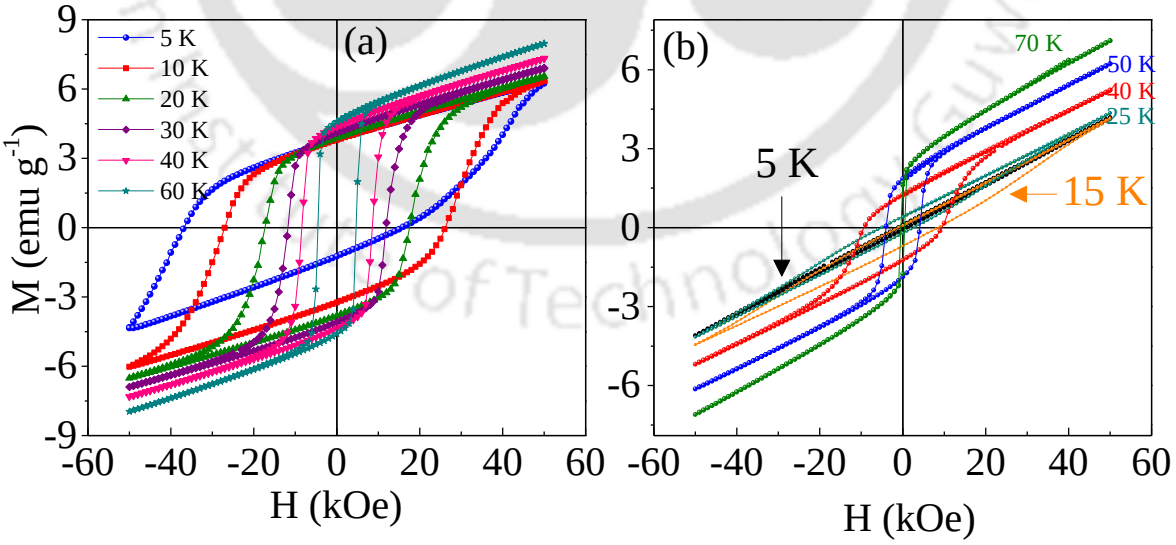

Figure 4.15. Magnetization versus field (*M-H*) hysteresis loops recorded at different temperatures after field cooling for (a) $Ti_{0.6}Mn_{0.4}Co_2O_4$, and (b) $Ti_{0.8}Mn_{0.2}Co_2O_4$.

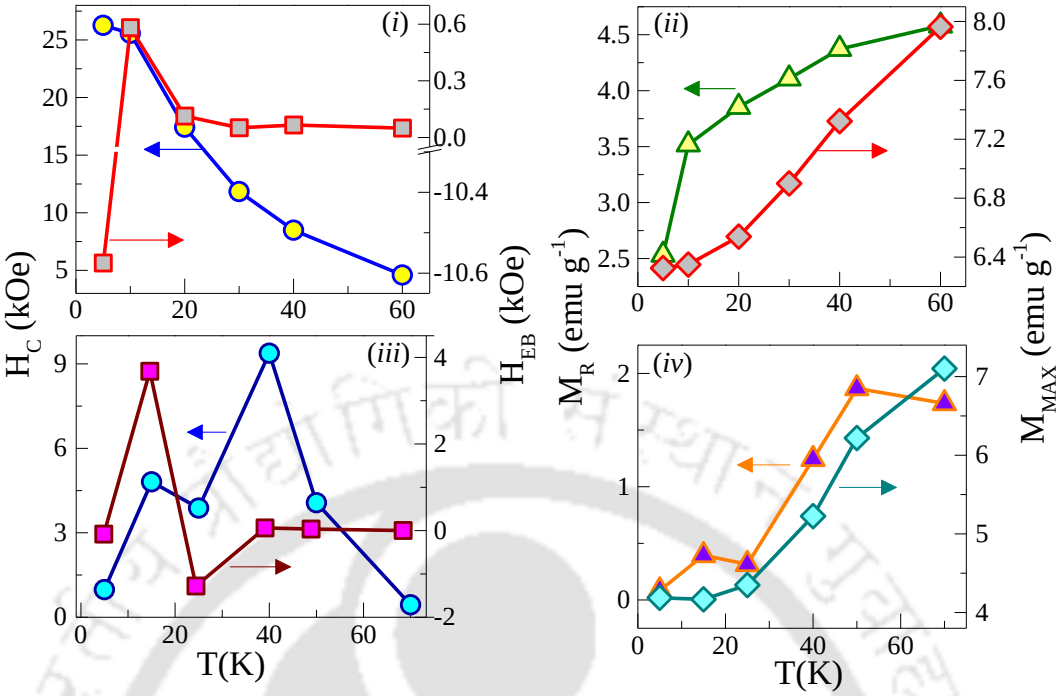

Figure 4.16. (*i*), (*iii*) Temperature dependence of coercive field H_C, and the exchange bias field H_{eb}. (*ii*), (*iv*) The remanence and high field magnetizations [M_R & M_{MAX}(at 50 kOe)] of $Ti_{0.6}Mn_{0.4}Co_2O_4$, and $Ti_{0.8}Mn_{0.2}Co_2O_4$ are also shown .

Such polarity change in the exchange bias is also associated with the negative magnetization. Whereas, the H_{EB} reaches its maximum value of −10.6 kOe at 5 K and the sign reversal of H_{EB} (~ +0.6 kOe at 10 K) was noticed when the temperature increases from 5 K to higher temperatures (H_{EB} reaches to zero as the temperature approaches 70 K). Similarly, we have evaluated the remanence magnetization M_R value at H = 0 Oe and the maximum magnetization M_{MAX} (at 50 kOe) for both the samples whose temperature dependence was shown in figures 4.16(*ii*) and (*iv*). Interestingly, both M_R and M_{MAX} increase progressively with the rise of temperature for both the compounds. The maximum M_R = 4.58 emu/g and 1.9 emu/g was observed for x = 0.4 and 0.2, respectively. A clear anomaly in $M_R(T)$ was noticed across 15 K for x = 0.2 which is consistent with the field induced transition noticed in $\chi_{ZFC}(T)$ (Figure 4.11(b)) and M_R decreases slightly across the T_{COMP} for this system.

4.4 Conclusions:

In this chapter we presented the results and analysis of crystal structure, electronic and magnetic properties of two different compositions of a *B*-site substituted $Mn_xTi_{1-x}Co_2O_4$ system by means of a detailed neutron diffraction, XPS, specific-heat, static and dynamic magnetization measurements. Based on the evidences gathered from the dc-magnetization data and ac-susceptibility we have specifically chosen two compositions x = 0.2 and 0.4 for a detailed neutron diffraction study because these two systems exhibit negative magnetization, magnetic compensation effect, reentrant spin-glass behavior and exchange-bias effect. The elemental analysis performed by XPS confirms the presence of trivalent state of all the octahedrally coordinated *B*-site cations [T_B = Ti($3d^1$), Mn($3d^4$) and Co($3d^6$)] and divalent electronic state of tetrahedrally coordinated *A*-site Co which are in-line with the neutron diffraction and magnetization data.

The refinements of the crystal structure in the space group $I4_1/amd$ provide the evidence of a weak tetragonal distortion with $c/a < 1$ for both the compositions. However, the refinements in the tetragonal structure give rise to weak changes of the apical and equatorial bond lengths. These changes are compatible with the trend which is expected for a Jahn-Teller activity of the Mn^{3+} ions having the $3d^4$ configuration. Our neutron diffraction study clearly shows the diffuse neutron scattering from (200) reflections which indicate the presence of canted local spin configuration (Yafet-Kittel like ordering) due to the transverse spin component at low-temperatures. Observation of the diffuse scattering and variation in canting angle with the Mn substitution are the most significant features of the current investigated system. Neutron diffraction studies also confirm the presence of strong ferrimagnetic coupling between the magnetic *A*- and *B*-site ions below T_{FN} = 110.3 K (for x = 0.4) and 78.2 K (for x = 0.2). Furthermore, an additional weak antiferromagnetic component was found lying perpendicular to the ferrimagnetic component. Although the moment directions of antiferromagnetic and ferrimagnetic components could not be determined, but it is possible to determine the spin sequence of the antiferromagnetic ordering in which the moments were assumed to be aligned parallel or perpendicular to the *c* axis. Thermal variation of the individual and net magnetic moments $2\mu_{FI}(T_B) - \mu_{FI}(Co_A)$, obtained from neutron diffraction agree with the $\chi_{dc}(T)$ data. However, the moments $\mu_{FI}(Co_A)$ and $\mu_{FI}(T_B)$ gradually decreases to zero in consonance with the $\chi_{dc}(T)$, but could not able to see any negative moment or any anomaly across the compensation point (~ 25.4 K for x = 0.2) which were observed in the $\chi_{dc}(T)$ data. This discrepancy is due to the fact that the neutron diffraction measurements were performed under zero-field case, whereas the dc magnetization experiments were performed in the presence of strong dc-field. The current neutron diffraction results demonstrate that the unequal growth of magnetic moments in the cations at tetrahedral *A* and octahedral *B* sites, and their different temperature dependence plays a significant role in realizing the magnetization reversal for all the compositions $x \leq 0.2$. Interestingly as compared to the parent compound $TiCo_2O_4$, $Ti_{0.6}Mn_{0.4}Co_2O_4$ sample exhibit giant H_C (~26 kOe), and negative H_{eb} (–10.6 kOe) at low temperatures which vanishes as the measuring temperature approaches towards T_{FN}.

From the $C_{P\text{-Total}}(T)$ we have evaluated the individual contributions of lattice and magnetic components. Accordingly, we have determined the Debye temperature Θ_D = 488.7 K (for $Ti_{0.6}Mn_{0.4}Co_2O_4$) which is significantly lower (by 72 K) than the Θ_D value of single crystal $TiCo_2O_4$. The frequency and temperature dependence of the dynamic-susceptibility $\chi_{ac}(f,T)$ data follows the AT-line criterion in *H*-*T* plane and empirical scaling laws (i.e. Vogel–Fulcher-law and Power-Law) for both the compositions x = 0.2 and 0.4 suggesting the spin-glass like ordering below T_F = 78.1 and 110.1 K with critical exponents $z\upsilon$ = 4.22 and 5.23, and relaxation time constant $\tau_0 = 1.48 \times 10^{-14}$ and 1.6×10^{-15} s.

Chapter 5

Neutron Diffraction Studies of Tetragonally Distorted $MnCo_{2-x}Cu_xO_4$

In continuation with the content of previous chapter, here we discuss the role of another Jan-Teller active ion (Cu^{2+}) on the structural and magnetic behavior of the inverse spinel $MnCo_2O_4$ using the neutron scattering technique. Main objective of this work is to probe the tetragonal distortion driven by the Jan-Teller effect when the Cu^{2+} replaces the octahedral Co^{2+} ions in the spinel lattice. Further, a detailed temperature dependence of ferromagnetic resonance (FMR) studies are instigated to understand the role of site anisotropy on the global magnetic behavior of the investigated system. The motivation and objectives of the present research work will be presented in the introductory section along with a detailed description of the gaps in literature on this system. The later sections present results and their discussion followed by the summary of important findings.

5.1 Brief Literature Review:

Tetragonally distorted ferrimagnetic spinel oxides are considered as the archetypal systems to study the low-temperature intriguing magnetic phenomena such as; geometrical frustration, Jahn-Teller distortion, magnetoelectric coupling, tunable exchange bias, reentrant spin-glass and negative magnetization including compensation phenomena [13,77,229-241]. Nonetheless, these oxides in the form of low-dimensional nanostructures have drawn immense attention recently because of their wide applications in renewable energy sector [196,242-244]. In particular, the inverse spinel $MnCo_2O_4$ has received widespread attention because of its diverse applications and novel magnetic properties [245-250]. The ferrimagnetic behavior in this compound arises due to the unequal moments of trivalent Mn and Co as well as divalent Co labelled by a formula unit $(Co^{2+})_A[Co^{3+}Mn^{3+}]_BO_4$ [251]. Earlier studies by Wickham and Croft reported long-range ordering in this compound with ordering temperatures as high as 191 K for $Mn_{1.2}Co_{1.8}O_4$, but, Blasse *et al.* reported slightly lesser ordering temperatures ~170 K for stoichiometric $MnCo_2O_4$ [251,252]. Recent studies reported enhanced multiferroic properties in the Bi and Y substituted $MnCo_2O_4$ ($Bi_xCo_{2-x}MnO_4$ ($0\leq x\leq 0.3$) and $Y_xCo_{2-x}MnO_4$ ($0\leq x\leq 0.2$)) in great detail [253,254]. Han *et al.* reported ferroelectricity at room temperature and enhanced ferrimagnetic ordering temperature (T_{FN} ~186 K) in Y substituted $MnCo_2O_4$ spinel [254]. Conversely, a significant decrease of T_{FN} (167 K and 165 K) and average magnetic moment (7.51 μ_B and 7.9 μ_B) has been observed in Cu and Zn substituted $MnCo_2O_4$ [157,255]. Moreover, these compounds under nanostructures exhibit spin-glass like characteristics with further reduction in T_{FN} (155 K and 157 K) [157,255]. It is important to note that a dedicated neutron diffraction study of $MnCo_2O_4$ based systems are rare in the literature [256,257]. Mandrus *et al*. first reported the neutron diffraction studies on $Co_2Ru_{1-x}Mn_xO_4$ system in which they reported two transitions at 100 K and 180 K providing the evidence for short-ranged correlations (≤100 Å) below the ferrimagnetic ordering temperature [257]. For moderate Ru^{3+} (S =1/2) content ($x\geq 0.5$), a mixture ground state of long-range ferrimagnetic order with the short-range order was reported, however, for lower Ru content the system exhibits long-range order [194]. For complete Mn dilution with Ru leads spin-glass like characteristics with spin freezing temperatures as low as 16 K [188]. Neutron diffraction study on Bi doped $MnCo_2O_4$ by Kaushik *et al.* revealed significant increase in the T_{FN} (200 K), Co-O bond length and relaxation in the CoO_6 polyhedra [256]. Except these two reports no other study is available in the literature focusing the neutron diffraction study on $MnCo_2O_4$ related systems. Therefore, motivated by the above results an attempt has been made here to fill all these gaps in the literature by performing a comprehensive study of neutron

diffraction experiments over a wide temperature range on $MnCo_{2-x}Cu_xO_4$ along with the temperature dependence of ferromagnetic resonance and dc-magnetization. These studies are primarily aimed to understand the crystal structure, magnetic ordering, and role of magnetocrystalline anisotropy in Cu substituted $MnCo_2O_4$ bulk system.

5.2 Experimental Details:

This section discusses the synthesis procedure and various characterization techniques employed to study the properties of $MnCo_{2-x}Cu_xO_4$ (x = 0 and 0.2) polycrystalline samples. All the samples were prepared by the solid-state reaction method using the binary transition metal oxides Co_3O_4, Mn_2O_3, and CuO as precursors. Appropriate amounts of these precursors were grounded in an agate mortar for 6 hours and pelletized using a hydraulic press with 50 kN pressure. These cylindrical pellets are finally sintered at 1200°C for 8 hours duration with 4 °C per minute heating and cooling rates. The structural characterization and phase purity of the sintered pallets was carried out by using Rigaku x-ray diffractometer (model: TRAX III) with Cu-K_α radiation (λ = 1.54056 Å) at room temperature. Neutron powder diffraction experiments on $MnCo_2O_4$ and $MnCo_{1.8}Cu_{0.2}O_4$ were carried out on the instruments E2, E6, and E9 at the BER II reactor of the Helmholtz-Zentrum Berlin. As statted in the previous chapter that the instrument E9 uses a Ge monochromator selecting the neutron wavelength λ = 1.3083 Å, while the instruments E2 and E6 use a pyrolytic graphite (PG) monochromator selecting the neutron wavelengths λ = 2.379 Å and λ = 2.423 Å, respectively. On these instruments powder patterns were recorded between the following diffraction angles: between 14.7 and 90.2° (E2), 5.5 and 136.6° (E6), and 5 and 141.8° (E9). The instrument E9 was used to investigate the crystal structure parameters of both $MnCo_2O_4$ and $MnCo_{1.8}Cu_{0.2}O_4$ from data sets collected at 2 and 295 K, respectively. In order to investigate a detailed magnetic structure neutron powder diffraction patterns were collected at T = 1.7 K on the instrument E2 with high counting statistics (24 h/pattern) using a 15-min collimation to improve the instrumental resolution. For comparison a second powder pattern was recorded at 200 K for both the compositions $MnCo_2O_4$ and $MnCo_{1.8}Cu_{0.2}O_4$. A detailed temperature dependence of the neutron powder diffraction was investigated on the instrument E6 for the samples. The refinements of crystal and magnetic structures were carried out with the *FullProf* program [206]. The nuclear scattering lengths b(O) = 5.805 fm, b(Mn) = −3.73 fm, b(Co) = 2.50 fm, and b(Cu) = 7.718 fm were used [207]. The magnetic form factors of the Mn^{3+}, Co^{2+} and Co^{3+} ions were taken from Ref. [208]. In the following sections we discuss our experimental results and analysis.

5.3 Results and Discussions:

5.3.1 Crystal Structural Analysis from E9:

Figure 5.1 shows the neutron powder diffraction pattern of $MnCo_2O_4$ and $MnCo_{1.8}Cu_{0.2}O_4$ collected on the instrument E9 at 295 (a, c) and 2 K (b, d) plotted along with the Rietveld refinement data. The calculated patterns (shown in red color line) are compared with the observed data (black open circles). In the lower part of each figure the difference pattern (blue line) as well as the positions of the nuclear (N) and magnetic (M) reflections of are shown. In the patterns collected at 2 K additional magnetic intensities are observed, where the strongest magnetic contribution is observed at the positions of the reflections (101) and (200)/(112) (see also Figure 5.2). In an earlier study it was shown that the inverse spinel $TiCo_2O_4$ was found to crystallize in the cubic space group *Fd-3m* (No. 227), while the Mn containing compounds $Ti_{0.8}Mn_{0.2}Co_2O_4$ and $Ti_{0.6}Mn_{0.4}Co_2O_4$ crystallize in the tetragonal space group $I4_1/amd$ (No. 141, cell choice 2) with the cell dimensions $a_t \times b_t \times c_t = a_c/\sqrt{2} \times b_c/\sqrt{2} \times c_c$ [14,258]. In this work it is found that the refinements of neutron diffraction patterns of

$MnCo_2O_4$ and $MnCo_{1.8}Cu_{0.2}O_4$ could also been performed in the lower symmetric space group $I4_1/amd$. For the copper containing sample $MnCo_{1.8}Cu_{0.2}O_4$ the Cu^{2+} ions are expected also to be located at the *A*-site, since the ionic radii of Co^{2+} (r = 0.58 Å) and Cu^{2+} (r = 0.57 Å) are practically the same [259]. In all these compounds the Co^{2+} (and Cu^{2+}) ions occupy the tetrahedral *A* site (labelled as Co_A and Cu_A), are located at the Wyckoff position 4*b*(0,¼,⅜), while at the *B*-site cations Mn^{3+} and Co^{3+} ions (labelled as Mn_B and Co_B) are positioned at 8*c*(0,0,0). Whereas the oxygen atoms occupy the position 16*h*(0,*y*,*z*), where *y* and *z* approximately have the values ~ 0.5 and ~ 0.25, respectively. The results of the Rietveld refinements of these two compounds are given in Table 5.1. The present samples contain some minor amounts of Co_3O_4 and CoO which were additionally formed during the preparation stage and their strongest reflections are marked with an asterisk in figure 5.1. This lead to a reduction of the Co content in the prepared spinels and the crystal structure refinement yields the chemical compositions: $(Co^{2+})_A[Mn_{1.148(7)}{}^{3+}Co_{0.852(7)}{}^{3+}]_BO_4$ and $(Co^{2+}Cu^{2+})_A[Mn_{1.171(6)}{}^{3+}Co_{0.829(10)}{}^{3+}]_BO_4$.

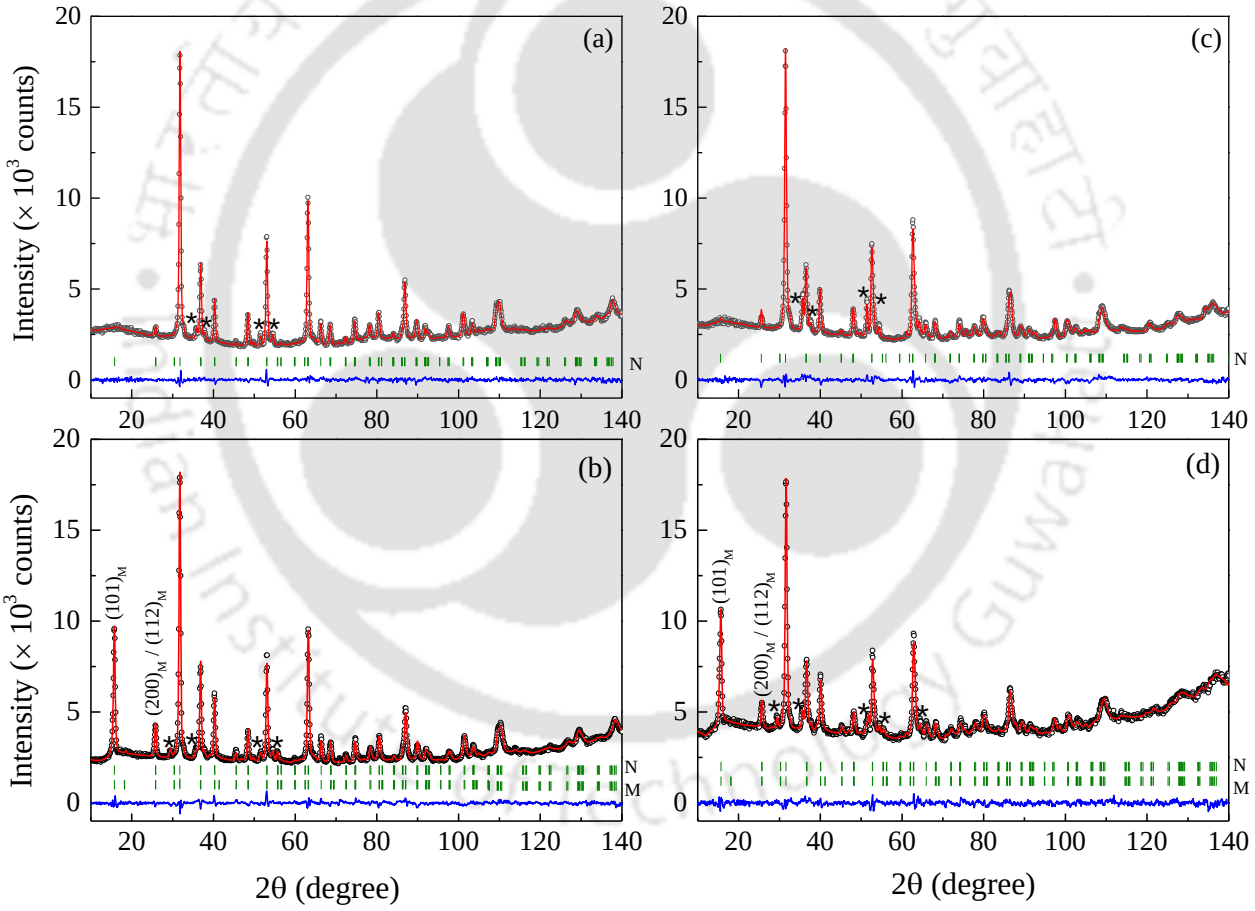

Figure 5.1. The neutron powder diffraction pattern and the corresponding Rietveld refinement data of $MnCo_2O_4$ and $MnCo_{1.8}Cu_{0.2}O_4$ collected on E9 at 295 K (a and c) and 2 K (b and d). The crystal structure was refined in the tetragonal space group $I4_1/amd$. The calculated patterns (red line) are compared with the observed measured patterns (black open circles). In the lower part of each diagram the difference pattern (blue line) as well as the positions of the nuclear (N) and magnetic (M) reflections are shown. A strongest magnetic contribution is observed for the reflections (101) and (200)/(112) (see also figure 5.2). The strongest nuclear and magnetic reflections of CoO and Co_3O_4 are marked with an asterisk.

Table 5.1. Results of the Rietveld refinements of the neutron powder diffraction data of $MnCo_2O_4$ and $MnCo_{1.8}Cu_{0.2}O_4$ collected on the instrument E9 at 2 and 295 K. The refinements were carried out in the tetragonal space group $I4_1/amd$. The given residuals are defined as $R_F = \sum||F_{obs}| - |F_{calc}||/\sum|F_{obs}|$. Listed are the positional parameters *y* and *z* of the O atom located at the site 16*h*(0,*y*,*z*) and the occupancies of the Mn_B and Co_B atoms at the site 8*c*(0,0,0). Further the bond distances in the T_BO_6 octahedra (T_B = Mn_B and Co_B), and the T_AO_4 tetrahedra (T_A = Co_B and Cu_B) as well as the lattice parameters are also given.

	$MnCo_2O_4$		$MnCo_{1.8}Cu_{0.2}O_4$	
T [K]	2	295	2	295
occ(Mn_B)	1.125(6)	1.145(7)	1.180(9)	1.173(7)
occ(Co_B)	0.875(6)	0.852(7)	0.820(9)	0.829(6)
y(O)	0.5271(4)	0.5244(5)	0.5261(7)	0.5245(8)
z(O)	0.2408(5)	0.2383(5)	0.2423(8)	0.2399(9)
a_t [Å]	5.8610(6)	5.8794(4)	5.8973(7)	5.9059(7)
c_t [Å]	8.2695(14)	8.2930(12)	8.3152(19)	8.3331(18)
$c_t/a_t\sqrt{2}$	0.9977(3)	0.9974(2)	0.9970(4)	0.9977(3)
V [Å^3]	284.07(7)	286.66(6)	289.19(10)	290.66(9)
$d_{ab}(T_B\text{-O}) \times 4$	1.964(2)	1.982(2)	1.980(3)	1.990(3)
$d_c(T_B\text{-O}) \times 2$	1.998(4)	1.981(4)	2.021(7)	2.004(7)
$d(Co_A\text{-O}) \times 4$	1.967(3)	1.972(3)	1.967(5)	1.974(6)
R_F	0.042	0.036	0.043	0.043

It is interesting to see that the cell volume of $MnCo_{1.8}Cu_{0.2}O_4$ is somewhat larger than that of $MnCo_2O_4$. This effect may not be simply ascribed to the Cu doping at the *A*-site, since the ionic radius of Cu^{2+} ($r \sim 0.58$ Å) is only slightly larger than that of Co^{2+} ($r \sim 0.57$ Å) [259]. Therefore, the bond lengths in the T_AO_4 tetrahedra are practically the same as given in Table 5.1. On the other hand, since the ionic radius of Mn^{3+} ($r \sim 0.645$ Å) at the *B*-site is larger than that of Co^{3+} [$r \sim 0.61$ Å (high-spin), $r \sim 0.545$ Å (low-spin)] one can expect increase in the cell volume as Co^{3+} is replace by Mn^{3+}. However, in $MnCo_{1.8}Cu_{0.2}O_4$, the Mn content is slightly larger than in $MnCo_2O_4$, which may not be enough to cause a significant increase of the cell volume. This trend could be found for other systems such as $Ti_{0.8}Mn_{0.2}Co_2O_4$ and $Ti_{0.6}Mn_{0.4}Co_2O_4$, where the larger ionic size of Ti^{3+} ($r \sim 0.67$ Å) leads to a slight increase in the cell volume [14]. However, in Table 5.1 it can be seen that the bond lengths in the T_BO_6 octahedra are significantly enlarged for the Cu containing compound. Therefore, the cause of the increase of the cell volume of $MnCo_{1.8}Cu_{0.2}O_4$ should be explained by other physical effects. For the Co^{2+} ions at the *A*-site, which have the $3d^7$ configuration, cooperative distortions of the CoO_4 tetrahedra through the Jahn-Teller effect are absent. On the other hand, the Jahn-Teller active Cu^{2+} ions at the *A*-sites, having the $3d^9$ electronic configuration, should lead to a decrease of the *c*/*a* ratio, similar to situation strongly established in the normal spinel $CuCr_2O_4$ [80]. But our study showed that a Cu doping of 20 atomic % does not significantly

change the c/a ratio from room temperature down to 3 K (Table 5.1). At this point it has to be noted that the strong tetragonal distortion in $CuCr_2O_4$ sets in concomitantly with the spontaneous onset of an orbital ordering and a structural phase transition is observed from cubic to tetragonal [80]. This may exclude the presence of charge ordering in $MnCo_{1.8}Cu_{0.2}O_4$. The T_BO_6 octahedra contain the Jahn-Teller active ions (T_B) Mn^{3+} and Co^{3+}, having the $3d^4$ and $3d^6$ configurations, respectively. For the Co^{3+} ions electronic energy can be gained if the $2t_g$ levels split into a lower d_{xy} level and a higher twofold generate d_{xz}/d_{yz} level. This would result in a tetragonal distortion with a c/a ratio smaller than 1, and also a shrinking of the apical bond $d_c(T\text{-O})$. However, it is important to note that the tetragonal distortion in $TiCo_2O_4$ is not able detected due to weak Jahn-Teller activity of the Ti^{3+} and Co^{3+} ions in this system [14]. On the other hand, previous studies on $Ti_{0.8}Mn_{0.2}Co_2O_4$ and $Ti_{0.6}Mn_{0.4}Co_2O_4$ showed that a replacement of Ti^{3+} ions at the B site by Mn^{3+} ions lead to a weak tetragonal splitting [258]. The same trend we observe for the current systems $MnCo_2O_4$ and $MnCo_{1.8}Cu_{0.2}O_4$, where the Co^{3+} ions at the B site are replaced by Mn^{3+} ions. Thus, it is possible that the Jahn-Teller effect of the different T_B^{3+} ions at the B site act along different directions as found earlier in the system $Ni_{1-x}Cu_xCr_2O_4$ and leads to a compensation of individual distortions [80].

The crystal structure refinements of $MnCo_2O_4$ and $MnCo_{1.8}Cu_{0.2}O_4$ showed that the apical bond length $d_c(T_B\text{-O})$ is slightly longer than the equatorial one $d_{ab}(T_B\text{-O})$. Similar kind of distortions observed in $Ti_{0.8}Mn_{0.2}Co_2O_4$ and $Ti_{0.6}Mn_{0.4}Co_2O_4$ [258]. It is worth to mention that the distortion of the T_BO_6 octahedron is even stronger in higher Mn content sample ($Ti_{0.6}Mn_{0.4}Co_2O_4$). Therefore, we can assume that the elongation of the apical bond $d_c(T\text{-O})$ can be ascribed to the Jahn-Teller activity of the Mn^{3+} ions having the $3d^4$ configuration. In this case electronic energy can be gained if the e_g level splits into a $d_{x^2-y^2}$ and a d_{z^2} level, where the fourth electron occupies the lower lying d_{z^2} level. This electronic configuration finally leads to an elongation of the T_BO_6 octahedra along the c axis.

5.3.2 Magnetic ordering using E2 and E6:

This subsection discusses the magnetic structure and ordering parameters of $MnCo_2O_4$ and $MnCo_{1.8}Cu_{0.2}O_4$ by analysing the E2 and E6 neutron powder diffraction patterns collected at below and above the magnetic ordering temperature T_{FN}. Figure 5.2 depicts the diffraction patterns collected at 2 and 200 K. The powder patterns collected at 2 K show the additional strongest magnetic intensities at the position of the (101) reflection indicating a ferrimagnetic (FIM) coupling between the atoms located at the A and B sites of both compounds. A much weaker magnetic intensity could be observed at the position of the reflection pair (110)/(002). Therefore, the two magnetic reflections are shown in the inset of Figure 5.2 in an enlarged view using a logarithmic scale. Both the reflection (110) and (002) are forbidden for the tetragonal space group $I4_1/amd$. Thus the presence of the magnetic intensity suggests the loss of a least one of the d-glide planes which indicate the presence of an additional antiferromagnetic (AFM) component. Due to the weak tetragonal splitting we were not able to distinguish the magnetic contribution of the individual reflections (110) and (002). Therefore, in the present case it is not possible to determine the directions of the AFM and FIM components. However, it is possible to determine the spin sequence of the B-site atoms (Co_B, and Mn_B) at the positions (0,0,0), (1/2,0,1/2), (1/4,3/4,1/4), (1/4,1/4,3/4). For this we assumed an AFM ordering within the ab plane and a FIM ordering along c axis which is referred as Model-I. FIM ordering within the ab plane and an AFM ordering along the c axis denoted as Model-II.

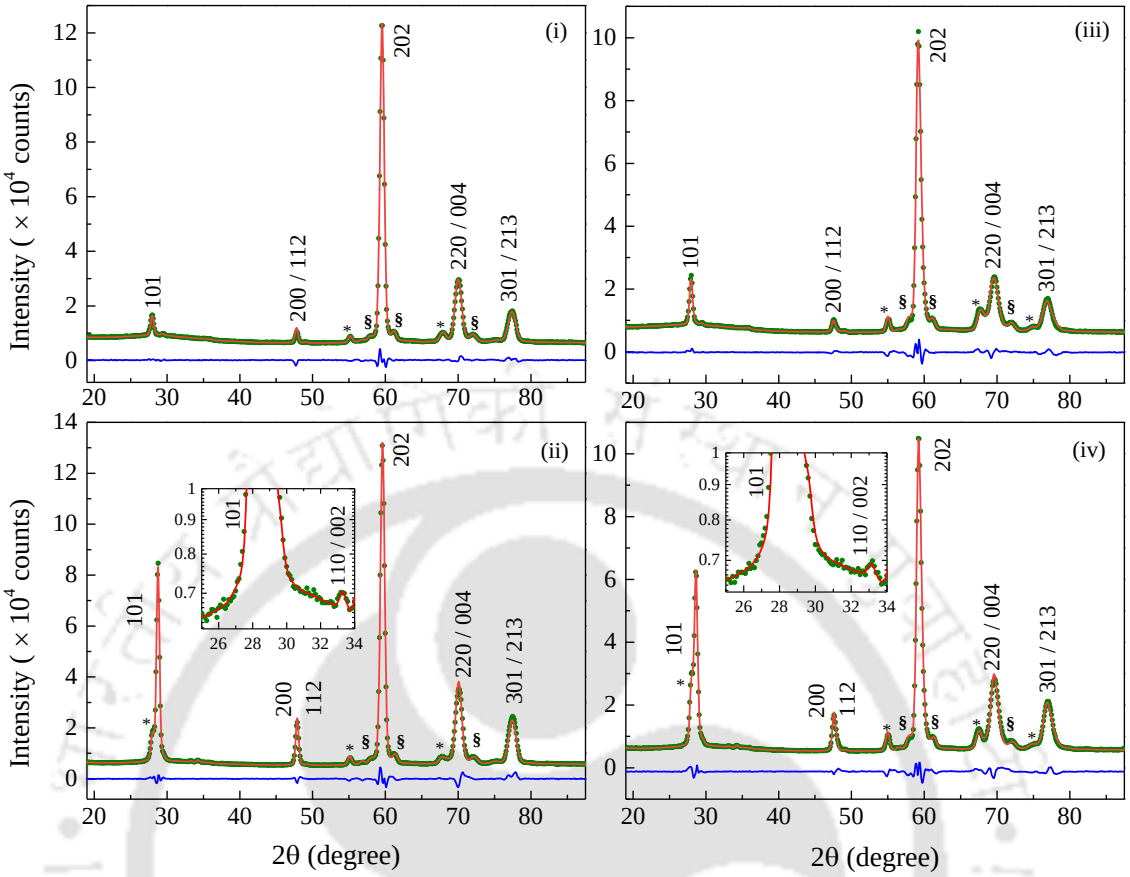

Figure 5.2. Neutron powder diffraction patterns of $MnCo_2O_4$ and $MnCo_{1.8}Cu_{0.2}O_4$ collected on the instrument E2 at 200 K (i and iii) and 2 K (ii and iv). The powder patterns in the lower part of the diagram show additional magnetic intensities due to the magnetic ordering of the Mn, Co (and Cu) atoms. The insets present prominent magnetic reflections $(101)_M$ and $(110)_M$ in enlarged form. Due to the weak intensity of the reflection pair $(110)/(002)_M$ we used a logarithmic scale. The calculated (red line) and observed patterns (black open circles) as well as the difference patterns (blue line) are shown. The positions of strongest reflections of the impurities CoO and Co_3O_4 are marked with the symbols ***** and **§**, respectively.

The magnetic structure is refined several times with the possible spin sequences: + + + +, + – + –, + + – –, and + – – + for the *B*-site cations in which we assumed the possible combination of Model-I and Model-II. However, with the individual spin sequence + – + – (Model-I) and + + – – (Model-II) no magnetic intensity is generated at the position of the reflection pair (110)/(002). On the other hand, for the spin sequence + – – +, the refinements generate correct magnetic intensity at the position of the reflection pair (110)/(002). Yet, the calculated magnetic intensity of the reflection (101) is too weak. Finally, the correct magnetic intensities are generated with the both spin sequences + + – – and + – + –.

A very similar behavior was found for $Ti_{0.8}Mn_{0.2}Co_2O_4$ and $Ti_{0.6}Mn_{0.4}Co_2O_4$, where titanium was replaced by manganese. The observed antiferromagnetic moments of the *B* site in the Ti containing spinels vary between 0.56-0.62 μ_B [258]. Such coexistence of an AF and FI ordering was also observed earlier in the $Ni_{1-x}Cu_xCr_2O_4$ system [80], where the FI ordering occurs in the *ab* plane and the AF component is aligned parallel to the *c* axis. In this system the antiferromagnetic component is much pronounced.

Table 5.2 presents the individual site moments calculated from the diffraction patterns collected at 1.7 and 1.9 K on E2 and E6, respectively. Both magnetic Mn^{3+} and Co^{3+} ions at the *B*-site in the $3d^4$ and $3d^6$ configurations have four unpaired electrons in the high-spin state. Therefore, for both ions the expected theoretical value of the high-spin state is $\mu_{eff} = g\,S\,\mu_B = 4.0\ \mu_B$. Here it is interesting to note that the magnetic moment of Co^{3+} at the *B*-site in Co_3O_4 was found to be zero, which can be explained by a large crystal-field splitting of the 3*d* orbitals by the octahedral cubic field [84]. The same behaviour was expected for the system $Mn_xCo_{3-x}O_4$, where the Mn^{3+} ions of $MnCo_2O_4$ reach moment values of 3.99 μ_B and 3.84 μ_B/Mn^{3+} [193,257]. Assuming that Co^{3+} carries the same moment as Mn^{3+} the averaged moments would be 1.99 and 1.92 μ_B/B^{3+} ion which are considerably smaller than the theoretical values given above. Further it is interesting to see that Mn_3O_4 reaches a moment value 3.55 μ_B/Mn^{3+} which is somewhat smaller than those obtained for $MnCo_2O_4$ given above [260]. This cannot confirm that the moment of Co^{3+} is exactly equal to zero, but shows that the moment of Co^{3+} should be strongly reduced. On the other hand, for $TiCo_2O_4$ an averaged moment of about 1.8 μ_B/B^{3+} ion was found [14], where Ti^{3+} and Co^{3+} occupy the *B*-site. This considerably smaller than the theoretical moment. Using the constraint $\mu(Co^{3+}) = 4 \times \mu(Ti^{3+})$ one obtains the individual moments 2.94 μ_B/Co^{3+} and 0.74 μ_B/Ti^{3+} [14]. The obtained moment of Ti^{3+} is in good agreement with 0.715 μ_B/Ti^{3+} found earlier for $YTiO_3$ [261]. Therefore, in the present case it is expected that Co^{3+} may carries finite magnetic moment and contributes to the overall magnetic ordering of the compounds $Ti_{0.8}Mn_{0.2}Co_2O_4$ and $Ti_{0.6}Mn_{0.4}Co_2O_4$ [257].

Table 5.2. Magnetic moments of the transition metal atoms in $MnCo_2O_4$ and $MnCo_{1.8}Cu_{0.2}O_4$ obtained from Rietveld refinements using neutron diffraction data collected on the instruments E2 and E6, respectively. The magnetic Co^{3+} and Mn^{3+} ions (*B* site) in the space group *Fd-3m* are located at the positions: (1) 0,0,0; (2) ¾,¼,½; (3) ¼,½,¾; (4) ½,¾,¼. The Co^{2+} ions (*A* site) are located at (1) ⅜,⅜,⅜; (2) ⅛,⅝,⅛. Shown are the results, where the moment $\mu(Co_B)$ was set equal to zero (upper part of the Table), and where the constraint $\mu(Mn_B) = \mu(Co_B)$ was used (below). The moment $\mu_{AF}(Mn_B)$, determined from the E2 data, was taken for the refinement of the E6 data and was not allowed to vary. The resulting ferromagnetic moments $\mu_{FI}(B) - \mu_{tot}(A)$ are also listed [$\mu_{FI}(A) = \mu_{FI}(Co_A/Cu_A)$]. These are compared with the spontaneous magnetizations *M* measured at 5 K.

Magnetic moment	$Mn_{1.173}Co_{1.827}O_4$ E2, at 1.7 K	$Mn_{1.173}Co_{1.827}O_4$ E6, at 1.9 K	$Mn_{1.173}Co_{1.827}O_4$ Ref.[193]	$Mn_{1.173}Co_{1.827}O_4$ Ref.[193]	$Mn_{1.145}Co_{1.855}Cu_{0.2}O_4$ E2, at 1.7 K	$Mn_{1.145}Co_{1.855}Cu_{0.2}O_4$ E6, at 1.9 K
$\mu_{FI}(Co_A/Cu_A)$ [μ_B]	3.04(3)	3.11(3)	3.09	3.03(5)	2.25(4)	2.35(3)
$\mu_{FI}(Mn_B)$ [μ_B]	3.51(5)	3.40(6)	3.72	3.77(8)	3.64(5)	3.70(6)
$\mu_{AF}(Mn_B)$ [μ_B]	0.55(8)	0.55	-	-	0.55(8)	0.55
$\mu_{tot}(Mn_B)$ [μ_B]	3.56(6)	3.45(6)	-	-	3.68(6)	3.74(6)
$\mu_{FI}(Co_B/Mn_B)$ [μ_B]	2.06(3)	2.00(4)	2.18	2.31(4)	2.09(3)	2.00(4)
$\mu_{AF}(Co_B/Mn_B)$ [μ_B]	0.33(6)	0.33	-	-	0.33(6)	0.33
$\mu_{tot}(Co_B/Mn_B)$ [μ_B]	2.09(3)	2.02(3)	-	-	2.11(3)	2.14(3)
$\mu_{FI}(B)$ [μ_B]	4.38(5)	3.99(7)	4.36	4.43(9)	4.17(5)	3.99(7)
R_M / R_F	0.027 / 0.0116	0.048 / 0.0127	-	-	0.0387 / 0.0261	0.0208 / 0.0120
$\mu_{FI}(B)/\mu_{FI}(A)$ [μ_B]	1.08(8)	0.88(10)	1.27	1.39(14)	1.92(9)	1.89(10)
M [μ_B]	0.89 -1.13	0.89 -1.13	1.13(5)	1.09	0.97 - 1.21	0.97 - 1.21

The magnitude of average magnetic moments obtained from the magnetic structure refinements are listed in Table 5.2. These results infer that the total moments of the Mn^{3+}/Co^{3+} ions lie between 2.29 and 2.36 μ_B/B ($MnCo_2O_4$) and 2.13 and 2.34 μ_B/B ($MnCo_{1.8}Cu_{0.2}O_4$). In the present study it has been found that $MnCo_2O_4$ contains more manganese than cobalt on the *B* site having the correct formula $(Co^{2+})_A[Mn_{1.15}{}^{3+}Co_{0.86}{}^{3+}]_BO_4$. Using the values of the system $Mn_xCo_{3-x}O_4$, given in Ref. [193], one expects the enlarged moment values 4.40 μ_B/B). This value is somewhat larger than 4.00 and 4.27 μ_B/B which have been determined in the present study. Accordingly, for sample $(Co^{2+}Cu^{2+})_A[Mn_{1.17}{}^{3+}Co_{0.83}{}^{3+}]_BO_4$ the values 3.76 and 4.07 μ_B/B have been obtained. At this point it has to be noted that the antiferromagnetic component of the *B* atoms was not observed in earlier studies [257,193]. Therefore, the total moment of the *B* site is slightly larger as given in table 5.2.

The magnetic moment of the Co^{2+} ion at the *A* site reaches in $MnCo_2O_4$ the values 2.94 and 3.00 μ_B, which are in a very good agreement with 3.08 μ_B given in Ref. [193]. The experimental moments practically reach the theoretical value $\mu_{eff} = g\,S\,\mu_B = 3.0\,\mu_B$ of the high-spin state of Co^{2+} ion which has three unpaired electrons in the $3d^7$ configuration. In contrast, for $MnCo_{1.8}Cu_{0.2}O_4$ the moment values of the *A* site vary between 2.31 and 2.46 μ_B which are somewhat smaller than those observed for $MnCo_2O_4$. This result can be ascribed due to the fact that 20 atomic % of the Co^{2+} ions at the *A* site are replaced by Cu^{2+} ions. In the $3d^9$ configuration these ions only have one unpaired electron giving the expected theoretical value in the high-spin state $\mu_{eff}(Cu^{2+}) = g\,S\,\mu_B = 1.0\,\mu_B$. Therefore, one obtains the theoretical moment $\mu_{eff}(Co^{2+}/Cu^{2+}) = g\,S\,\mu_B = 2.6\,\mu_B$. At this point it has to be mentioned that the total moments of the ions at the *A* site can differ, especially due to the presence of spin-orbital coupling. Nevertheless, we have tried to estimate the individual moment values at the *A* site using the constraint $\mu(Co^{2+}) = 3 \times \mu(Cu^{2+})$. By means of the experimental moments which vary between 2.31 and 2.46 μ_B the individual moments are estimated to differ as follows: between 2.49 and 2.74 μ_B for Co^{2+}, between 0.83 and 0.91 μ_B for Cu^{2+}, respectively.

For both the compounds $MnCo_2O_4$ and $MnCo_{1.8}Cu_{0.2}O_4$ the thermal variation of the magnetic moments located at the *A* and *B* sites are shown in figure 5.3 which show a FIM coupling. Due to the different moment values at the *A* and *B* sites one obtains a resulting ferrimagnetic component which is defined as $2\mu_{FI}(T_B) - \mu_{FI}(T_A)$ (T_A = Co_A and Cu_A, T_B = Mn_B and Co_B). For both the *A* and *B* sites the averaged moment values as well as the different moment values are plotted in figure 5.3.

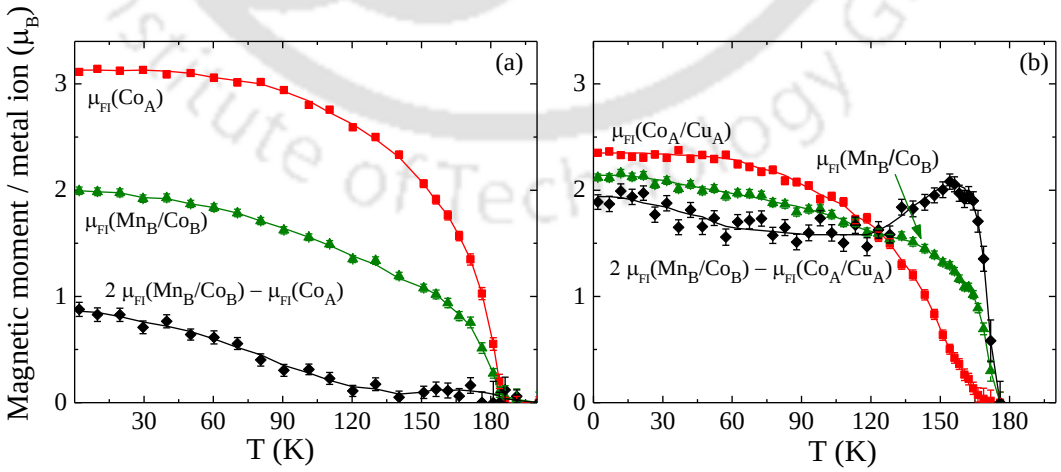

Figure 5.3. The temperature dependence of the experimentally obtained magnetic moments of the ions in (a) $MnCo_2O_4$ and (b) $MnCo_{1.8}Cu_{0.2}O_4$ located at the *A* and *B* sites. The *A* site is only occupied with Co^{2+} (and Cu^{2+}) ions [labelled as Co_A (and Cu_A)], while the *B* site contains Mn^{3+}, and Co^{3+} (labelled as Mn_B and Co_B). Thermal variation of the difference moment ($2\mu_{FI}(Co_B/Mn_B) - \mu_{FI}(Co_A/Cu_A)$) of the two ferrimagnetically ordered sublattices is also shown. The bold lines are guide for visualization.

In order to probe the contribution of magnetocrystalline anisotropy of the investigated samples we performed the ferromagnetic resonance (FMR) absorption spectra at different temperatures. Figure 5.4(a,c) shows the FMR absorption spectra of $MnCo_2O_4$ and $MnCo_{1.8}Cu_{0.2}O_4$ polycrystalline samples recorded at different temperatures using the X-band frequency 9.8 GHz. Using these plots we have calculated the absorption intensity of each spectrum. The temperature dependence of absorption intensity is shown in figure 5.4(b, d). It is interesting to see that there is a close resemblance between the temperature dependence of FMR intensity and the temperature dependence of magnetic susceptibility $\chi(T)$ shown in the inset of figure 5.4(b) and (d). The FMR intensity drops to zero across the ferrimagnetic Néel temperature T_{FN} (~184 K and 171.8 K) for both the samples. Due to large magneto-crystalline anisotropy (150-0.8 J/m^3) of these systems we noticed significant drop in the FMR intensity at temperatures below T_{FN} [250]. Since the FMR field is within multi-domain range the signal is weak. These FMR studies reveal that the sample $MnCo_{1.8}Cu_{0.2}O_4$ shows significantly high magneto-crystalline anisotropy as compared to the undoped case due to the substitution of Jahn-Tell active Cu^{2+} ion at tetrahedral sites.

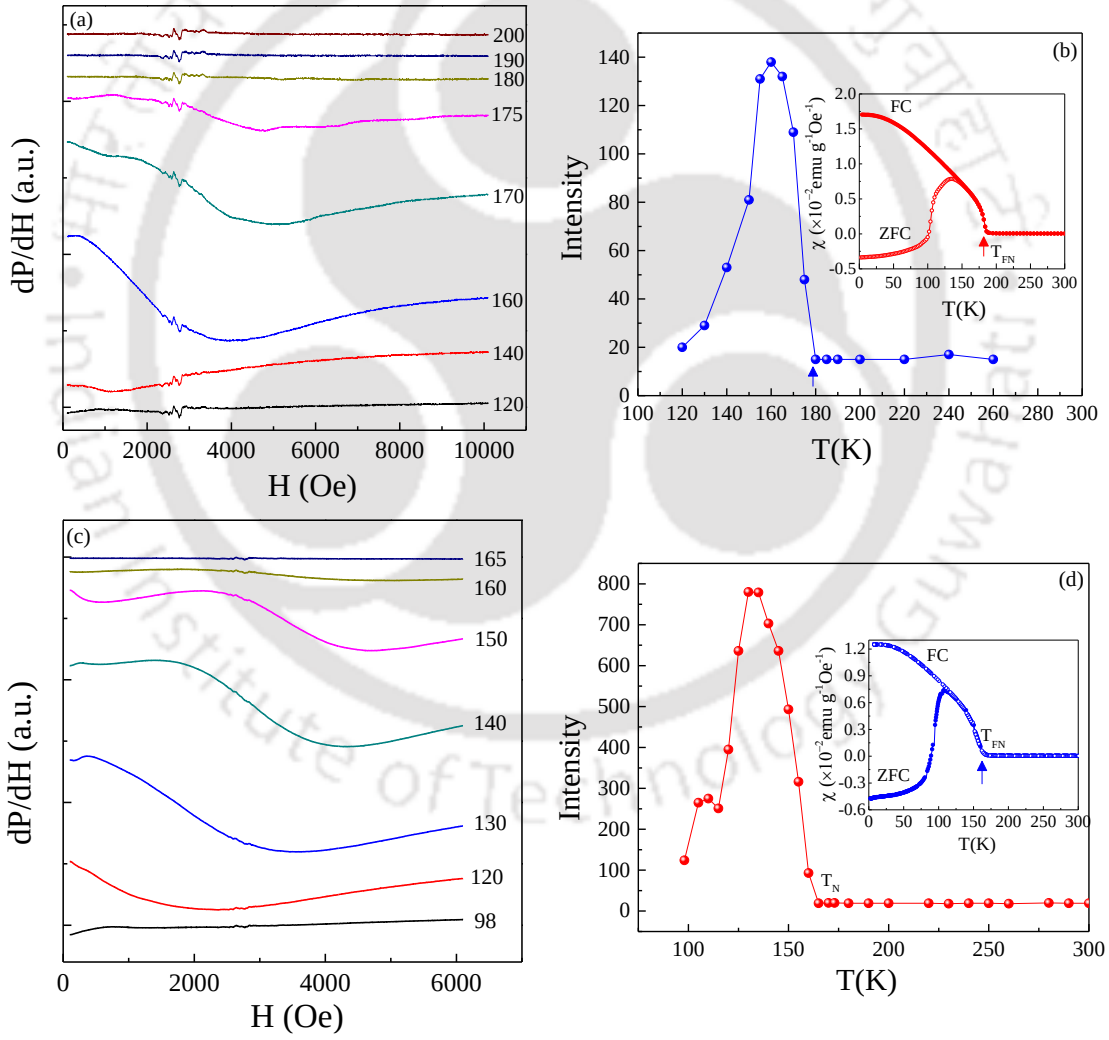

Figure 5.4. The FMR spectra of (a) $MnCo_2O_4$ and (c) $MnCo_{1.8}Cu_{0.2}O_4$ polycrystalline samples measured at different temperatures at 9.8 GHz excitation frequency. (b) and (d) show the temperature dependence of the FMR integrated intensity for $MnCo_2O_4$ and $MnCo_{1.8}Cu_{0.2}O_4$, respectively. Insets of (b, d) show the $\chi(T)$ of $MnCo_2O_4$ and $MnCo_{1.8}Cu_{0.2}O_4$ measured under ZFC and FC conditions in the presence of external dc-magnetic field of 1000 Oe. The arrow marks represent the ferrimagnetic ordering temperature T_{FN}.

5.4 Conclusions:

In this chapter we studied the crystal structure and magnetic properties of polycrystalline inverse spinels $MnCo_{2-x}Cu_xO_4$ (x = 0 and 0.2) using neutron diffraction. The crystal structure of these compounds at 2 K were refined in the tetragonal space group $I4_1/amd$ in which the Co_A and Cu_A are located at the Wyckoff position 4*b*(0,1/4,3/8), while the *B* site cations Mn^{3+} and Co^{3+} ions are positioned at 8*c*(0,0,0). Our results demonstrate that both the compounds exhibit weak tetragonal distortion with a c/a ratio smaller than 1 due to the presence of Jahn-Teller active ion Mn^{3+} in the T_BO_6 octahedra. The nuclear (N) and magnetic (M) reflections provide evidence that the strongest magnetic contribution arises from (101) and (200)/(112) coherent Bragg reflections with spin sequences $++--$ and $+-+-$ below T_{FN}. Analysis of these results provide the evidence for weak tetragonal distortion with $c/a < 1$. Here both the systems exhibit ferrimagnetic ordering below 184 K and 171.8 K with net moment $2\mu_{FI}(Mn_B/Co_B) - \mu_{FI}(Co_A)$ = 0.89 μ_B and 1.93 μ_B for x = 0 and 0.2, respectively at 2 K. Nonetheless, the temperature dependence of net ferrimagnetic moment $\Delta\mu_{FI}(T)$ exhibit maximum (2.081 μ_B) at 154.1 K for x = 0.2, whereas, the undoped system does not exhibit any cusp in $\Delta\mu_{FI}(T)$. The presence of additional magnetic reflections (110) and (002) in both the compositions suggests the loss of a least one of the *d*-glide planes signifies the existence of additional antiferromagnetic component lying perpendicular to the ferrimagnetic component. On the other hand, the temperature dependence of ferro-magnetic-resonance spectra reveals high magneto-crystalline anisotropy in Cu substituted system as compared to the undoped case.

Chapter 6

Nanostructures of Cu and Zn Diluted $MnCo_2O_4$: Focus on relaxation Dynamics and Exchange Interactions

In this chapter we focus on the growth and characterization of Cu and Zn diluted $MnCo_2O_4$ under low dimensional nanostructures. A detailed formation mechanism, morphology and magnetic properties of these nanostructures will be discussed. Our primary aim is to understand the role of finite-size/surface effects on the magnetic exchange interactions and probe the relaxation dynamics in these nanostructures. In the introductory section we present necessary background including their applications and gaps in the literature. The following sections present the experimental details focusing on the growth, formation mechanism, microstructure and various other characterization methods employed in this study. In the later sections we discuss the results and summarize the important results.

6.1 Introduction:

The low-dimensional nanostructures of $MnCo_2O_4$ and its composites have gained special attention over other 2D transition metal oxides because of their unique electrochemical performance and supercapacitor applications [157,199,250,262,263]. Also, these compounds are very useful in renewable/sustainable energy sector such as in fuel-cells, batteries and catalysis [71-75,163,183,245,264-266]. From the fundamental point of view, this system exhibits weak tetragonal distortion in the form of bulk and thin films [267,268]. However, such distortion is expected to relax when surface and finite size effects play a dominant role on the physical properties of $MnCo_2O_4$ [268]. On the other hand, the magnetic properties of the base compound $Mn_xCo_{3-x}O_4$ polycrystals ($0 \le x \le 2$) was first reported by Wickham and Croft [251]. These authors reported ferromagnetic ordering with highest Curie temperature T_C = 191 K for x = 1.2 and proposed the configurations $Co^{2+}[Co^{3+}_{2-x}Mn_x^{3+}]O_4$ and $Co^{2+}_{3-x}Mn^{2+}_{x-2}[Mn_2^{3+}]O_4$ for $0 \le x \le 2$ and $2 \le x \le 3$, respectively [251]. Later, Blasse reported the ferromagnetic behavior of $MnCo_2O_4$ system with $T_C \sim 170$ K and Curie constant $C_M \sim 5.73$ [252] which are contrary to the ferrimagnetic ordering proposed by Lotgering [269]. In 1992, Tamura reported the pressure dependence of magnetic permeability studies for polycrystalline $MnCo_2O_4$ [248]. For $T < T_C$ (= 185 K), the temperature dependence of relative magnetic permeability $\mu_r(T)$ exhibits a peak at T_H = 175 K due to the Hopkinson-effect in which both T_C and T_H decreases linearly with pressure from 0 to 1.71 GPa [248, 270]. Joy and Date reported that $MnCo_2O_4$ exhibits unusual magnetic hysteresis behavior below 130 K in which the virgin magnetization curve at higher fields lies outside the main hysteresis loop [249]. For bulk $MnCo_2O_4$, these authors further reported T_C = 184.5 K obtained using both dM/dT versus T method and linear extrapolation of the magnetization to the x-axis; This is consistent with the $T_C \sim 185$ K reported by Tamura and others who also reported that T_C is highly sensitive to the external pressure and oxygen stoichiometry [248,249, 271].

In contrast to the bulk $MnCo_2O_4$ system, the reported results on the magnetic behavior of $MnCo_2O_4$ nanostructures is quite limited [250,271-273]. Borges *et al.* reported the reduced T_C values (174.8 K) in 50 nm spherical nanoparticles of $MnCo_2O_4$ synthesized using Pechini method employing a polymeric precursor [273]. These authors also reported significant variation in the lattice parameter from 8.162 Å to 8.307 Å on changing the particle size from 6.2 nm to 204 nm [273]. Bazuev *et al.* reported the magnetic behavior of spinel $MnCo_2O_{4+\delta}$ (δ = 0.275 and 0.62) fabricated by thermal decomposition of binary oxalates $Mn_{1/3}Co_{2/3}C_2O_4 \cdot 2H_2O$ in air at 220 and 500˚C [271]. For δ = 0.275 the differential magnetic susceptibility plot ($d\chi/dT$ versus T) exhibits a minimum

across 167.5 K less than the T_C ~ 183 K for stoichiometric spinel $MnCo_2O_4$ [271]. These authors also reported that for T > 230 K, $\chi(T)$ of $MnCo_2O_{4.275}$ obeys the Curie-Weiss law ($\chi = C/(T - \theta)$), with C = 4.07 emu-K/mole-Oe and Weiss temperature θ = 329.5 K . On the other hand, Thota *et al.* reported reduced T_C (176 K) and spin-glass like properties across 165 K together with the memory and relaxation effects in $MnCo_2O_4$ nanocrystallites of average size 28 nm [272]. Such exciting phenomena of ferrimagnetic state to spin-glass and vice-versa occurs mainly due to the collapse of the long-range order by competing magnetic interactions instead of thermal excitations [274-277]. It has been shown in the literature that the T_C values may vary markedly depending upon the oxygen stoichiometry δ in $MnCo_2O_{4\pm\delta}$ [271-273].

Our main motivation in substituting Cu and Zn in $MnCo_2O_4$ is to probe the changes occurring in the tetragonal symmetry of the inverse spinel and study the lift in orbital degeneracy caused by the incorporation of Cu ions which has completely different electron configuration than Co. Generally, in tetrahedral crystal field, the d orbitals split into e_g and t_{2g} levels having lower and higher energies, respectively. The $Cu^{2+}(3d^9)$ ions provide an odd number of electrons to the e_g and t_{2g} levels and may cause the lattice distortion. Such distortion may elongate the lattice along the c axis, the t_{2g} levels may further split into a d_{xy} lower and two doubly degenerate levels (d_{xz} and d_{yz}) with higher energy [77,278]. Thus, the Cu substitution at the tetrahedral sites may invoke a constructive approach to probe the discontinuity in the fourfold symmetry by partially filling the doubly degenerate levels. Also, when a spinel hosts more than one Jahn-Teller active cation, it undergoes several symmetry breaking structural distortions (e.g. Cr- and V-Spinels) including the breakdown of degeneracy in spin configurations, popularly known as spin-Jahn-Teller transformations which occur at the magnetic ordering temperature [77,275,279]. Due to the above fundamental reasons, we undertook the investigations of the effect of Cu substitution at the tetrahedral sites on the electronic and magnetic properties of $MnCo_2O_4$ system. While Zn is substituted both at tetrahedral and octahedral sites of $MnCo_2O_4$ to understand the role of dilution on the overall magnetic ordering and exchange interactions.

6.2 Experimental details:

For the synthesis of nanocrystallites, viz; $MnCo_{2-x}Cu_xO_4$, $MnCo_{2-x}Zn_xO_4$ and $Mn_{1-x}Zn_xCo_2O_4$, we employed the sol–gel process. For the Cu substituted samples manganese acetate tetrahydrate $[Mn(CH_3COO)_2{\cdot}4H_2O]$, cobalt acetate tetrahydrate $[Co(CH_3COO)_2{\cdot}4H_2O]$ and copper acetate hydrate $[Cu(CO_2CH_3)_2{\cdot}nH_2O]$ are used as precursors. Whereas, the Zn-substituted samples were prepared using the same precursors along with zinc-acetate dihydrate $[ZnC_4H_6O_4.2H_2O]$. According to the chosen sample composition appropriate amounts of the acetate salts were dissolved in the ethanol in a Pyrex beaker under constant stirring. Dropwise addition of the oxalic acid to the above prepared solution leads to the formation of thick gel which was dried between 80°C and 120°C to obtain pink color powder. On the basis of Thermogravimetric analysis we calcined this ovendried product at 700°C for 4 h in air to obtain the desired phase. The phase purity and the crystal structure information of these nano-composites were studied from the X-ray powder diffraction measured using a Rigaku X-ray diffractometer (model: TRAX III) with Cu-K_α radiation (λ = 1.54056 Å). The morphology of the particles was examined using a transmission electron microscope (TEM, JEOL JEM 2100) operating at 200 KeV. Elemental analysis of the investigated system was probed by a dual source X-ray photoelectron spectroscope of Al-Kα and Mg-Kα sources of energies 1486.8 eV and 1253.6 eV, respectively from VG Microtech equipped with ultra-high vacuum (8×10^{-10} Torr) chamber. Detailed low-temperature dc- and ac-magnetization measurements were performed using a SQUID based magnetometer (MPMS) from Quantum Design.

6.3 Results and Discussion:

6.3.1 Crystal structure and Morphology:

This sub-section describes the structural analysis and morphology of the site diluted $MnCo_2O_4$ Nano-compositions. The XRD pattern recorded at room temperature and their Rietveld refinement analysis confirms the spinel cubic phase (*Fd-3m* (227) space group) for all nanoparticles of $MnCo_{2-x}Cu_xO_4$, $Mn_{1-x}Zn_xCoO_4$, and $MnCo_{2-y}Zn_yO_4$ ($0 \le x, y \le 0.2$) without any secondary phases. Based on the XRD analysis we have chosen three different compositions ($MnCo_{1.8}Cu_{0.2}O_4$, $Mn_{0.8}Zn_{0.2}Co_2O_4$ and $MnCo_{1.9}Zn_{0.1}O_4$) for detailed magnetic properties. From the Rietveld refinements we determine the lattice parameter a_o for $MnCo_{2-x}Cu_xO_4$ ($0 \le x \le 0.2$) nanoparticles which varies between 8.25 ± 0.004 and 8.215 ± 0.003 Å as the Cu concentration increases from 0 to 20 at.%. Whereas, the refinements yield a_o = 8.233 and 8.270 Å for $Mn_{0.8}Zn_{0.2}Co_2O_4$ and $MnCo_{1.9}Zn_{0.1}O_4$ nanoparticles respectively. Figures 6.1 and 6.2 show bright field TEM images of Cu and Zn-doped $MnCo_2O_4$ nanoparticles, respectively. These micrographs clearly show the formation of mixed morphology of both spherical and hexagonal-shaped particles with sharp edges. The corresponding selected area electron diffraction (SAED) patterns are shown in figures 6.1 (b, d) and 6.2 (c, d) which matches well with the standard spinel cubic phase of $MnCo_2O_4$. Figures 6.1 (e) and 6.2 (e, f) displays the high-resolution-transmission electron microscope (HRTEM) image which provides the uniform lattice spacing of 2.47 and 2.5 Å which is consistent with the inter-planar spacing d_{hkl} corresponding to (311) lattice planes of the XRD analysis for $MnCo_{1.8}Cu_{0.2}O_4$, $Mn_{0.8}Zn_{0.2}Co_2O_4$ sample, respectively. Using the 'ImageJ' software we performed histogram analysis to determine the size-distribution of the nanocrystals (figure 6.1 (f) and 6.2 (g,h)) [280,281]. Accordingly, the size distribution is fitted with the log-normal distribution function: $f(D) = \frac{1}{D\lambda_D\sqrt{2\pi}} exp\left\{-\frac{[\ln(D/D_o)]^2}{2\lambda_D{}^2}\right\}$, where D_o corresponds the median crystallite diameter, λ_D is the width of the distribution with average size $\langle D \rangle = D_o \exp(\lambda_D^2/2)$ and the standard deviation $\sigma = \langle D \rangle [\exp(\lambda_D^2) - 1)]^{1/2}$. In the histogram the solid lines represent the log-normal fitting which yielding <D> = 25, 31 and 60 nm for $MnCo_{1.8}Cu_{0.2}O_4$, $Mn_{0.8}Zn_{0.2}Co_2O_4$ and $MnCo_{1.9}Zn_{0.1}O_4$ nanocrystallites, respectively.

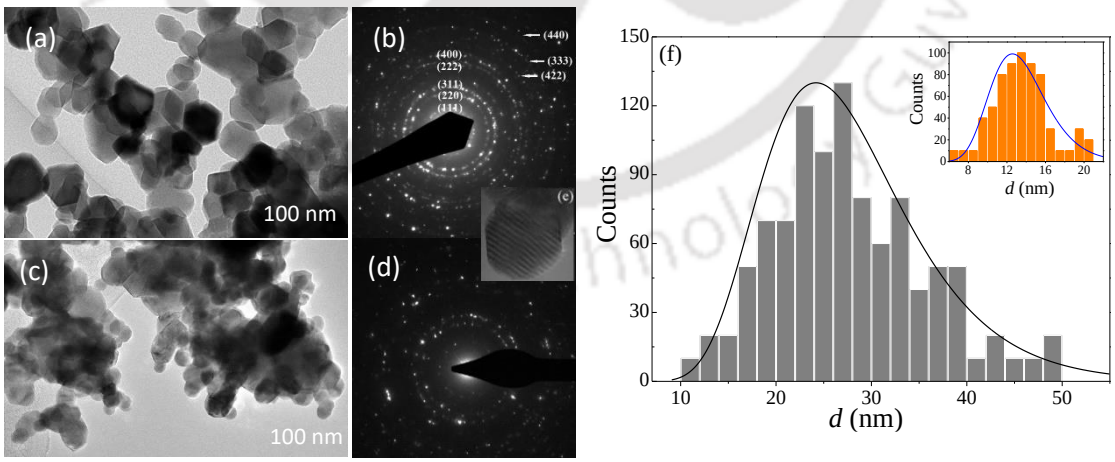

Figure 6.1. The transmission-electron micrographs (TEM) of (a) undoped $MnCo_2O_4$ and (c) $MnCo_{1.8}Cu_{0.2}O_4$ nanocrystallites, respectively. Figures (b) and (d) shows their corresponding SAED pattern. Figure (e) shows the corresponding high-resolution-transmission electron microscope image of $MnCo_2O_4$. Figure (f) presents the histogram analysis for nanocrystalline $MnCo_{2-x}Cu_xO_4$ (x = 0) and x = 0.20 (inset figure). The solid lines represent the best fits to the log-normal size distribution.

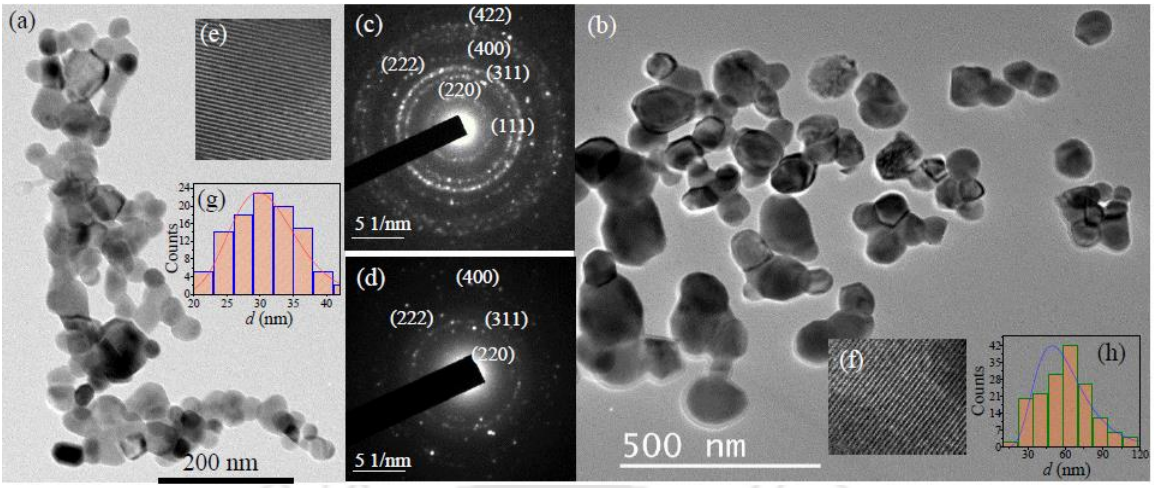

Figure 6.2. The TEM micrographs of (a) $MnCo_{1.9}Zn_{0.1}O_4$ and (b) $Mn_{0.8}Zn_{0.2}Co_2O_4$ nanocrystallites. The corresponding selected area electron diffraction patterns are shown in (c) and (d). Figures (e) and (f) show the high resolution TEM images for $MnCo_{1.9}Zn_{0.1}O_4$ and $Mn_{0.8}Zn_{0.2}Co_2O_4$, respectively. Figures (g) and (h) show the corresponding histogram analysis for the individual samples fitted with log-normal size distribution.

6.3.2 Local Atomic Environment using XPS:

Figure 6.3 show the high-resolution narrow-scan core level X-ray photoelectron spectra of $MnCo_2O_4$, $MnCo_{1.8}Cu_{0.2}O_4$ samples, respectively. Here all the spectra were calibrated using the binding energy of carbon C-1*s* orbitals centered at E_C = 284 eV. For $MnCo_2O_4$, the XPS spectra of Co-2*p* de-convoluted into four major peaks identified as doublets of Co(II) and Co(III), and three broad satellite peaks (Figure 6.3 (a)). The binding energy separation (ΔE) between the doublets [$\Delta E_{Co3+}(2p_{1/2}–2p_{3/2})$ and $\Delta E_{Co2+}(2p_{1/2}–2p_{3/2})$] are 15.34 eV and 15.8 eV, respectively, clearly suggesting the two different oxidation states of Co i.e. Co^{3+} and Co^{2+} [156,282]. However, the Co-2*p* spectrum for the $MnCo_{1.8}Cu_{0.2}O_4$ sample exhibits an additional peak at 770.9 eV due to the multiple splitting effect caused by Cu doping (figure 6.3 (b)) [203,283-285]. Also, we observed significant increase in the binding energy separation between the doublets of $\Delta E_{Co3+}(2p_{1/2}–2p_{3/2})$ = 15.60 eV and $\Delta E_{Co2+}(2p_{1/2}–2p_{3/2})$] = 16.37 eV. On the other hand, the Mn-2*p* XPS spectra (Figure 6.3 (c)) exhibit doublet: Mn-$2p_{3/2}$ (~ 641.48 eV) and Mn-$2p_{1/2}$ (~ 652.69 eV), with spin-orbit splitting ΔE = 11.21 eV providing the signature of trivalent oxidation state of Mn. For the $MnCo_{1.8}Cu_{0.2}O_4$ sample, the Mn-2*p* spectra (Figure 6.3 (d)) resolved into two peaks Mn-$2p_{3/2}$ (~ 641.96 eV) and Mn-$2p_{1/2}$ (~ 649.47 eV) without any satellite peaks confirming the presence of Mn^{3+}. The binding energy separation of Mn^{3+} doublets ($2p_{3/2}$ and $2p_{1/2}$) in $MnCo_{1.8}Cu_{0.2}O_4$ sample significantly decreases to ~ 7.51 eV as compared to the $MnCo_2O_4$; this decrease is due to the incorporation of Cu atoms. Moreover, the Cu-2*p* XPS spectrum contains spin-orbit doublet Cu-$2p_{3/2}$ (at 934.33) and Cu-$2p_{1/2}$ (954.07) along with prominent satellite peaks positioned at 942.52 eV and 962.48 eV (Figure 6.3 (g)). Earlier XPS studies of many Cu based compounds have suggested that the presence of shake-up satellite peaks in Cu-2*p* spectra are the characteristics of the divalent nature of Cu [286-293]. In the present case for $MnCo_{1.8}Cu_{0.2}O_4$, the Cu-2*p* XPS spectrum is fitted with a minimum of five Gaussian (60%) - Lorentzian (40%) peaks to reproduce the experimentally observed Cu-2*p* spectra. These Gaussian doublets are separated by ΔE ~ 19.7 eV in their binding energy scale, which confirms the presence of Cu^{2+}. Finally, the Oxygen spectra (O-1*s*) shown in Figure 6.3 (e,f) for both the systems has been resolved into three Gaussian- Lorentzian (GL) peaks

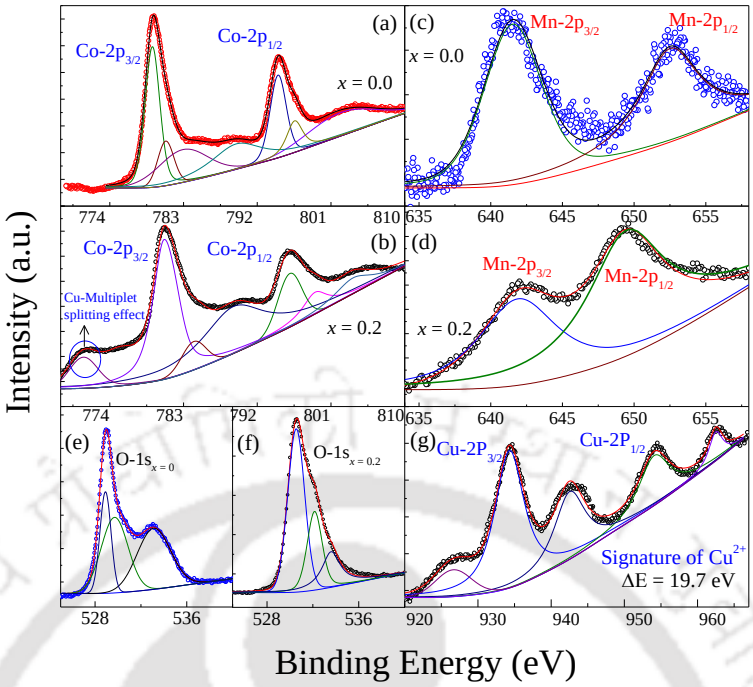

Figure 6.3. The X-ray photoelectron spectra (XPS) of $MnCo_{2-x}Cu_xO_4$ samples. (a), (c) and (e) show Co-2*p*, Mn-2*p* and O-1*s* core level XPS spectra respectively, for $MnCo_2O_4$. Whereas, the figures (b), (d), (f) and (g) show the XPS spectra of Co-2*p*, Mn-2*p*, O-1*s* and Cu-2*p*, respectively for $MnCo_{1.8}Cu_{0.2}O_4$.

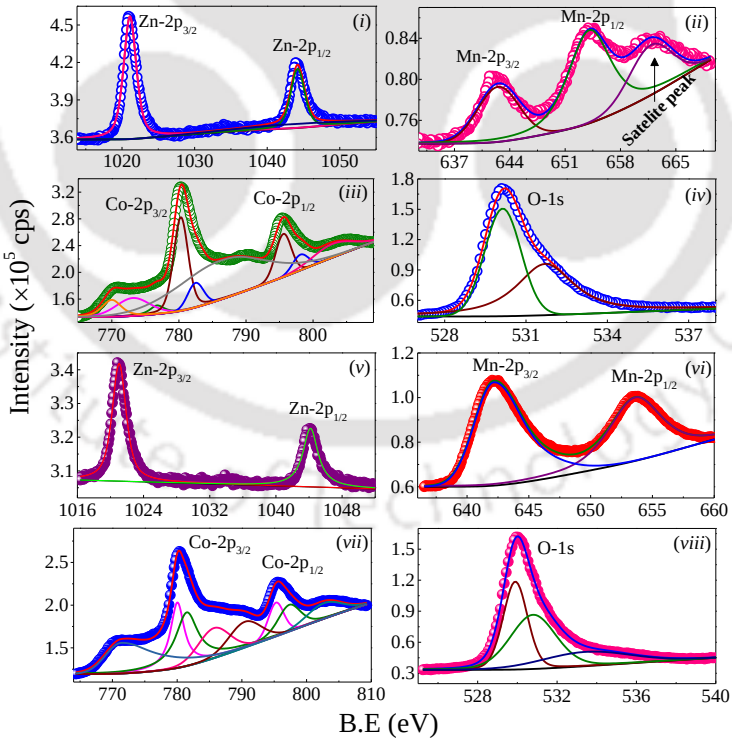

Figure 6.4. The XPS spectra of 2*p* and 1*s* levels of Zn, Mn, Co and O atoms present in $Mn_{0.8}Zn_{0.2}Co_2O_4$ and $MnCo_{1.9}Zn_{0.1}O_4$ compounds. Figures (*i*), (*ii*), (*iii*), (*iv*) are corresponding to the core level XPS spectra of Zn-2*p*, Mn-2*p* Co-2*p* and O-1*s* for $Mn_{0.8}Zn_{0.2}Co_2O_4$. Whereas, the figures (*v*), (*vi*), (*vii*), and (*viii*) represent the core level spectra of the atoms Zn-2*p*, Mn-2*p* Co-2*p* and O-1*s* for $MnCo_{1.9}Zn_{0.1}O_4$.

centered at 530.5 eV, 532.16 eV and 533.6 eV associated with the oxygen-metal bonding, surface oxygen and some extent of additional oxygen at surface, respectively [153,155,282]. On the other hand, the XPS spectra of $Mn_{0.8}Zn_{0.2}Co_2O_4$ and $MnCo_{1.9}Zn_{0.1}O_4$ (shown in figure 6.4) confirms the presence of divalent and trivalent oxidation sates of Co. Whereas, the core level XPS of Mn and Zn ions corroborates the trivalent and divalent oxidation states [267,268,294-296]. Thus, on the basis of the analysis gathered from the Rietveld refinement of XRD data and electronic states obtained from XPS results we determined the following cationic distribution: $(Co^{2+})_A[Mn^{3+}Co^{3+}]_BO^{2-}$ and $(Co_{1-x}{}^{2+}\Sigma_x)_A[Mn^{3+}Co^{3+}]_BO^{2-}$ (where Σ: Cu and Zn) for $MnCo_2O_4$ and Cu/Zn doped samples, respectively.

6.3.3 Magnetic Properties:

In this sub-section we focus on the magnetic properties and exchange interactions of site diluted (Cu and Zn doped) $MnCo_2O_4$ nanoparticles. Figures 6.5 and 6.6 display the temperature dependence of dc-magnetic susceptibility $\chi_{dc}(T)$ (= M/H) of $MnCo_{2-x}Cu_xO_4$ ($0 \le x \le 0.2$), $Mn_{0.8}Zn_{0.2}Co_2O_4$ and $MnCo_{1.9}Zn_{0.1}O_4$ nanocrystals measured under ZFC and FC conditions. All the graphs demonstrate that the present nanoparticles exhibit ferrimagnetic ordering with a giant bifurcation between the $\chi_{ZFC}(T)$ and $\chi_{FC}(T)$ ($\Delta\chi = \chi_{FC} - \chi_{ZFC}$) curves below the peak temperatures (T_P) which signifies superparamagnetic (SPM) blocking /or spin-glass (SG) freezing behavior of these nanoparticles. The insets of figure 6.6 show (for Zn-system) that the peak in χ_{ZFC} significantly shift towards lower temperature with increasing the H_{DC} typical to SPM or SG behavior (T_P ~125.3 K (for 50 Oe) and 15.4 K (for 10 kOe) for $Mn_{0.8}Zn_{0.2}Co_2O_4$. Similar shift was noticed in case of $MnCo_{1.9}Zn_{0.1}O_4$ (T_P ~155.2 K (for 50 Oe) and 15.2 K (for 10 kOe)).

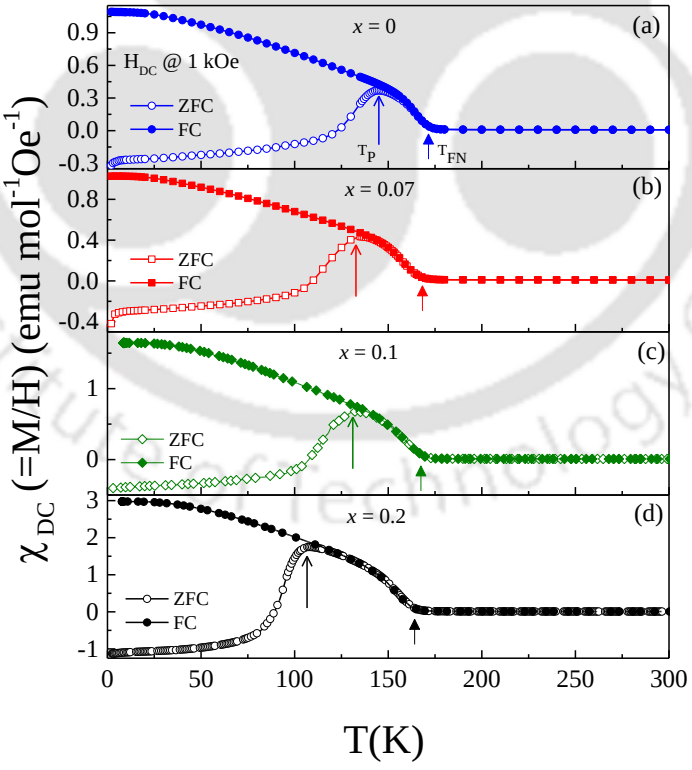

Figure 6.5. Temperature dependence of dc-magnetic susceptibility $\chi_{dc}(=M/H_{dc})$ for nanocrystalline $MnCo_{2-x}Cu_xO_4$: (a) x = 0, (b) x = 0.07 (c) x = 0.1 (d) x = 0.2 samples measured under both ZFC and FC conditions at H_{dc} = 1 kOe.

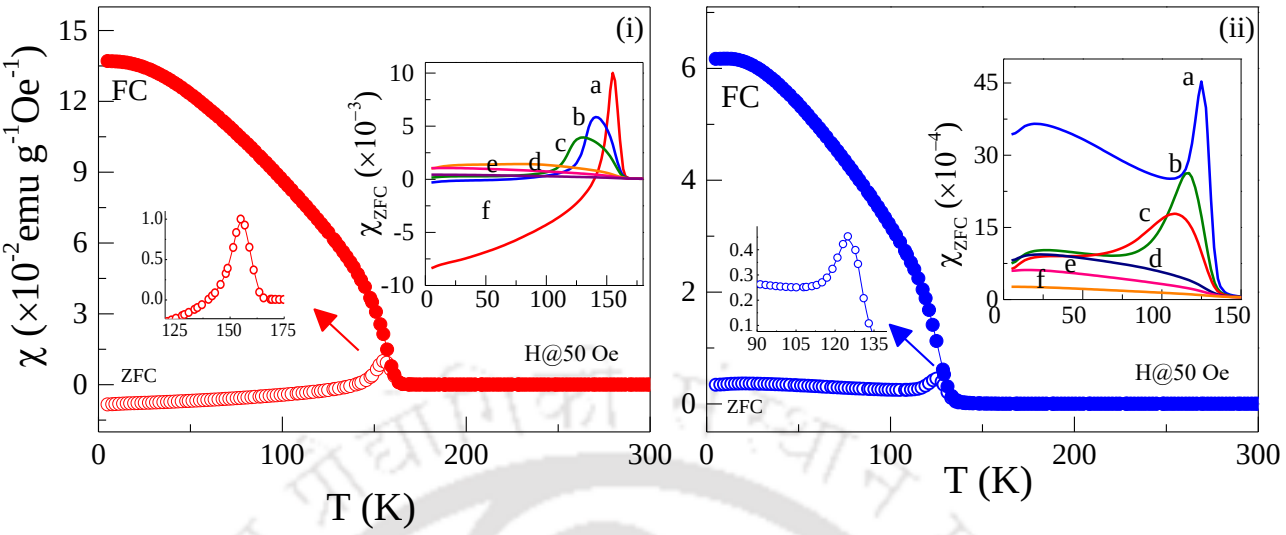

Figure 6.6. Temperature dependence of dc-magnetic susceptibility (χ(*T*)) measured under both ZFC and FC conditions under H_{dc} = 50 Oe for (i) $Mn_{0.8}Zn_{0.2}Co_2O_4$ and (ii) $MnCo_{1.9}Zn_{0.1}O_4$ nanocrystals. Insets show χ_{ZFC} measured at different dc fields [(a) 50 Oe, (b) 500 Oe, (c) 1000 Oe, (d) 5000 Oe, (e) 10 kOe, and (f) 30 kOe].

In case of undoped $MnCo_2O_4$ (x = 0), nanoparticles exhibit the ferrimagnetic ordering below the ferrimagnetic Néel temperature T_{FN} ~ 177 K (figure 6.5 (a)). Moreover, the T_{FN} and T_P decreases gradually towards low temperature with the increasing percentage of doping concentration. The arrow marks in figure 6.5 indicate that the T_{FN} (T_P) values decreases from 165 K (144.8 K) to 155 K (107.6 K) as the Cu-concentration increases from 0 to 20 at.%. However, for $Mn_{0.8}Zn_{0.2}Co_2O_4$ and $MnCo_{1.9}Zn_{0.1}O_4$ systems the T_{FN} (and T_P) values being 127 K (and 125.3 K), and 157 K (and 155.2 K), respectively. Decreasing value of T_{FN} and T_P therefore can be described due to the doping effect of Cu and Zn inside the $MnCo_2O_4$ matrix.

In order to see the role of Cu and Zn substitution on the exchange interactions of $MnCo_2O_4$ we analyzed the high temperature inverse magnetic susceptibility data with the Néel's expression for ferrimagnets. Figure 6.7 shows $\chi_{ZFC}^{-1}(T)$ of undoped as well as doped $MnCo_2O_4$ nanocrystallites for $T > T_{FN}$. Here, the open circles in different colors represent the experimental data points recorded under the ZFC condition, and the solid lines represent the fits to the Néel's expression for ferrimagnets as given below [7]:

$$(1/\chi) = (T/C) + (1/\chi_0) - [\sigma_0/(T - \theta)] \qquad 6.1$$

In the above equation, C is the Curie constant, θ is the Curie–Weiss temperature, χ_0 and σ_0 are constants, and $T_a = C/\chi_0$ is the asymptotic Curie temperature. Generally, T_a represents the strength of the antiferromagnetic exchange coupling between the tetrahedral *A*-site and the octahedral *B*-site cations. Using the relation $C = N\mu_{eff}^2/3k_B$ one can estimate the effective magnetic moment μ_{eff} per formula unit (f.u.). For the undoped $MnCo_2O_4$ nanoparticles we calculated the effective magnetic moment μ_{eff} ~7.92 μ_B/f.u. Considering the spin-only magnetic moment μ(A) = 3.87 μ_B for Co^{2+} ions with spin S = 3/2 and g = 2 at the tetrahedral *A*-sites, the magnetic moment on the octahedral B-site has been evaluated as $\mu(B) = \sqrt{\mu_{eff}^2 - \mu^2(A)}$ = 6.9 μ_B. The experimentally obtained $\mu(B)$ value is much higher than the theoretical value for the spin only moment of Mn^{3+} ($= \mu(B) = g\sqrt{S(S+1)}\mu_B$ = 4.9 μ_B) ions having S = 2 and g = 2.

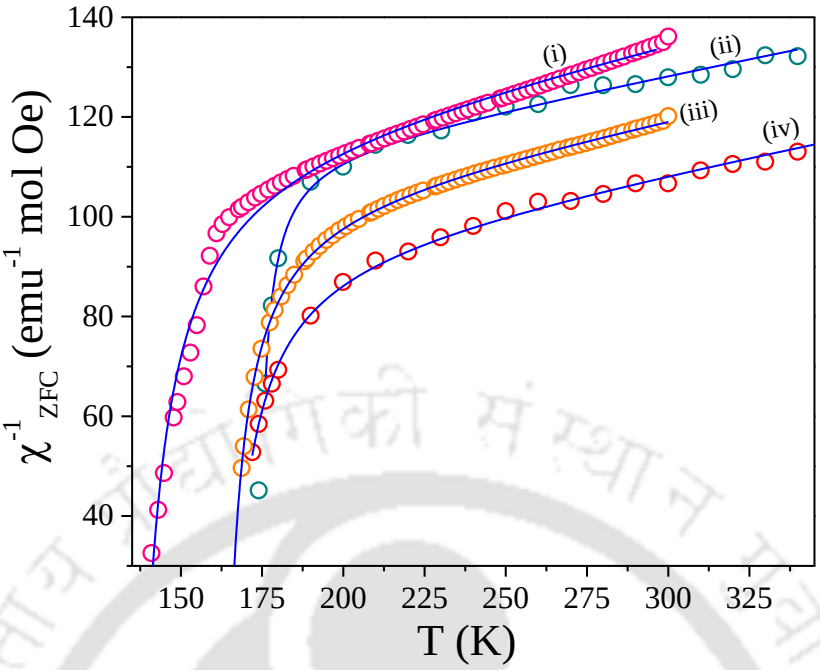

Figure 6.7. Temperature variation of the inverse-magnetic susceptibility $\chi^{-1}_{ZFC}(T)$ of the nanocrystals: (i) $Mn_{0.8}Zn_{0.2}Co_2O_4$, (ii) $MnCo_2O_4$, (iii) $MnCo_{1.9}Zn_{0.1}O_4$ and (iv) $MnCo_{1.8}Cu_{0.2}O_4$. The solid lines represent best fitting of Néel's expression for the ferrimagnets.

Table 6.1 List of parameters obtained from the temperature dependent inverse magnetic susceptibility data $\chi^{-1}(T)$ of undoped $MnCo_2O_4$, and Cu and Zn doped $MnCo_2O_4$ nano-particles using the Néel's expression for ferrimagnets. Total magnetic moment of system = μ_{eff}; molecular field constant = λ_{ij}; and exchange constants = J_{ij}.

Sample	μ_{eff}	$\mu(A)$ [$\mu(B)$]	(λ_{ij})	(J_{ij}/k_B)
$MnCo_2O_4$	7.92 μ_B	3.87 μ_B [6.9 μ_B]	λ_{AA} = 43.8 λ_{BB} = 85.2 λ_{AB} = 110.9	J_{AA} = 8.2 J_{BB} = 21.3 J_{AB} = 13.8
$MnCo_{1.8}Cu_{0.2}O_4$	7.51 μ_B	3.11 μ_B [6.83 μ_B]	λ_{AA} = 21.8 λ_{BB} = 65.2 λ_{AB} = 89.8	J_{AA} = 4.1 J_{BB} = 16.3 J_{AB} = 13.9
$MnCo_{1.9}Zn_{0.1}O_4$	7.88 μ_B	3.3 μ_B [7.1 μ_B]	λ_{AA} = 21.1 λ_{BB} = 72.1 λ_{AB} = 117.8	J_{AA} = 3.9 J_{BB} = 18.1 J_{AB} = 14.7
$Mn_{0.8}Zn_{0.2}Co_2O_4$	7.5 μ_B	4.3 μ_B [6.2 μ_B]	λ_{AA} = 27.1 λ_{BB} = 103.2 λ_{AB} = 107.5	J_{AA} = 5.1 J_{BB} = 25.8 J_{AB} = 13.4

Moreover, the $Co^{3+}(3d^7)$ ions present in the octahedral *B*-site show zero magnetic moments due to the high octahedral crystal field splitting (Δ = 10 Dq ~ 19, 000 cm^{-1} i.e., complete filling of t_{2g} levels) [84]. The difference between the theoretical and experimental value confirms the presence of orbital angular moment of Mn and Co ions. Similarly, we have calculated the magnitude of magnetic moments for other compositions which are listed in Table-6.1. Also, by means of the fitted parameters of the Néel's expression we have evaluated the molecular field constants (λ_{AA}, λ_{BB} and λ_{AB}) and antiferromagnetic exchange constant (J_{AA}, J_{BB}, and J_{AB}) for

these nanoparticles and these values are listed in Table-6.1. Generally, these constants follow the general trends $\lambda_{AB} > |\lambda_{BB}|, |\lambda_{AA}|$ for spinels and all the three interactions are of antiferromagnetic in nature and they are of comparable, except some special cases, where J_{BB} dominates over the other two, which may lead to the development of geometrical frustration [7]. From all the listed values of Table-6.1 one can clearly see the significant changes in the exchange interaction between the magnetic ions in the Cu/Zn doped $MnCo_2O_4$ sample as compared to the undiluted case ($J_{AA}/k_B \sim 8.2$ K, $J_{BB}/k_B \sim 21.3$ K, $J_{AB}/k_B \sim 13.8$ K). The magnitude of all the fitting parameters including the magnetic moments of *A*- and *B*- sites for the nanostructures $MnCo_2O_4$, $MnCo_{1.8}Cu_{0.2}O_4$, $Mn_{0.8}Zn_{0.2}Co_2O_4$ and $MnCo_{1.9}Zn_{0.1}O_4$ are listed in Table-6.1.

In order to understand the nature of peak maxima in $\chi_{ZFC}(T)$ versus T plots observed below T_{FN}, we have performed the temperature dependence of ac-magnetic susceptibility $\chi_{ac}(T)$ across the transition for different frequencies (f) between 0.17 Hz and 1202 Hz and at different bias fields H_{DC}. Therefore, in the following section we focus our discussion mainly on the $\chi_{ac}(T,f)$ and a detailed analysis of $\chi_{ac}(T, H_{DC})$. Figures 6.8 and 6.9 show the temperature dependence of real and imaginary component of the ac-susceptibility $\chi_{ac}(T)$ for $MnCo_2O_4$, $MnCo_{1.8}Cu_{0.2}O_4$, $Mn_{0.8}Zn_{0.2}Co_2O_4$ and $MnCo_{1.9}Zn_{0.1}O_4$ nanoparticles measured using the dynamic field of peak-to-peak amplitude h_{ac} = 4 Oe with zero-dc-bias field. The cusp centered around 155 K in both $\chi'(T)$ and $\chi''(T)$ of $MnCo_2O_4$ nanocrystals shift towards high temperature side with increasing f. Such frequency dispersion indicates the presence of either superparamagnetic or spin-glass nature of the nanocrystallites. A convenient measure for distinguishing between the spin-glass behaviour and superparamagnetic blocking processes is to determine by the relative shift (Ω) of the peak temperature (T_P) in both $\chi'(T)$ and $\chi''(T)$ per decade frequency from the expression ($\Omega = \Delta T_P/(T_P(\Delta \log f))$, where ΔT_P is the change in T_P with change in $\Delta \log f$ [24].

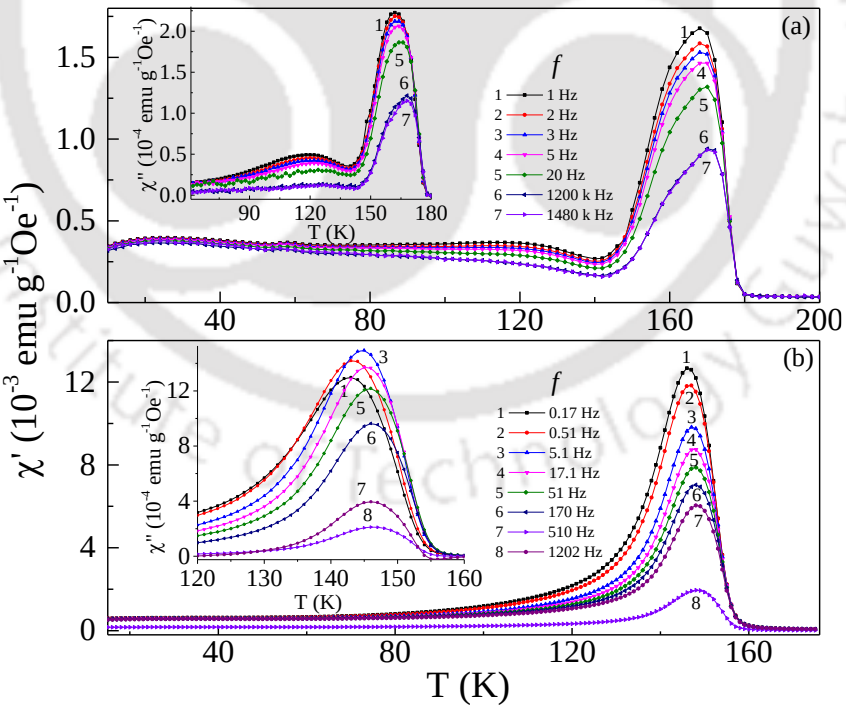

Figure 6.8. Temperature dependence of the real component of ac-magnetic susceptibility $\chi'(T)$, $\chi''(T)$ of (a) $MnCo_2O_4$ and (b) $MnCo_{1.8}Cu_{0.2}O_4$ nanocrystallites recorded at various frequencies in the range 0.17 Hz ≤ f ≤ 1480 Hz under warming condition using ac-signal amplitude h_{ac} = 4 Oe and zero static magnetic field. The insets show temperature dependence of imaginary component of ac-magnetic susceptibility $\chi''(T)$.

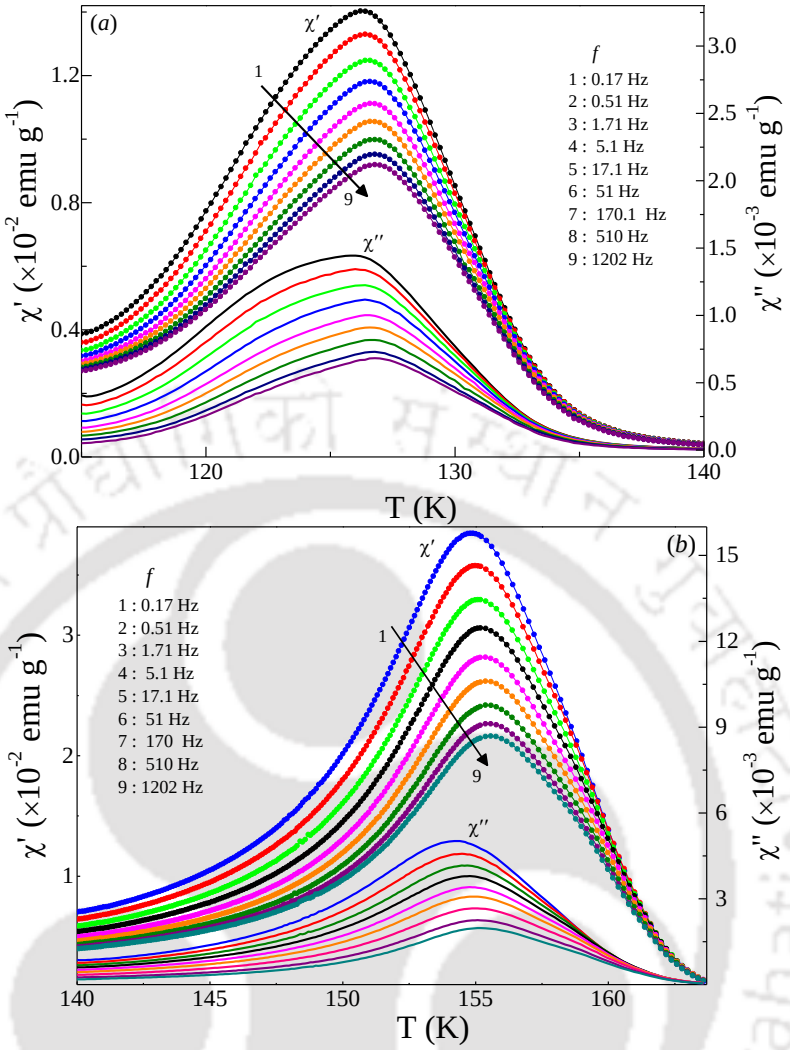

Figure 6.9. Temperature variation of $\chi'(T)$ (left-hand-side scale) and $\chi''(T)$ (right-hand-side scale) of $\chi_{ac}(T)$ for (a) $Mn_{0.8}Zn_{0.2}Co_2O_4$ and (b) $MnCo_{1.9}Zn_{0.1}O_4$ nanocrystallites recorded at various frequencies (f) for H_{dc} = 0 Oe using the constant h_{ac} = 4 Oe.

In the present case, the Ω values of nanoparticles for different compositions are lies between 0.0045 and 0.011. It is well known that Ω should lie between 0.0045 and 0.05 for canonical spin-glasses, but for superparamagnetic system it should be between 0.05 and 0.13. However, the strength of the interparticle interactions decreasing with increasing magnitude of Ω, and Ω > 0.13 for superparamagnetic particles without any interparticle interaction [24, 297-300]. Thus, based on the above discussion and the magnitude of Ω from the $\chi_{ac}(T)$ plots, the present investigated nanoparticles of each composition exhibits spin-glass ordering. To further analyze the above results, we carried out a detailed quantitative analysis of the frequency dependence of peak temperature variation using two empirical scaling laws: (a) Power law $\tau = \tau_0((T/T_F) - 1)^{-z\nu}$ and (b) Vogel–Fulcher law $\tau = \tau_0 \exp(E_a/k_B(T_f - T_0)$. The parameters in the above expressions are defined as follows: τ_0 is the microscopic relaxation time constant, T_0 is a measure of the interaction between magnetic clusters, k_B is the Boltzmann constant, E_a is the activation energy, and $z\nu$ is a critical exponent. Figure 6.10 shows the variation of $\ln\tau$ versus $\ln(T/T_F - 1)$ and the solid lines represent the best-fitting of the experimental data to the Power-

law which yields the following parameters for $MnCo_2O_4$, $MnCo_{1.8}Cu_{0.2}O_4$ nanoparticles, respectively: τ_0 = 1.6×10^{-8} and 8.9×10^{-11}s, T_F = 162.5 and 138.16 K and $z\nu$ = 6.01 and 8.91. Similarly, for $Mn_{0.8}Zn_{0.2}Co_2O_4$ and $MnCo_{1.9}Zn_{0.1}O_4$ system we obtained $\tau_0 = 4.4\times10^{-15}$ and 5.4×10^{-14}s, T_F = 125.7 and 154.3 K and $z\nu$ = 6.17 and 5.2, respectively. In order to estimate the activation energy of spins in glassy state, we used the Vogel–Fulcher law. Using τ_0 values obtained from Power-law analysis, we plotted the logarithmic variation of relaxation time versus peak temperature in Figure 6.11 (ln τ versus $1/(T_f - T_0)$ and $1/(\ln\tau/\tau_0)$ versus T_f), and the experimental data is fitted to the Vogel–Fulcher law which yields the following parameters: E_a = 12.6 and 16.5 k_B, and T_0 = 162 and 140.4 K for $MnCo_2O_4$ and $MnCo_{1.8}Cu_{0.2}O_4$ nanoparticles, respectively. Congruently, we also determined E_a = 29.8 and 10.6 k_B and T_0 = 125.2 and 154.1 K for $Mn_{0.8}Zn_{0.2}Co_2O_4$, $MnCo_{1.9}Zn_{0.1}O_4$ systems, respectively. Further we recalculated the $z\nu$ value from the equation which describes the relation between the Vogel-Fulcher law and the Power-law as: $\ln\left(\frac{40k_BT_0}{E_a}\right) \sim \frac{25}{z\nu}$ established by Souletie and Tholence [218]. The recalculated $z\nu$ values matches well with above results obtained from the Power law analysis and confirms the accuracy of our fitting analysis [218]. For a typical spin-glass system, the magnitude of critical exponent $z\nu$ should lie between 4 and 12 and the relaxation time τ_0 should be of the order of 10^{-9}–10^{-16} s [218,301].

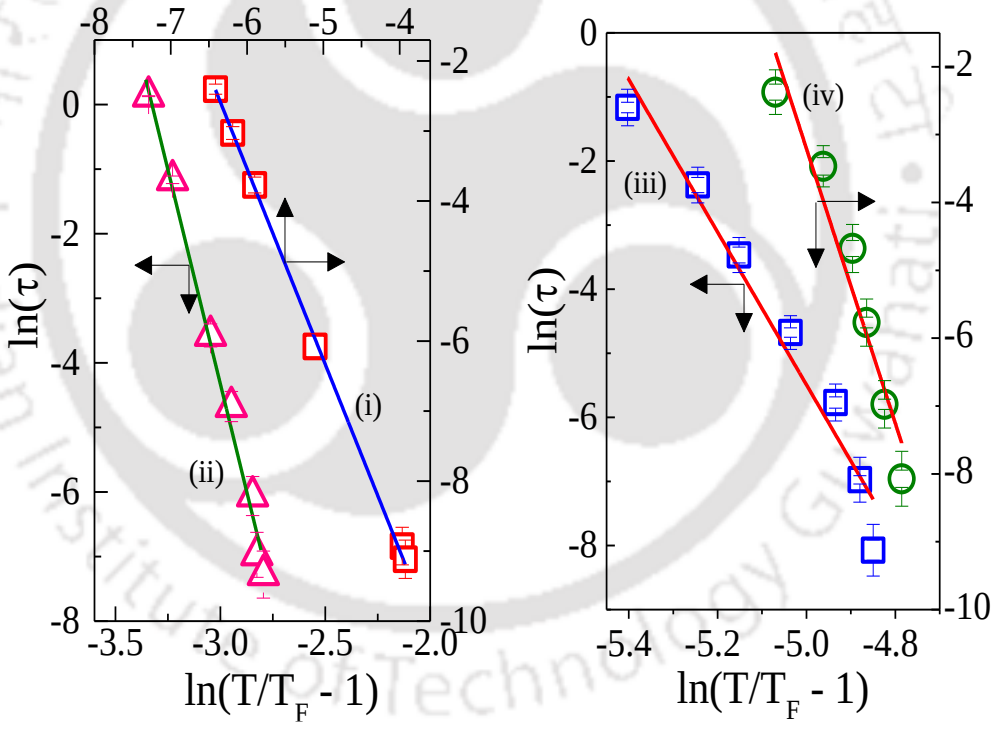

Figure 6.10. Logarithmic variation of the relaxation time ln(τ) plotted as a function of $\ln(T/T_F - 1)$ corresponding to the Power-law. The hollow scattered symbols represent the peak temperature obtained from χ''. Solid lines are mathematical fits corresponding to the experimental data for the nanostructures (i) $MnCo_2O_4$ (ii) $MnCo_{1.8}Cu_{0.2}O_4$ (iii) $Mn_{0.8}Zn_{0.2}Co_2O_4$ and (iv) $MnCo_{1.9}Zn_{0.1}O_4$.

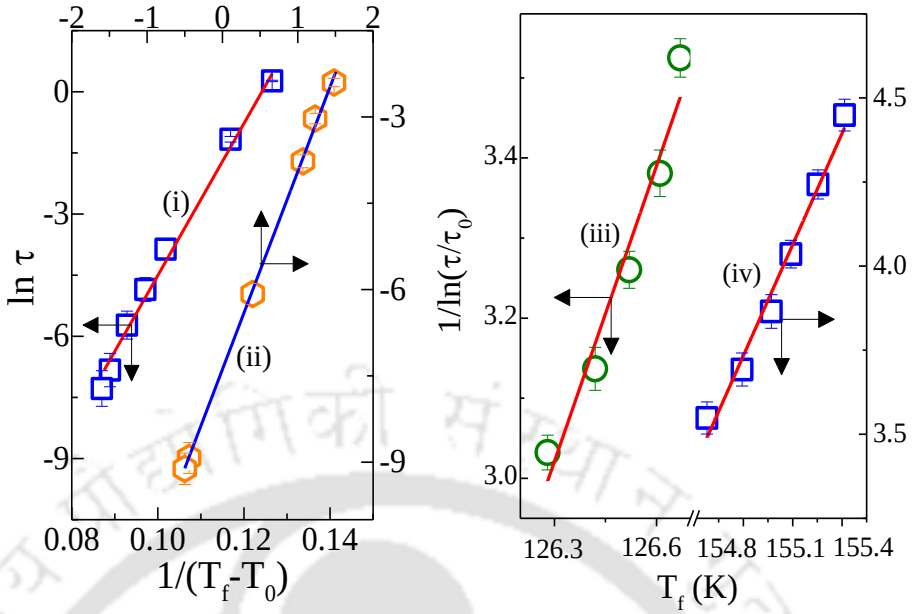

Figure 6.11. Logarithmic variation of the relaxation time ln(τ) plotted as a function of the peak temperature (T_f) corresponding to the Vogel-Fulcher law for (i) $MnCo_2O_4$, (ii) $MnCo_{1.8}Cu_{0.2}O_4$, (iii) $Mn_{0.8}Zn_{0.2}Co_2O_4$ and (iv) $MnCo_{1.9}Zn_{0.1}O_4$ nanoparticles. The hollow scattered symbols represent the peak temperature obtained from χ'' and the solid lines are least square fits to the experimental data.

Figures 6.12 present the $\chi_{ac}(T, H_{dc})$ plot for $MnCo_{1.8}Cu_{0.2}O_4$, $Mn_{0.8}Zn_{0.2}Co_2O_4$ and $MnCo_{1.9}Zn_{0.1}O_4$ samples. All the data shown in figures 6.12 measured at a constant frequency f = 51 Hz with h_{ac} = 3 Oe of ac-field superimposed with H_{DC} (0 Oe-300 Oe). From figures 6.12 one can clearly see that the magnitude of χ'' decreases significantly with a gradual shift in their peak position towards lower temperatures with increasing H_{dc}, which is a typical characteristic of the glassy system. Such variation with increasing H_{dc} can be described by the de Almeida-Thouless (AT) line criterion $T_P(H) \propto T_{P0}(1-H/H_K)^{2/3}$ [302,303]. Here, AT line defines the onset of a transition from the frozen spin-glass like state to the reversible magnetic behavior at the peak temperature T_P in ac-susceptibility under the zero bias-field. The insets of Figure 6.12 (a, b, c) represent the variation of peak maximum temperature (T_P) obtained from χ_{ac} plotted as a function of $H^{2/3}$. The scattered symbols represent the experimentally obtained $T_P(H)$ values for different magnitudes of H_{dc}, and the straight lines are the best fit corresponding to the AT-line equation. Extrapolation of the AT-line back to zero H_{dc} provides the spin-glass freezing temperature T_F = 145.6 K and 156.4 K (127.7 K) for $MnCo_{1.8}Cu_{0.2}O_4$ and $MnCo_{1.9}Zn_{0.1}O_4$ ($Mn_{0.8}Zn_{0.2}Co_2O_4$) systems, respectively (obtained from the χ'' versus T plots). It is possible that T_P cannot be accurately represented because of the variation in nanoparticle size distribution which causes a large change in the interparticle interactions and average freezing temperatures. The competition between the magnetic dipolar interactions and the external magnetic field leads to a spin-glass like behavior in these nanocrystallites. Besides, the $H^{2/3}$ dependence of T_P also suggests the diverging relaxation times due to the competing interactions among the disordered surface-spins than the spins residing in the core of nanoparticles. Usually, the AT-line analysis along with the Power-law is used as one of the tests to identify the spin-glass properties in various magnetic systems, including the nanostructures and bulk compounds [217,218,301,304]. These observations provide the signatures of coexistence of ferrimagnetic ordering (due to longitudinal spin component) at T_{FN} and spin-glass state (due to the transverse spin component) below T_F in the nanostructures of Cu and Zn substituted $MnCo_2O_4$.

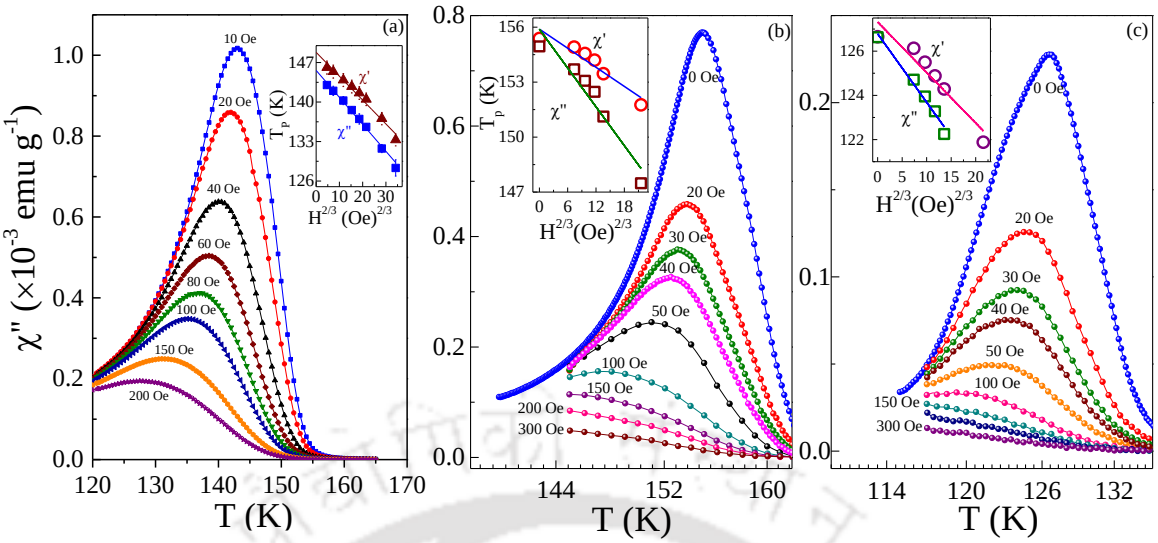

Figure 6.12. Temperature dependence of the imaginary component of ac-magnetic susceptibility (χ'') for different bias fields H_{dc} (0 Oe ⩽ H_{dc} ⩽ 300 Oe) of (a) $MnCo_{1.8}Cu_{0.2}O_4$, (b) $MnCo_{1.9}Zn_{0.1}O_4$ and (c) $Mn_{0.8}Zn_{0.2}Co_2O_4$ nanocrystallites for f = 51 Hz and h_{ac} = 4 Oe. Inset shows the variation of T_P plotted as a function of $H^{2/3}$. This analysis is performed for both the cases, T_P obtained from both χ'(T) and χ''(T). Here the solid lines represent least-squares fitting of the experimental data with the AT-Line equation.

6.4 Conclusions:

This chapter provides some major results of nanostructured $(Co_{1-x}^{2+}\Sigma_x)_A\,[Mn^{3+}Co^{3+}]_B\,O^{2-}$(where Σ: Cu and Zn) systems which are summarized as follows: For the x = 0 nanocrystallites of $MnCo_{2-x}Cu_xO_4$, T_{FN} ~ 165 K is significantly lower than T_{FN} ~ 184 K for the bulk system and this decrease is interpreted to be due to finite-size and surface effects. Moreover, the frequency dependence of the dynamic susceptibility cusp at 165 K exhibits significant dispersion indicating the spin-glass like character. As the Cu substitution level increases (to x = 0.2) a still lower T_{FN} ~ 152 K was observed in these nanostructures with strong spin-glass like character. The analysis obtained from the magnitude of relative shift parameter 'Ω' determined from the change in the peak positions of the $\chi_{ac}(T)$ with change in the measuring frequency clearly indicate the spin-glass ordering in the nanocrystalline of compositions x = 0 and x = 0.2. Further analysis using the dynamic scaling laws; namely Vogel-Fulcher law and Power law, of χ_{ac}-T provides evidence of spin-glass transition T_F just below T_{FN} for both the compositions x = 0 and x = 0.2. The dc-field (H) dependence of $\chi_{ac}(T)$ data reveals that the peak maximum follows the expected $H^{2/3}$ variation (AT-Line analysis) of the spin glass transition T_F which further supports the presence of spin–glass state below the T_{FN} for both the compositions x = 0 and 0.2. It is expected that similar results will be valid for other composition mentioned in this work although a detailed $\chi_{ac}(T)$ measurements in these compositions are not carried out. In the paramagnetic regime, the $\chi^{-1}(T)$ data for x = 0 sample, fits well with the Néel expression for ferrimagnets. Consequently we calculated the effective magnetic moment μ_{eff} = 7.92 μ_B/f.u for undoped $MnCo_2O_4$, with $\mu(A)$ = 3.87 μ_B for Co^{2+} ions with spin S = 2 and μ(B) = 6.9 μ_B. This result is slightly higher than the theoretically obtained value ($\mu(B) = \mu(Mn^{3+})$ = 4.9μ_B) signifying the contribution from orbital magnetic moment μ_L.

For the higher Cu substitution (x = 0.2), μ_{eff} = 7.51 μ_B/f.u with A-site contributions from both Co^{2+} ions (3.87 μ_B) and Cu^{2+} (1.73 μ_B) yields the total magnetic moment $\mu(A)$ = 3.11 μ_B. However, the magnetic moment on the tetrahedral B-site is due to the presence of high-spin Mn^{3+}(S = $2_{H.S}$) and leads to $\mu(B)$ = 6.8 μ_B. On the other

hand, a systematic study of the dc- and ac-magnetic susceptibility of the Zn substituted $MnCo_2O_4$ compounds reveals the presence of ferrimagnetic ordering like the Cu doped system discussed above with different ordering temperatures T_{FN} ~ 157 K for 10 at% Zn dilution at tetrahedral *A*-site. However, T_{FN} ~ 127 K was observed for $MnCo_2O_4$ nanostructures diluted with 20 at% of Zn at the octahedral *B* site of spinel lattice. However, both the compounds under reduced dimensions exhibit super spin-glass characteristics with freezing temperatures T_F ~ 125.7 K ($Mn_{0.8}Zn_{0.2}Co_2O_4$) and T_F ~ 154.3 K ($MnCo_{1.9}Zn_{0.1}O_4$). The antiferromagnetic exchange constants (J_{ij}) evaluated from the $\chi^{-1}(T)$ (for $T > T_{FN}$) and Néel fitting analysis for both the compounds. The nanostructures diluted at *A*-sites leads to a decrease in the exchange interaction by ~ 15% as compared to the undiluted compound. Nevertheless, *B*-site dilution leads to increase in the exchange interaction by 17%, contrary with the 37.5% decrease in case of bulk sample. Moreover, the magnitude of μ_{eff} obtained from $\chi^{-1}(T)$ is ~ 7.5 μ_B for 20at% Zn diluted system and 7.8 μ_B for 10at% of *A*-site Zn diluted system.

Chapter 7
Conclusions and Prospective for Future Work

7.1 Conclusions:

This chapter summarize the important contributions in the field of spinel-Pyrochlore oxides and describe an outlook for the possible future research. In this work we studied the crystal structure and magnetic properties of few spinel oxides by means of neutron scattering and magnetization measurements. This thesis has explored the study on the dynamic behavior of few nanocomposites and bulk systems. Below we sum-up all the results presented in the individual chapters and conclude this chapter by discussing the possible future research work related to the magnetic exchange interactions, spectroscopic and dielectric properties.

Our results reveal that $GeCo_2O_4$ orders antiferromagnetically (AFM) at T_N =20.4 K but with significant short-range ferromagnetic (FM) order up to $T \sim 5T_N$. The paramagnetic susceptibility (χ) fits the modified Curie-Weiss law, $\chi = \chi_o + C/(T - \theta)$, with θ = +51 K for 100 K < T < 800 K. The fit to high-temperature-series expansion (HTS) of χ(T) yields J_1/k_B = 14.7 K as the dominant FM exchange coupling for the pyrochlore lattice of Co^{2+} spins consisting of alternate planes of Kagomé (KGM) and Triangular (TRI) spins lying perpendicular to [111] direction. From the analysis of the *M-H* Isotherms at 2 K, three critical fields are identified: $H_d \sim 11$ kOe due to AFM domains, $H_{C1} \approx 44$ kOe related to spin-flips and FM ordering of the TRI spins, and $H_{C2} \approx 97$ kOe related to FM ordering of the KGM spins. When the external magnetic field greater than H_{C2}, $GeCo_2O_4$ act as a forced ferromagnet with some canting of the spins. Magnetic field dependence of T_N follows the relation $T_N(H) = T_N(0) - D_1H^2$ valid for antiferromagnets with $D_1 = 6.63\times10^{-10}$ K/Oe^2. This magnitude of $T_N(H)$ along with the temperature dependence of three critical fields H_d, H_{C1}, and H_{C2} are used to construct the *H-T* phase diagram which is completely a new analysis. From the magnitudes of the Curie constant (C) and the saturation magnetization at 2 K it is shown that Co^{2+} ions in $GeCo_2O_4$ have the ground state with effective spin S = 1/2. The optical absorption studies using diffusive reflectance spectroscopy of $GeCo_2O_4$ show that its energy band gap $E_g \simeq 3.16$ eV, is in agreement with E_g = 3.28 eV obtained from our DFT+U calculations presented in this thesis work.

Chapter 4 demonstrates the presence of weak Jahn-Teller distortion, negative magnetization, canting spin arrangement and magnetic compensation in $Mn_xTi_{1-x}Co_2O_4$ inverse spinel. In this study we employed neutron diffraction technique along with the magnetic susceptibility measurements extensively over a wide temperature interval 2 K ≤ T ≤ 300 K to unveil the above mentioned phenomena. Specifically, the neutron diffraction study reveals cooperative distortions of the TO_6 octahedra in $Mn_xTi_{1-x}Co_2O_4$ system for all the Jahn-Teller active ions T = Mn^{3+}, Ti^{3+} and Co^{3+}, having the electronic configurations $3d^1$, $3d^4$ and $3d^6$, respectively which are confirmed by the X-ray photoelectron spectroscopy. Two specific composition (x = 0.2 and 0.4) have been chosen in this study because these two systems show unique features such as; (*i*) Noncollinear Yafet-Kittel type magnetic ordering, and (*ii*) Weak tetragonal distortion with c/a < 1, in which the apical bond length d_c(T-O) is longer than the equatorial bond length d_{ab}(T_B-O) due to the splitting of the e_g level of Mn^{3+} ions into $d_{x^2-y^2}$ and d_{z^2}. For the composition x = 0.4, the distortion in the T_BO_6 octahedra is stronger as compared to x = 0.2 because of the higher content of trivalent Mn. Ferrimagnetic ordering in $Ti_{0.6}Mn_{0.4}Co_2O_4$ and $Ti_{0.8}Mn_{0.2}Co_2O_4$ sets in at 110.3 and 78.2 K, respectively due to the unequal magnetic moments of cations occupying at the octahedral (Ti^{3+}, Mn^{3+}, Co^{3+}) and tetrahedral (Co^{2+}) sites. For both compounds an additional weak

antiferromagnetic component could be observed lying perpendicular to the ferrimagnetic component. The analysis of static and dynamic magnetic susceptibilities combined with the heat-capacity data reveal the magnetic compensation phenomena at T_{COMP} = 25.4 K in $Ti_{0.8}Mn_{0.2}Co_2O_4$ system and reentrant spin-glass behaviour in $Ti_{0.6}Mn_{0.4}Co_2O_4$ with freezing temperature ~ 110.1 K. The compensation phenomena in this compound is characterized by sign reversal of magnetization and giant bipolar exchange bias effect below T_{COMP} with its magnitude depending on the direction of external magnetic field and the cooling protocol.

In Chapter 5 we examined the role of Cu on the crystal and magnetic structure of $MnCo_2O_4$ by means of a detailed temperature dependence of neutron diffraction study and ferromagnetic resonance for two specific compositions x = 0 and 0.2. At low temperatures $T \leq 2$ K, the crystal structure of these compositions can be realized in the tetragonal space group $I4_1/amd$ in which the Co_A and Cu_A are having the Wyckoff position 4*b*(0,¼,⅜), while the *B* site cations Mn^{3+} and Co^{3+} ions are located at 8*c*(0,0,0). The nuclear (N) and magnetic (M) reflections of both the compositions reveal that the strongest magnetic contribution arise from (101) and (200)/(112) coherent Bragg reflections with spin sequences $++--$ and $+-+-$ below T_{FN}. Analysis of these results demonstrate that both compounds exhibit noncollinear spin arrangement and weak tetragonal distortion with $c/a < 1$ (due to the Jahn-Teller active ions Mn^{3+} and Co^{3+} in the TO_6 octahedra). Both these systems display ferrimagnetic ordering with T_{FN} ~ 184 K (x = 0) and 171.8 K (x = 0.2) and the net moment $2\mu_{FI}(Mn_B/Co_B) - \mu_{FI}(Co_A) = 0.89\ \mu_B$ for x = 0 and $2\mu_{FI}(Mn_B/Co_B) - \mu_{FI}(Co_A/Cu_A) = 1.93\ \mu_B$ for x = 0.2 at 2 K. Nonetheless, the temperature dependence of net ferrimagnetic moment $\Delta\mu_{FI}(T)$ exhibit maximum (2.081 μ_B) at 154.1 K for x = 0.2, whereas, the undoped system does not exhibit any cusp in $\Delta\mu_{FI}(T)$. Moreover, the presence of additional magnetic reflections (110) and (002) in both the compositions suggest the loss of a least one of the *d*-glide planes which signify the existence of additional antiferromagnetic component lying perpendicular to the ferrimagnetic component.

Next we extended our study to the low-dimensional nanostructures of Cu and Zn diluted $MnCo_2O_4$ with special emphasis on their exchange interactions and magnetization dynamics. In case of Cu doped $MnCo_2O_4$ nanoparticles we performed a detailed comparison for two specific compositions x = 0 and x = 0.2. Our preliminary characterization details such as electronic structure determined from XPS and Rietveld analysis from the XRD patterns reveal the structure to be: $(Co_{(1-x)}^{2+}Cu_x^{2+})_A[Mn^{3+}Co^{3+}]_BO_4$ i.e. Cu^{2+} substitutes for Co^{2+} on the tetrahedral *A*-sites. The bulk samples exhibit higher ferrimagnetic ordering temperature (184 K) for x = 0 as compared to the x = 0.2 system with T_{FN} = 167 K. For the nanosize x = 0 (0.2) samples, the lowered T_{FN} = 165 K (155 K) are observed due to the finite size effects. The exchange interactions between the *A* and *B* site cations of $MnCo_{2-x}Cu_xO_4$ are: J_{AA}/k_B ~ 8.2 K (4.1 K), J_{BB}/k_B ~ 21.3 K (16.3 K) and J_{AB}/k_B ~ 13.8 K (13.9 K) for x = 0 (0.2). Temperature dependence of ac susceptibilities $\chi'(T)$ and $\chi''(T)$ at different frequencies (f) show that in bulk samples of x = 0 and x = 0.2, the transition at T_{FN} is second order in nature. However, the $\chi_{ac}(T,f)$ data of nanostructured samples reveals re-entrant spin-glass behavior at lower temperatures; T_F ~ 162.5 K (138.16 K) for x = 0 (x = 0.20), respectively. Analysis of the $\chi'(T)$ and $\chi''(T)$ data in terms of two different scaling laws: (i) Vogel-Fulcher law ($\tau = \tau_o \exp(E_a/(k_B(T_f - T_o)))$); and (ii) power law of critical slowing-down $\tau/\tau_o = (T/T_F - 1)^{-z\nu}$ confirm the existence of glassy behavior below T_F with the parameters $z\nu$ = 6.01 (8.91), $\tau_o \sim 1.6\times10^{-8}$ s (8.9×10^{-11} s) and T_F ~ 162.5 K (138.16 K) for the samples x = 0 (0.2). The linear behavior of the peak maximum in $\chi_{ac}(T)$ versus $H_{dc}^{2/3}$ (AT-line) further supports the existence of glassy states in nanosize samples. On the other hand, the XPS and XRD results of bulk and nanostructures of Zn diluted $MnCo_2O_4$ reveal the following cationic distribution: $(Co^{2+}_{1-y}Zn^{2+}_y)_A[Mn^{3+}Co^{3+}]_BO_4$ for *A*-site dilution, whereas, *B*-site dilution results the configuration $(Co^{2+})_A[Mn^{3+}_{1-x}Zn^{2+}_xCo^{3+}]_BO_{4\pm\delta}$. The frequency and temperature dependence of dynamic-susceptibility ($\chi_{ac}(f,T)$) studies reveal

the co-existence of ferrimagnetism with spin-glass like behavior below the freezing temperature $T_F \sim 125.7$ K and 154.3 K in the Zn diluted $MnCo_2O_4$. Relaxation time τ follows the Power-Law variation with a dynamical critical exponent $z\nu = 6.17$ (5.2), and microscopic spin relaxation time $\tau_o = 4.4\times10^{-15}$ s (5.4×10^{-14} s) for $Mn_{0.8}Zn_{0.2}Co_2O_4$ ($MnCo_{1.9}Zn_{0.1}O_4$) nanostructures, respectively. The amplitude and peak position in $\chi_{ac}(T)$ decreases with increasing the dc-bias fields indicating that the spin-glass phase can survive in the presence of low-fields forming a critical line with an exponent 2/3 supporting the *de* Almeida–Thouless (AT-line in the *T*-*H* plane) criterion of spin-glass state below T_F. Moreover, the strength of exchange interaction J_{ij} in these inverse spinels decreases by ~15% for A-site dilution relative to the undiluted case. However, B-site dilution results enhancement in J_{ij} by 17%.

7.2 Prospective for Future Work:

The results reported in this thesis embody almost all the characteristics features of the cobalt based insulating oxide spinels based on extensive neutron scattering and magnetic measurements. Nevertheless, some extensions of the current work are possible which are listed below.

(i) In chapter 3, we have discussed the magnetic ground state of $GeCo_2O_4$ sample and determined the exchange constants in detail. However, one can study the phonon dynamics and optical properties at low temperatures because this system exhibits a structural distortion across 16 K below the magnetic long-range ordering temperature ($T_N \sim 21$ K). Hence, in our future work we plan to study a detailed temperature dependence of optical properties.

(ii) Next we extend our work on $Mn_xTi_{1-x}Co_2O_4$ system with a special focus on the magnetic refrigeration application. We plan to perform a detailed characterization pertaining to the magnetic-entropy change (ΔS_M) across the ordering temperature and tune the magnitude and polarity of ΔS_M as a function of Mn concentration. Furthermore, we plan to calculate the density of states and determine the changes occurring in the optical energy band gap as the Mn substitution increases. Analyzing such changes may open a constructive approach for the design and development of magnetocaloric devices.

(iii) In chapter 5 and 6 we studied the effects of Cu^{2+} substitution on the electronic and magnetic structure of the pristine compound $MnCo_2O_4$ only for the few compositions, however it is worth to extend these studies for higher compositions ($x > 0.2$) to realize prominent structural distortion in the parent compound due to Jahn-Teller effect. Also, we planned to study the C-V characteristics of these higher composition samples under low-dimensional nanostructures for battery related applications.

[1] L. Brillouin, Phys. radium. **8**, 74 (1927).
[2] P. Curie, Ann. chim. et phys. (7) **5**, 289 (1895).
[3] R.M. Bozorth, Ferromagnetism (Wiley, Hoboken 2003).
[4] J. C. Slater, J. Appl. Phys. **8**, 385 (1937).
[5] L. Pauling, Phys. Rev. **54**, 899 (1938).
[6] Stephen Blundell, Magnetism in Condensed Matter, Oxford University Press Inc., New York (2001).
[7] Allan H. Morrish, The Physical Principles of Magnetism, Wiley-IEEE Press; 1 edition (2001).
[8] Mathias Getzlaff, Fundamentals of Magnetism, Springer Science & Business Media (2007).
[9] J. C. Slater, Phys. Rev. **35**, 509 (1930).
[10] J. C. Slater, Phys. Rev. **36**, 57 (1930).
[11] G. Hans and S. Karl, Handbuch der physic, Julius Springer (1933).
[12] K. H. J. Buschow, Phys. Status Solidi A **7**, 199 (1971).
[13] J. Hubsch and G. Gavoille, Phys. Rev. B **26**, 3815 (1982).
[14] S. Thota et al., Phys. Rev. B **96**, 144104 (2017).
[15] A. Banerjee, J. Sannigrahi, S. Giri, and S. Majumdar, Phys. Rev. B **98**, 104414 (2018).
[16] F. Varret, A. Hamzic, and I. A. Campbell, Phys. Rev. B **26**, 5285 (1982).
[17] A. Kumar and S. M. Yusuf, Phys. Rep. **556**, 1 (2015).
[18] G. Chern, Lance Horng, W. K. Shieh, and T. C. Wu, Phys. Rev. B **63**, 094421 (2001).
[19] G. Toulouse, Commun. Phys. **2**, 115 (1977).
[20] J. Villain, J. Phys. **C10**, 1717 (1977).
[21] J. Vannimenus and G. Toulouse, J. Phys. C: Solid State Phys. **10**, L537 (1977).
[22] J. S. Gardner, M.J.P. Gingras and J.E. Greedan, Rev. Mod. Phys. **82**, 53 (2010).
[23] A. P. Ramirez, G. P. Espinosa, and A. S. Cooper, Phys. Rev. Lett. **64**, 2070 (1990).
[24] J. A. Mydosh, Spin glasses: an experimental introduction, Taylor & Francis, London, Washington, DC (1993).
[25] K. Binder and A. P. Young, Rev. Mod. Phys. **58**, 801 (1986)
[26] S. F. Edwards and P. W. Anderson, J. Phys. **F5**, 965 (1975).
[27] P. Nordblad, L. Lundgren, L. Sandlund, J. Magn. Magn. Mater., **54**, 185–186 (1986).
[28] C. A. M. Mulder, A. J. van Duyneveldt, and J. A. Mydosh, Phys. Rev. B **23**, 1384 (1981).
[29] B. V. B. Sarkissian, J. Phys. F: Metal Phys. **11**, 2191 (1981).
[30] C. Dekker, A. F. M. Arts, and H. W. de Wjn, J. Appl. Phys. **63**, 4334 (1988).
[31] H. Yoshizawa, S. Mitsuda, H. Aruga, and A. Ito, Phys. Rev. Lett. **59**, 2364 (1987).
[32] V. Cannella and J. A. Mydosh, Phys. Rev. B **6**, 4220 (1972).
[33] W.H. Meiklejohn, C.P. Bean, Phys. Rev. **102**, 1413 (1956).
[34] W.H. Meiklejohn, C.P. Bean, Phys. Rev. **105**, 904 (1957).
[35] J. Hong, J. Kane, J. Hashimoto, M. Yamagishi, K. Noma, and H. Kanai, IEEE Trans. Magn. **38**, 15 (2002).
[36] K. Stoev, F. Liu, Y. Chen, X. Dang, P. Luo, J. Chen, J. Wang, K. Kung, M. Lederman, and M. Re, J. Appl. Phys. **93**, 6552 (2003)
[37] C. Tsang, T. Lin, S. MacDonald, M. Pinarbasi, N. Robertson, H. Santini, M. Doerner, T. Reith, L. Vo, T. Diola, and P. Arnett, IEEE Trans. Magn. **33**, 2866 (1997).
[38] C. Tsang et al., IEEE Trans. Magn. **35**, 689 (1999).
[39] Lin T, Mauri D and Luo Y, IEEE Trans. Magn. **36**, 2563 (2000).
[40] F. H. Liu et al., IEEE Trans. Magn. **36**, 2140 (2000).
[41] A. M. Mack et al., IEEE Trans. Magn. **37**, 1727 (2001).
[42] A. Matsuzono, S. Terada, H. Ono, A. Furukawa, T. Sone, S. Sasaki, Y. Kakihara, Y. Takeda, N. Chiyokubo and H. Matsuki, J. Appl. Phys. **91**, 7267 (2002).
[43] Zhang J, Huai Y and Lederman M, J. Appl. Phys. **91**, 7285 (2002).
[44] A. Tanaka, Y. Shimizu, Y. Seyama, K. Nagasaka, R. Kondo, H. Oshima, S. Eguchi and H. Kanai, IEEE Trans. Magn. **38**, 84 (2002).
[45] J. Sort, S. Suriñach, J. S. Muñoz, M. D. Baró, J. Nogués, G. Chouteau, V. Skumryev and G. C. Hadjipanayis Phys. Rev. B **65**, 174420 (2002).

[46] J. Sort, J. Nogués, X. Amils, S. Suriñach, J. S. Muñoz *and* M. D. Baró, Appl. Phys. Lett. **75**, 3177 (1999).
[47] E.Y. Chen, S. Tehrani, T. Zhu, M. Durlam and H. Goronkin, J. Appl. Phys. **81**, 3992 (1997).
[48] S.S.P. Parkin, X. Jiang, C. Kaiser, A. Panchula, K. Roche and M. Samant, Proc. IEEE **91**, 661 (2003).
[49] G.A. Prinz, Science **282**, 1660 (1998).
[50] G.A. Prinz, J. Magn. Magn. Mater. **200**, 57 (1999).
[51] S.A. Wolf, D.D. Awschalom, R.A. Buhrman, J.M. Daughton, S. Von Molnár, M.L. Roukes, A.Y. Chtchelkanova, D.M. Treger, Science **294**, 1488 (2001).
[52] B. Dieny, V.S. Speriosu, S.S.P. Parkin, B.A. Gurney, D.R.Wilhoit, D. Mauri, Phys. Rev. B **43**, 1297 (1991).
[53] B. Dieny, J. Magn. Magn. Mater. **136**, 335 (1994).
[54] J.C.S. Kools, IEEE Trans. Magn. **32**, 3165 (1996).
[55] E.P. Wohlfarth, Adv. Phys. **8**, 87 (1959).
[56] J. S. Kouvel, J. Phys. Chem. Solids **24**, 795 (1963).
[57] N. H. March, P. Lambin and F. Herman, J. Magn. Magn. Mater. **44**, 1 (1984).
[58] J. Nogu´es and I. K. Schuller, J. Magn. Magn. Mater. **192**, 203 (1999).
[59] J. F. Bobo, L. Gabillet and M. Bibes, J. Phys.: Condens. Matter **16**, S471 (2004).
[60] J. Nogués, J. Sort, V. Langlais, V. Skumrye, S. Suriñach, J.S. Muñoz and M.D. Baró, Phys. Rep. **422**, 65 (2005).
[61] O´. Iglesias, A. Labarta and X. Batlle, J. Nanosci. Nanotechnol. **8**, 2761 (2008).
[62] K.O'Grady, L.E.Fernandez-Outon and G. Vallejo-Fernandez, J. Magn. Magn. Mater. **322**, 883 (2010).
[63] J. S. Kouvel and C. D. Graham Jr., J. Phys. Chem. Solids **11**, 220 (1959).
[64] J. S. Kouvel, J. Phys. Chem. Solids **21**, 57 (1961).
[65] J. S. Kouvel and A. RazzaqW, J. Magn. Magn. Mater. **53**, 139 (1985).
[66] D. Niebieskikwiat and M. B. Salamon, Phys. Rev. B **72**, 174422 (2005).
[67] A. Berger, Ch. Binek, D.T. Margulies, A. Moser, E.E. Fullerton Physica B **372**, 168 (2006).
[68] D. Paccard, C. Schlenker, O. Massenet, R. Montmory, A. Yelon, Phys. Status Solidi b **16**, 301 (1966).
[69] H. Bethe, Annalen der Physik **395**, 133 (1929).
[70] J. H. Van Vleck, J. Chern. Phys. **3**, 803 (1935).
[71] G. Huang, S. Xu, Z, Xu, H. Sun and L. Li ACS Appl. Mater. Interfaces **6**, 21325 (2014).
[72] P. Arun, B. Ranjith and S. Shibli, Environ. Sci. Technol. **47**, 2746 (2013).
[73] T. Nissinen, T. Valo, M. Gasik, J. Rantanen and M. Lampinen, J. Power Sources **106**, 109 (2002).
[74] E. Rios, J. L. Gautier, G. Poillerat and P. Chartier, Electrochim. Acta **44**, 1491 (1998).
[75] E. Jabrya, A. Roussetb and A. Lagrange, Phase Transit. **13**, 13 (1988).
[76] Y. Nii, H. Sagayama, H. Umetsu, N. Abe, K. Taniguchi, and T. Arima, Phys. Rev. B **87**, 195115 (2013).
[77] K. H. Lee, H. Chang, I. Y. Hwang, J.-H. Chung, H. W. Kang, S. J. Kim and S. Lee, Phys. Rev. B **91**, 064404 (2015).
[78] T. Tanaka and S. Ishihara, Phys. Rev. B **79**, 035109 (2009).
[79] S. Ohtani, Y.Watanabe, M. Saito, N. Abe, K. Taniguchi, H. Sagayama, T. Arima, M. Watanabe, and Y. Noda, J. Phys. Condens. Matter **22**, 176003 (2010).
[80] M. Reehuis, M. Tovar, D. Tobbens, P. Pattison, A. Hoser, and B. Lake, Phys. Rev. B **91**, 024407 (2015).
[81] F. Guillou, S. Thota, W. Prellier, J. Kumar, and V. Hardy, Phys. Rev. B **83**, 094423 (2011).
[82] T. Hoshi, H. A. Katori, M. Kosaka, and H. Takagi, J. Magn. Magn. Mater **310**, e448 (2007).
[83] G. Srinivasan and M. S. Seehra, Phys. Rev. B **28**, 1 (1983).
[84] W. Roth, J. Phys. Chem. Solids **25**, 1 (1964).
[85] K. Tomiyasu, H. Ueda, M. Matsuda, M. Yokoyama, K. Iwasa, and K. Yamada, Phys. Rev. B **84**, 035115 (2011).
[86] T. Suzuki and T. Katsufuji, J. Phys. Conf. Ser. **150**, 042195 (2009).
[87] B. C. Melot, J. E. Drewes, R. Seshadri, E. Stoudenmire, and A. P. Ramirez, J. Phys.: Condens. Matter **21**, 216007 (2009).
[88] M. C. Kemei, S. L. Mo_tt, D. P. Shoemaker, and R. Seshadri, J. Phys.: Condens. Matter **24**, 046003 (2012).
[89] R. Tackett, G. Lawes, B. C. Melot, M. Grossman, E. S. Toberer, and R. Seshadri, Phys. Rev. B **76**, 024409 (2007).

[90] T. Suzuki and T. Katsufuji, Phys. Rev. B **77**, 220402 (2008).
[91] S. Hirai, A. M. dos Santos, M. C. Shapiro, J. J. Molaison, N. Pradhan, M. Guthrie, C. A. Tulk, I. R. Fisher, and W. L. Mao, Phys. Rev. B **87**, 014417 (2013).
[92] C. Kim, E. Jo, B. Kang, S. Kwon, S. Lee, J. H. Shim, T. Suzuki, and T. Katsufuji, Phys. Rev. B **86**, 224420 (2012).
[93] R. Padam, S. Pandya, S. Ravi, A. Nigam, S. Ramakrishnan, A. Grover, and D. Pal, Appl. Phys. Lett. **102**, 112412 (2013).
[94] H. Zhang, Z. Wang, E. Liu, W. Wang, M. Yue, and G. Wu, J. Appl. Phys. **117**, 17B735 (2015).
[95] J. Kulikowski and A. Le_sniewski, J. Magn. Magn. Mater. **19**, 117 (1980).
[96] M. Carey, S. Maat, P. Rice, R. Farrow, R. Marks, A. Kellock, P. Nguyen, and B. Gurney, Appl. Phys. Lett. **81**, 1044 (2002).
[97] C. Jiang, L. Wu, W. Wei, C. Dong, and J. Yao, Nanoscale Res. Lett. **9**, 584 (2014).
[98] W. Hu, N. Qin, G. Wu, Y. Lin, S. Li, and D. Bao, J. Am. Chem. Soc. **134**, 14658 (2012).
[99] G. E. L. Processing, J. Am. Chem. Soc. **127**, 6135 (2005).
[100] D. Levy and M. Zayat, The Sol-Gel Handbook (2015).
[101] L. L. Hench and J. K. West, Chem. Rev. **90**, 33 (1990).
[102] R. Corriu and N. Trong Anh, Molecular Chemistry of Sol-Gel Derived Nanomaterials (2009).
[103] V. G. Kessler, in Sol-Gel Handb. pp. 195–224 (2015).
[104] C. Brinker and G. Scherer, Adv. Mater. **3**, 912 (1990).
[105] S. Thota, T. Dutta, and J. Kumar, J. Phys. Condens. Matter **18**, 2473 (2006).
[106] D. C. Joshi, S. Nayak, A. Kumar, A. Mohanta, D. Pamu, and S. Thota, J. Appl. Phys. **119**, 74303 (2016).
[107] C. Kittel, Introduction to Solid State Physics (Publication, New York, NY : Wiley, 1953).
[108] J. Rodríguez-Carvajal, Lab. Léon Brillouin (CEA-CNRS), CEA/Saclay, 91191 Gif Sur Yvette Cedex, France (2015).
[109] W. Kraus and G. Nolze, J. Appl. Crystallogr. **29**, 301 (1996).
[110] J. F. Moulder, Handbook of X-Ray Photoelectron Spectroscopy: A Reference Book of Standard Spectra for Identification and Interpretation of XPS Data (1992).
[111] J. J. Shea, IEEE Electr. Insul. Mag. **19**, 73 (2003).
[112] P. S. Bagus, E. S. Ilton, and C. J. Nelin, Surf. Sci. Rep. **68**, 273 (2013).
[113] http://www.rowbo.info/XPS.html
[114] J. Clarke and A. I. Braginski, The SQUID Handbook (2005).
[115] R. L. Fagaly, Rev. Sci. Instrum. **77**, 101101 (2006).
[116] S. Ran, Gravity Probe B: Exploring Einstein's Universe with Gyroscopes-einstein NASA p. 26 (2004).
[117] S. Shapiro, Phys. Rev. Lett. **11**, 80 (1963).
[118] M. Buchner, K. Höfler, B. Henne, V. Ney and A. Ney, J. Appl. Phys. **124**, 161101 (2018).
[119] S. H.Liao and Y. K. Su, Sens. Actuator B-Chem. **238**, 66 (2017).
[120] Physical Property Measurement System, Heat Capacity Option User's Manual (Quantum Design, 2010).
[121] J. S. Hwang, K. J. Lin, and C. Tien, Rev. Sci. Instrum. **68**, 94 (1997).
[122] G.L. Squires, Introduction to the Theory of Thermal Neutron Scattering (Cambridge University Press, Cambridge, U.K., 1978).
[123] S. W. Lovesey, Theory of Neutron Scattering from Condensed Matter, vol. 2, Clarendon Press, Oxford, (1984).
[124] T. Chatterji, Neutron scattering from magnetic materials, Elsevier (2005).
[125] G. Shirane, S. M. Shapiro and J. M. Tranquada, Neutron scattering with a triple-axis spectrometer, volume Cambridge, Great Britain 2002.
[126] G. Wang, X.P. Gao, P.W. Shen, J. Power Sources **192**, 719 (2009).
[127] S. Jin, G. Yang, H. Song, H. Cui and C. Wang, ACS Appl. Mater. Interfaces **7**, 24932 (2015).
[128] Y. Sharma, N. Sharma, G. Subba Rao, B. Chowdari, Adv. Funct. Mater. **17**, 2855 (2007).
[129] S. Yuvaraj, R. Hari Vignesh, L. Vasylechko, Y. S. Lee and R. Kalai Selvan, RSC Adv. **6**, 69016 (2016).
[130] K. De Strooper, A. Govaert, C. Dauwe, G. Robbrecht, phys. stat. sol. (a) **37**, 127 (1976).

[131] K. De Strooper, phys. stat. sol. (a) **39**, 431 (1977).
[132] J. Hubsch and G. Gavoille, J. Magn. Magn. Mater. **66**, 17 (1987).
[133] S. Thota, V. Narang, S. Nayak, S. Sambasivam, B. C. Choi, T. Sarkar, M. S. Andersson, R. Mathieu and M. S. Seehra, J. Phys. Condens. Matter **27**, 166001 (2015).
[134] J. K. Srivastava, S. Ramakrishnan, V. R. Marathe, G. Chandra, and R. Vijayaraghavan, J. Appl. Phys. **61**, 3622 (1987).
[135] E. Harmon, D. J. Simkin, R. J. Haddad, and W. B. Muir, J. Phys. Colloq. **38**, CI-131 (1977).
[136] P. W. Anderson, Phys. Rev. **102**, 1008 (1956).
[137] S. Diaz, S. de Brion, M. Holzapfel, G. Chouteau, and P. Strobel, Physica B **346**, 146 (2004).
[138] S. Diaz, S. de Brion, G. Chouteau, B. Canals, V. Simonet, and P. Strobel, Phys. Rev. B **74**, 092404 (2006).
[139] M. Matsuda, T. Hoshi, H. Aruga-Katori, M. Kosaka, and H. Takagi, J. Phys. Soc. Jpn. **80**, 034708 (2011).
[140] T. Watanabe, S. Hara, and S. I. Ikeda, Phys. Rev. B **78**, 094420 (2008).
[141] M.S. Seehra, V Singh, S Thota, J. Appl. Phys. **110**, 113907 (2011).
[142] M.S. Seehra, V Singh, S Thota, B Prasad and J Kumar, Appl. Phys. Lett. **97**, 112507 (2011).
[143] W. Schiessl, W. Potzel, H. Karzel, M. Steiner, G. M. Kalvius, A. Martin, M. K. Krause, I. Halevy, J. Gal, W. Schäfer, G. Will, M. Hillberg, and R. Wäppling, Phys. Rev. B **53**, 9143 (1996).
[144] Y. Horibe, M. Shingu, K. Kurushima, H. Ishibashi, N. Ikeda, K. Kato, Y. Motome, N. Furukawa, S. Mori, and T. Katsufuji, Phys. Rev. Lett. **96**, 086406 (2006).
[145] J. C. Lashley, R. Stevens, M. K. Crawford, J. Boerio-Goates, B. F. Woodfield, Y. Qiu, J. W. Lynn, P. A. Goddard, and R. A. Fisher, Phys. Rev. B **78**, 104406 (2008).
[146] P. T. Barton, M. C. Kemei, M. W. Gaultois, S. L. Moffitt, L. E. Darago, R. Seshadri, M. R. Suchomel, and B. C. Melot, Phys. Rev. B **90**, 064105 (2014).
[147] X. Fabréges, E. Ressouche, F. Duc, S. de Brion, M. Amara, C. Detlefs, L. Paolasini, E. Suard, L.-P. Regnault, B. Canals, P. Strobel, and V. Simonet, Phys. Rev. B **95**, 014428 (2017).
[148] K. Tomiyasu, A. Tominaga, S. Hara, H. Sato, T. Watanabe, S. Ikeda, H. Hiraka, K. Iwasa and K. Yamada, J. Phys. Conf. Ser. **320**, 012038 (2011).
[149] K. Tomiyasu, M. K. Crawford, D. T. Adroja, P. Manuel, A. Tominaga, S. Hara, H. Sato, T. Watanabe, S. I. Ikeda, J. W. Lynn, K. Iwasa, and K. Yamada, Phys. Rev. B **84**, 054405 (2011).
[150] S. Okubo, H. Ohta, T. Ijima, T. Yamasaki, W. Zhang, S. Hara, S. Ikeda, H. Oshima, M. Takahashi, K, Tomiyasu, and T. Watanabe, Z. Phys. Chem. **231**, 827 (2017).
[151] M E Lines, Phys. Rev. **131**, 546 (1963).
[152] Z. Wang and M. S. Seehra, J. Phys. Condens. Matter **29**, 225803 (2017).
[153] N. McIntyre and D. Zetaruk, Anal. Chem. **49**, 1521 (1977).
[154] T. H. Ko, K. Devarayan, M. K. Seo, H. Y. Kim and B. S. Kim, Sci. Rep. **6**, 20313 (2016).
[155] H. Nesbitt and D. Banerjee, Am. Mineral. **83**, 305 (1998).
[156] M. Oku and K. Hirokawa, J. Electron Spectrosc. Relat. Phenom. **8**, 475 (1976).
[157] P. Pramanik, S. Thota, S. Singh, D. C. Joshi, B. Weise, A. Waske and M. S. Seehra, J. Phys. Condens. Matter **29**, 425803 (2017).
[158] W. E. Morgan and J. R. Van Wazer, J. Phys. Chem. **77**, 964 (1973).
[159] R. Gopalakrishnan, B.V.R. Chowdari and K.L. Tan, Solid State Ion. **51**, 203 (1992).
[160] L. Jiang, A. G. Fitzgerald, M. J. Rose, K. Christova, A. Manov and V. Pamukchieva, J. Optoelectron. Adv. Mater. **3**, 841 (2001).
[161] S. K. Wang, H.G. Liu, A. Toriumi, Appl. Phys. Lett. **101**, 061907 (2012).
[162] K. Prabhakaran, T. Ogino, Surf. Sci. **325**, 263 (1995).

[163] S. Thota, and S. Singh Nature of magnetic ordering in cobalt-based spinels, Chapter 4 in 'Magnetic Spinels– Synthesis, Properties and Applications', edited by M. S. Seehra (InTech Publishers, Rijeka,2017).
[164] P. Burgardt and M. S. Seehra, Solid State Commun. **22**, 153 (1977).
[165] H.-J. Schmidt, A. Lohmann and J. Richter, Phys. Rev. B **84**, 104443 (2011).
[166] J. D. Rall and M. S. Seehra, J. Phys. Condens. Matter **24**, 076002 (2012).
[167] J. W. Orton, Electron Paramagnetic Resonance (London: Illiffe Books Ltd, 1968) p 202.
[168] M E Fisher, Phil. Mag. **7**, 1731 (1962).
[169] V. Narang, D. Korakakis and M. S. Seehra, J. Magn. Magn. Mater **368**, 353 (2014).
[170] Y. Shapira and S. Foner, Phys. Rev. B **1**, 3083 1970.
[171] M.S. Jagadeesh and M. S. Seehra, Phys. Rev. B **23**, 1185 (1981).
[172] P. Hohenberg and W. Kohn, Phys. Rev. **136**, B864 (1964).
[173] W. Kohn and L. J. Sham, Phys. Rev. **140**, A1133 (1965).
[174] P. E. Blochl, Phys. Rev. B **50**, 17953 (1994).
[175] G. Kresse and D. Joubert, Phys. Rev. B **59**, 1758 (1999).
[176] G. Kresse and J. Furthmuller, Phys. Rev. B **54**, 11169 (1996).
[177] G. Kresse and J. Furthmuller, Comput. Mater. Sci. **6**, 15 (1996).
[178] G. Kresse and J. Hafner, Phys. Rev. B **47**, 558 (1993).
[179] J. P. Perdew, K. Burke, and M. Ernzerhof, Phys. Rev. Lett. **77**, 3865 (1996).
[180] S. L. Dudarev, G. A. Botton, S. Y. Savrasov, C. J. Humphreys, and A. P. Sutton, Phys. Rev. B **57**, 1505 (1998).
[181] P. Kubelka and F. Munk, Z. Tech. Phys. **12**, 593 (1931).
[182] P. Kubelka, J. Opt. Soc. Am. **38**, 448 (1948).
[183] S. Thota, A. Kumar and J. Kumar, Mater. Sci. Eng. B **164**, 30 (2009).
[184] S. Ghosh, S. Singh, D. C. Joshi, P. Pramanik, S. Ghosh, P. K. Mishra, and S. Thota, Phys. Rev. B **98**, 235119 (2018).
[185] M. S. Seehra and T. G. Castner, JR., Phys. Rev. B **1**, 2289 (1970).
[186] K. Krezhov and P. Konstantinov, J. Phys. Condens. Matter **4**, L543 (1992).
[187] S. Thota and M. Seehra, J. Appl. Phys. **113**, 203905 (2013).
[188] D. Mandrus, V. Keppens, and B. Chakoumakos, Mater. Res. Bull. **34**, 1013 (1999).
[189] C. Li, T. Yan, C. Chakrabarti, R. Zhang, X. Chen, Q. Fu, S. Yuan, and G. O. Barasa, J. Appl. Phys. **123**, 093902 (2018).
[190] C. Fu, G. Li, D. Luo, X. Huang, J. Zheng, and L. Li, ACS Appl. Mater. Interfaces **6**, 2439 (2014).
[191] S. Molin, P. Jasinski, L. Mikkelsen, W. Zhang, M. Chen, and P. V. Hendriksen, J. Power Sources **336**, 408 (2016).
[192] Z. Yang, G. Xia, S. P. Simner, and J. W. Stevenson, J. Electrochem. Soc. **152**, A1896 (2005).
[193] B. Boucher, R. Buhl, R. D. Bella and M. Perrin J. Phys. **31** 113 (1970).
[194] G. Granroth, D. Mandrus, V. Keppens, and S. Nagler, Journal of magnetism and magnetic materials **272**, 1306 (2004).
[195] A. K. Mondal, D. Su, S. Chen, A. Ung, H.-S. Kim, and G. Wang, Chemistry-A European Journal **21**, 1526 (2015).
[196] L. Li et al., Electrochim. Acta **116**, 467 (2014).
[197] J. C. Arrebola, A. Caballero, L. Hernán and J. Morales J. Nanomater. **2008**, 16 (2008).
[198] J. K. Srivastava, J. A. Kulkarni, S. Ramakrishnan, S. Singh, V. R. Marathe, G. Chandra, V. S. Darshane and R. Vijayaraghavan J. Phys. C: Solid State Phys. **20**, 2139 (1987).
[199] K. J. Kim and J. W. Heo, J. Korean Phys. Soc. **60**, 1376 (2012).
[200] H. Wei, J. Ma, B. Li, L. An, J. Kong, P. Yu, and D. Xia, NPG Asia Mater. **8**, e255 (2016).
[201] J.-G. Kim, D. Pugmire, D. Battaglia, and M. Langell, Appl. Surf. Sci. **165**, 70 (2000).

[202] NIST 2000 NIST X-Ray Photoelectron Spectroscopy Database (NIST Standard Reference Database vol 20) (Gaithersburg MD: National Institute of Standards, Technology) p 20899
[203] M. C. Biesinger, L. W. Lau, A. R. Gerson, and R. S. C. Smart, Appl. Surf. Sci. **257**, 887 (2010).
[204] V. V. Atuchin, V. G. Kesler, N. V. Pervukhina, and Z. Zhang, J. Electron. Spectrosc. Relat. Phenom. **152**, 18 (2006).
[205] L. Aswaghosh, D. Manoharan, and N. V. Jaya, Phys. Chem. Chem. Phys. **18**, 5995 (2016).
[206] J. Rodríguez-Carvajal, Physica B: Condensed Matter **192**, 55 (1993).
[207] V. F. Sears, in International Tables for Crystallography, edited by A. J. C. Wilson, Vol. C (Kluwer Academic Publishers, Dordrecht/Boston/London, 1995) p. 383.
[208] P. J. Brown, International Tables for Crystallography, edited by A. J. C. Wilson, Vol. C (Kluwer Academic Publishers, Dordrecht/Boston/London, 1995) p. 391.
[209] R. A. Cowley, G. Shirane, R. J. Birgeneau, and H. J. Guggenheim, Phys. Rev. B **15**, 4292 (1977).
[210] R. Chakravarthy, L. M. Rao, S. Paranjpe, S. Kulshreshtha, and S. Roy, Phys. Rev. B **43**, 6031 (1991).
[211] P. Z. Wong, S. V. Molnar, T. T. M. Palstra, J. A. Mydosh, H. Yoshizawa, S. M. Shapiro, and A. Ito Phys. Rev. Lett. **55**, 2043 (1985).
[212] N. S. Murthy, M. Natera, S. Youssef, R. Begum, and C. Srivastava, Phys. Rev. **181**, 969 (1969).
[213] J. Villain *Z. Phys. B Condens. Matter.* **33**, 31 (1979).
[214] M. Bouvier, P. Lethuillier and D. Schmitt, Phys. Rev. B **43**, 13137 (1991).
[215] E. Gopal, Speci_c heats at low temperatures, International cryogenics monograph series (Plenum Press, New York, 1966).
[216] S. Ogawa and S. Waki, J. Phys. Soc. Jpn. **20**, 540 (1965).
[217] J. De Almeida and D. J. Thouless, J. Phys. A **11**, 983 (1978).
[218] J. Souletie and J. Tholence, Phys. Rev. B **32**, 516 (1985).
[219] S. Nakamura, S. Soeya, N. Ikeda, and M. Tanaka, J. Appl. Phys. **74**, 5652 (1993).
[220] M. Mukadam, S. Yusuf, P. Sharma, S. Kulshreshtha, and G. Dey, Phys. Rev. B **72**, 174408 (2005).
[221] M. K. Singh, R. S. Katiyar, W. Prellier, and J. Scott, J. Phys. Condens. Matter **21**, 042202 (2008).
[222] C. Djurberg, K. Jonason, and P. Nordblad, Eur. Phys. J. B **10**, 15 (1999).
[223] H. Bouchiat and P. Monod, J. Magn. Magn. Mater. **54**, 124 (1986).
[224] T. Taniguchi and Y. Miyako, J. Phys. Soc. Jpn. **57**, 3520 (1988).
[225] H. A. Katori and A. Ito, J. Phys. Soc. Jpn. **62**, 4488 (1993).
[226] S. Shtrikman and E. Wohlfarth, Phys. Lett. A **85**, 467 (1981).
[227] K. Binder and A. P. Young, Rev. Mod. Phys. **58**, 801 (1986).
[228] J. Tholence, Solid State Commun. **35**, 113 (1980).
[229] A. P. Ramirez, Annu. Rev. Mater. Sci. **24**, 453 (1994).
[230] C. Urano, M. Nohara, S. Kondo, F. Sakai, H. Takagi, T. Shiraki and T. Okubo, Phys. Rev. Lett. **85**, 1052 (2000).
[231] N. Tristan, J. Hemberger, A. Krimmel, H-A. Krug von Nidda, V. Tsurkan and A. Loidl, Phys. Rev. B **72**, 174404 (2005).
[232] M. M. Thackeray, W. I. F. David, P. G. Bruce and J. B. Goodenough, Mater. Res. Bull. **18**, 461 (1983).
[233] Y. Chen, X.-Y. Zhang, C. Vittoria and V. G. Harris, Appl. Phys. Lett. **94**, 102906 (2009).
[234] Q. Zhang, K. Singh, F. Guillou, C. Simon, Y. Breard, V. Caignaert and V. Hardy, Phys. Rev. B **85**, 054405 (2012).
[235] D. P. Shoemaker, E. E. Rodriguez and R. Seshadri, Phys. Rev. B **80**, 144422 (2009).
[236] R. K. Zheng, G. H. Wen, K. K. Fung and X. X. Zhang, J. Appl. Phys. **95**, 5244 (2004).
[237] Y. Muraoka, H. Tabata and T. Kawai, Appl. Phys. Lett. **76**, 1179 (2000).
[238] K. Tomiyasu, J. Fukunaga and H. Suzuki, Phys. Rev. B **70**, 214434 (2004).
[239] Y. Kwak, J. Song and T. Koo, J. Korean Phys. Soc. **69**, 263 (2016).
[240] H. Chang, I. Y. Hwang, J. H. Chung, J. R. Stewart, W. Higemoto and Y. Miyake, Phys. Rev. B **97**, 014406 (2018).
[241] V. Tsurkan, S. Zherlitsyn, S. Yasin, V. Felea, Y. Skourski, J. Deisenhofer, H.-A. Krug von Nidda, J. Wosnitza and A. Loidl, Phys. Rev. Lett. **110**, 115502 (2013).
[242] Y. Yang, Y. Zhao, L. Xiao and L. Zhang, Electrochem. Commun. **10**, 1117 (2008).

[243] L. Li, G. Jiang and J. Ma, Mater. Res. Bull. **104**, 53 (2018).
[244] Z. Li, X. Huang, J. Hu, A. Stein and B. Tang, Electrochim. Acta **247**, 1 (2017).
[245] H. Wang, Y. Yang, Y. Liang, G. Zheng, Y. Li, Y. Cui and H. Dai, Energy Environ. Sci. **5**, 7931 (2012).
[246] S. Sahoo, K. K. Naik and C. S. Rout, Nanotechnology **26**, 455401 (2015).
[247] S. M. A. Shibli, P. S. Arun and A. V. Raj, RSC Adv. **5**, 19393 (2015).
[248] S. Tamura, J. Phys. Soc. Jpn. **61**, 752 (1992).
[249] P. Joy and S. Date, J. Magn. Magn. Mater. **210**, 31 (2000).
[250] S. Singh, P. Pramanik, S. Sangaraju, A. Mallick, L. Giebeler and S. Thota, J. Appl. Phys. **121**, 194303 (2017).
[251] D. Wickham and W. J. Croft, Phys. Chem. Solids Trans. **7**, 351 (1958).
[252] G. Blasse, Phil. Res. Rep. **18**, 383 (1963).
[253] N. E. Rajeevan et al., J. Phys. Condens. Matter **21**, 406006 (2009).
[254] T. C. Han, S. S. Pan and Y. H. Liu, J. Appl. Phys. **116**, 244104 (2014).
[255] P. Pramanik, D. C. Joshi, N. Tiwari, T. Sarkar, S. Pittala, O. O. Salman, M. M. Manga and S. Thota, J. Appl. Phys. **125**, 124302 (2019).
[256] S. D. Kaushik, N.E. Rajeevan and R. Kumar, Physica B Condens. Matter **55**, 46 (2018)
[257] D. Mandrus, V. Keppens, B. C. Chakoumakos, G. E. Granroth and S. E. Nagler, Mater. Res. Soc. Symp. Proc. **547**, 177 (1999).
[258] P. Pramanik, D. C. Joshi, M. Reehuis, A. Hoser, J.-U. Hoffmann, R. S. Manna, T. Sarkar, and S. Thota, J. Phys. Condens. Matter **32**, 245801 (2020).
[259] R. D. Shannon, Acta Cryst. B **65**, 925 (1969).
[260] B. Boucher, R, Buhl, and M. Perrin, J. Appl. Phys. **42**, 1615 (1971).
[261] C. Ulrich, G. Khaliullin, S. Okamoto, M. Reehuis, A. Ivanov, H. He, Y. Taguchi, Y. Tokura, and B. Keimer, Phys. Rev. Lett. **89**, 167202 (2002).
[262] Y. Kang, D. Zou, J. Zhang, F. Liang, K. Hayashi, H. Wang, D. Xue, K. Chen, K. R. Adair and X. Sun, Electrochim. Acta **244**, 222 (2017).
[263] Y. Li, M. Wu and C. Ouyang, Appl. Surf. Sci. **349**, 510 (2015).
[264] R. Alcantara, M. Jaroba, P. Lavela and J. L. Tirado, Chim. Mater. **1**, S108 (2002).
[265] P. Umadevi and C. L. Nagendra, Sens. Actuator A-Phys. **96**, 114 (2002).
[266] Y. Shimizu and M. Shiotsuka, Jpn. J. Appl. Phys. **41**, 6243 (2003).
[267] X. Liu, H. Liu, W. Zhang, X. Li, N. Fang, X. Wang and J. Wu, Nanoscale Res. Lett. **10**, 195 (2015).
[268] C. Wagner, W. Riggs, L. Davis, J. Moulder and G. Muilenberg, in *Handbook of X-ray Photoelectron Spectroscopy* (Perkin-Elmer Corporation, Eden Prairie, MN, 1979), pp. 74–80.
[269] F. K. Lotgering, Philips Res. Rep. **11**, 337 (1956).
[270] K. He, H. Xu, Z. Wang and L. Cheng, J. Mater, Sci. Technol. **16**, 145 (2000).
[271] G.V. Bazuev and A.V. Korolyov, J. Magn. Magn. Mater **320**, 2262 (2008).
[272] S. Thota, S. K. Das, A. Kumar, S. Sangaraju and B. C. Choi, IEEE Trans. Magn. **49**, 3 (2013).
[273] F. M. M. Borges, D. M. A. Melo, M. S. A. Camara, A. E. Martinelli, J. M. Soares, J. H. de Araujo and F.A.O. Cabral, J. Magn. Magn. Mater. **302**, 273 (2006).
[274] A. J. Bray, Phys. Rev. B. **60**, 720 (1988).
[275] T. Sato, T. Ando and T. Ogawa, Phys. Rev. B. **64**, 184432 (2001).
[276] M. Fricke and J. Hesse, Hyperfine Interactions **93**, 1537 (1994).
[277] Y. Iijima, Y. Kamei, N. Kobayashi, J. Awaka, T. Iwasa, S. Ebisu, S. Chikazawa and S. Nagata, Philosophical Magazine **83**, 2521 (2003).
[278] I. B. Goldberg and T. M. McKinney, in Laboratory Techniques in Electroanalytical Chemistry, edited by P. Kissinger and W. Heineman (Marcel Dekker, New York, 1996), Chap. 29.
[279] A. Wa´skowska, L. Gerward, J. Staun Olsen, S. Steenstrup and E. Talik, J. Phys. Condens. Matter **13**, 2549 (2001).
[280] C. A. Schneider, W. S. Rasband and K. W. Eliceiri, Nat. Methods **9**, 671 (2012).
[281] K. L. Pisane, E. C. Despeaux and M. S. Seehra, J. Magn. Magn. Mater. **384**, 148 (2015).
[282] T.J. Chuan, C.R. Bridle and D.W. Rice, Surf. Sci. **59,** 413 (1976).
[283] E.Z. Kurmaev et al., J. Phys. Condens. Matter. **10,** 4081 (1998).

[284] D.H. Youn, H.T. Kim, B.G. Chae, Y.J. Hwang, J.W. Lee, S.L. Maeng and K.Y. Kang, J. Vac. Sci. Technol. A **22**, 719 (2004).
[285] S.W. Goh, A.N. Buckley, R.N. Lamb, R.A. Rosenberg and D. Moran, Geochim. Cosmochim. Acta **70**, 2210 (2006).
[286] S. Poulston, P.M. Parlett, P. Stone and M. Bowker, Surf. Interface Anal. **24,** 811 (1996).
[287] J. C. Otamiri, S. L. T. Andersson and A. Andersson, Appl. Catal. **65**, 159 (1990).
[288] P. Velásquez, D. Leinen, J. Pascual, J.R. Ramos-Barrado, P. Grez, H. Gómez, R. Schrebler, R. Del Río and R. J. Córdova, Phys. Chem. B **109**, 4977 (2005).
[289] D. N. Wang, A.C. Miller and M. R. Notis, Surf. Interface Anal. **24**, 127 (1996).
[290] L. Meda and G.F. Cerofolini, Surf. Interface Anal. **36**, 756 (2004).
[291] L. Feng, L. Zhang, D.G. Evans and X. Duan, Colloids Surf. A **244**, 169 (2004).
[292] L. J. Kundakovic and M. Flytzani-Stephanopoulos, Appl. Catal. A **171**, 13 (1998).
[293] P. Salvador, J.L.G. Fierrom, J. Amador, C. Cascales and I. Rasines, J. Solid State Chem. **81**, 240 (1989).
[294] S. Ameen, M. S. Akhtar, H.-K. Seo, Y. S. Kim and H. S. Shin, Chem. Eng. J. **187**, 351 (2012).
[295] D. Joshi, S. Nayak, P. Suresh, K. Suresh, B. M. Kumar and S. Thota, Phys. Status Solidi B **252**, 2323 (2015).
[296] S. Wang, Y. Hou and X. Wang, ACS Appl. Mater. Interfaces **7**, 4327 (2015).
[297] S.D. Tiwari and K.P. Rajeev, Phys. Rev. B **72**, 104433 (2005).
[298] G.F. Goya and M.P. Morales, J. Metal. Nanocryst. Mater. **20**, 673 (2004).
[299] M. S. Seehra and K. L. Pisane, J. Phys. Chem. Solids. **93**, 79 (2016).
[300] K. L. Pisane, S. Singh and M. S. Seehra, Appl. Phys. Lett. **110**, 222409 (2017).
[301] C. Lacabane and D. Chatain, J. Phys. Chem. **79**, 283 (1975).
[302] M. Suzuki, S. I. Fullem, I. S. Suzuki, L. Wang and C.-J. Zhong, Phys. Rev. B **79**, 024418 (2009).
[303] F. Jiménez-Villacorta, J. Sánchez-Marcos, E. Céspedes, M. García-Hernández and C. Prieto, Phys. Rev. B **82**, 134413 (2010).
[304] D. Thouless, J. de Almeida and J. Kosterlitz, J. Phys. C Solid State Phys. **13**, 3271 (1980).